ANL-AFCI-285

Resolution of Qualification Issues for Existing Structural Materials

Nuclear Engineering Division

ANL-AFCI-285

Resolution of Qualification Issues for Existing Structural Materials

Prepared for
U.S. Department of Energy
Reactor Campaign

K. Natesan, Meimei Li, and S. Majumdar
Argonne National Laboratory

and

R. K. Nanstad and T. -L. Sham
Oak Ridge National Laboratory

September 2009

EXECUTIVE SUMMARY

This report gives a detailed assessment of several key technical issues that needs resolution for the existing structural materials with emphasis on application in liquid metal reactors (LMRs), in particular, sodium cooled fast reactors. The work is a combined effort between Argonne National Laboratory (ANL) and Oak Ridge National Laboratory (ORNL) with ANL as the technical lead, as part of Advanced Structural Materials Program for the Advanced Fuel Cycle Initiative (AFCI) Reactor Campaign. The report is the second deliverable in FY09 (M2505050201) under the work package "Advanced Materials Code Qualification".

The overall objective of the Advanced Materials Code Qualification project is to evaluate the key technical requirements for the qualification of currently available and future advanced materials for application in sodium reactor systems and the resolution of issues that the U.S. Nuclear Regulatory Commission (NRC) has raised in the past on structural materials in support of the design and licensing of the LMR. Advanced materials are a critical element in the development of sodium reactor technologies. Enhanced materials performance not only improves safety margins and provides design flexibility, but also is essential for the economics of future advanced sodium reactors. Qualification and licensing of advanced materials are prominent needs for developing and implementing advanced sodium reactor technologies. However, the development of sufficient database and qualification of these materials for application in LMRs require considerable amount of time and resources. In the meantime, the currently available materials will be used in the early development of fast reactors.

Nuclear structural component designs in the U.S. comply with the ASME Boiler and Pressure Vessel Code Section III (Rules for Construction of Nuclear Facility Components) and the NRC grants licensing. As the LMR will operate at higher temperatures than the current light water reactors (LWRs), the design of elevated-temperature components must comply with ASME Section III Subsection NH (Class 1 Components in Elevated Temperature Service). Assessment of materials performance issues and high temperature design methodology issues pertinent to the LMR were presented in an earlier report (Natesan et al. 2008). In a subsequent report (Majumdar et al. 2009), we addressed the needs in high temperature methodologies for design of various high temperature components in sodium cooled fast reactor.

The present report addresses several key technical issues for the currently available structural materials such as Type 304 and 316 austenitic stainless steels and ferritic steels such as 2.25Cr-1Mo and modified 9Cr-1Mo. The 60-year design life for the LMR presents a significant challenge to the development of database, extrapolation/prediction of long-term performance, and high temperature structural design methodology. The current Subsection NH is applicable to the design life only up to 34 years. No experimental data contain test durations of 525,000 hours, and it is impractical to conduct such long-term tests in any types of testing. So far the longest creep tests for Grade 91 and Grade 92 steels have run up to 100,000 hours. It has been noted that there is a large drop in creep rupture strength in long-term tests for these high-Cr creep-resistant steels, which may result in overestimation of the long-term creep strength and allowable stress. The report addresses in detail the need for a mechanistic understanding of the structural materials, from the standpoint of the effects of thermal aging, creep deformation, creep fracture, fatigue and creep-fatigue, creep-fatigue predictive models, fatigue and creep crack

growth, and fracture toughness. Based on an in-depth assessment of the available data and mechanistic understanding, key technical issues are identified and discussed for each of the property areas. Furthermore, we have proposed viable approaches to resolve the issues and prioritized our recommendations.

Table of Contents

ACRONYMS

AFCI	Advanced Fuel Cycle Initiative
ANL	Argonne National Laboratory
ASME	American Society of Mechanical Engineers
CRBR	Clinch River Breeder Reactor
DOE	Department of Energy
F-M	Ferritic-Martensitic
HAZ	Heat Affected Zone
IHX	Intermediate Heat Exchanger
INRA	International Nuclear Recycling Alliance
LMFBR	Liquid metal fast breeder reactor
LMP	Larson-Miller Parameter
LMR	Liquid Metal Reactor
LWR	Light Water Reactor
ORNL	Oak Ridge National Laboratory
OSD	Orr-Sherby-Dorn
PHTS	Primary Heat Transport System
PRISM	Power Reactor Innovative Small Module
R&D	Research and Development
SG	Steam Generator
WSRF	Weldment Strength Reduction Factor

RESOLUTION OF QUALIFICATION ISSUES FOR EXISTING STRUCTURAL MATERIALS

1. INTRODUCTION

The objectives of the Advanced Fuel Cycle Initiative (AFCI) are to expand the use of nuclear energy to meet the increasing global energy demand and to address the nuclear waste management. As part of the AFCI program, the Reactor Campaign plans to develop liquid metal reactor (LMR) technologies for commercial use in a closed nuclear fuel cycle in the United States. The campaign is focusing on the sodium-cooled reactor concept because of its technical maturity. The current needs are for larger, more reliable, more economical reactors suitable for commercial nuclear power generation. Research and development focuses on three areas including advanced materials, innovative components and systems, and computer models and simulation.

Economic competitiveness is a key element in the development of advanced reactor technologies. Advanced materials allow compact and simple design of sodium cooling systems and reactor structure, and have the potential to reduce the construction and operational costs for sodium reactors. Heat-, corrosion- and irradiation-resistant alloys are being selected based on economics, reliability, and flexibility of the LMR design. The AFCI Advanced Materials under Reactor Campaign is responsible for developing materials for improved economics, reliability, safety, and design flexibility. The code qualification of advanced materials is in support of the LMR applications.

Nuclear structural component construction in the U.S. complies with the ASME Boiler and Pressure Vessel Code Section III and NRC grants the construction/operation license for the nuclear plant. As the LMR is a sodium-cooled reactor with an outlet temperature of 500-550°C and a 60-year design life, significantly different from the current light water reactors (LWRs), the design of elevated-temperature components must comply with ASME Section III Subsection NH, and also must consider time-dependent effects on mechanical properties such as creep, creep-fatigue, and creep ratcheting. The NRC licensing review of the Clinch River Breeder Reactor (CRBR) and the Power Reactor Innovative Small Module (PRISM) project identified a number of technical issues including weldment safety evaluation, creep-fatigue evaluation, etc, and many of these issues currently remain unresolved.

Subsection NH provides the high temperature design rules for components in nuclear service. The rules were developed in support of the U.S. liquid metal fast breeder reactor (LMFBR) program in 1960s and 70s. Subsection NH has a rather limited choice of materials with only five materials qualified that include Types 304 and 316 austenitic stainless steels, 2.25Cr-1Mo steel, modified 9Cr-1Mo, and Alloy 800H. In addition to developing adequate data for advanced materials, high temperature design rules must also be developed to account for high temperature damages such as creep rupture, excessive creep deformation, creep buckling, cyclic creep ratcheting, and creep fatigue and consider environmental effects. A detailed in-depth assessment of materials' qualification and licensing needs was conducted earlier (Natesan et al. 2008). Several of the technical issues on high temperature design methodology were addressed in a later report

(Majumdar et al. 2009). In particular, the operating condition allowable stresses were presented for NH-approved materials.

Qualification and licensing of advanced materials are prominent needs for developing and implementing advanced sodium reactor technologies. However, the development of sufficient database and qualification of these materials for application in LMRs require considerable amount of time and resources. In the meantime, the currently available materials will be used in the early development of fast reactors.

The present report addresses several key technical issues for the currently available structural materials such as Type 304 and 316 austenitic stainless steels and ferritic steels such as 2.25Cr-1Mo and modified 9Cr-1Mo. The 60-year design life for the LMR presents a significant challenge to the development of database, extrapolation/prediction of long-term performance, and high temperature structural design methodology. The report addresses in detail the need for mechanistic understanding of the structural materials, from the standpoint of the effects of thermal aging, creep deformation, creep fracture, fatigue and creep-fatigue, creep-fatigue predictive models, fatigue and creep crack growth, and fracture toughness. Based on an in-depth assessment of the available data and mechanistic understanding, key technical issues are identified and discussed for each of the property areas. Furthermore, we have proposed viable approaches to resolve the issues and prioritized our recommendations.

2. MATERIALS SELECTION FOR MAJOR COMPONENTS IN LMRs

The sodium-cooled fast reactor is designed to transmute the recycled transuranics to produce energy while also reducing the long-term radiotoxicity and decay-heat loading in the repository. The primary objectives of the prototype LMR are (1) to demonstrate reactor-based transmutation of transuranics, (2) to qualify the transuranics-containing fuels and advanced structural materials needed for a full-scale LMR, and (3) to support R&D and demonstration required for certification of an LMR standard design by the NRC. Additional objectives include (1) incorporation and demonstration of innovative design concepts and features, (2) demonstration of improved technologies for safeguards and security, and (3) the support of development of the design, fabrication and construction, testing and deployment of systems, structures and components infrastructure for the LMR in the U.S. Based on these objectives, a pre-conceptual design for an advanced recycling test reactor was developed by Argonne National Laboratory (ANL), and a report was issued in 2006 (ANL-ABR-1 2006).

Four industry teams were selected by the U.S. Department of Energy (DOE) in 2007 to further develop pre-conceptual designs, technology development roadmaps, and business plans and to provide industry perspectives for potential deployment and commercialization of recycling and reactor technologies in the U.S. The four industry consortia are Energy*Solutions*, General Atomics, General Electric-Hitachi, and the International Nuclear Recycling Alliance (INRA), led by AREVA and Mitsubishi Heavy Industries. The U.S. DOE released detailed reports and presentations developed by the four industry consortia on May 28, 2008. The reports describe pre-conceptual designs, including cost and schedule for an initial nuclear fuel recycling center and advanced recycling reactor. The key plant design parameters for the ARR concept

proposed by ANL and four industrial consortia are summarized in Table 2.1. All designs incorporate passive shutdown and decay heat removal features.

Five alloys have been qualified for elevated temperature structural applications by the ASME Code Subsection NH, namely, Type 304 SS, Type 316 SS, 2.25Cr-1Mo, mod.9Cr-1Mo (Grade 91) and Alloy 800H. There has been extensive experimental and operational experience with most of these materials in liquid metal fast breeder reactors. Table 2.2. summarizes the structural applications of these alloys in previous sodium-cooled reactors worldwide, and Table 2.3 summarizes the Subsection NH materials and their allowables for design.

Table 2.1. Key design parameters for the LMR concepts

Key Parameters	ANL Design	Industrial Teams			
		Energy*Solutions*	GE-Hitachi (PRISM)	GA	INRA
Reactor Power	380 MWe	410 MWe	311 MWe	285 MWe	500 MWe
Reactor type	Pool	Pool	Pool	?	Two-loop
Fuel	Metal; Backup: Oxide	Metal; Backup: MOX	Metal	Metal	Oxide
Cladding material	HT-9	HT-9	HT-9	?	ODS ferritic steel
Coolant	Sodium	Sodium	Sodium	Sodium	Sodium
Coolant Outlet/Inlet	510/355°C	550/395°C	499/360°C	?	?
Reactor Vessel Size	5.8 m dia, 14.8 m H	10.5 m ID 20.5 m H	5.74 m dia, 16.9 m H	?	?
Reactor Vessel Material	Austenitic SS	?	316 SS	?	
IHX Design	Tube-Shell	No IHX	Tube-Shell	?	
IHX Material	?		304 SS	?	
Piping	?	?	Single wall	?	Double wall
Piping material	?	?	2.25Cr-1Mo	?	High- Cr steel
Steam Generator Design	?	Double wall, straight/helical	Helical coil	?	Straight double wall
Steam Generator Material	?	?	2.25Cr-1Mo	?	High-Cr steel
Structural and Piping Material	Austenitic stainless steel	?	316 SS	?	?
Primary Pump	4 EM pumps; Backup: mechanical (centrifugal)	4 EM pumps	Two EM pumps	?	?
Power Conversion Cycle	Rankine steam cycle Backup: CO_2 Brayton cycle	Rankine steam cycle	Rankine steam cycle	?	?
Plant life	30 yr with expectation of 60-yr extension	60 yr	60 yr	60 yr	60 yr
Critical Path	?	Licensing and Economics	Licensing and Commercialization	?	Technology and Licensing

Table 2.2. Materials used in past sodium-cooled reactors.

Country	Reactor	Vessel	IHX	Steam Generator	
				Evaporator	Superheater
USA	Fermi	304	304	Fe-2.25Cr-1Mo	Fe-2.25Cr-1Mo
	EBR-II	304	304	Fe-2.25Cr-1Mo	Fe-2.25Cr-1Mo
	FFTF	304	316	a	a
	CRBR	304	304	Fe-2.25Cr-1Mo	Fe-2.25Cr-1Mo
UK	DFR	316	316	321	321
	PFR	321	321	Fe-2.25Cr-1Mo	316H
Russia	BOR-60	304	304	Fe-2.25Cr-1Mo	Fe-2.25Cr-1Mo
	BN-350	304	304	Fe-2.25Cr-1Mo	Fe-2.25Cr-1Mo
	BN-600	304	304	Fe-2.25Cr-1Mo	304
Germany	SNR-300	304	Fe-2.25Cr-1Mo-Nb	Fe-2.25Cr-1Mo-Nb	Fe-2.25Cr-1Mo-Nb
France	Rapsodie	316L	316	a	a
	Phenix	316L	316	Fe-2.25Cr-1Mo	321
	SuperPhenix	316	316	Alloy 800 tubes 304, 316L shell	b
Japan	Joyo	304	304	a	a
	Monju	304	304	Fe-2.25Cr-1Mo	304

[a]sodium to air heat exchanger; [b]evaporator and superheater are combined in a single unit.

Table 2.3. Materials included in Subsection NH and allowables.

Material	Temperature (°C)	
	Primary stress limits[a]	Fatigue
304	816	704
316	816	704
2.25Cr-1Mo	593[b]	593
Mod.9Cr-1Mo	649	538
800H	760	760

[a]Allowable stresses extend to 300,000 h (34 years).
[b]Temperatures up to 649°C allowed for no more than 1,000 h.

3. GENERAL DESCRIPTION OF CANDIDATE MATERIALS

ASME Section III Subsection NH currently includes five materials: 304 and 316 stainless steel, 2.25Cr-1Mo, mod.9Cr-1Mo and Alloy 800H. Materials of interests for LMR applications are austenitic stainless steels and ferritic steels. The following sections will focus on 304 and 316 austenitic stainless steels, and 2.25Cr-1Mo and mod.9Cr-1Mo ferritic steels.

3.1 Austenitic Stainless Steels

Austenitic stainless steels have been widely used for fast reactor applications, including reactor core, reactor vessel, grid plate, sodium piping, primary heat exchangers, and sodium pumps. Austenitic stainless steels have excellent high temperature mechanical properties and

corrosion resistance, good fabricability and weldability. Compared to the ferritic steels, they are more expensive, and have higher thermal expansion coefficient, and lower thermal conductivity.

Austenitic stainless steels are essentially Fe-Cr-Ni alloys and Table 3.1 lists the chemical compositions of 304 and 316 stainless steels according to the ASTM-A-240 specification.

Table 3.1. Chemical composition of Type 304 and 316 stainless steels.

	Chemical composition (in weight percent)									
Steel	Cr	Ni	Mo	Mn	C	N	Si	S	P	Fe
316 SS	16-18	10-14	2-3	2 max	0.08 max	0.1 max	0.75 max	0.03 max	0.045 max	Bal.
304 SS	18-20	8-12	-	2 max	0.08 max		1 max			

Austenitic stainless steels are normally given a solution treatment at high temperature (1010-1120°C), which results in a fully austenitic solid solution. The initially solution-treated state is thermodynamically unstable. Further changes in microstructure can be made by thermo-mechanical treatment. Long-term thermal aging promotes precipitation of carbides and intermetallics.

The precipitation reactions at high temperature in austenitic stainless steels are complex processes. The precipitates formed at lower temperatures are primarily carbides. Intermetallic compounds form at higher temperatures (Marshall 1984). The major carbide phase in 304 and 316 austenitic stainless steels is $M_{23}C_6$, where M can be a mixture of metallic elements including Fe, Cr, Mo, and Mn, depending on the steel composition and its heat treatment. Chromium is generally the primary metallic element in $M_{23}C_6$ carbides. The precipitation of this carbide phase is a long-range diffusion process, and therefore, precipitation can be avoided by rapid cooling from the solution treatment temperature. Carbides, such as $M_{23}C_6$ primarily precipitate at the austenite grain boundaries, and its precipitation can change the chemistry in the vicinity of grain boundaries. The depletion of Cr atoms at grain boundaries causes susceptibility of the steel to intergranular corrosion cracking. Laves phase, Fe_2Mo and σ phase are the major intermetallic phases. Laves phase forms at temperatures above 600°C in 316 SS (Marshall 1984). It precipitates mostly within grains, and occasionally at grain boundaries. The σ phase is a hard, brittle intermetallic phase with a nominal composition of FeCr. This phase precipitates at triple points, grain boundaries, or incoherent twins or within grains after long-term exposure at high temperatures (Marshall 1984).

Significant issues identified by the NRC in using austenitic stainless steels for fast reactor structural applications include erosion-corrosion and property degradation in sodium environment, effects of neutron embrittlement for a 60-year lifetime, sensitization and stress corrosion cracking at elevated temperatures, effects of secondary phases, hot cracking and creep-fatigue fracture.

The specifications, product forms, types, grades, or classes of 304 and 316SS that are permitted in ASME Code, Section III, Subsection NH are listed in Table 3.2. The specified minimum yield strength at room temperature for all the product forms, types, grades and classes is 207 MPa. Depending on the product form, type, grade and class, the specified minimum tensile

strength at room temperature for the 316SS is either 517 MPa or 483 MPa. The information Subsection NH provides on Types 304 and 316 stainless steels is given in Tables 3.3 and 3.4.

Table 3.2. Product forms of 316SS permitted under Subsection NH.

Permitted 304 and 316SS for Subsection NH [Notes (1) to (3)]		
Spec. No.	Product Form	Types, Grades, or Classes
SA-182	Fittings & Forgings	F304, F304H, F 316, F 316H
SA-213	Seamless Tube	TP304, TP304H, TP 316, TP 316H
SA-240	Plate	304, 304H, 316, 316H
SA-249	Welded Tube	TP304, TP304H, TP 316, TP 316H
SA-312	Welded & Seamless. Pipe	TP304, TP304H, TP 316, TP 316H
SA-358	Welded Pipe	304, 304H, 316, 316H
SA-376	Seamless Pipe	TP304, TP304H, TP 316, TP 316H
SA-403	Fittings	WP304, WP304H, WP304W, WP304HW WP 316, WP 316H, WP 316W, WP 316HW
SA-479	Bar	304, 304H, 316, 316H
SA-965	Forgings	F304, F304H, F 316, F 316H
SA-430	Forged & Bored Pipe	FP304, FP304H, FP 316, FP 316H

Notes:
(1) These materials shall have minimum specified room temperature yield strength of 207 MPa and a minimum specified carbon content of 0.04%.
(2) For use at temperatures above 540°C, these materials may be used only if the material is heat treated by heating to a minimum temperature of 1040°C and quenching in water or rapidly cooling by other means.
(3) Appendix X of Subsection NH provides non-mandatory guidelines on additional specification restrictions to improve performance when materials are used within the temperature regimes of 425°C to 595°C.

Table 3.3. Type 304 stainless steel information in Subsection NH

Quantity	Max. T (°C)	Max. Time (h)	Source
Tensile strength value (S_0)	800	NA	Table NH-3225-1
Tensile and yield strength reduction factor due to long time prior elevated temperature service	NA	NA	Table NH-3225-2
Maximum allowable stress intensity, S_0	816	NA	Table I-14.2
Allowable stress intensity values, S_{mt}	800	300,000	Table I-14.3A
Allowable stress intensity values, S_t	800	300,000	Table I-14.4A
Yield strength values, S_y	816	NA	Table I-14.5
Expected minimum stress-to-rupture values, S_r	800	300,000	Table I-14.6A
Stress rupture factors for welds	750	300,000	Table I-14.10 A-1 to 3
Design fatigue strain range, ε_t	705	1E6 cycles	Table I-1420-1A
Creep-fatigue damage envelope			Figure T-1420-2
Temperature limit for isochronous stress-strain curves	816	300,000	Table T-1820-1 Figs. T-1800-A-1 to 15

Table 3.4. Type 316 stainless steel information in Subsection NH

Quantity	Max. T (°C)	Max. Time (h)	Source
Tensile strength value (S_0)	800	NA	Table NH-3225-1
Tensile and yield strength reduction factor due to long time prior elevated temperature service	NA	NA	Table NH-3225-2
Maximum allowable stress intensity, S_0	816	NA	Table I-14.2
Allowable stress intensity values, S_{mt}	800	300,000	Table I-14.3B
Allowable stress intensity values, S_t	800	300,000	Table I-14.4B
Yield strength values, S_y	816	NA	Table I-14.5
Expected minimum stress-to-rupture values, S_r	800	300,000	Table I-14.6B
Stress rupture factors for welds	750	300,000	Table I-14.10 B-1 to 3
Design fatigue strain range, ε_t	705	1E6 cycles	Table I-1420-1B
Creep-fatigue damage envelope			Figure T-1420-2
Temperature limit for isochronous stress-strain curves	816	300,000	Table T-1820-1 Figs. T-1800-B-1 to 15

3.2 Ferritic Steels

3.2.1 2.25Cr-1Mo Steel

The ferritic 2.25Cr-1Mo steel is widely used as tubes for boilers and heat exchangers and as components for pressure vessels. It has been extensively studied as much if not more than any other boiler materials. It is being considered as structural material for steam generators of sodium-cooled fast reactors. 2.25Cr-1Mo steel has low cost, high thermal conductivity, good fabricability, and good resistance to stress corrosion cracking in aqueous and steam media. The drawbacks of 2.25Cr-1Mo steel are its low design stress allowables, corrosion in sodium, and atmospheric rusting (Natesan et al. 2008). The chemical specification of ASTM T22 (A213) is: 0.05-0.15 C, ≤0.50 Si, 0.30-0.60 Mn, ≤0.025 P, ≤0.025 S, 1.90-2.60 Cr, 0.87-1.13Mo (wt.%). The minimum value of the room-temperature yield strength is 275 MPa, and tensile strength 415 MPa.

The strength of 2.25Cr-1Mo steel depends on the microstructure, which in turn, depends on the thermal-mechanical processing. Three common heat treatment practices for 2.25Cr-1Mo steel are fully anneal, isothermal anneal, and normalization and tempering. The full-anneal treatment is often carried out at the austenizing temperature (e.g. 927°C) for a given time (e.g. 1h) for austenitization and furnace cooled. The isothermally annealing treatment refers to annealing and furnace cooling from the austenitizing temperature, and holding at a temperature in the range of 677-732°C for a given time, and then furnace cooled (Klueh 1977). In the fully annealed and isothermally annealed conditions, the microstructure of 2.25Cr-1Mo is primarily proeutectoid ferrite with different amounts of bainite and pearlite. The relative amount of bainite and pearlite depends on the cooling rate during the heat treatment (Klueh 1981). The microstructure of normalized-tempered 2.25Cr-1Mo is essentially 100% tempered bainite.

The isothermally annealed 2.25Cr-1Mo steel showed significantly better tensile properties after neutron irradiation. For example, the isothermally-annealed 2.25Cr-1Mo irradiated at ≈50°C to 9 dpa and tested at 300°C has uniform and total elongations of 6.7 and 10.1%, respectively, compared with uniform and total elongation of less than 1 and 4%, respectively, for normalized-and-tempered 2.25Cr-1Mo steel (Klueh 1983).

The allowable stress values and isochronous stress-strain curves for 2.25Cr-1Mo in ASME Code Case 1592 are based on data for air-melted material in the annealed condition. Table 3.5 lists the Subsection NH information for 2.25Cr-1Mo steel.

Table 3.5. 2.25Cr-1Mo steel information in Subsection NH

Quantity	Max. T (°C)	Max. Time (h)	Source
Tensile strength value (S_0)	650	NA	Table NH-3225-1
Tensile and yield strength reduction factor due to long time prior elevated temperature service	575 650	300,000 1000	Table NH-3225-2 Table NH-3225-3A, 3B
Maximum allowable stress intensity, S_0	593	NA	Table I-14.2
Allowable stress intensity values, S_{mt}	575 650	300,000 1000	Table I-14.3D
Allowable stress intensity values, S_t	575 650	300,000 1000	Table I-14.4D
Yield strength values, S_y	650	NA	Table I-14.5
Expected minimum stress-to-rupture values, S_r	575 650	300,000 1000	Table I-14.6D
Stress rupture factors for welds	650	300,000	Table I-14.10 D-1
Design fatigue strain range, ε_t	595	1E6 cycles	Table I-1420-1D
Creep-fatigue damage envelope			Figure T-1420-2
Temperature limit for isochronous stress-strain curves	593 649	500,000 1000	Table T-1820-1 Figs. T-1800-D-1 to 11

3.2.2 Modified 9Cr-1Mo Steel

Modified 9Cr-1Mo (Grade 91) is a Fe-9%Cr-1%Mo ferritic steel modified with V and Nb. The alloy has superior creep properties and corrosion resistance to 2.25Cr-1Mo, lower thermal expansion coefficient, higher thermal conductivity, and better resistance to stress corrosion cracking in aqueous and chloride environments than austenitic stainless steels. The maximum allowable stress intensity of G91 exceeds that of 2.25Cr-1Mo at all temperatures, and is equivalent to that of type 304 SS at 600°C, as shown in Fig. 3.1. The high-temperature strength of Grade 91 relies on tempered martensitic microstructure stabilized by $M_{23}C_6$ carbides and a fine distribution of vanadium/niobium rich carbo-nitride (MX) precipitates. Molybdenum in the solution also contributes to the strength of Grade 91. The improved high temperature strength of Grade 91 allows construction of thinner-wall components, resulting in lower thermal stresses during transients and lower material costs. However, the superior properties of Grade 91

highly depend on the creation of an appropriate microstructure from fabrication and heat treatment and maintenance of the microstructure during service.

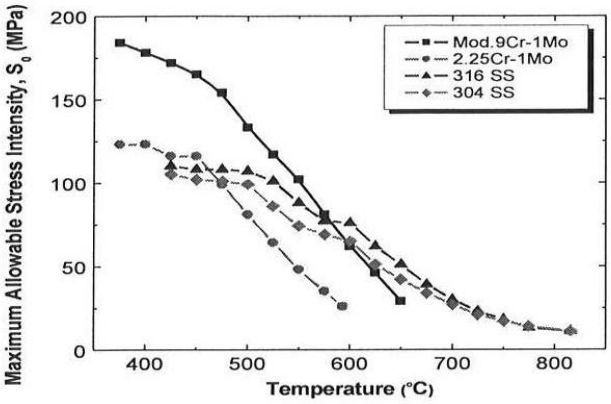

Figure 3.1. Maximum allowable stress intensity for the NH materials. Values are from NH Table I-14.2.

Modified 9Cr-1Mo steel was developed in the late 1970s for Intermediated Heat Exchanger and steam generator applications for liquid metal reactors (LMRs) in the U.S. In 1974, the U.S. DOE initiated a three-phase study for developing a new alloy for the use in LMRs. Mod.9Cr-1Mo was selected, based on creep strength and microstructural considerations. A development program for mod.9Cr-1Mo steel started in the early 1980s, and considerable information on mod.9Cr-1Mo steel was generated through the DOE-sponsored programs and industrial development. Over 800 tons of mod.9Cr-1Mo material was melted and processed. An extensive mechanical properties database was established in air environment, including tensile, toughness, creep, and fatigue properties. Some creep-fatigue data were also obtained, but were considered insufficient. The general findings were that the alloy has good long-term performance for out-of-core structural applications in LMRs, and is resistant to irradiation swelling. Limited data in sodium showed no significant deleterious effects on mechanical properties. Long-term testing data in sodium are lacking. Regarding the joining behavior of mod.9Cr-1Mo, it was concluded that no major problems were discovered with the weldability of the alloy. However, data are needed on mechanical properties of weldments and the effects of long-term aging. In recent years, with increased usage and industrial experience, more problems have been identified with mod.9Cr-1Mo welds.

Modified 9Cr-1Mo steel was first approved for use in the ASME Section I in 1984. It was approved in 1993 in the AMSE Power Piping Code, B31.1 for seamless pipe in Specification SA-335 and plate in Specification SA-387. An initial data package was submitted to ASME for inclusion of G91 in Section III, Code Case N-47 in 1983. A revised data package was submitted in November 1984 with a more extensive set of tensile, creep, fatigue, and creep-fatigue data. Specifications of mod.9Cr-1Mo steel have been included in the ASTM standards for plate, tube, pipe, and forgings. The same specifications were also included in ASME Code. The product forms, types, grades, or classes, and chemical specifications for Grade 91 permitted in ASME III-NH are given in Table 3.6. The alloy is recommended for use in normalized and tempered condition. The specified minimum yield strength and tensile strength at room temperature for all the product forms, types, grades and classes are 415 MPa (60 ksi) and 585 MPa (85 ksi), respectively. The maximum temperature permitted by Subsection NH for Grade 91 is 649°C (1200°F).

The permissible weld materials for G91 includes SFA-5.5 (E90XX-B9), SFA-5.23 (EB9), and SFA-5.28 (ER90S-B9).

Table 3.6. ASME III-NH permissible chemical specifications for mod.9Cr-1Mo steel

Specification No	SA-182 [Note (1)]	SA-213	SA-335	SA-387
Product Form	Forgings	Seamless Tube	Seamless Pipe	Plate
Types/Grade/Class	F91	T91	P91	91
Element	Composition in weight percent			
C	0.08-0.12	0.08-0.12	0.08-0.12	0.08-0.12
Mn	0.30-0.60	0.30-0.60	0.30-0.60	0.30-0.60
P	0.020 max	0.020 max	0.020 max	0.020 max
S	0.010 max	0.010 max	0.010 max	0.010 max
Si	0.20-0.50	0.20-0.50	0.20-0.50	0.20-0.50
Ni	0.40 max	0.40 max	0.40 max	0.40 max
Cr	8.0-9.5	8.0-9.5	8.0-9.5	8.0-9.5
Mo	0.85-1.05	0.85-1.05	0.85-1.05	0.85-1.05
Nb	0.06-0.10	0.06-0.10	0.06-0.10	0.06-0.10
N	0.03-0.07	0.03-0.07	0.03-0.07	0.03-0.07
Al	0.04 max	0.04 max	0.04 max	0.04 max
V	0.18-0.25	0.18-0.25	0.18-0.25	0.18-0.25
Ti			0.01 max	
Zr			0.01 max	

Note: (1) This specification limits forging size to 4540 kg (10,000 lb).

The baseline tensile and creep properties of G91 have been documented in the Nuclear Systems Materials Handbook (NSMH). Properties in NSMH include yield strength, tensile strength, tensile ductility, creep strain-time behavior, creep rupture strength, time to tertiary creep, and creep rupture ductility. Table 3.7 lists the information for G91 in Subsection NH.

Table 3.7. Information for G91 in Subsection NH

Quantity	Max. T (°C)	Max. Time (h)	Source
Tensile strength value (S_0)	650	NA	Table NH-3225-1
Tensile and yield strength reduction factor due to long time prior elevated temperature service	650	300,000	Table NH-3225-2 Table NH-3225-4
Maximum allowable stress intensity, S_0	650	NA	Table I-14.2
Allowable stress intensity values, S_{mt}	650	300,000	Table I-14.3E
Allowable stress intensity values, S_t	650	300,000	Table I-14.4E
Yield strength values, S_y	650	NA	Table I-14.5
Expected minimum stress-to-rupture values, S_r	650	300,000	Table I-14.6F
Stress rupture factors for welds	650	NA	Table I-14.10 E-1
Design fatigue strain range, ε_t	540	1×10^8 cycles	Table I-1420-1E
Creep-fatigue damage envelope			Figure T-1420-2
Temperature limit for isochronous stress-strain curves	649	300,000	Table T-1820-1 Figs. T-1800-E-1 to 11

Industrial experience on Grade 91 in the U.S. includes G91 tubing installed in fossil-fired steam power plants (DiStefano et al. 1986) and two pipe sections of G91 installed in the EBR-II secondary sodium system operated at 454°C in 1984.

4. THERMAL AGING EFFECTS

4.1 Assessment of Thermal Aging Effects

Long-term exposure at LMR operating temperatures can result in microstructural changes and associated mechanical property degradation even in Code-qualified structural materials. Long-term aging and its effects on mechanical performance of reactor structural components have been a concern. Correlation between microstructure and mechanical properties is important for extrapolating materials behavior to anticipated design lifetime of 60 years or more.

4.1.1 Austenitic Stainless Steels

Several reviews on the mechanical properties and microstructure of thermally aged 304 and 316 stainless steels are available in the literature. Horak et al. (1983, 1985) reviewed the mechanical properties and microstructures of Type 304 and 316 SS wrought alloys, welds, and castings after long-term aging in air to 125,000 h at temperatures between 427 and 649°C. The data were generated in the US DOE LMFBR Materials and Structures Program. Tensile properties at aging temperatures and microstructure of Type 316 SS were also described. Effects of aging under creep and fatigue loading on tensile properties were also presented. Microstructure of aged and creep-tested specimens was characterized. Creep-fatigue data of thermally aged specimens for times to several thousand hours were also reported. The paper also discussed the effects of thermal aging on Charpy impact properties.

Yukawa (1993) performed a comprehensive review on the long-term elevated temperature exposures on toughness of austenitic steels and nickel alloys. The review focused on the effects of thermal aging on toughness of those materials, but included information on tensile properties as well. The wrought austenitic steels considered were primarily Types 304, 316, 321, 347, and 310, some manganese containing steels of the 200 and XM series, some of the CF series cast austenitic steels, and the welds commonly used for welding of austenitic stainless steels. The report by Yukawa (1993) also presents results on elevated temperature testing and effects of thermal aging on the fracture toughness behavior of the austenitic stainless steels, primarily in the form of the ductile initiation fracture toughness, J_{Ic}, and the resistance to crack propagation by ductile tearing as determined by the slope of the J-R curve (J-integral vs crack extension, also characterized as tearing modulus, T). Results from ten different experimental studies with only unaged materials (Types 304, 316L, 316, 321, and 347 stainless steels) were also reviewed.

For aging to about 600°C, the minimum curves for the unaged material provide a reasonable lower bound of behavior for the aged material, while even to 700°C, the yield strength data are only slightly below the curve. Some ductility data fall below the minimum curves of the unaged material. Up to about 600°C, the bulk of the data below the curves are for aging times of 25,000 h and greater, although there are some results below the curves for times as low as 4,000 h. Although some of the tensile ductility values are below the minimum property curves, the

lowest values observed for the uniform elongation, total elongation, and reduction of area are still at least, 10, 25, and 25%, respectively, and these values are considered adequate.

There is a significant reduction in creep resistance for the aged materials relative to the unaged condition. The amount of reduction is greater for the higher stress level. These results show that thermal aging at 565°C for 10,000 h increased the time to rupture, whereas aging at 649°C for the same period decreased the rupture time.

Results of the effects of aging on room-temperature Charpy V-notch (CVN) impact energy showed that energy values were sharply reduced by thermal aging, especially when the aging temperature was higher than 482°C (Sikka 1982). After thermal aging for 50,000 h in the WR orientation (now designated TL orientation), the results showed a reduction from about 200J in the unaged condition to about 80J and 27J for aging temperatures of 482 and 649°C, respectively. Changes in minimum creep rate and time to rupture were only slightly more pronounced for the thermal aging results at 649°C than at 565°C, and that the ratio of time to onset-of-tertiary creep to time to rupture for the aged specimens appears to be slightly lower than that for the unaged material.

Thermal aging of 316SS at 593°C for 5,000 h introduced intergranular precipitates, and when tested at 593°C, accelerated crack propagation rates were obtained under hold times. However, the environmental role in producing accelerated crack growth in 316SS is not well understood (Brinkman 1980). Although very long-term aging data are not available, aging of Type 304 stainless steel for 1000-5000 h at 538-649°C (1000-1200˚F) improves both creep ductility at a given rupture time and creep-fatigue life at a given tensile hold time, relative to those of unaged specimens (Majumdar et al. 1981).

Solution-annealed Types 304 and 316 stainless exhibit metastable microstructure. Their microstructure evolves with time to a more stable state during service. Precipitation reactions in austenitic stainless steels during prolonged aging at elevated temperatures are quite complex. For solution annealing at temperatures of 1000°C and above, a substantial amount of carbon is dissolved in austenite matrix. When rapidly cooled from the solution anneal, carbon remains in solution in a supersaturated state. Thermally aging for a long period time leads to carbide precipitation. $M_{23}C_6$ is the primary carbide in unstabilized austenitic stainless steels and its formation can lead to reduction in tensile properties and toughness and intergranular stress corrosion cracking. The time-temperature-precipitation (TTP) diagrams for 316 SS are shown in Fig. 4.1 (Marshall 1984). The precipitates formed at temperatures of 500-600°C are predominantly carbides, while at higher temperatures intermetallic phases form. At temperatures above 600°C, σ phase and laves phase also form. In 316 SS η-carbide (M_6C) has been observed after long aging times (>1500 h) at 649°C (Marshall 1984).

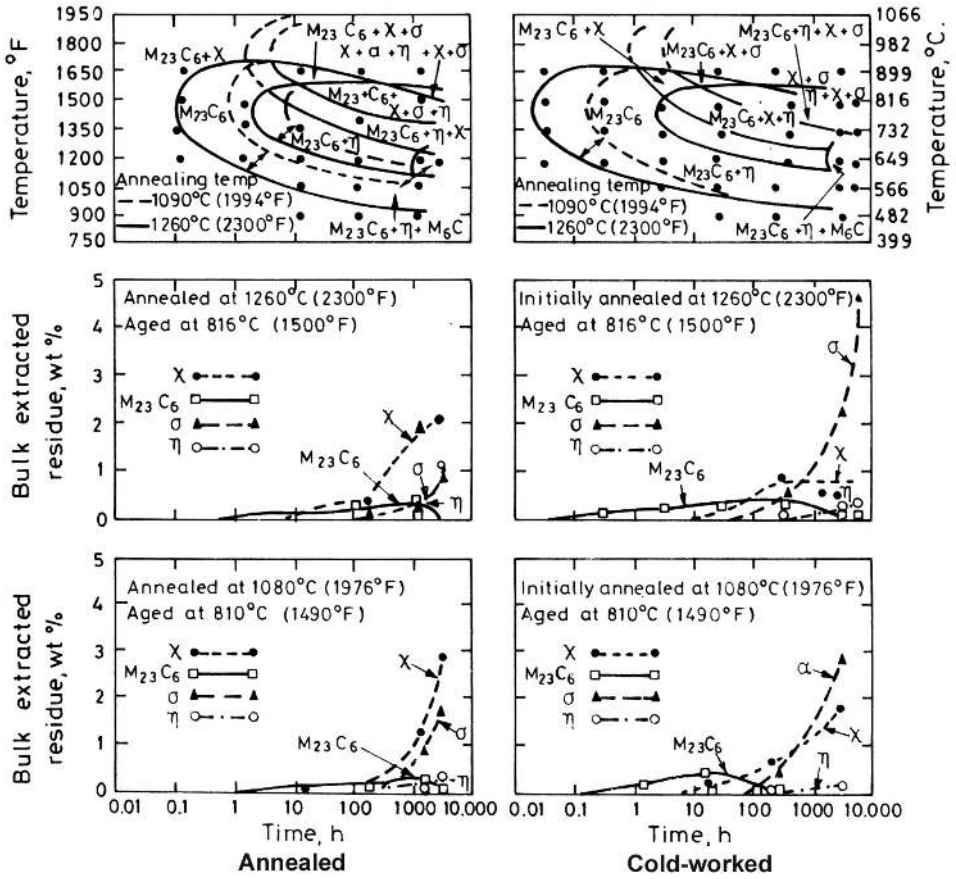

Figure 4.1. The time-temperature-precipitation (TTP) diagram for 316 SS (Marshall 1984).

4.1.2 Ferritic Steels

4.1.2.1 2.25Cr-1Mo Steel

The initial microstructure formed in 2.25Cr-1Mo steel during heat treatment is thermodynamically unstable. Carbide phases will undergo transformation during elevated-temperature exposure. The carbide phases in normalized steel are primarily M_7C_3 and $M_{23}C_6$ with a small amount of M_2C carbide; in the normalized and tempered steel $M_{23}C_6$ and M_6C carbides are primary phases. Thermal aging of the material at temperatures between 550 and 700°C lead to the formation of M_6C carbide according to the sequence:

$$\text{Banite} \quad \begin{bmatrix} \varepsilon - carbide \\ + \\ Cementie \end{bmatrix} \rightarrow (cementite) \rightarrow \begin{bmatrix} Cementite \\ + \\ M_2C \end{bmatrix} \begin{bmatrix} \rightarrow M_7C_3 \\ \rightarrow M_{23}C_6 \end{bmatrix} \rightarrow M_6C$$

$$\text{Ferrite} \quad M_2C \rightarrow M_6C$$

Fine precipitates of Mo_2C formed within the ferrite during heat treatment may transform to coarse $M_{23}C_6$ and M_6C, depleting Cr and Mo from the matrix and loss of both solid solution hardening and precipitate hardening capability.

The thermal stability of 2.25Cr-1Mo steels has been evaluated by an isothermal exposure and by a step cooling method. The step cooling method is an accelerated aging technique to characterize thermal aging response and should be cautiously used in design (Ishiguro et al. 1982, Prager 1998). There is an extensive database of the effects of prior thermal aging on microstructural evolution and mechanical properties. Table 4.1 shows a compilation of thermal aging data that are available in the open literature.

Table 4.1. Isothermal aging data for 2.25Cr-1Mo steel.

Material	Aging T (°C)	Aging Time (h)	Post-aging tests	References
Ann. 2.25Cr-1Mo	454, 510, 566	20,000 max	Tensile	Klueh 1977
Ann. 2.25Cr-1Mo	566	26,500	Creep rupture	Klueh 1981
Ann. 2.25Cr-1Mo	427-538	10,000	Fatigue	Booker and Majumdar 1982
2.25Cr-1Mo	482	5,000; 10,000; 30,000	Charpy impact	Prager 1998
Bainite 2.25Cr-1Mo	430-515	50,000 max	Charpy impact	Kim et al. 2006
2.25Cr-1Mo	425-475	54,000 max	Charpy impact	Kohno and Katsumata 1992
Ann. 2.25Cr-1Mo	45-650	100,000 max	Microstructure	Kushima et al. 2005

Klueh (1977) studied the effects of thermal aging on tensile properties. Four commercially annealed tubing heats, Heats 36202, 72768, 72871, and X6216, were initially in isothermally annealed condition. All aging specimens were given a stress relief treatment at 650°C for 0.25 h prior to aging. Tensile specimens were aged at 454, 510 and 566°C for 1000, 2500, 10,000 and 20,000 h. Tensile tests after aging were carried out at room temperature and the aging temperature at a strain rate of 0.0007/sec. Klueh (1981) reported the results of creep and rupture behavior of thermally annealed 2.25Cr-1Mo steel. Thermal aging was performed at 566°C for 25,000 h in an inert atmosphere. Creep rupture tests were carried out at 566°C.

Booker and Majumdar (1982) reported the effects of thermal aging on the fatigue properties of 2.25Cr-1Mo steel. Prior thermal aging was carried out at temperatures of 427 to 538°C for 10,000 h. Fatigue tests were carried out at the aging temperature. The aging behavior of 2.25Cr-1Mo is dominated by carbide precipitation. In annealed 2.25Cr-1Mo steel with proeutectoid ferrite, Mo_2C precipitates form (during thermal aging) with a high number density of fine needles or platelets, giving rise to strengthening. Mo_2C carbides are however, unstable, and transform to large, globular eta-carbide (Klueh 1977). Thermal aging can also significantly affect the alloy strength, particularly at the aging temperature. The yield and tensile strengths can be reduced up to 40% after aging at 566°C (Klueh 1977).

The most significant effect of thermal aging in 2.25Cr-1Mo steel is on creep rupture properties. Prior thermal aging at 566°C for 25,000 h produced the rupture strengths below the average for that of annealed 2.25Cr-1Mo steel. The difference was greater for short rupture times. At long rupture times, the rupture strength of the aged material approached the minimum for the annealed alloy (Klueh 1981).

There is insignificant effect of thermal aging on the fatigue life in 2.25Cr-1Mo Steel. Prior thermal aging for 10,000 h at the test temperature appeared to have little influence on subsequent fatigue life at 427-538°C. The reduction factor in fatigue life is <1.5 (Booker and Majumdar 1982).

National Institute for Materials Science (NIMS) has published the 4th volume of "Metallographic Atlas of Long-term Crept Materials" which is for 2.25Cr-1Mo (Kushima et al. 2005). Microstructural evolution during long-term creep is described in detail for three types of 2.25Cr-1Mo steels with different initial microstructure of ferrite/pearlite, bainite, and tempered martensite. The Metallographic Atlas of 2.25Cr-1Mo steels contains a number of optical micrographs showing the changes in microstructure during long-term creep exposure beyond 100,000 h at temperatures in the range of 450-650°C, in addition to creep rupture and hardness data. Optical micrographs of near fractured surface, gage, and head portion of creep-tested specimens with magnifications of 100, 400, and 1000 are also available. Transmission electron micrographs are also included. An example is shown in Fig. 4.2 for optical micrographs of the gage section of annealed 2.25Cr-1Mo specimens that were creep tested for times of 300 to 100,000 h at temperatures of 450 to 650°C. These micrographs systematically demonstrate the influence of time and temperature on microstructural evolution.

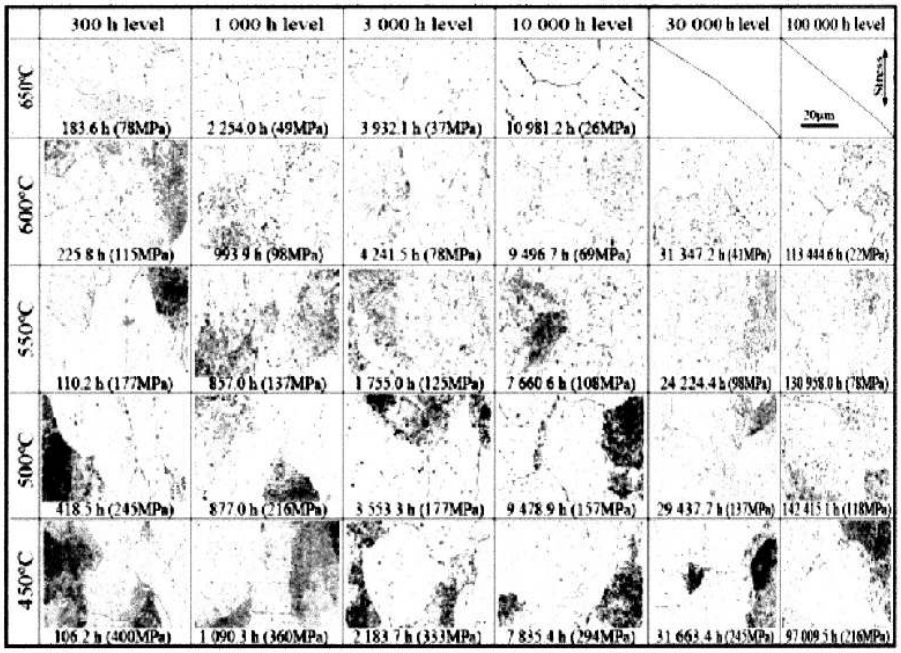

Figure 4.2. Metallographic Atlas of creep-tested specimens for times up to 100,000 h at temperatures of 450 to 650°C for annealed 2.25Cr-1Mo (Kushima et al. 2005).

4.1.2.2 Modified 9Cr-1Mo Steel

The effect of thermal aging on microstructure, tensile, impact, creep, and fatigue properties of G91 has been studied extensively. A substantial amount of thermal aging experiments were performed as part of the development of modified 9Cr-1MoV during the 1970s and 1980s. Additional data have been generated and are available in the literature in recent years. Thermal aging data from in-service components are also available. Table 4.2 summarizes the thermal aging data and post-aging mechanical tests from a number of sources.

Table 4.2. Thermal aging data and post-aging mechanical tests for G91

Material	Aging T (°C)	Aging Time (h)	Post-aging tests	References
3 heats of plates	482-704	5,000-75,000	Tensile and impact	Brinkman et al. (1990)
3 heats of plates	482-704	5,000-75,000	Creep (550-625°C/100 MPa)	Swindeman et al. (2000)
Tubing	552	130,000	Tensile test (20-650°C)	Swindeman et al. (2000)
Tubing	552	130,000	Creep (550-625°C/100 MPa)	Swindeman et al. (2000)
P91	625, 650	1000; 3000; 10,000	Tensile and impact	Cumino et al. (2002)
Boiler tube	-	116,000; 143,000	-	Swindeman (2001)
P91	650	10,000	Creep (600°C/100-250 MPa)	Sklenicka et al. (2003)
P91	500-600°C	500 – 10,000	Microstructure	Paul et al. (2008)
Heat 30394	593	5000	Fatigue at 593°C	Kim and Weertman (1988)
P91	650	10,000	Microstructure	Sanchez-Hanton and Thomson (2007)
Mod.9Cr-1Mo	550, 650	500; 5000	RT fatigue crack growth	Chaswal et al. (2005)
Mod.9Cr-1Mo	538, 593		Fatigue, creep-fatigue	Gieseke et al. (1993)

Major findings of prior-aging effects on mechanical properties include:

- There is little effect on room temperature tensile properties after thermal aging at lower temperatures (≤ 600°C); tensile strength was reduced after thermal aging at 650-700°C.
- Thermal-aging-induced softening is more evident when tested at aging temperatures.
- These is significant reduction in impact properties (DBTT increase and upper shelf energy decrease) after thermal aging at lower temperatures (≤ 600°C); impact properties were improved after thermal aging at 650-700°C; the maximum degradation in toughness occurs after aging at 500-550°C.
- Thermal aging accelerated the creep rate and shortened the creep rupture life, depending on the aging and testing conditions; the 552°C/130,000 h service-exposed specimens showed a creep rate ten times higher than that of unexposed specimens (see Fig. 4.3 from Swindeman et al. 2000); on a Larson-Miller plot for unexposed and aged specimens, the rupture lives for the aged materials fell in the lower strength or shorter life side of the scatter band for the un-aged material.
- Little effect on the fatigue life was observed after thermal aging for 5,000 h at 593°C, even though the aged specimen showed a slower cyclic stress range than that in the unaged specimen; after 50,000 h of aging at 593°C, continuous-cycling fatigue life is clearly lower than that of the unaged material.
- Thermal aging increased the stress intensity range threshold, but has little effect on the Paris-law regime of fatigue crack growth rate.

Extensive microstructural characterization has been performed in thermally-aged G91 specimens for temperatures of 482 to 649°C and times up to 85,000 h (DiStefano et al. 1986, Brinkman et al. 1990, Cumino et al. 2002, Sklenicka et al. 2003, Paul et al. 2008), and for T91 superheater tubing after service exposure of 538°C/30,000 h and 552°C/130,000 h (Swindeman et al. 2000). There is general agreement between laboratory-aged specimens and those from

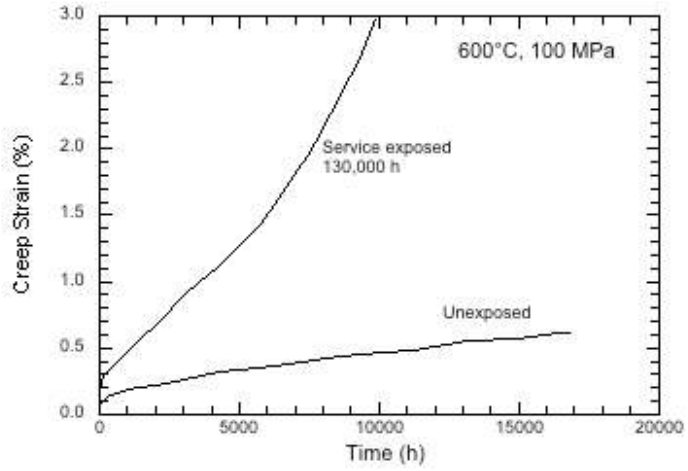

Figure 4.3. The 552°C/130,000 h service-exposed specimens showed a dramatically larger creep rate than that of the unexposed specimens (Swindeman et al. 2000).

in-service components for comparable exposure conditions. Thermal aging causes significant recovery, formation of subgrains, and precipitate coarsening. Grain and subgrain boundary structure remained stable during long-term aging at temperatures up to 593°C. Significant recovery and substructure coarsening were observed at 650°C and higher. $M_{23}C_6$ carbides coarsened, while MX particles were relatively stable. Substantial precipitation and coarsening of Laves phase was observed after thermal aging. Laves phase formed at 482 and 593°C and showed a maximum at 538°C after 25,000 h. Laves phase was observed after 3,000 h at 650°C in P91, and it grew to micron size after 10,000 h aging. It must be pointed out that microstructure evolution of G91 can be significantly accelerated under mechanical loading at high temperature (Fournier 2009).

4.2 ASME Guidelines for Thermal Aging Effects

ASME NH recognizes that long-time, elevated-temperature service may results in the reduction of the subsequent yield and tensile strengths. The yield and tensile strength reduction factors are provided in Tables NH-3225-2, -3A and -3B in Subsection NH for 304, 316 austenitic stainless steels, 2.25Cr-1Mo and mod.9Cr-1Mo steels, and Alloy 800. The yield and tensile strength reduction factors are 1 and 0.8, respectively for 304 and 316 austenitic stainless steels for temperatures ≥ 480°C (Table 4.3).

The yield and tensile strength reduction factors for 2.25Cr-1Mo steel are given as a function of the accumulated time-temperature history to which the component has been exposed, prior to the event under analysis with the maximum time of 300,000 h at temperatures ≤575°C and the maximum time of 1,000 h between 600 and 650°C. The yield strength reduction factors as a function of time and temperature are shown as an example in Fig. 4.4. For mod.9Cr-1Mo steel, the yield strength reduction factor is 1 at all temperatures ≥480°C, and the tensile strength reduction factor is given as a function of time and temperature up to 650°C for the maximum time of 300,000 h.

When the yield and tensile strengths are reduced by elevated temperature service, the values of S_{mt} and S_m are redefined as the lower of (a) through (f) below, and the values of S_m redefined as the lower of (b) through (f) below:

(a) the S_{mt} values in NH Table I-14.3;

(b) (1/3) x S_u(20°C) x tensile strength reduction factor;

(c) (1/3) x S_u(T(°C)) x tensile strength reduction factor;

(d) (2/3) x S_y(20°C) x yield strength reduction factor;

(e) (2/3) x S_y(T(°C)) x yield strength reduction factor for 2.25Cr-1Mo and mod.9Cr-1Mo;

(f) (0.9) x S_y(T(°C)) x yield strength reduction factor for 304 SS and 316 SS;

Table 4.3. Yield and tensile strength reduction factors for NH materials

Material	Service Temperature (°C)	YS reduction factor	TS reduction factor
304SS	≥ 480°C	1.00	0.80
316SS	≥ 480°C	1.00	0.80
9Cr-1Mo-V	≥ 480°C	1.0	Temp-, time-dependent
2.25Cr-1Mo	≥ 425°C	Temp-, time-dependent	Temp-, time-dependent

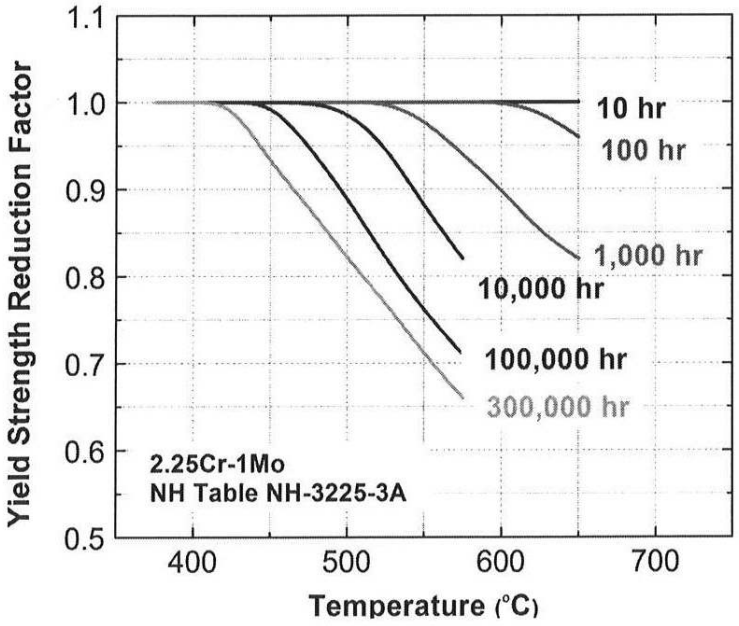

Figure 4.4. Yield strength reduction factor as a function of temperature and time for 2.25Cr-1Mo. Values are from NH Table NH-3225-3A.

4.3 Issues and Resolutions

Thermal aging is a temperature-time-stress dependent process. Effects on degradation of tensile properties, fracture toughness, creep rupture and creep-fatigue endurance could comprise design margins, particularly for off normal condition near the end of the design life. A number of thermal aging related issues relevant to the NH materials and the design rules have been identified as outlined below. Research needed to resolve these issues are proposed.

***Issue**: Thermal aging effects on design allowables for the 60-year design life*

There is a sufficient database to assess the long-term thermal aging effects on the mechanical properties of NH materials. The ASME NH recognizes the aging degradation and provides the yield and tensile strength reduction factors due to long-term aging as a function of the accumulated time-temperature history for the maximum time of 300,000 h. These aging-induced strength reduction factors need to be extended to 600,000 h.

A 60-year design life at high temperature is a challenging task. The available database on thermal aging effects has data for times up to ≈100,000 h. Additional information is needed to determine the strength reduction factors for the 60-year design life.

Resolution:

- Thermodynamic and kinetic modeling of microstructural evolution during thermal aging with experimental validation are needed to develop a better understanding of the thermal aging effects for reliable data extrapolation to the 60-year design life. Areas include precipitation and coarsening kinetics and synergistic effects of thermal aging and mechanical loading.

- Thermally aged, long-term creep-tested specimens should be collected for detailed microstructural characterization. "Microstructure Atlas" of long-term aged materials can be constructed using obtained mechanical and microstructural information.

- Mechanistic models need to be developed to correlate microstructural changes during long-term thermal aging with associated mechanical properties. Confirmatory tests of aged and cyclic-softened materials are needed to validate the models.

- Strength reduction factors caused by thermal aging needs to be extended to 600,000 h.

- Considering the cost and limitation of performing long-term tests, accelerated testing techniques need development to accurately assess material behavior in relatively short time periods and in simulated reactor operating conditions. These techniques need to be based on improved understanding of thermal aging effects and mechanistic models.

***Issue**: Incorporation of thermal aging effects in creep-fatigue design rules*

There are several concerns with the creep-fatigue design rules in terms of thermal aging effects. The ASME NH isochronous stress-strain curves are based on unaged materials, and they may not be applicable to aged components. For mod.9Cr-1Mo steel, significant cyclic softening and relaxation occurs during cycling. There is insufficient understanding on how the softening effects will affect the creep-fatigue response. Available data are not necessarily adequate to support that the creep-fatigue design rule is not underestimating the creep damage of softened materials.

Resolution:

A proper creep-fatigue database of thermally aged materials should be established. Additional testing is needed to better understand the thermal aging effects on creep-fatigue damage, particularly for cyclic softened materials such as ferritic steels. An improved creep-fatigue design methodology should be developed to incorporate the material's softening behavior due to aging. Confirmatory tests are needed to validate the improved design rules.

***Issue**: Long-term thermal aging effects on weldments*

Long-term thermal aging can be more problematic in weldments than in the base metal due to the complexity of weldment microstructure. The effects of long-term thermal aging in weldments have been characterized far less extensively than in the base metal. The microstructural evolution in different regions of a weldment during long-term aging needs to be well characterized and their effect on weldment cracking should be fully understood.

Weldment strength reduction factors in the ASME NH are currently applicable to maximum 300,000 h. The weldment reduction factors need to be extended to 600,000 h. Specific design rules are required for mod.9Cr-1Mo weldments to address Type IV cracking.

Resolution:

- The effects of long-term thermal aging on weldment properties need to be characterized. Focus should be on mod.9Cr-1Mo weldments. Microstructural characterization of the weldments of mod.9Cr-1Mo steel should be conducted on thermally aged or creep-tested weldment specimens. Material currently in service should also be characterized if possible for comparison with laboratory data.
- Thermodynamic and kinetic modeling of microstructural evolution under dynamic welding processes should be pursued with experimental validation. Specimens with simulated microstructure should be tested to obtain mechanical response data. Mapping of microstructure in the HAZ and their associated tensile properties will provide valuable information in understanding weldment cracking under mechanical and thermal loading.
- Establish a creep-fatigue database of thermally aged weldments, and perform additional creep-fatigue tests on weldments to fill data gaps. Creep-fatigue tests of softened weldment specimens should be conducted to support the development of improved creep-fatigue design rules for weldments.
- Incorporate aging effects in creep-fatigue design rules for weldments.

5. CREEP DEFORMATION AND CREEP RUPTURE

5.1 ASME Deformation and Strain Limits

The rules of construction in the American Society of Mechanical Engineers (ASME) Boiler and Pressure Vessel Code, Section III, Subsection NH are based on the Design-by-Analysis approach. Limits are placed on two basic types of controlled quantities: (1) load-controlled, and (2) deformation-controlled. The deformation and strain limits have been devel-

oped, together with the fatigue limit, to ensure the structural integrity of components whose load controlled stresses are evaluated by the rules of Subsection NH. The limits on inelastic strain in regions expecting elevated temperatures are:

(a) Strain averaged through the thickness, 1%
(b) Strains at the surface, due to an equivalent linear distribution through the thickness, 2%
(c) Local strains at any point, 5%.

Step-by-step rules are provided in Subsection NH for employing elastic methods and simplified inelastic methods, which are based on elastically calculated stresses and strains, to establish conservative bounds on deformation and strains of structural components. However, where creep effects are presumed significant, inelastic analysis is generally required to provide a quantitative assessment of deformation and strains. Yet no guidance is provided for the inelastic analysis approach in Subsection NH. The results of an evaluation of strain limits and creep-fatigue damage are quite sensitive to the specific features of the material model employed in the analysis. Thus, the development of validated constitutive equations is necessary in applying the inelastic analysis approach to regions where design limits cannot be met by the conservative elastic and simplified inelastic approaches.

5.2 Deformation Behavior

High temperature deformation behaviors that are important for constitutive models to capture include strain rate dependence, creep and stress relaxation, cyclic hardening (austenitic stainless steels) or softening (Cr-Mo steels), dynamic strain aging, and ratcheting. Effects of thermal aging on these deformation behaviors are also important.

5.2.1 Austenitic Stainless Steels

Austenitic stainless steel cyclically hardens at all application temperatures of interest. Figure 5.1 shows the stress-strain curves of 304 stainless steel from strain cycling at room temperature. The strain amplitude was 1% and the data were from Hassan and Kyriakides (1994). As can be seen from Fig. 5.1, Type 304 stainless steel cyclically hardened as the stress at a given strain level increased with the number of cycles. The amount of cyclic hardening was large in the first few cycles and the hysteresis loops stabilized, or saturated, after about 20 cycles.

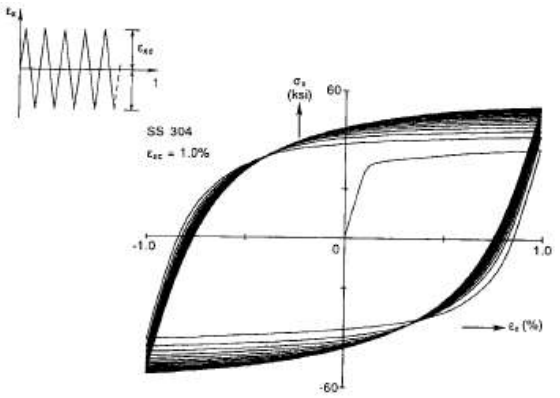

Figure 5.1. Hysteresis loops for 304 stainless steel at room temperature (Hassan and Kyriakides 1994).

An important deformation behavior for sodium fast reactor applications is ratcheting. This phenomenon corresponds to the progressive incremental strain accumulation, cycle-by-cycle, induced by the simultaneous application of a primary load and s secondary cyclic load.

Figure 5.2 shows the stress-strain curves obtained from strain-controlled ratcheting tests performed by Ohno et al. (1998) on 316FR stainless steels at 300 and 650°C. One cycle in the straining history consisted of a compressive strain $\delta\varepsilon_{-} = 0.2\%$ and tensile strain $\delta\varepsilon_{+} = 0.3\%$, except for the first cycle, where $\varepsilon_{\max}^{(1)} = 0.1\%$ and $\varepsilon_{\min}^{(1)} = -0.067\%$. Thus, for the second and subsequent cycles, the maximum strain was increased by 0.1% every cycle. The tests were performed at a constant strain rate of $|\dot{\varepsilon}| = 10^{-5}/\mathrm{s}$. The uniaxial stress-strain curves are superposed in the plots. For both temperatures, the stress-strain hysteresis loops close almost completely. The tip of each loop lies nearly on the superposed monotonic stress-strain curve. Ohno et al. (1998) observed that the cyclic plastic strain in each cycle induced negligible isotropic hardening, and they concluded that the isotropic hardening depends on maximum plastic strain rather than the accumulated plastic strain. The stress range increased for every cycle at 650°C, but not significantly at 300°C. Thus isotropic hardening is not very strong at 300°C.

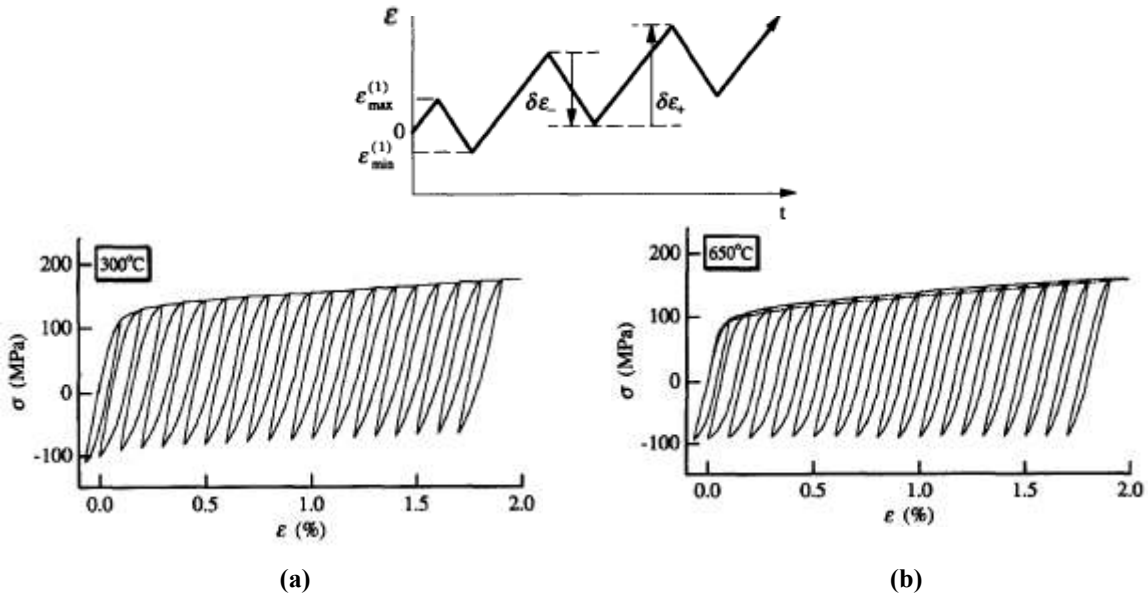

Figure 5.2. Stress-strain curves obtained from strain-controlled ratcheting tests on 316FR stainless steel at (a) 300°C, and (b) 650°C. Uniaxial tensile curves are superposed in the plots. Straining history is shown schematically in the figure inset (Ohno et al. 1998).

A series of ratcheting tests under tension-torsion biaxial conditions were performed by Kawashima et al. (1997) on 316FR stainless steel at 650°C. The test specimens were subjected to a push-pull axial strain superposed with a constant shear stress. Tests were conducted at several axial strain ranges, axial strain rates, and constant shear stresses. Examples on the accumulation of torsional strains, $\gamma/\sqrt{3}$ (γ = engineering shear strain) in the first 5 cycles of the tests conducted by Kawashima et al. (1997) at an axial strain range of 0.01, axial strain rate of $|\dot{\varepsilon}| = 10^{-3}/\mathrm{s}$ are shown in 5.3 for two values of the constant shear stress τ. The cyclic stress-

strain hysteresis loops from the first 3 cycles of a test with a constant shear stress of $\tau = 24.5/\sqrt{3}$ MPa are shown in Fig. 5.4. Kawashima et al. (1997) concluded from the test results that the accumulation of racheting shear strain increases with increasing cyclic axial strain range and the magnitude of the applied constant shear stress.

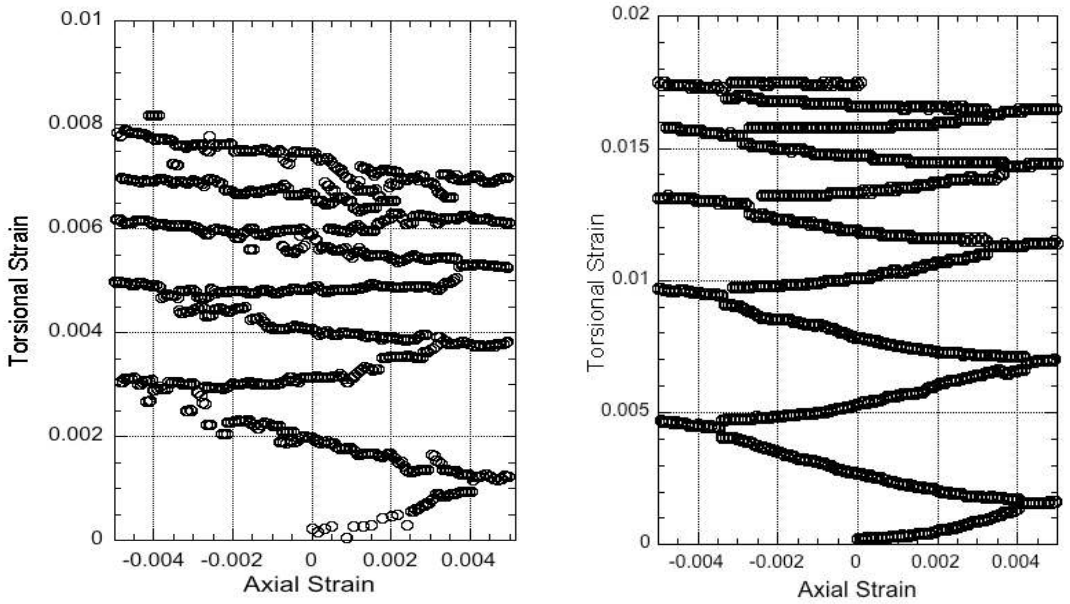

(a) **(b)**

Figure 5.3. Behavior of shear strain progression in the first 5 cycles from tension-torsion ratcheting tests on 316FR stainless steel at 650°C, (a) $\tau = 49/\sqrt{3}$ MPa, and (b) $\tau = 73.5/\sqrt{3}$ MPa (Kawashima et al. 1997).

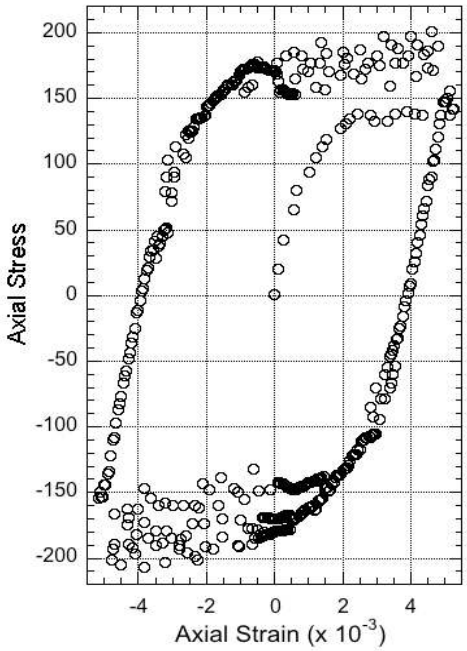

Figure 5.4. Cyclic stress-strain curves in the first 3 cycles from tension-torsion ratcheting tests on 316FR stainless steel at 650°C (axial strain range = 0.01, $|\dot{\varepsilon}| = 10^{-3}/s$, $\tau = 24.5/\sqrt{3}$ MPa (Kawashima et al. 1997).

5.2.2 Mod. 9Cr-1Mo Steel

The monotonic engineering stress-strain curves are shown in Fig. 5.5 for Mod. 9Cr-1Mo (Swindeman 1988). The effect of temperature on the stress-strain curve is illustrated in 5.5(a). The tests were conducted at a constant strain rate of 6.7×10^{-5}/s. The stress-strain curves for strain rates of 6.7×10^{-4}, 6.7×10^{-5}, and 6.7×10^{-6}/s at 600°C are depicted 5.5(b). The strain at which the ultimate strength occurs decreases with temperature. At temperatures of 500°C and above, Mod. 9Cr-1Mo steel exhibits a flow softening behavior and the ultimate strengths occur at very low strain levels (≈1% at 600°C), but necking develops very gradually and the tensile failure strains are beyond 10%.

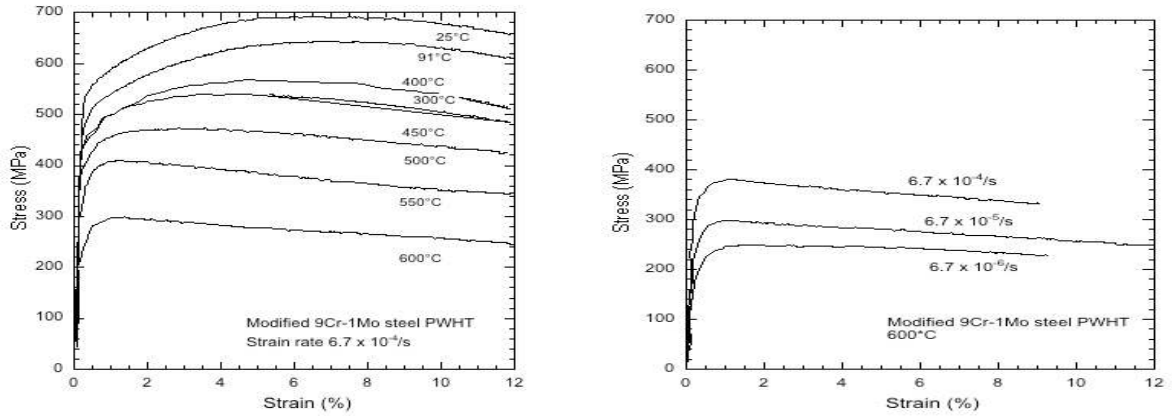

(a) **(b)**

Figure 5.5. Monotonic engineering stress-strain curves for Mod. 9Cr-1Mo. (a) Effects of temperature at a strain rate of 6.7×10^{-5}/s. (b) Strain rate effects at 600°C (Swindeman 1988).

The stress versus strain hysteresis loops are shown in Fig. 5.6, from Swindeman (1988). The effect of cycling at temperatures of 25, 200, 450, and 600°C, and for a total strain range of 0.95% and a constant strain rate of 10^{-4}/s are given in Fig. 5.6(a). The hysteresis loops are shown at the 1st, 100th, and 1000th cycles. Cyclic strain softening is evident and the softening effect increases with temperature. The hysteresis loops at half-life from different constant strain rate tests, from 10^{-4} to 10^{-7}/s, and at 550°C are plotted in Fig. 5.6(b). The strain rate effect on cyclic behavior is also evident.

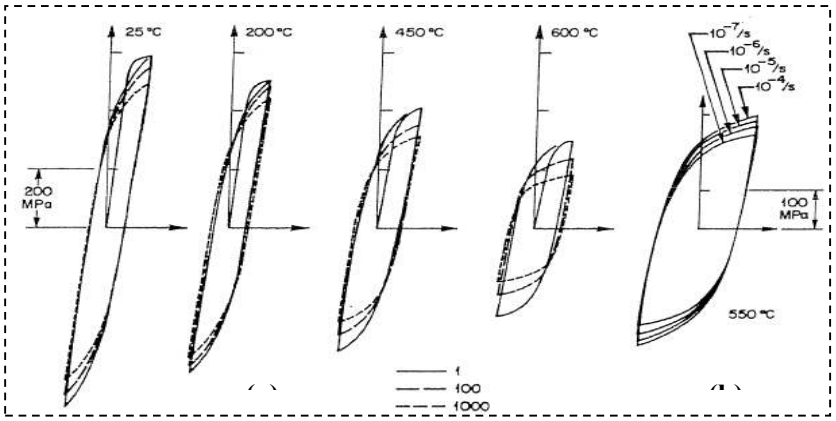

Figure 5.6. Stress versus strain hysteresis loops for 0.95% strain range, showing (a) the effect of cycle number at a strain rate of 10^{-4}/s, and (b) the effect of strain rate at 550°C (Swindeman 1988).

Figure 5.7 shows the creep curves for several stresses and temperatures in log-log plots from Swindeman (1988). The tests were performed to develop creep laws in the primary and secondary creep regimes. The creep data show that there is a tendency for parabolic hardening at low strains, leading to very large changes in the creep rate during primary creep. The secondary creep regime is established at rather low strain levels, typically below 1%. Swideman (1988) found that a creep law of the form:

$$\varepsilon^{cr} = Bt^{1/3} + \dot{\varepsilon}_m t \tag{5.1}$$

where ε^{cr} is the creep strain, t is time, and B and $\dot{\varepsilon}_m$ are functions of stress and temperature. The explicit dependence of these two functions is given in Swindeman (1988).

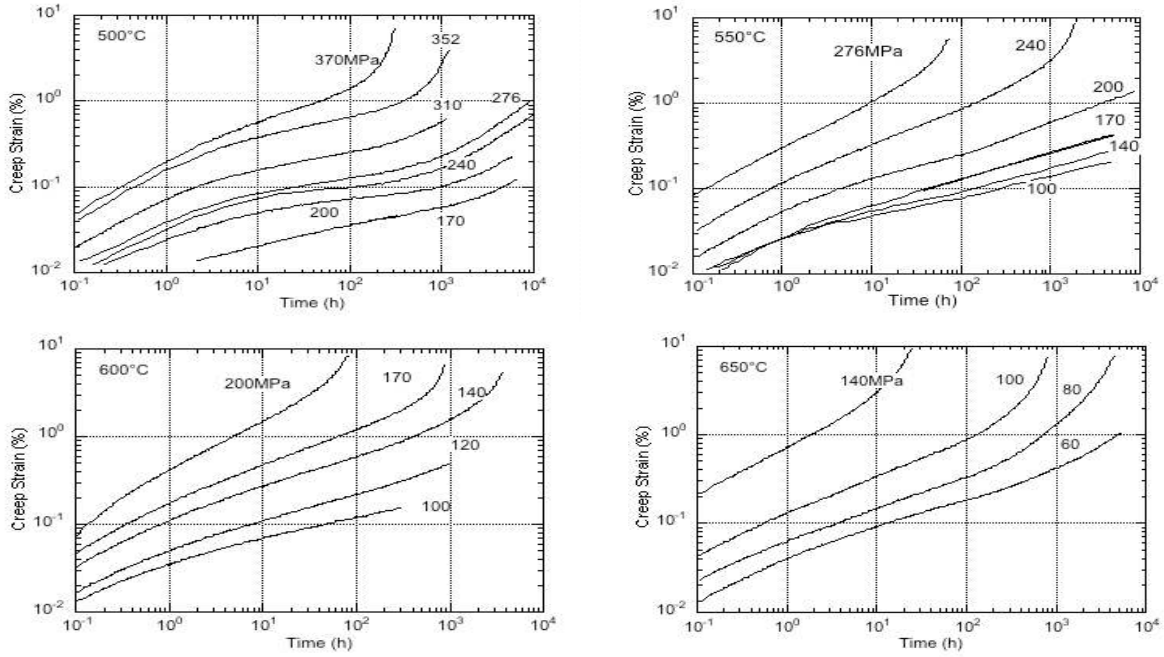

Figure 5.7. Creep strain versus time curves for different stresses and temperatures in log-scale (Swindeman 1988).

Figure 5.7 shows the effects of short time stress reversal on the creep behavior, from Swindeman (1988). The tests were conducted in the following manner. A tensile creep stress of 276 MPa was applied. Such a creep stress would cause creep rupture at approximately 10,000 hours. Instead of maintaining the creep stress for all times, Swindeman (1988) applied a periodic short time stress reversal, from 276 MPa to −276 MPa and then back to 276 MPa. The ramp time was 10 seconds. Three tests were conducted, one at a stress reversal frequency of 1 cycle per hour, the second at 12 cycles per hour and the third at 100 cycles per hour. At 1 cycle per hour, no acceleration of the creep rate was observed and the test was discontinued after several hundred hours. Creep rate acceleration was observed for the test at 12 cycles per hour and the specimen failed by creep rupture at around 600 hours. The creep rate for the last test at 100 cycles was accelerated even further and the specimen failed only after 145 hours, but failed in a fatigue mode.

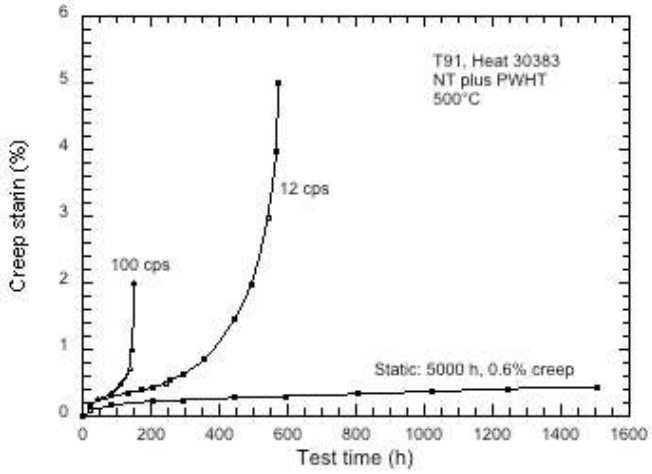

Figure 5.8. Effect of short time stress reversals on the creep at 276 MPa and 500°C (Swindeman 1988).

Figure 5.9 shows the short-term stress relaxation response of Mod. 9Cr-1Mo from tests conducted at 400 and 550°C by Yaguchi and Takahashi (1999). The test specimens were loaded to a tensile strain of 1.5% under different constant strain rates before strain hold for the stress relaxation tests begun. As the creep rate is proportion to the negative stress rate during stress relaxation, it is seen from the figure that the higher the prior strain rate, the higher the creep rate at a given time is higher in the transient region. The data also show the effect of prior strain rate on the residual relaxation strength of Mod. 9Cr-1Mo, the higher the prior strain rate, the lower the residual relaxation strength.

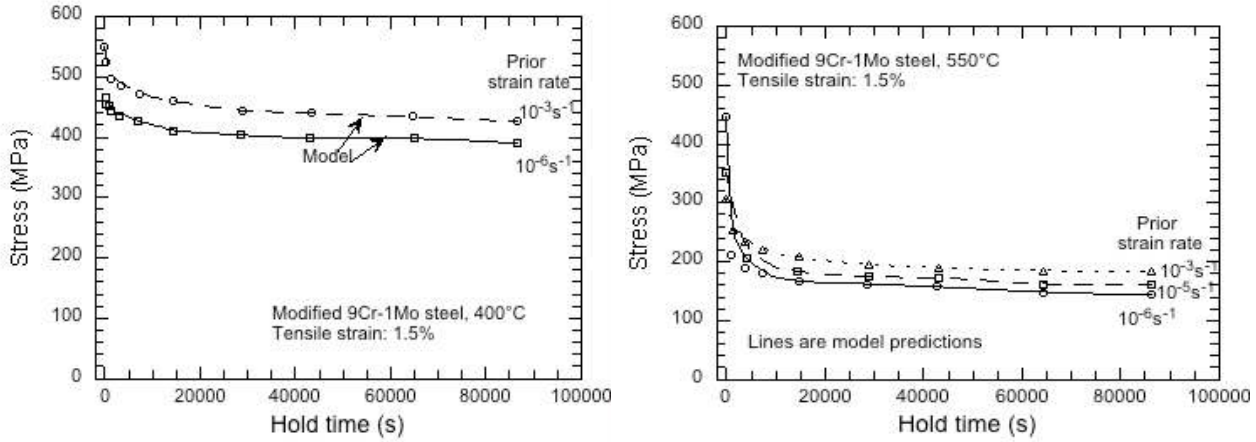

(a) **(b)**

Figure 5.9. Stress relaxation behavior with different prior strain rates at (a) 400ºC, and (b) 550ºC for Mod. 9Cr-1Mo (Yaguchi and Takahashi 1999).

The values of the stress just prior to stress relaxation ("peak stress") and the relaxed stress level after 24 hours hold time for different prior strain rates and test temperatures from the tests conducted by Yaguchi and Takahashi (1999) are shown in Figure 5.10. At temperatures at 500°C and above, positive rate sensitivity is observed with "normal" relaxation behavior. This is also the case at 200°C. "Normal" relaxation behavior refers to the behavior where the stress associated with the highest prior strain rate is the lowest for equal duration of relaxation periods.

For temperatures at 400°C and below, the peak stress is independent of the prior strain rate, indicating that the monotonic stress-strain curve is strain rate independent. However, the stress relaxation behavior is dependent on prior strain rate. Yaguchi and Takahashi (1999) attributed this behavior to the effect of dynamic aging. Thus novel constitutive modeling method is required to capture such behavior for Mod. 9Cr-1Mo.

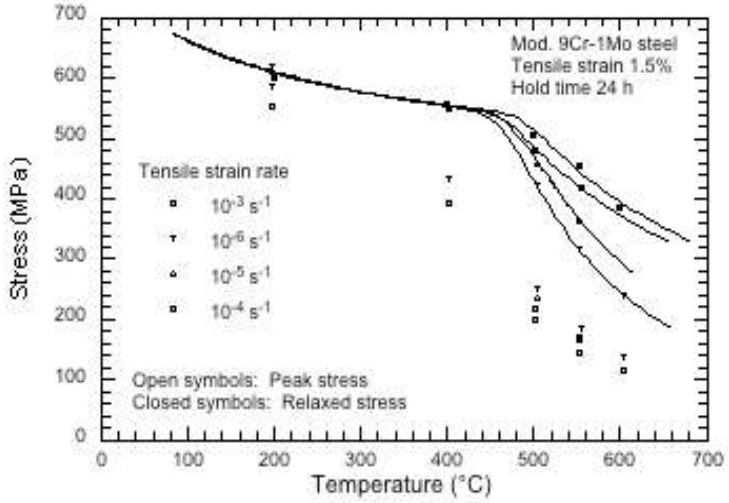

Figure 5.10. Temperature dependency of peak stress and relaxed stress for Mod. 9Cr-1Mo (Yaguchi and Takahashi 1999).

Uniaxial and multiaxial ratcheting tests were conducted by Yaguchi and Takahashi (2005a) at temperatures between 200 and 600°C on Mod. 9Cr-1Mo. Figure 5.11 shows the results from uniaxial ratcheting tests at 550°C where the maximum stress was 400 MPa, and stress ratios of 0, –0.25, –0.5, –0.75, and –1 were applied. The ratcheting tests were performed by cyclic push-pull loading with nominal stress control at a high stress rate of 50 MPa/s. It is observed that the ratcheting rate (maximum strain per cycle) differed by 1000X amount the test conditions considered.

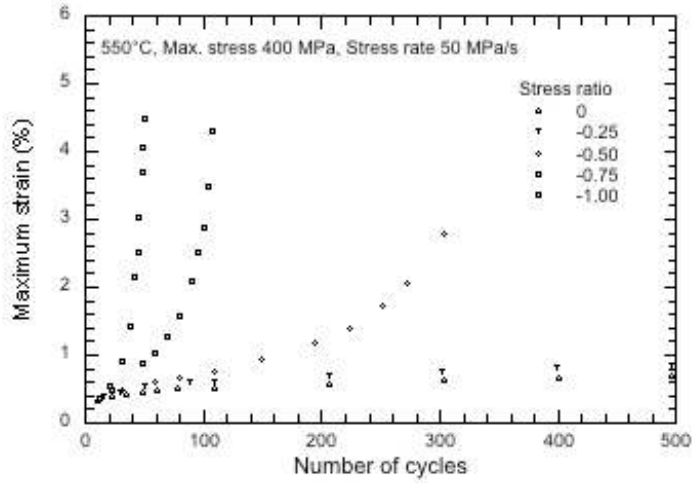

Figure 5.11. Results of uniaxial ratcheting tests at 550°C for Mod. 9Cr-1Mo. Tests were performed at the same maximum stress of 400 MPa but for several negative stress ratios (Yaguchi and Takahashi 2005a).

The mean strain as a function of cycle number from uniaxial ratcheting tests at 550°C and at negative stress ratios of –1.0, –1.025, –1.05, –1.063 and –1.075 are shown in Fig. 5.12. Stress

ratio smaller than −1.0 corresponds to subjecting the test specimen into compression, during part of the ratcheting cycle. Even at a stress ratio of −1.025, ratcheting occurred in the tensile direction. For stress ratio of −1.05 or smaller, ratcheting progressed in the compressive direction. Figure 5.13 shows the stress-strain hysteresis loops from uniaxial ratcheting test at 550°C and at a stress ratio of −1.025. It is seen that the strain range grew significantly with the increase in the number of cycles.

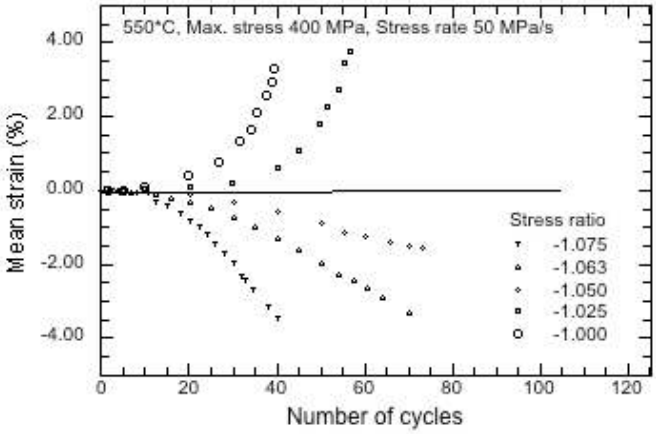

Figure 5.12. Mean strain versus number of cycles from uniaxial ratcheting tests for Mod. 9Cr-1Mo at 550°C and stress ratios ≤−1 (Yaguchi and Takahashi 2005a).

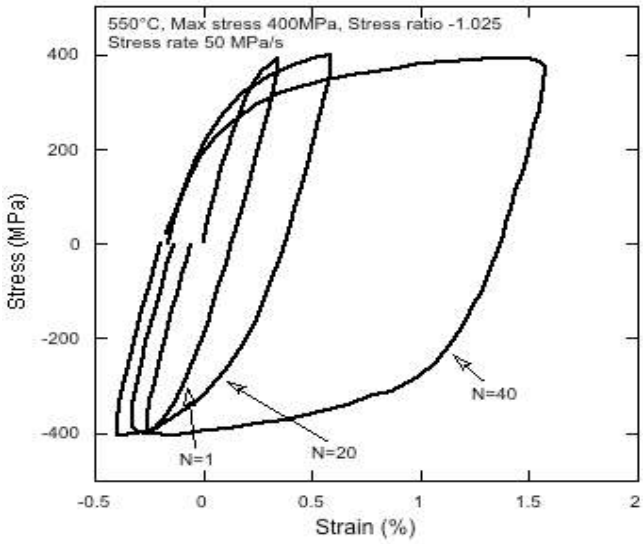

Figure 5.13. Stress-strain hysteresis loops from uniaxial ratcheting test for Mod. 9Cr-1Mo at 550°C and a stress ratio of −1.025 (Yaguchi and Takahashi 2005a).

The multiaxial ratcheting tests of Yaguchi and Takahashi (2005a) were conducted at 550°C under constant tensile stress with cyclically controlled shear strain. The test program studied the effects of the parameters: (i) tensile stress, (ii) shear strain range, (iii) shear strain rate, and (iv) shear strain hold times. Figure 5.14 shows the results of some of the test conditions. The ratcheting behavior under multiaxial conditions depends on the combination of test parameters. However, for the tests conducted, Yaguchi and Takahashi (2005a) observed that the amount of multiaxial ratcheting was relatively small in comparison with that of the uniaxial ratcheting.

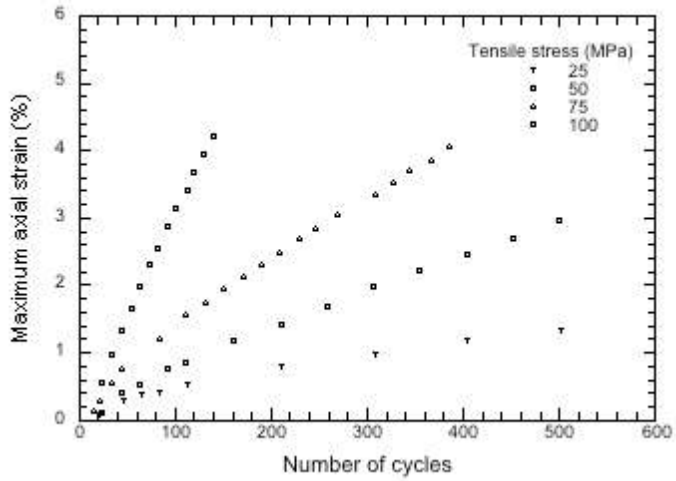

Figure 5.14. Maximum axial strain versus number of cycles from tension-torsion ratcheting tests for Mod. 9Cr-1Mo at 550°C and several values of the constant axial stress (Yaguchi and Takahashi 2005a).

5.3 Constitutive Models

5.3.1 Classical Creep-Plasticity Model

Classical approach to the modeling of inelastic thermo-mechanical behaviors was based on the separation of inelastic deformation into time dependent creep components and time independent plastic components, as was employed in some early liquid metal reactor design analyses. In the classical approach, the total strain rates $\dot{\varepsilon}_{ij}$ are given as

$$\dot{\varepsilon}_{ij} = \dot{\varepsilon}_{ij}^{el} + \dot{\varepsilon}_{ij}^{th} + \dot{e}_{ij}^{pl} + \dot{e}_{ij}^{cr} \tag{5.2}$$

where the superscripts denote the elastic, thermal, plastic, and creep contributions to the total strain rates. Incompressible plastic and creep deformations are assumed and the quantities $\dot{e}_{ij}^{pl}$ and $\dot{e}_{ij}^{cr}$ are the deviatoric strain rates, given generally as $\dot{e}_{ij} = \dot{\varepsilon}_{ij} - \dot{\varepsilon}_{kk}/3$. Isotropic material behavior is considered.

A typical form for the creep law is given by

$$\dot{e}_{ij}^{cr} = f(\bar{\sigma}, \bar{e}^{cr}) \frac{s_{ij}}{\bar{\sigma}} \tag{5.3}$$

where s_{ij} are the deviatoric stresses given as $s_{ij} = \sigma_{ij} - \sigma_{kk}/3$, σ_{ij} are the stresses, $\bar{\sigma}$ is the effective stress given as $\bar{\sigma} = \sqrt{1.5 s_{ij} s_{ij}}$, and $\bar{e}^{cr}$ is the effective creep strain given as $\bar{e}^{cr} = \int \dot{\bar{e}}^{cr}\, dt$ where $\dot{\bar{e}}^{cr}$ is the effective creep strain rate given by $\dot{\bar{e}}^{cr} = \sqrt{(2/3)\dot{e}_{ij}^{cr}\dot{e}_{ij}^{cr}}$. The creep law is formulated independently of plasticity using creep data. Using a power law for the function f that includes only the dependence on $\bar{\sigma}$, the secondary creep or Norton's law is reproduced by Eq. 5.3.

In the classical approach, plasticity is in turn independent of creep deformation and a representative rate independent plasticity law is

$$\dot{e}_{ij}^{pl} = \dot{\lambda}\frac{\partial h}{\partial \sigma_{ij}} \tag{5.4}$$

where h is the yield function and $\dot{\lambda}$ is the flow factor. The yield function depends on $\bar{\sigma}$ and can depend on accumulated plastic strain, or plastic work, and on the kinematic stresses.

Some qualitative predictions of classical creep and plasticity models were compared to experimental data by Krempl (1999). The creep equation (5.3) predicts that the creep curves from two different specimens of the same material are the same when the applied stress and initial effective creep strain are the same. Krempl (1999) observed that test data on 316 stainless steel of Ohashi et al. (1986) (see Fig. 5.15) showed different result. Four creep tests at an applied stress of 140 MPa were performed at 650ºC. The first creep test was performed when the applied stress equal to 140 MPa was reached upon initial loading. The corresponding creep curve is denoted by the + symbols in the figure. The remaining three creep tests were performed after the specimens were loaded beyond 140 MPa to different stress levels and were then unloaded back to 140 MPa. This resulted in different prior plastic strains before the creep tests were carried out. The maximum stress levels and the resulting plastic strain accumulations before the creep tests were performed are shown in the legend of the figure. While the prior plastic strains were different, the applied stress and initial effective creep strain were the same for the four specimens. However, the creep curves, as shown in the figure, are very much different. There is a definite influence of prior plastic strain accumulation on the subsequent creep behavior, or there is creep-plasticity interaction. The conventional explanation is that the prior plastic straining hardens the material and hence retards the creep rate in a subsequent creep test. The test data from Ohahi and Kawai (1986) show that the creep deformation depends on prior deformation history, or is path dependent, which is at variance with the prediction of Eq. 5.3.

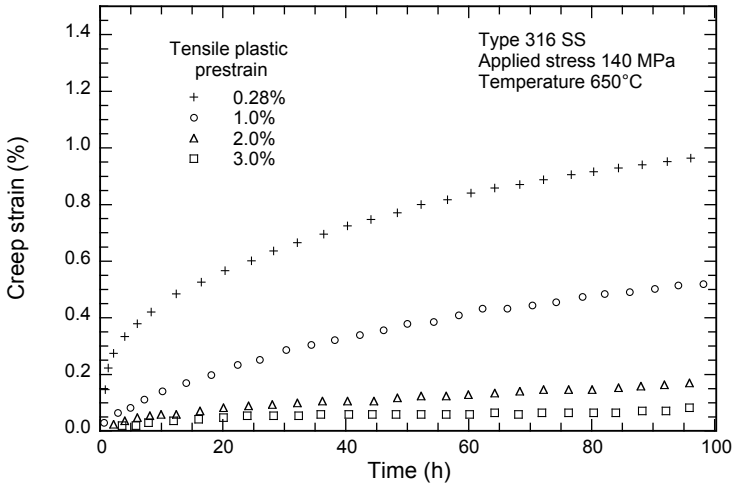

Figure 5.15. Different creep rates at the same stress level but with different prior plastic strains, or maximum stress levels, 316SS (Ohashi et al. 1986).

Other types of creep-plasticity interaction were demonstrated by a series of critical tests performed by Pugh et al. (1972) on 304 stainless steel. In the first test, a specimen was crept at

649ºC for a total creep time of 3,016 hours under a creep loading history where 0.84% creep strain was accumulated. The specimen was subsequently subjected to cyclic loading at room temperature. The stress-strain response of the specimen to the cyclic loadings imposed after the creep test had been completed is shown in Fig. 5.16. The monotonic stress-strain curve from a virgin specimen made of the same heat of 304 stainless steel is included in the figure for comparison. There is clearly shown that there is an influence of prior creep deformation on the subsequent tensile behavior. The classical theory predicts that the effects of plastic strain or creep strain on residual tensile behavior are the same. Thus, it is anticipated that the residual tensile curve (after prior creep deformation) would be similar to that for a virgin specimen when the origin of the post-creep tensile curve is offset by the amount of prior accumulated creep strain. However, as shown in Fig. 5.16, the stress level of the residual tensile curve exceeds that from the stress-strain curve of the virgin specimen (point A).

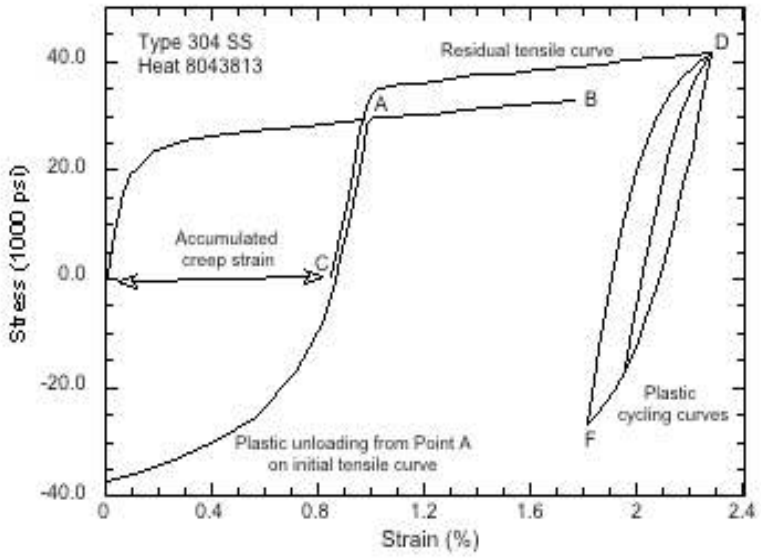

Figure 5.16. Influence of prior creep behavior on tensile behavior, 304SS (Pugh et al. 1972).

Prior room temperature plastic cycling also has an influence on the subsequent creep behavior. The accumulated creep strain versus accumulated time under stress plots of three 304 stainless steel specimens from the tests conducted by Pugh et al. (1972) are shown in Fig. 5.17. The first and second specimens were crept at 649ºC under various creep loading histories from a virgin state. The third specimen was first subjected to a series of room temperature constant strain range cycles (~2.5%) that had gone into the plastic range. The specimen was then subsequently subjected to a creep loading history at 649ºC. The creep strain at 12.5 ksi of the first specimen (crept from the virgin state) is much larger than that of the third specimen, which was cycled at room temperature prior to the creep loading. This shows that when this material is cyclically hardened by prior plastic cycling, the subsequent creep strain accumulation is reduced. This is another manifestation of creep-plasticity interaction that is not accounted for by the classical theory.

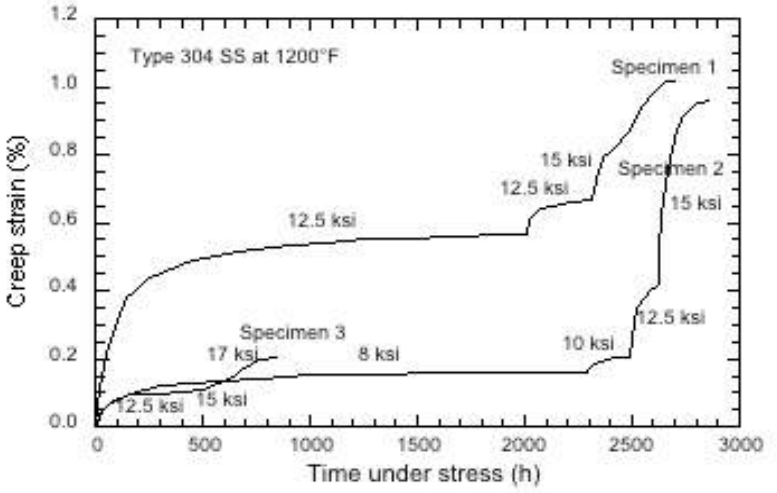

Figure 5.17. Influence of prior creep behavior on tensile behavior, 304SS (Pugh et al. 1972).

There is also an influence of prior creep deformation on the fatigue behavior. The third specimen shown in Fig. 5.17 was subjected to room temperature cycling subsequent to the creep loading. The hysteresis loops from the virgin state and after the creep test sequence are shown in Fig. 5.18. The stress amplitude for post-creep cyclic loading is much higher than that for the virgin material.

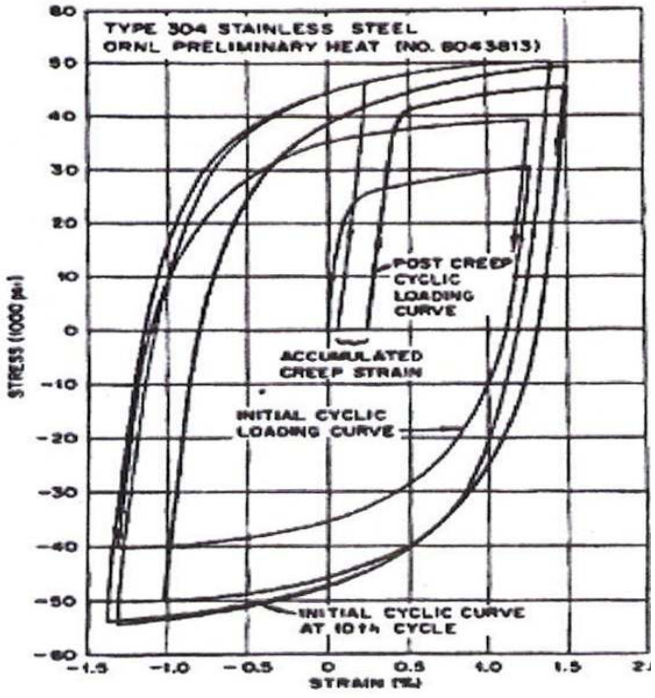

Figure 5.18. The influence of prior creep deformation on the room temperature cycling behavior, 304SS (Pugh et al. 1972).

These examples show that there is creep-plasticity interaction at the small strains that are appropriate for design. The use of classical creep-plasticity model in inelastic analysis would not lead to correct prediction of strain accumulation in structural components. Thus, new formulations of material models are required for the purpose of satisfying the strain limits in Subsection NH using the inelastic analysis approach.

5.3.2 Unified Viscoplastic Constitutive Models

5.3.2.1 Overall Framework

Viscoplasticity formulations have been developed to address the inadequacy of the classical creep-plasticity models. Viscoplasticity is sometimes referred to as a unified theory as all inelastic deformations are considered to be rate dependent and are treated in their totality. There is no distinction between plastic and creep deformation. Although the theory is phenomenological, it is consistent with the viewpoint from deformation mechanisms where inelastic deformation is caused by changes in the defect structure such as nucleation, motion and annihilation of dislocations, the interaction among dislocations and with other defects, grain boundary sliding, and mass transport. These changes would usually occur simultaneously and they cannot be separated into rate independent and rate dependent contributions.

While there are many different formulations of viscoplasticity theory for different materials, they can be broadly described by the following framework. The total strain rates are given as

$$\dot{\varepsilon}_{ij} = \dot{\varepsilon}_{ij}^{el} + \dot{\varepsilon}_{ij}^{th} + \dot{e}_{ij}^{in} \tag{5.5}$$

where the superscripts denote the elastic, thermal, and inelastic contributions to the total strain rates. Incompressible, isotropic inelastic deformation is considered.

A flow rule for the inelastic strain rates can be given in the form, Lemaitre and Chaboche (1994),

$$\dot{e}_{ij}^{in} = \frac{3}{2}\dot{p}\frac{s_{ij} - X_{ij}}{\Gamma} \tag{5.6}$$

where X_{ij} are the deviatoric back stresses, and $s_{ij} - X_{ij}$ are referred to as the overstresses. The deviatoric back stresses are not considered as macroscopically observable quantities and they are treated in the phenomenological theory as internal or state variables. The quantity Γ is the effective overstress given by

$$\Gamma = \sqrt{1.5(s_{ij} - X_{ij})(s_{ij} - X_{ij})} \tag{5.7}$$

and $\dot{p}$ is the effective inelastic strain rate defined as $\dot{p} = \sqrt{(2/3)\,\dot{e}_{ij}^{in}\dot{e}_{ij}^{in}}$. The effective inelastic strain rate is constitutively related to the effective overstress and other state variables. It is usually given in the form

$$\dot{p} = \langle f(h) \rangle \tag{5.8}$$

where the bracket $\langle\ \rangle$ is defined by $\langle f(h)\rangle \equiv f(h)H(h)$. The function $f(h)$ is the viscoplastic flow function, and $H(h)$ is the Heaviside step function. It is required that the viscoplastic flow function $f(h)$ is a strictly increasing function of its argument. It is often given in a power-law form as $f(h)=h^n$. Sometimes, other forms of the viscoplastic flow function are used; e.g., a hyperbolic sine function, $f(h)=a\ \sinh^n(h)$. Various functional forms that have been proposed for h include

$$h=\frac{\Gamma^2-Y^2}{D},\quad \text{due to Robinson (1984)} \tag{5.9}$$

$$h=\frac{\Gamma-Y}{D},\quad \text{due to Chaboche and Nouailhas (1989)} \tag{5.10}$$

where D is the drag stress, a state variable, and Y is the "yield stress state variable" that serves as a cut-off value for the effective overstress, Γ, below which the inelastic strain rates $\dot{e}_{ij}^{in}$ are zero, i.e., only thermo-elastic deformation occurs.

Evolution equations for the back stresses in the form of ordinary differential equations and appropriate initial conditions are generally required to capture the changes in macroscopically observable quantities such as stresses and strains in response to different loading and straining conditions. The evolution of the back stress is also consistent with the deformation mechanism viewpoint on evolving defect structures. A typical set of evolution equations for X_{ij} can be expressed as

$$\dot{X}_{ij} = \underbrace{\frac{2}{3}\,C\,\dot{e}_{ij}^{in}}_{\text{viscoplastic hardening}} - \underbrace{\gamma(p)\,\dot{p}\,X_{ij}}_{\text{dynamic recovery}} - \underbrace{G(\bar{X})\,X_{ij}}_{\text{static (thermal) recovery}} \tag{5.11}$$

where each term on the right hand side represents a phenomenological repository for the deformation mechanism identified. In the equation, C is a material parameter, $\gamma(p)$ is a material function of the accumulated inelastic strain, p, defined as $p=\int \dot{p}\,dt$ over the deformation history, and $G(\bar{X})$ is a thermal recovery function that depends on the effective back stress, $\bar{X}$, given as $\bar{X}=\sqrt{1.5X_{ij}X_{ij}}$. The evolution equations given in Eq. 5.11 are valid for isothermal conditions. For thermal mechanical loading, a temperature rate term is required to augment the right hand side of Eq. 5.11. Evolution equations for D and Y, and additional state variables together with their evolution equations, can be introduced in order to model more complex deformation behavior.

5.3.2.2 316 Stainless Steel and Mod. 9Cr-1Mo Steel

There have been a number of viscoplastic constitutive models developed for austenitic stainless steels and mod.9Cr-1Mo, with varying degrees of success in capturing the important deformation behaviors of these materials. As reviewed in the previous sections, a key difference in

the deformation behavior of these materials is the cyclic hardening behavior of austenitic stainless steels versus the cyclic softening behavior of Cr-Mo steels such as Mod. 9Cr-1Mo. This in turn affects the ratcheting behavior. For example, the amount of ratcheting is initially large for austenitic stainless steels but it saturates after some number of cycles. Opposite ratcheting behavior is observed for Mod. 9Cr-1Mo.

A unified constitutive model for cyclic viscoplasticity was developed by Chaboche and Nouailhas (1989) and applied to 304 (room temperature) and 316 (600 and 625°C) stainless steels under isothermal conditions. Qualitative agreement between the model predictions and test data was achieved. In the Chaboche-Nouailhas model, a Macaulay bracket as in Eq. 5.8 was retained in the flow function, and hence a viscoplastic flow surface was employed. Only viscoplastic strain hardening and dynamic recovery, but not static recovery, were employed in the back stress evolution equations. A memory surface in the plastic strain space, the so-called plastic strain memorization method as introduced by Chaboche et al. (1979) and Ohno (1982), was employed to handle cyclic plasticity behavior. Tertiary creep was not modeled. The material parameters of the Chaboche-Nouailhas model were identified by Rive et al. (1991) from test data for 316 SPH stainless steel at 20, 200, 400 and 600°C.

Ohno et al. (1998) had modified the viscoplastic formulation of Ohno and Wang (1993) for nonlinear kinematic hardening, and applied the resulting model to describe the constitutive behavior, in particular the ratcheting behavior, of 316FR stainless steel. The modification was related to their observation that isotropic hardening depends on maximum plastic strain instead of accumulated plastic strain under ratcheting conditions, as summarized in the previous sections.

A constitutive model for Mod. 9Cr-1Mo steel was developed by Moosbrugger (1992). It was based on the constitutive framework of Chaboche and Nouailhas (1989) on cyclic plasticity and viscoplasticity. As in the Chaboche model, a viscoplastic flow surface was used. Temperature rate terms were introduced in the evolution equations for the state variables to model non-isothermal conditions. A single isotropic softening state variable was introduced, where it can be partitioned between the yield stress, drag stress, and the saturation level of the back stress, to model flow softening and cyclic softening behavior of Mod. 9Cr-1Mo. A procedure for determining the material parameters in the constitutive model was outlined. The model predictions were compared to test data generated at ORNL, e.g., Swindeman (1988). The agreement was good in general, except that the observed behavior of increasing strain softening with decreasing strain rate at 538C was found to be direct opposite to the model prediction. The ratchet strain in a two-bar structure was significant over-predicted by the Moosbrugger model when compared with data.

Yaguchi and Takahashi (2005b) have investigated the capability of several viscoplastic models in predicting the ratcheting behavior of Mod. 9Cr–1Mo steel at 550°C. The work of Ohno and Wang (1993) and Ohno and Abdel-Karim (2000) was collectively referred to as the Ohno-Wang (OW) model. Three variants of the Ohno-Wang model (differed by the dynamic recovery term in the back stress evolution equations) and the model developed by Yaguchi and Takahashi (2000) were used to predict the ratcheting.

The OW-I model has a tendency to underestimate the ratcheting except in cases where marked multiaxial ratcheting was observed. The OW-II model gave good simulation results for multiaxial ratcheting, while it did not always predict uniaxial ratcheting adequately. OW-III model predicted the ratcheting better than the other constitutive models, however, improvement in the case of the uniaxial ratcheting would still be desirable. The Yaguchi and Takahashi (2000) model had a strong tendency to overestimate the ratcheting under both uniaxial and multiaxial conditions. Yaguchi and Takahashi (2005b) theorized that this was due to the Armstrong-Frederick kinematic hardening rule adopted in the back stress evolution equations.

As none of the models considered gave satisfactory ratcheting prediction, Yaguchi and Takahashi (2005b) developed a new constitutive model by incorporating tension-compression asymmetry into the OW-I model, which contains a state recovery term in the back stress evolution equations, and accounts for a strain range dependency in the cyclic softening behavior. While the new constitutive model of Yaguchi and Takahashi (2005b) improved the prediction of uniaxial ratcheting as compared with all other models that they investigated, it did not always give accurate prediction. For multiaxial ratcheting the predictions from the new model generally overestimated the results.

High temperature deformation behaviors such as strain rate sensitivity, creep and stress relaxation, cyclic hardening/softening, dynamic strain aging, and ratcheting for austenitic stainless steels and Cr-Mo steels are very complex to model. The use of viscoplasticity instead of the classical creep-plasticity theory has greatly enhanced the capability in modeling the deformation behaviors of these materials. However, improvement in the predictive capability of these models is still required before they can be used with confidence for inelastic design analyses.

5.4 Creep Rupture/Fracture

5.4.1 ASME Design Limits

Creep rupture from long-term loading and creep-fatigue failure are significant failure modes for structural components under elevated temperature cyclic service. Stress rupture strength, S_r, and creep rupture time, t_r, are two key material properties used in the design rules of Subsection NH to guard against these failure modes. The stress rupture strength is one of the properties used to establish the time dependent, Operating Condition allowable stress, S_t. The rupture time is used in the creep-fatigue procedure to determine creep damage through the time-fraction rule. Design limits for these two properties are developed from creep rupture data. For an illustration, a plot of the creep rupture data at different test temperatures is shown in Fig. 5.19 for 316 stainless steels, from Brinkman (2001). It is typical that a majority of data in a creep rupture database consists of rupture times that are less than 50,000 to 60,000 hours. They are usually supplemented by limited long-term data where the rupture times are over 100,000 hours. Since the design life for non-replaceable high temperature structural components in sodium fast reactor is 60 years, extrapolation of the creep rupture data to cover such design life time is necessary.

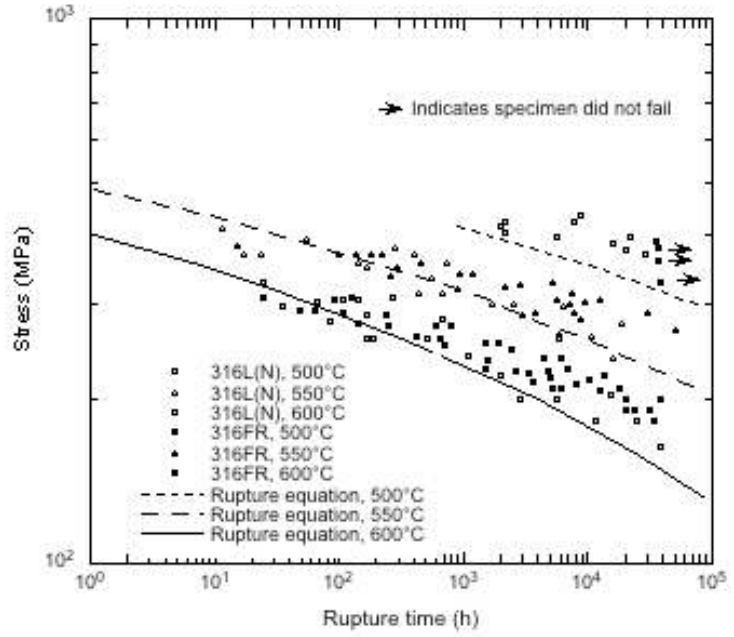

Figure 5.19. Creep rupture data for 316 stainless steels (Brinkman 2001).

The extrapolation of creep rupture data to longer times is generally based on time-temperature parameters, such as the Larson-Miller parameter (LMP) or the Orr-Sherby-Dorn (OSD), defined as

$$\text{LMP} = T(C + \log_{10} t_r) \tag{5.12}$$

$$\text{OSD} = \frac{Q}{2.3RT} - \log_{10} t_r \tag{5.13}$$

where T is the temperature in Kelvin, R is the universal gas constant, and C and Q are fitting parameters. A correlation function that relates stress, temperature and time is then obtained by equating the time-temperature parameter to a stress polynomial. For example, the correlation function in terms of LMP is

$$T(C + \log_{10} t_r) = a_0 + a_1 \log_{10} S + a_2 \left(\log_{10} S\right)^2 + a_3 \left(\log_{10} S\right)^3 \tag{5.14}$$

where S is the applied stress, and a_0, a_1, a_2, and a_3 are additional fitting parameters.

Swindeman (2008) has compiled the creep rupture databases for Subsection NH materials as a part of the effort in Task 6 of the DOE/ASME Gen IV Materials Project on Operation Condition allowable stress values. The Larson-Miller plots in Fig. 5.20 databases summarize the database for 304H and 316H stainless steels, 2¼ Cr-1Mo steel, and Mod. 9Cr-1Mo. The descriptions of these databases are given in Table 5.1.

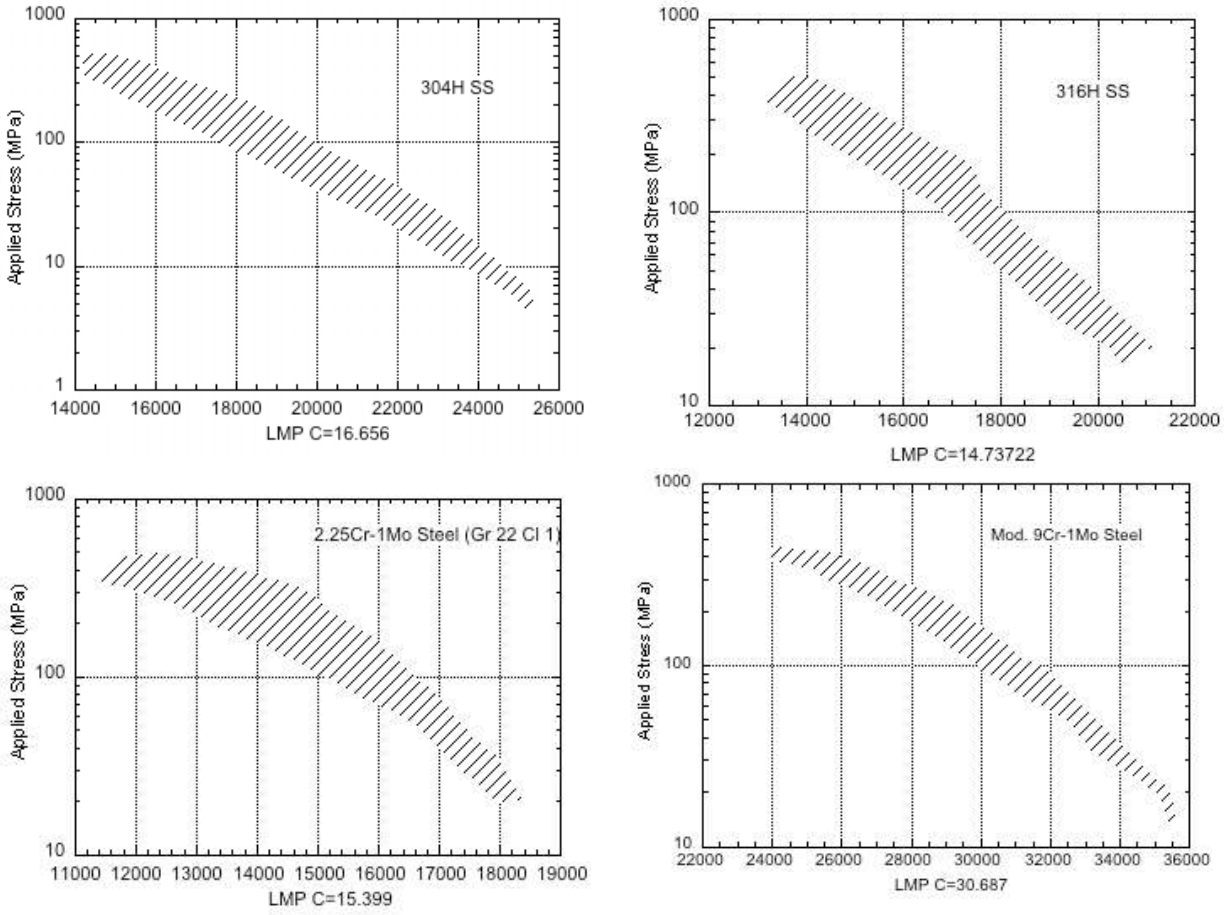

Figure 5.20. Larson-Miller plot of creep rupture data for (top left) 304H, (top right) 316H, (bottom left) 2¼ Cr-1Mo, and (bottom right) Mod. 9Cr-1Mo (Swindeman 2008).

Table 5.1. Description of creep rupture databases compiled by Swindeman (2008)

Material	No. of lots	No. of creep rupture data	Longest rupture life in database (h)
304H stainless steel	75	1170	179,000
304H stainless steel	106	1940	222,000
2¼ Cr-1Mo steel	189	1632	213,000
Mod. 9Cr-1Mo	104	1600	110,000

The use of time-temperature parameters allows the extrapolation of high stress, short-term data to typically low stress and long time (60 years) service conditions, hence reducing the testing effort significantly. However, the time-temperature parameters are essentially empirical parameters that are not based on the understanding of creep deformation and fracture mechanisms. Thus such extrapolation could potentially lead to non-conservative design properties.

5.4.2 Fracture Mechanisms

Ashby et al. (1979) has classified the fracture mechanism of metals into low temperature ($\leq 0.3\ T_m$) and high temperature ($\leq 0.3\ T_m$) modes as shown in Fig. 5.21, where T_m is the melting temperature. In the low temperature regime, cleavage fracture can occur either transgranularly or intergranularly. For more ductile materials in the low temperature regime, fracture can occur by the mechanism of nucleation, plastic growth and coalescence of voids in the grains; by the formation of localized shear bands; or by necking. At higher temperatures where creep deformation is present, the fracture mechanism can involve the nucleation, growth by diffusion and/or creep deformation, and coalescence of voids on grain boundaries; by formation of grain boundary wedge cracks; or by rupture due to dynamic recovery or recrystallization.

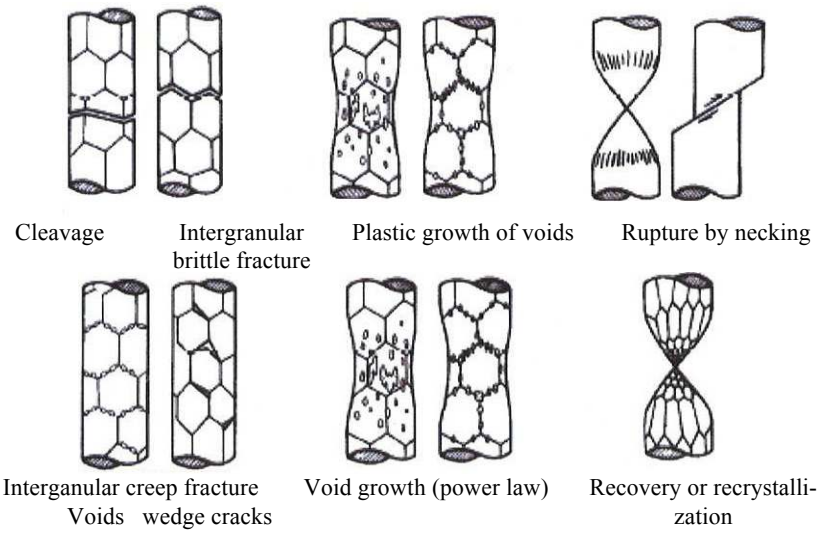

Figure 5.21. Classification of fracture mechanisms (Ashby et al. 1979).

Since a material can show all of these failure modes, Ashby et al. (1979) introduced the concept of a fracture mechanism map to show graphically the conditions under which each failure mode occurs, and of how these conditions might change for different materials. The fracture mechanism map can be constructed by coupling the understanding of plasticity and creep with each fracture mechanism, and thereby predict the range of dominance of each failure mode. Alternatively, the range of dominance can be determined from examination of failed specimen, and the stress, temperature, and time in which each fracture mechanism appears can be displayed in the map.

Figure 5.22 shows fracture mechanism map of 316 (L)N stainless steel determined by Li and Zinkle (2007) using the first approach. The fracture mechanism maps constructed by Fields et al. (1980) using the second approach for of 316 (low boron) stainless steel and 2¼ Cr-1Mo steel are shown in Figs. 5.23 and 5.24, respectively.

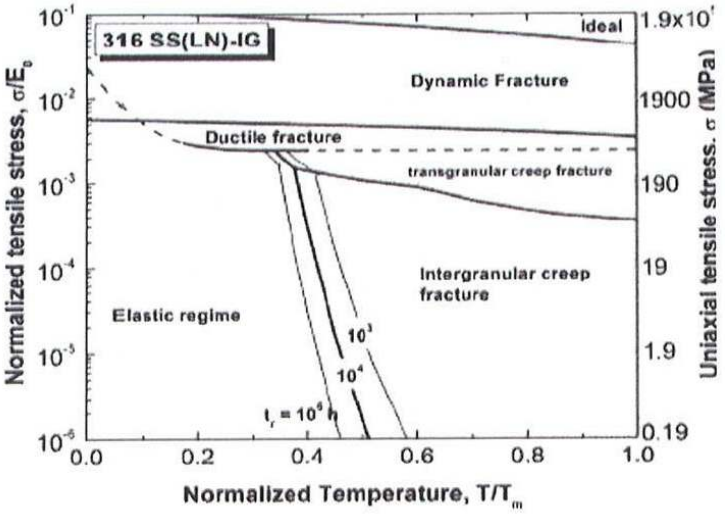

Figure 5.22. Fracture mechanism map for 316(LN) stainless steel (Li and Zinkle 2007).).

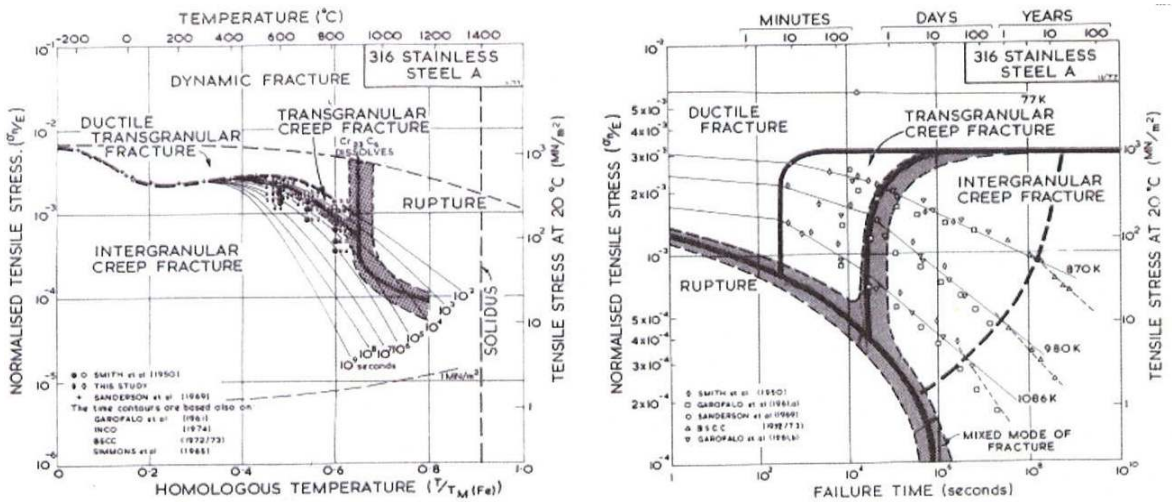

Figure 5.23. Fracture mechanism maps for (low boron) 316 stainless steel (Fields et al. 1980).

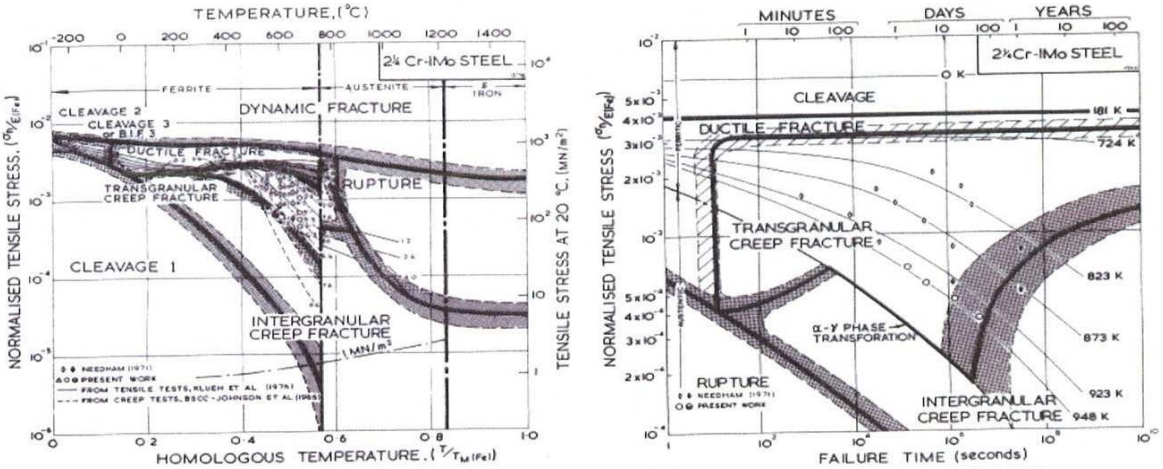

Figure 5.24. Fracture mechanism maps for 2¼ Cr-1Mo steel (Fields et al. 1980).

Concerning the issue of extrapolation of creep rupture data to establish low stress and long term design limits, the plots of the fracture mechanism map in the form of stress versus failure time as shown in Figs. 5.23(b) and 5.24(b) are particularly revealing. If the creep rupture data, e.g., from Fig. 5.19, are overlaid on the fracture mechanism map of Fig. 5.23(b), then it can be determined easily whether all the data fall into one fracture mechanism region or they spread across a number of regions. If it is the former, then the extrapolated results can be used with higher confidence. If not, the fracture mechanism map can be used to segregate the data into appropriate fracture mechanism regions and extrapolation of data within a fracture mechanism region can be performed.

5.5 Issues and Resolutions

5.5.1 Viscoplastic Constitutive Equations

The elastic and simplified inelastic criteria for satisfying the strain limits by using the elastic stress analysis results, while simpler, are very conservative. Critical, high stress locations might not be shown acceptable by these criteria and hence limits design options. Thus, validated inelastic analysis capabilities are important tools for designers to overcome such difficulty by performing a more accurate, and potentially less restrictive, strain evaluation.

As reviewed in the previous sections, unified viscoplastic constitutive equations for austenitic stainless steels and Cr-Mo steels have had success in modeling the deformation behaviors of these materials. However, two particularly important aspects of these models need to be addressed. One is related to the more accurate modeling of uniaxial and multiaxial ratcheting behavior and the other is to account for thermal aging of these materials in the constitutive equations.

In terms of modeling ratcheting behavior, various approaches such as Burlet and Cailletaud (1986) and Ohno and Abdel-Karim (2000) provide good predictions under special loading conditions. Thus, a dynamic recovery term in the back stress evolution equations that can distinguish between uniaxial and multiaxial loading conditions holds the key to successful modeling of ratcheting behavior.

As austenitic stainless steels and Cr-Mo steels thermally aged, the deformation behaviors of these materials could be significantly different in the later part of their design life. Thus, a state variable that can be used as a depository in the viscoplastic constitutive equations for modeling the thermal aging effect needs to be developed. Stress-strain curves from thermally aged materials will be required to support such modeling development.

5.5.2 Extrapolation of Creep Rupture Data to 60 Years

There are significant issues in the current code approach to extrapolate high stress and short term creep rupture data to determine design limits for low stress and long term (60 years) conditions, since the fracture mechanism associated with the test data might not be the same as that for a structural component under service conditions. However, extrapolation of test data is unavoidable because it takes too long to generate data that are prototypical. This issue can be resolved by mapping out the regions of dominance for each of the potential fracture mechanisms,

e.g., in the form of the Ashby fracture mechanism map, so that it can be used to guide the data extrapolation process.

However, problem will arise if the actual failure data are used to construct the fracture mechanism map, as in the approach of Fields et al. (1980), since very long-term failure data are required to construct the boundaries between fracture mechanism regions. The use of simple models, as in the approach of Li and Zinkle (2007), suffers from a lack of fidelity in the failure models used to construct the fracture mechanism boundaries. This difficulty can be overcome by employing an integrated approach that combines micromechanical finite element simulations of applicable fracture mechanisms with selective accelerated creep rupture testing.

6. FATIGUE AND CREEP-FATIGUE INTERACTION

Fatigue at high temperature is a complex phenomenon because of a number of time-dependent processes involved. When components are loaded under cyclic loading at high temperature, additional damage processes are superimposed on fatigue damage. Time-dependent creep deformation can significantly reduce fatigue life, and in turn, fatigue deformation can seriously reduce creep life. The interaction of fatigue and creep, so-called "creep-fatigue interaction," is a significant structural failure mode that must be considered in the design of elevated-temperature components. Other processes such as oxidation, microstructural evolution, dynamic strain aging, etc., further complicate creep-fatigue interaction behavior. Since creep-fatigue interaction can have a detrimental effect on the performance of structural components operating at high temperatures, creep-fatigue interaction has been studied extensively to understand the phenomenon, quantify the effect, and develop life prediction models. Despite significant progress in this area, understanding of the complex mechanisms involved in creep-fatigue is far from complete.

In the following sections, the database of creep-fatigue for austenitic stainless steels, 304 and 316, and ferritic steels, 2.25Cr-1Mo and mod.9Cr-1Mo steels is evaluated. The available creep-fatigue life prediction models are described. The ASME Code creep-fatigue design rules are summarized, and the issues with current design rules and proposed resolutions are discussed.

6.1 Assessment of Creep-Fatigue Database

6.1.1 Austenitic Stainless Steels

Base Metal

Creep-fatigue properties of austenitic stainless steels at elevated temperatures depend on several factors, including strain range, strain rate, temperature, waveform, hold time and environment. Different types of waveforms have been used to investigate the creep-fatigue interaction of a material, as shown in Fig. 6.1. Abbreviations for each type of waveform to be used in the following sections are given in the figure.

There is an extensive database of fatigue and creep-fatigue interaction on type 304 SS and 316 SS. The ASME creep-fatigue design rules for austenitic stainless steels were developed,

primarily based on the data generated in 1970s, by the U.S. DOE LMR reactor program. Many creep-fatigue data have been generated in nuclear programs in other countries, e.g. Japan, France, India, etc. as well. These data are however, generally not available in the open literature. Table 6.1 summarizes the creep-fatigue data for 304 and 316 stainless steels from various sources.

Majumdar and Maiya (1978) summarized the creep-fatigue data of 304 SS tested at 593°C. The effects of wave form on the fatigue life was studied by using slow-fast, fast-slow, and slow-slow waveforms with a fast strain rate of 10^{-2}/sec and a slow strain rate of 10^{-4}/sec, or with a fast strain rate of 10^{-3}/sec and a slow strain rate of 10^{-6}/sec. The hold-time tests were carried out with tension hold only, symmetric hold in tension and compression, or unsymmetric hold in tension and compression. Thirteen tests were reported with total strain range, plastic strain rage, stress range, and life to failure.

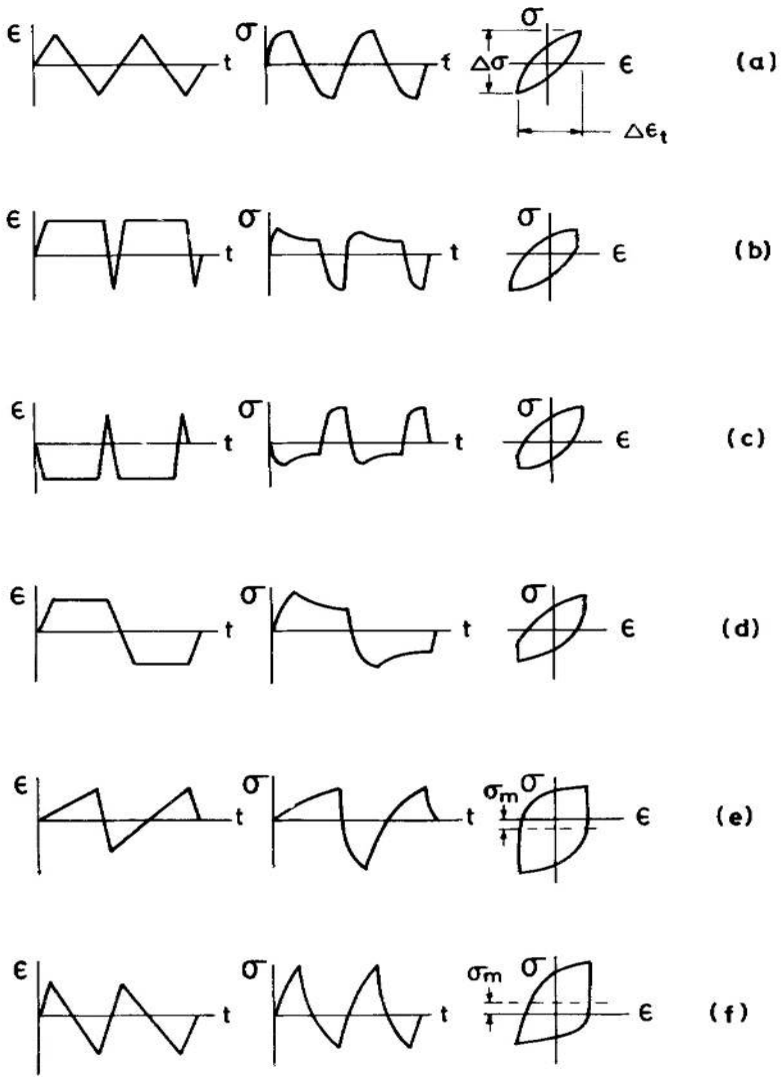

Figure 6.1. Different types of waveforms: (a) continuous cycling (CC), (b) tension hold only (TH), (c) compression hold only (CH), (d) tension and compression hold (TCH), (e) slow-fast waveform, (f) fast-slow waveform. (Note: slow-slow waveform refers to a balanced waveform with a slower strain rate).

Table 6.1. Creep-fatigue data of austenitic stainless steels, 304 and 316.

Alloy	T (°C)	Strain ranges (%)	Test type	Hold time (min)	Environment	References
304 SS	593	1-2	Slow-fast, fast-slow, slow-slow, TH, CH	5-15	Air	Majumdar and Maiya 1978
304 SS	482-593	0.5-2	CC, slow-slow	-	Air	Majumdar et al. 1981
304 SS	482-593	0.35-2	TH, CH, TCH	1-600	Air	Majumdar et al. 1981
304 SS	593	0.35-2	CC, TH	1-600	Air	Burke and Weiss 1983
304 SS	650	0.3-2	CC, TH	1-180		Berling and Conway 1969
304 SS	482, 593	1-2	TH	1-600	Air	Ermi and Moteff 1982
304 SS	650, 820		Slow-fast, fast-slow, slow-slow	-	Air, Vac	Coffin 1977
304L SS	530, 600, 650		TH	1-30	Air	Rie et al. 1988
304L SS	550, 592	1.5-2.5	TH	10, 30	Argon	Yong et al. 2000
304, 316 SS	450-750		TH, CH, TCH	48 h max		Schmitt and Scheibe 1983
304, 316 SS	430, 650, 816		Slow-slow	-	Air	Berling and Slot 1969
316 SS	593	0.5-2	CC, TH	6-600	Air	Brinkman et al. 1972
316 SS	600	1.4-2.5	TH	10-500		Dawson et al. 1967
316 SS	625		TH	48 h max	Air	Wood et al. 1980
316 SS	570-625	0.6 min	TH	24 h max	Air	Warening 1981
316 SS	20-800		Slow-slow		vac	Furuya et al. 1980

Majumdar et al. (1981) reported a large number of fatigue and creep-fatigue data of type 304 SS at temperatures of 482 to 593°C. Tests were carried out either under continuous cycling with a strain rate of 10^{-3}/sec, or a much slower strain rate. Hold-time tests were conducted with the hold time imposed at peak strains in tension only, in compression only, or in both tension and compression. The hold time varied from 1 minute to 10 h. A wide range of strain ranges, 0.35-2% was studied. All tests were done in air environment.

Burke and Weiss (1983) reported the creep-fatigue data of 304 SS tested at 593°C in air. The tests were conducted in strain control with the hold time applied at tensile peak strains with the period from 1 minute to 10 hours. The strain ranges covered from 0.35% to 2.0%. The data were summarized in a time-to-failure vs. cycles-to-failure log-log plot. The need for data at low strain ranges is clearly demonstrated. Berling and Conway (1969) reported pure fatigue and hold-time creep fatigue data of 304 SS at 650°C. A hold time ranging from 1 minute to 180 minutes was applied in tensile peak strain at total strain ranges of 0.3 to 2%. Ermin and Moteff (1982) reported hold-time creep-fatigue data for 304 SS at 482 and 593°C in air. Tension-only hold time from 1 minute to 10 hours was used. The total strain ranges examined were 1-2%.

Coffin (1977) studied the strain rate effects on the fatigue life of 304 SS. Fatigue tests were conducted at 650 and 820°C in air or in vacuum. Waveforms of slow-fast, fast-slow, and slow-slow were used. Rie et al. (1988) reported the creep-fatigue data of 304 SS at temperatures of 530, 600, and 650°C. The tests were carried out in push-pull, fully reversed strain control. Hold times were superimposed at tensile peak strains with the time between 1 and 600 minutes.

Yong et al. (2000) reported the hold-time fatigue data on 304L SS at 550 and 592°C in argon atmosphere. The tension hold time was 10 and 30 minutes.

Schmitt and Scheiber (1983) reported the hold-time creep-fatigue data for 304 and 316 SS. A hold time up to 48 h was applied at peak strains either in tension, or in compression, or in both tension and compression. Berlin and Slot (1969) reported the results of strain-controlled, low-cycle fatigue experiments on annealed 304, 316 and 348 SS at temperatures of 430, 650, and 816°C. Effects of strain rates on fatigue life were investigated by applying three different strain rates during continuous cycling, i.e. 4×10^{-3}, 4×10^{-4}, 4×10^{-5} /sec. Brinkman et al. (1972) reported the creep-fatigue data of 316 SS tested at 593°C in air. These data were obtained on hourglass specimens tested in fully reversed strain control. Tensile or hold times were employed at peak strains with the longest hold time of 10 hours. Dawson et al. (1967) published the hold-time fatigue data on 316 SS at 600°C. The hold time was applied in tension with the time up to 500 minutes.

Wood et al. (1980) reported the creep-fatigue data of 316 SS at 625°C. Tests were conducted in strain control, and the hold-time between 0.2 and 48 h was applied at peak tensile strains. Warening (1981) reported the creep-fatigue data of four different heats of 316 SS in the temperature range of 570 to 625°C. Tests were carried out under strain-controlled push-pull conditions in air. The hold time was applied at peak tensile strains and the long hold time was 24 hours. The minimum strain range was 0.6%. For two heats of materials tested at 593 and 625°C, the loss of fatigue life was recovered at longer hold times. Furuya et al. (1980) reported the fatigue data of 316 SS at temperatures of 20-800°C in vacuum. Tests were done under push-pull, strain-controlled mode under continuous cycling with strain rates of 5×10^{-3} to 5×10^{-5} /sec.

In summary, the fatigue and creep-fatigue data of 304 SS cover a wide range of temperatures from 482 to 650°C (with some slow strain rate tests up to 820°C) using various types of waveforms. The longest hold time applied was 10 h. Tests were carried out mostly in air with some tests done in vacuum and Argon to eliminate the environmental effects. Compared to 304 SS, creep-fatigue tests on 316 SS were conducted primarily by applying tensile hold times in air environment at temperatures ≤625°C. The maximum hold time was 48 h. The major findings of the creep-fatigue behavior of type 304 and 316 SS are:

- Tension holds are more damaging than compression holds or combined tension and compression holds.
- Fatigue life decreases with increasing hold time without clear indication of saturation effect of the hold time up to 10 h.
- Exploratory tests with hold times imposed at zero stress or zero stress relaxation points on the hysteresis loops reduce fatigue life, but less damaging than hold times applied at peak tensile strains.
- Fatigue life decreases as the strain rate decreases under continuous cycling.
- Slow-fast waveform is more damaging than fast-slow or equal strain rate waveforms in air.

- Slow-fast waveform is as nearly damaging in vacuum as the corresponding air test, while the balanced waveform in a vacuum test produced several times higher fatigue life than that in air.
- Cyclic strain hardening occurs in fatigue and creep-fatigue tests.
- Tensile holds or slow-fast waveforms lead to intergranular fracture. The fracture surface shows rounded cavities (r-type cavity) at grain boundaries that are normal to tensile stress. Wedge cracking (w-type cavity) near grain boundary triple-point junctions was also observed. As the hold time increases or strain rate decreases, creep damage becomes more prominent with increasing creep-fatigue interaction.
- In general, for relatively short hold time tests at large strain amplitudes, wedge cracks tend to predominate, while for long hold time tests at low strain amplitudes, r-type cavities tend to be dominant. The distribution of cavities is inhomogeneous. Some grain boundaries are highly resistant to cavitation while others are prone to cavitation. For grain boundaries with cavitation, the number and spacing of cavities depend on the strain rate and time in addition to metallurgical factors such as grain size and distribution and size of grain boundary precipitates.
- Specimens that are tested under compressive-hold or symmetrical-loading cycles (e.g., symmetrical continuous or symmetrical hold-time tests) fail by transgranular cracking.

One of the major factors that influence the fatigue properties at high temperature is the environment. High-temperature fatigue tests in air in austenitic stainless steels, 304 and 316 yield shorter fatigue life than in vacuum or in low-oxygen sodium. Comparison of vacuum fatigue data with air fatigue data showed an improvement in fatigue life with factors of 3 to 5 at strain ranges of 0.5 to 2.0%. The difference in fatigue life between air and vacuum tests tends to diminish as the length of tensile hold time increases. The beneficial effect of sodium environment on the fatigue life was attributed to delayed crack initiation and possibly decreased crack growth rates in sodium. The dynamic strain aging (DSA) phenomenon was observed in stainless steels when cycled above temperatures of ≈500°C. The DSA effect in austenitic stainless steels is associated with dislocation locking by carbon and nitrogen interstitial solutes. It is assumed that the mechanisms of DSA cyclic deformation are similar to those observed under monotonic loading.

Most of failure modes associated with creep-fatigue cyclic loading in austenitic stainless steels can be categorized into three types: fatigue-dominated, creep-dominated, and creep-fatigue-interaction. The fatigue-dominated failure is characterized by transgranular fracture, and it is often observed in high strain range and short hold time tests. Creep-dominated failures are characterized by intergranular fracture, and failure occurs by interlocking of internal grain boundary damage. Mixed mode fractures of creep-fatigue interaction occur by the interactive propagation of a surface fatigue crack into cavitated material. High strain ranges and short hold time tests tend to show fatigue-dominated failure; small strain range and long hold time tests are susceptible to creep-dominated damage.

Weldments

Most of the elevated-temperature fatigue data on 304 and 316 SS weldments were generated under the DOE LMR reactor programs and other international nuclear programs in 1970s

and 1980s. Data on 304 SS weldments with 304 and 308 filler metals and with different welding processes and heat treatments are available up to 593°C. Fatigue data on 316 SS weldments are available to 625°C with 16-8-2 and 316 as filler metals and with different welding parameters. The ASME Code fatigue strength reduction factor for weldments was primarily based on the ORNL review of fatigue data at elevated temperature on weldment materials available during that time of period (Corum 1990).

Specimens used in weldment fatigue studies are often three types, as shown in Fig. 6.2 (Corum 1990). Weld metal specimens are taken either longitudinally or transversely and used for the characterization of fatigue behavior of weld metal. Specimens taken transversely across the weld contain base metal, HAZ and weld metal.

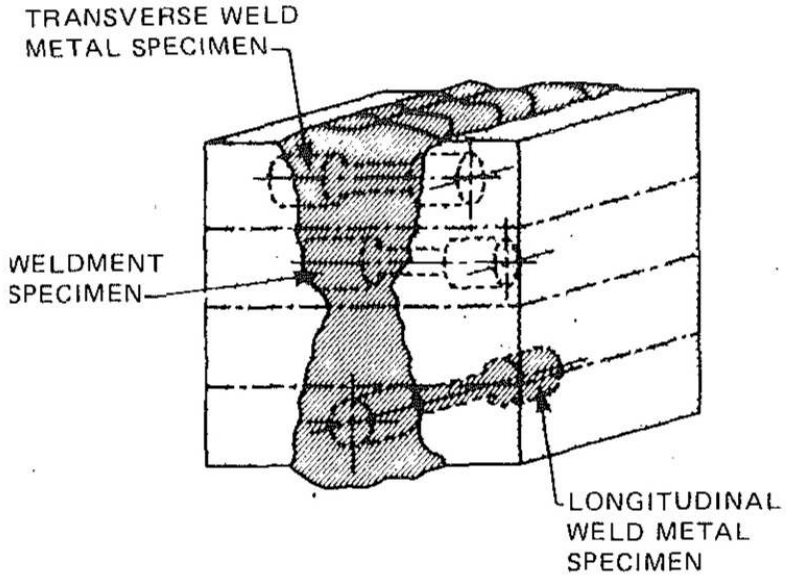

(a) Specimen orientation

Figure 6.2. Weldment fatigue specimen types (Corum 1990).

Brinkman et al. (1973) reported the results of fatigue tests of 304/308 weldments between room temperature and 593°C. Specimens were taken from different positions and orientations with double-U groove heavy section weldments. Fatigue tests were conducted in strain control in air. Depending on the orientation of the specimens, the fatigue life of weld specimens was either below or equivalent to that of the base metal at 593°C. Raske (1977) studied the fatigue and creep-fatigue properties of Type 16-8-2 (16%Cr-8%Ni-2%Mo) stainless steel weld metal. Continuous cycling and tension-hold time fatigue tests were conducted at 593°C. The hold time varied from 6 min to 5h. Korth and Harper (1976) studied fatigue and creep-fatigue behavior of 304/308 welds at 482 and 593°C in air. Tests were done in strain-controlled, fully reversed uniaxial mode. Creep-fatigue interaction was investigated by applying hold times at peak tensile strains with the period of hold time from 0.01 to 0.5 h. The strain ranges were from 0.5 to 2%.

Corum (1990) reported the fatigue data of 316 SS weldments of tubular specimens. The work was to confirm the fatigue strength reduction factor in the Code and provide further understanding of the metallurgical notch effect in fatigue. Specimens were made from weldments with gas tungsten arc process and filler metal of 16-8-2. The base metal was solution annealed

before welding and no heat treatment was performed after welding. Longitudinal and circumferential weldment specimens were fatigue tested at 550°C in either axial or torsional strain control. The main conclusions were that the reduction factor of 2 on fatigue life is appropriate, and cyclic shear strain on the fusion zone did not seem to be more detrimental than cyclic normal strain.

Bhanu et al. (1990) reported low cycle fatigue data of 304 base metal, 308 SS weld metal and 304-308 weldments at 550 and 650°C in air. Weldments were prepared by metal arc welding process. Tests were conducted in axial strain control at strain ranges of 0.5 to 1.6%. The base metal showed superior fatigue resistance to that of the weldment. Solution annealing of weldments before testing improved the fatigue life. Rao et al. (1996) studied fatigue and creep-fatigue behavior of 304 SS base metal, 308 weld metal, and 304/308 weldments, and 316L(N) SS base metal, 316 weld metal, and 316L(N)/316 weld joint. The weldments were made by shielded metal arc welding process. Weld specimens were prepared from the Single-V or double-V weld joints. Fully-reversed, axial strain-controlled tests were conducted in air at 550 and 650°C. Hold time effects were investigated by applying a hold time in tension, or compression, or both tension and compression up to 10 minutes. Tension holds were found to be most damaging. Reduction in fatigue life increased with increasing hold time in tension. It is noted that cyclic hardening occurs in base metal, cyclic hardening occurs in weld metal, and initial cyclic hardening followed by cyclic softening was observed in weld joint in solution annealed 304 and 316 SS. In weld metal, σ phase formation induced from δ ferrite causes stress concentration around σ phase and leads to early crack initiation.

Goyal et al. (2009) reported on the effect of thermal aging on fatigue life of 316 SS welds. Weldments were prepared by shielded metal arc welding process using 316 electrodes. Thermal aging prior to fatigue testing was carried out at 550 and 600°C for 10,000 h. Fatigue tests were conducted at 550 and 600°C with strain ranges of 0.5 to 1.2%. The fatigue life of aged weldments was shorter than that of the unaged samples. Available fatigue and creep-fatigue data of 304 and 316 SS weldments are summarized in Table 6.2.

The general trends of the fatigue data of 304 and 316 SS weldments are: (1) the longitudinal weld metal fatigue strength is close to that of the base metal; (2) weldment and traverse weld metal specimens showed inferior fatigue properties in the mid-cycle region. The reduction factors varied between 1.5 and 1.8. Creep-fatigue data of 304 and 316 austenitic stainless steel welds are very limited.

Table 6.2. Creep-fatigue data of austenitic stainless steels and their weldments

Alloy	T (°C)	Strain ranges (%)	Type of tests	Hold time (min)	Environment	References
304/308	25-593	-	CC	-	Air	Brinkman 1975
304/308	482, 593	0.5-2	CC, TH	1-30	Air	Korth & Harper 1975
16-8-2	593		CC, TH	6-300		Raske 1977
316/16-8-2	550	-	CC	-	-	Corum 1990
304/308	550, 650	0.5-1.6	CC	-	-	Bhanu et al. 1990
304/308, 316L(N)/316	550, 650	0.5-2	CC, TH, CH, TCH	1-10	Air	Rao et al. 1996
Aged 316 weld	550, 650	0.5-1.2	CC	-	-	Goyal et al. 2009

6.1.2 Ferritic Steels

6.1.2.1 2.25Cr-1Mo Steel

Base Metal

A significant amount of fatigue and creep-fatigue data has been generated for annealed or isothermally annealed 2.25Cr-1Mo steel. The influence of environment, temperature, strain range, strain rate, hold times, waveform, heat treatment, and heat-to-heat variations on the fatigue and creep-fatigue behavior of this alloy has been evaluated. Available fatigue and creep data of 2.25Cr-1Mo steel are summarized in Table 6.3.

A huge database of fatigue data were generated in 1970s on annealed and isothermally annealed 2.25Cr-1Mo steel with a number of different heats (Brinkman 1978, Majumdar 1981). Fatigue design curve of 2.25Cr-1Mo in the ASME Code was primarily based on these fatigue data. Fatigue tests were carried out on smooth hourglass shaped specimens in fully reversed load-controlled or strain-controlled modes at room temperature to 593°C in air environment. Comparison of fatigue data between annealed specimens and isothermally annealed specimens showed no difference in the low cycle fatigue life regime.

The fatigue behavior of 2.25Cr-1Mo steel depends on metallurgical state, strain rate, waveform, environment (e.g. oxidation) and classical creep damage. Temperature was found to have little or no effect on low-cycle fatigue life below 315°C. Dynamic strain aging (DSA) occurs in the temperature range of 316 to 427°C. It was recommended that for applications involving low strain rates, where DSA is possible, the design curve for 427°C be modified to take into account the reduction caused by the DSA. The ASME fatigue design curves do not take into account the DSA, and are valid only for the strain rate of 4×10^{-3}/sec.

The effect of melting practice and post-weld heat treatment on the fatigue life was also evaluated. Fatigue data from air-melted and annealed materials and data from vacuum-arc remelted (VAR) and electro-slag remelted (ESR) material with the post-weld heat treatment at 538°C were compared, and no influence of these variables on the fatigue life was observed. Small heat-to-heat variations were observed at 427°C primarily in the high cycle regime. The differences in the fatigue life were attributed to small differences in chemistry and/or heat treatment effect. The material with a lower carbon content showed inferior fatigue resistance, which implies that decarburization at high temperature could have significant effect on fatigue strength.

Environmental effects on fatigue life were investigated by fatigue tests in air, vacuum, low-oxygen containing sodium, and simulated high-temperature gas-cooled reactor helium environments at temperatures in the range of 538 to 593°C. The fatigue life was increased by factors of 2 to 4 in sodium compared to air data. Fatigue data generated in impure helium showed equivalent or slightly increased fatigue life in comparison to air data.

Recently, Yamaguchi et al. (2006) examined the influence of heat treatment on fatigue life. The fatigue data, generated by National Institute for Materials Science (NIMS), for normal-

ized and tempered 2.25Cr-1Mo steel were compiled and compared with annealed 2.25Cr-1Mo steel and ASME fatigue design curves (shown in Fig. 6.3).

Table 6.3. Summary of creep-fatigue data for 2.25Cr-1Mo steel

Alloy/Heat Treatment	T (°C)	Type of tests	Strain range (%)	Hold time (min)	Environment	References
Iso. Ann. (Heat 3P5601)	25-538	CC	0.35-2	-	Air	Majumdar 1981
A+PWHT (Heat 3P5601)	427, 538	CC	0.3-2	-	Air	Majumdar 1981
A (Heat 91775)	427, 538	CC	0.31-3.2	-	Air	Majumdar 1981
A (Heat 56447)	427, 538	CC	0.3-2	-	Air	Majumdar 1981
A (Heat Z2013)	510-593	CC	0.4-3.4	-	Air	Majumdar et al. 81
A (C7409)	427-593	CC	0.35-4	-	Air	Majumdar et al. 81
Iso. Ann (C7409)	427-593	CC	0.35-4	-	Air	Majumdar et al. 81
GE tubsheet	538	CC	0.4-3	-	Air	Majumdar 1981
GE shell plate	538	CC	0.4-3	-	Air	Majumdar 1981
Heat 20017	25-538	CC	0.25-3	-	Air	Majumdar 1981
Heat 3P5601	316-538	CC	0.25-2	-	Air	Majumdar 1981
Heat 3P5601	316-538	CC, slow-slow	0.5-2	-	Air	Majumdar 1981
Heat 20017	24-371	CC, slow-slow	0.4-2	-	Air	Majumdar 1981
A	371, 427, 482, 538	TH, CH, TCH	-	60 min max.	Air	Brinkman et al. 1976, Booker and Majumdar 1982
A+PWHT	510, 566	Strain-hold	-	-	Air	Booker and Majumdar 1982
Heat 3P5601, 20017	427, 482, 538	TH, CH, TCH	0.4-2	30 max.	Air	Majumdar 1981
A+PWHT	234, 454	Strain-hold	-	-	Air	Booker and Majumdar 1982
A	482, 538, 593	CC, TH, CH, TCH	0.5%	6	He	Booker and Majumdar 1982
A	538	Fast-slow	-	-	Na	Booker and Majumdar 1982
A	538	Slow-fast	-	-	Na	Booker and Majumdar 1982
A+Na Exp	538	Fast-slow	-	-	Na	Booker and Majumdar 1982
A+Na Exp	538, 593	Slow-fast	-	-	Na	Booker and Majumdar 1982
A+PWHT	454, 510, 566	Strain-hold	-	-	Na	Booker and Majumdar 1982
NT+PWHT	565	CC, TH, CH, TCH	0.5	6	Air, vac	Kschinka and Stubbins 1989
A	500, 600	TH, CH	1	2	Air, vac	Hecht and Weertman 1998
2.25Cr-1Mo	470	CC, CH, TH, CH TCH	-	1-10	-	Sonoya et al. 1991

Fatigue tests were carried out under axial strain control in air at temperatures of 400, 500 and 600°C at strain rates of 10^{-2} and 10^{-3}/s. The study suggested that the ASME fatigue design curve developed, based on the fatigue data of annealed 2.25Cr-1Mo, is not conservative for normalized-tempered 2.25Cr-1Mo.

In summary, there are a sufficient number of fatigue data for annealed and isothermally annealed 2.25Cr-1Mo steel. Question remains if and how the DSA is incorporated in the design fatigue curves.

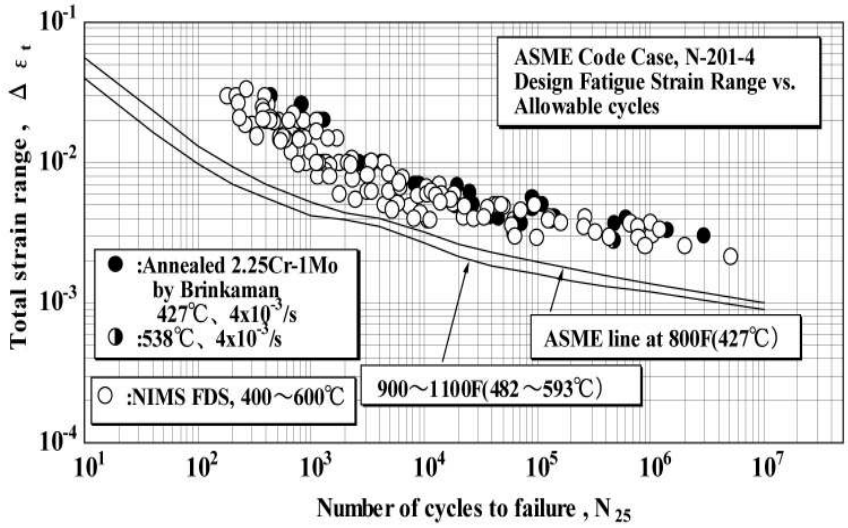

Figure 6.3. Comparison of fatigue data of normalized and tempered 2.25Cr-1Mo with data of annealed 2.25Cr-1Mo and ASME fatigue design curves.

A majority number of creep-fatigue data for 2.25Cr-1Mo steel were obtained from the US DOE reactor program (Brinkman et al. 76, Booker and Majumdar 82). Data from the open literature are also included in Table 6.3. Creep-fatigue data for the steel were mostly obtained from strain-controlled fatigue tests in air with hold times imposed at peak tensile strains, or compressive strains, or both. The temperature range covers from 371 to 593°C. The influence of sodium environment on creep-fatigue properties of 2.25Cr-1Mo steel was also explored to a great extent. Other types of creep-fatigue tests performed on 2.25Cr-1Mo steel include tests with hold times employed at zero stress or at a point on the hysteresis loop such that no stress relaxation occurred during the hold, and hold times applied at peak stresses in tension, or compression, or both, during which the stress was held constant and strain increased to a fixed strain limit.

Kschinka and Stubbins (1989) studied the creep-fatigue-environment interaction in bainitic 2.25Cr-1Mo steel. The test material was supplied by ORNL (Heat 646363), and then heat-treated to create a 100% bainite microstructure. Uniaxial strain-controlled fatigue tests were performed at 565°C in air or in vacuum. Hold times were applied in either tension, or compression, or both tension and compression at peak strains with the time period up to 6 minutes. Notched specimens were also tested.

Hecht and Weertman (1998) reported the creep-fatigue data for 2.25Cr-1Mo steel at 500 and 600°C in air or in vacuum. Tests were carried out using hourglass-shaped specimens in uniaxial total strain control. A hold time of 2 min was applied at either peak tensile strain or peak compressive strain. The total strain range applied was 1%, and strain rate was 4.3×10^{-3}/sec.

Sonoya et al. (1991) reported the fatigue and creep-fatigue data of 2.25Cr-1Mo at 470°C. Tests were carried out in strain control with the hold time of 1-10 minutes applied in either tension or compression, or in both tension and compression. The data were used to develop the creep-fatigue life prediction method using Diercks equation.

Creep-fatigue in 2.25Cr-1Mo steel is a complex phenomenon, especially when tested in air. It is associated with several mechanisms involving oxidation, classical creep-fatigue damage, and dynamic strain aging. The creep-fatigue behavior of 2.25Cr-1Mo steel is substantially different from that of austenitic stainless steels in several aspects. Characteristics of creep-fatigue behavior of 2.25Cr-1Mo steel are summarized below:

- Compressive hold times are more damaging than tensile hold times, particularly at low strain ranges.
- Fracture failure modes were often transgranular when tested in air, with or without hold times with severe oxidation; consistent patterns of circumferential oxide cracking was observed in specimens tested with compressive hold times. However, it is unclear if prolonged exposure to elevated temperatures under cyclic loading would result in intergranular fracture.
- Fatigue life is dependent on loading frequency; fatigue life was reduced as frequency decreased, even at relatively low temperatures (371-427°C), where creep and oxidation appear insignificant. Dynamic strain aging effect may play a role in this region.
- Hold times at zero stress or hold times involving no creep or relaxation can result in significant life reduction at high temperatures.
- At temperatures of 538°C and above in protective environments, e.g. sodium or helium, tensile holds become more damaging; under a slow-fast waveform in low-oxygen sodium environments, grain boundary cavitation was observed, indicating classical creep damage. Heat-treated, bainitic 2.25Cr-1Mo, however, showed different waveform dependence; in air tests, tensile holds were more damaging than compressive holds and combined tensile-compressive holds were most damaging, while when tested in vacuum, compressive holds resulted in even longer fatigue life than pure fatigue, and any waveforms with a tensile hold is much more damaging (Kschink and Stubbins 1989).

Fatigue tests carried out in impure helium showed that tensile hold times tend to be more damaging than compressive holds at temperatures of 538°C and above. The fatigue life in helium is generally longer than that in air, except in tests with tensile holds only where the fatigue life in helium is slightly shorter than that in air (Booker and Majumdar 1982). The fatigue life of isothermally annealed 2.25Cr-1Mo in sodium is significantly longer than in air under pure fatigue cycling. Fatigue tests under slow-fast waveform showed life reduction and intergranular cracking in sodium, while the fast-slow waveform and zero-stress-holds have no damaging effect on fatigue resistance (Booker and Majumdar 1982).

Oxidation-fatigue interaction has been suggested to be responsible for the damaging effect of a compressive hold in high-temperature air tests. This is in contrast to austenitic stainless steels where classical creep-fatigue interaction is the primary cause of fatigue failure. Challenger et al. (1981) suggested that the more damaging effect of compressive holds is due to oxide growth during compressive holds, which results in increased tensile strains during the tensile cy-

cle. While a vast amount of information of precipitate evolution is available under static loading, only limited information has been reported on microstructural changes under creep-fatigue loading. The aging effect on creep-fatigue performance has not been addressed and incorporated into the creep-fatigue analysis.

Annealed 2.25Cr-1Mo experiences cyclic hardening, cyclic softening, or a mixture of cyclic hardening and softening, depending on temperatures, strain rate, and hold times. The cyclic stress-strain response of isothermally annealed 2.25Cr-1Mo was measured for the first 100 fully reversed strain cycles at strain ranges of 0.4 to 3.0% at a strain rate of 8.33×10^{-5}/sec at temperatures between room temperature to 593°C (Jaske et al. 1975). Cyclic hardening was observed below 427°C; cyclic softening was observed at 593°C; initial cyclic hardening followed by cyclic softening was observed between 482 and 538°C.

Significant cyclic softening and stress relaxation was reported on bainitic 2.25Cr-1Mo steel (Kschinka and Stubbins 89). Rapid cyclic softening occurred during the first 20% of fatigue life followed by softening at a decreased softening rate. Considerable stress relaxation takes place during constant-strain-hold period. The stress relaxed dramatically in the first few seconds and slowly decreased thereafter. Stress relaxation behavior is essentially identical in tension hold and in compression hold. One of the important conclusions in the study by Kschinka and Stubbins (1989) was that the initial strength advantage of the bainitic structure in 2.25Cr-1Mo steel was lost via cyclic softening. The cyclic softening behavior has been shown to have a dramatic effect on the strength properties of a material, particularly at elevated temperatures. In particular, the creep strength of the bainitic 2.25Cr-1Mo steel was drastically reduced after only a few cycles of fatigue loading.

Booker and Majumdar (1982) proposed that the predictive models, including the linear damage rule, frequency separation equation, strain range partitioning equation, and damage rate equation, need to be modified to account for oxidation and aging effects in the 2.25Cr-1Mo steel. It is essential that dominant damage mechanisms be incorporated into the predictive methods, particularly where extrapolation of an existing database is required. Booker and Majumdar (1982) further concluded that while it is clear that a complete understanding of creep-fatigue behavior of 2.25Cr-1Mo requires a significant amount of new information and test data, a creep-fatigue design rule for 2.25Cr-1Mo steel can be developed using existing data.

Weldments

Elevated-temperature fatigue data on 2.25Cr-1Mo weldments were generated to support the CRBRP design, under the DOE LMR reactor programs. Brinkman et al. (1970) reported low-cycle fatigue data for 2.25Cr-1Mo weldments tested at temperatures from 22 to 593°C. Annealed 2.25Cr-1Mo steel plates were welded by gas tungsten-arc welding process using ERNiCr-1 filler metal. Weldments were stress relieved prior to machining the specimens. Hourglass-shaped specimens were fabricated from both the transverse and longitudinal orientations with the fusion line. Fatigue tests were carried out in air in axial strain control at applied total strain ranges from 0.4 to 3%. Forty-five test data were reported.

Creep-fatigue data on the HAZ simulated material, base metal, and weld joint of 2.25Cr-1Mo steel were reported by Ogata and Yaguchi (2005). Creep-fatigue tests were conducted at 600°C at a strain range of 0.5% with tensile hold time of 60 minutes. Two weld joint specimens were additionally tested at a strain range of 0.3% with a hold time of 60 minutes and at the strain range of 0.5% with the hold time of 600 minutes. Type IV cracking was observed in a fine grain region of the weld joint under creep-fatigue loading. Large accumulation of creep strain and ductility loss from triaxial stress state in the fine grain region was suggested to be responsible for the Type IV cracking.

6.1.2.2 Modified 9Cr-1Mo Steel

Base Metal

A large number of fatigue data of mod.9Cr-1Mo were generated through the US DOE reactor program in 1970s and 1980s (DiStefano 1986). Fatigue tests were carried out at temperatures between 25 and 593°C in air under axial strain-controlled and fully reversed modes. A few multi-axial fatigue tests were also conducted at 538°C to assess fatigue strength criteria based on the von Mises equivalent strain criterion. Fatigue data of mod.9Cr-1Mo showed no significant temperature dependence. However, heat-to-heat variations of fatigue resistance were observed. The heat with lower tensile strength has an inferior fatigue resistance. The comparison of multi-axial fatigue data with baseline uniaxial fatigue data indicated that the von Mises equivalent strain range criterion is adequate for fatigue strength criteria for G91.

A large number of creep-fatigue tests were carried out on N&T and N&T and aged G91 of five different heats in JAPC-USDOE joint study (ORNL/9Cr/90-2, 91-1, 92-2, Gieseke et al. 1993). Test temperatures were in the range of 482 to 593°C. The total strain ranges were between 0.4-1%. Hold times up to 2 h were applied in tension only. A majority of tests were carried out in air. To investigate the environmental effect, tension-hold tests were also performed in vacuum at 593°C at a strain range of 0.5%.

A series of hold-time fatigue tests were carried out at temperatures of 500 to 600°C in air by Japan Nuclear Cycle Development Institute (JNC 2003). Hold times were applied in either tension or compression, or both in tension and compression. The longest hold time applied was 10 hours. Hold-time tests with a slow strain rate (10^{-5}/sec) were performed at 550°C. Twenty-seven test data were reported. The CEA tests were performed at 550°C in air with hold times in either tension or compression (Cabrillat et al. 2006, CEA-SRMA 1992).

Ruggles and Ogata (1994) summarized the fatigue and creep-fatigue data by EPRI and CRIEPI. EPRI conducted 12 fatigue tests at temperatures between 20 and 550°C. Tests were carried out using tubular specimens at strain ranges of 0.5-1.4% in axial strain control. CRIEPI fatigue tests were conducted at temperatures between 200 and 600°C in axial strain control with the strain ranges of 0.5-1.4%. Cylindrical round fatigue specimens were used. Sixteen tests were reported. Thirteen biaxial fatigue tests were carried out at 550°C. Thin-walled tubular specimens were used. Both in-phase and out-of-phase loadings were applied. The von Mises equivalent strain ranges were 0.5, 1.0, and 1.4%. Thirteen tests were reported.

EPRI reported fatigue data under various types of waveforms. Tests were done under slow-slow, fast-slow, and slow-fast cycling with the fast strain rate of 10^{-3}/sec and the slow strain rate of 10^{-5}/sec. Thin-walled tubular specimens were used. The test temperature was 550°C, and the strain ranges covered the range of 0.7 to 1.4%.

CRIEPI hold-time tests were carried out at 550°C with tensile holds, compressive holds or both tensile and compressive holds. The longest hold time was 60 minutes. The strain ranges applied were 0.5 and 1%. Nine hold-time tests were reported. Six biaxial tension-torsion creep-fatigue tests were performed at 550°C with hold times of 10 minutes and 1 h imposed at peak tensile strains. Both in-phase and out-of-phase loadings were applied. The von Mises equivalent strain range was 1%.

Srinivasan et al. (2005) reported hold-time fatigue tests in air at 550-600°C with hold times applied in tension only, or in compression only. The total strain range was 1.2%. Kim and Weertman (1988) reported creep-fatigue data on mod.9Cr-1Mo steel tested at 482-704°C in air and in vacuum with a 2-minute hold at the peak tensile or compressive strain. The plate material (Heat 30394) was obtained from Oak Ridge National Laboratory. Hourglass specimens were machined with the longitudinal axis parallel to the plate rolling direction. Specimens were tested in fully reversed, total diametral strain control, with a majority of tests done at 593°C.

Shankar et al. (2006) reported creep-fatigue data on normalized and tempered mod.9Cr-1Mo steel tested in air at 600°C. Hold times were introduced at peak tension or peak compression strains for periods of 1-10 minutes. Tests were carried out under fully reversed, total axial strain control mode. The total strain ranges were 0.5-2.0%. Shankar et al. (2004) reported fatigue data on mod.9Cr-1Mo tested at different strain rates, 3×10^{-2}, 3×10^{-3}, 3×10^{-4} /s at 500-600°C in air at a strain range of 1.2%. The effects of dynamic strain aging on the fatigue life were investigated.

Sonoya et al. (1991) reported the fatigue and creep-fatigue data of mod.9Cr-1Mo at 600°C. Tests were carried out in strain control with the waveform of fast-fast, slow-fast, fast-slow and slow-slow with the fast strain rate of 1%/sec and the slow strain rate of 0.004%/sec. A hold time of 5 minutes was applied in tension, in compression, or in both tension and compression. The data were used to develop the creep-fatigue life prediction method using Diercks equation. Fournier et al. (2006, 2009) reported creep-fatigue data for mod.9Cr-1Mo tested at 550°C in air and in vacuum. Tests were carried out under total strain control. The hold time was imposed at peak tensile strain with either total strain held constant or stress held constant. Similar hold-time tests were conducted with the hold time applied at peak compressive strains. The longest hold time was 90 minutes. Vacuum tests were carried out with a 2-minute hold time applied in tension or in compression at the constant total strain with the total strain range of 0.7%.

Fatigue tests were carried out at 538°C in air on mod.9Cr-1Mo specimens pre-exposed to liquid sodium at 538°C for 6000 h (Natesan et al. 2009). Sodium exposure has little effect on fatigue life of G91. Kannan et al. (2009) reported the fatigue data of mod.9Cr-1Mo steel tested in flowing sodium. Fatigue tests were conducted under fully reversed, total axial strain control at 550 and 600°C. A beneficial effect to the fatigue life was observed in sodium, and the lack of surface oxidation in sodium environment is suggested to be responsible for delayed crack initia-

tion and improved fatigue life. Table 6.4 summarizes the fatigue and creep-fatigue data in strain control for mod.9Cr-1Mo. The strain rate in fast-fast continuous cycling and in hold-time tests is 10^{-3}/sec.

Major findings of creep-fatigue interaction in mod.9Cr-1Mo steel are:

- The fatigue life of mod.9Cr1-Mo was found to be insensitive to test temperature under pure fatigue loading, according to DiStefano (1986), while EPRI/CRIEPI data showed evident temperature dependence of the fatigue life, particularly at lower strain ranges.
- Compressive holds tend to be more damaging to fatigue resistance than equivalent tensile holds, especially when surface oxidation is present.
- The slower the strain rate, the shorter the fatigue life; the fatigue life is shorter under fast-slow cycling than under slow-fast cycling.
- Hold times in compression produce detectable mean tensile stress and tensile hold times produce mean compressive stress. The magnitude of the mean stress depends on strain ranges and duration of the hold time. The lower the strain range and the longer the compressive hold period, the greater the magnitude of the tensile mean stress and the lower the fatigue life.
- Surface oxidation was observed in creep-fatigue tests in air, though not nearly as extensive as in 2.25Cr-1Mo.
- No cavitation is observable when the environment plays a role in creep-fatigue interaction and damage accumulation.
- Creep-fatigue tests at 600°C in vacuum showed a significant reduction in fatigue life with tension hold times, or under slow tension-fast compression cyclic waveforms. Cavities and intergranular cracking was observed in these tests, suggesting creep-fatigue damage similar to that observed in austenitic stainless steels.
- Tests performed at 550°C in vacuum showed fatigue life reduction due to hold times. The more damaging effect of compressive hold times is suppressed, instead, tensile hold times showed deleterious effect on fatigue life. However, no cavitation was observed, and fatigue transgranular cracking is evident.
- Most of hold-time fatigue data were obtained with a hold time no longer than 60 minutes. No clear saturation effect was observed in these tests.
- Biaxial low-cycle fatigue life can be correlated with the equivalent strain range for both in-phase and out-phase tests.

Mod.9Cr-1Mo steel undergoes considerable cyclic softening under strain-controlled cyclic loading. The stress amplitude decreases as the number of cycle increase during cycling. This is in contrast with austenitic stainless steels, 304 and 316, which cyclically harden. The cyclic behavior is also different from annealed 2.25Cr-1Mo, in that annealed 2.25Cr-1Mo first hardens and then softens.

Cyclic softening in mod.9Cr-1Mo steel occurs at all temperatures between 25 and 600°C in both continuous fatigue and creep-fatigue tests (DiStefano 1986, Kim and Weertman 1988). When hold times are introduced in fatigue cycles, cyclic softening is accelerated in comparison with pure fatigue, as shown in Fig. 6.4 (Kim and Weertman 1988). The cyclic softening effect is further enhanced when tested in air environment. The initial high strength advantage of the alloy

is lost even after a small number of loading cycles. Depending on the strain range and strain rate, this stress may drop to nearly one-half of its starting value (Swindeman 1985, Matsuoka et al. 1984). Remarkable stress relaxation during hold times is also evident in Fig. 6.4.

Table 6.4. Summary of fatigue and creep-fatigue data of mod.9Cr-1Mo

Heat Treatment	T (°C)	Strain rang-es (%)	Type of tests	Hold time (min)	Environment	Reference source
NT	25, 371, 482, 538, 593	-	CC	-	Air	DiStefano 1986
NT	538	0.5-1.2	CC, multi-axial	-	Air	DiStefano 1986
NT	593	0.4-1.2	CC	-	Air	DiStefano 1986
NT	482	1	TH	6	Air	JAPC-USDOE
NT	538	0.5-1	TH	30-120	Air	JAPC-USDOE
NT	593	0.4, 0.5, 1	TH	30-60	Air	JAPC-USDOE
NT	593	0.5	TH	30-60	Vac	JAPC-USDOE
NT+aged 50kh	538	0.71-0.78	CC, TH	15-60	Air	JAPC-USDOE
NT+aged 50kh	593	0.47-0.5	CC, TH	30-60	Air	JAPC-USDOE
NT+aged 75kh	538	0.51	CC, TH	15-30	Air	JAPC-USDOE
NT	500	0.5-1.5	CC,CH	1-60	Air	JNC
NT	550	0.5-1.5	TH,CH, TCH	30-90	Air	JNC
NT	550	0.345-0.724	TH, SSR	6 – 600	Air	JNC
NT	600	0.518-1	TH, CH	20-60	Air	JNC
NT	550	0.6-1	TH, CH	30-120	Air	CEA
NT	20, 300, 500, 550	0.5-1.4	CC	-	Air	EPRI
NT	200 400, 550, 600	0.5-1.4	CC	-	Air	CRIEPI
NT	550	0.5-1.4	CC, biaxial	-	Air	CRIEPI
NT	500	0.7, 1, 1.4	Slow-fast, fast-slow, slow-slow	-	Air	EPRI
NT	550	0.5, 1.0	TH, CH, TCH	10-60	Air	CRIEPI
NT	550	1%	TH biaxial	10-60	Air	CRIEPI
NT	550-600	1.2	CC, TH, CH	1-30	Air	Sinivasan et al. 2005
NT	593	0.72-2.5	CC,TH, CH	2	Air	Kim & Weertman 1988
NT	593	0.71-2.62	CC, TH, CH	2	Vac	Kim & Weertman 1988
NT	600	0.5-2	CC,TH, CH, TCH	1-10	Air	Shankar et al. 2006
NT	500-600	1.2	Slow-slow	NA	Air	Shankar et al. 2006
G91	600		CC, Slow-fast, fast-slow, slow-slow, TH CH, TCH	5	-	Sonoya et al. 1991
NT	550	0.4-1	CC, CH, TH, strain-hold, stress-hold	90 max	Air, Vac	Fournier et al. 2006, 2009
NT + 538°C/ 6000 h in Na	538	0.4-1	CC	-	Air	Natesan et al. 2009
NT	550, 600	0.8-2	CC	-	Na	Kannan et al. 2009

Cyclic softening in mod.9Cr-1Mo steel is accompanied by pronounced microstructural changes (Jones 1981, Kim and Weertman 1988, Shankar et al. 2006, Sauzay et al. 2008, Fournier et al. 2006, Fournier et al. 2009). The initial lath structure transforms to equiaxed subgrain structure with decreased dislocation density. Coarsening of carbide precipitates also occurs during cycling, as shown in Fig. 6.5 (Fournier et al. 2006). The application of hold time accelerated microstructural evolution during cycling. Microstructural evolution is also faster under fatigue and creep-fatigue loading than under creep loading or isothermal annealing at high temperature. Fournier et al. (2009) reported that the microstructural coarsening measured in relaxation fatigue and creep-fatigue tests at 550°C is comparable to that in creep tests above 600°C, but occurs much faster. Dislocation cell formation with decreased dislocation density, disappearance of low-angle boundaries, and carbide coarsening are suggested to be responsible for cyclic softening.

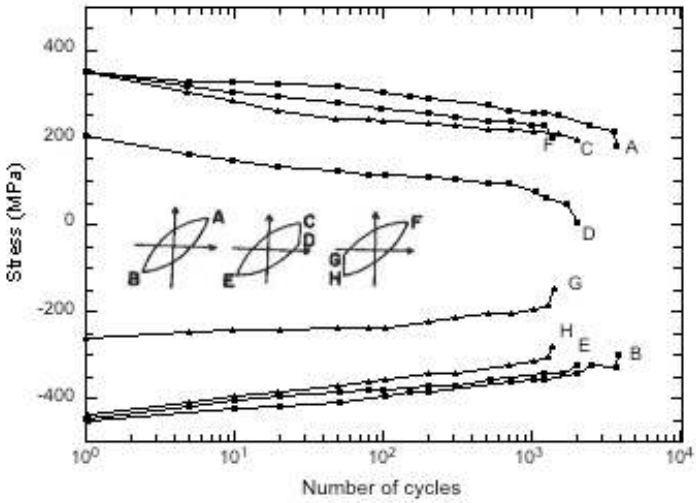

Figure 6.4. Cyclic softening in pure fatigue and creep-fatigue tests at 593°C in air (Kim and Weertman 1988).

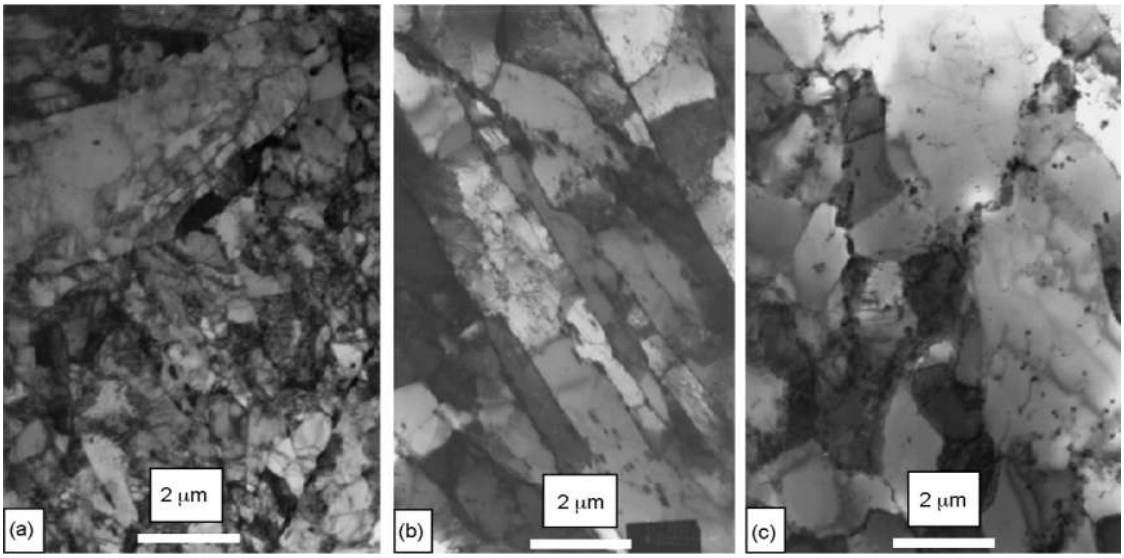

Figure 6.5. TEM micrographs showing microstructural changes after fatigue deformation (a)as-received, (b) pure fatigue (0.7%/550°C), (c) creep-fatigue (0.7%/550°C/hold time of 90 min) (Fournier et al. 2006).

Weldments

Extensive mechanical property testing including tensile, creep, Charpy, fatigue, and creep-fatigue was conducted on mod.9Cr-1Mo steel weldments in the DOE development program of mod.9Cr-1Mo steel. According to DiStefano (1986), 157 weldments of mod.9Cr-1Mo steel were prepared at Oak Ridge National Laboratory. Ninety-one weldments were produced with the gas tungsten-arc (GTA) welding process, 32 with the shielded metal-arc (SMA) welding process, and 34 with the submerged arc (SA) welding process. The material thickness has ranged from 3 to 50 mm, and the product forms included tubing, plate, and pipe.

DiStefano (1986) reported that weldments with all three welding processes and with both standard and modified 9Cr-1Mo filler metals were tensile tested at a wide range of temperatures of room temperature to ≈700°C. The yield strengths of all weldments exceed the minimum values for the base metal up to 600°C. The ultimate tensile strengths for all but two weldments meet or exceed the base metal minimum value. Reductions of area values for all weldments exceed the minimum value of 55% for the base metal for all test temperatures. It was concluded that G91 weldments have no problem meeting the minimum properties for the base metal.

Creep data of mod.9Cr-1Mo steel weldments obtained between 538 and 677°C were compiled and normalized to the base metal average or minimum creep properties. Weldment stress ratios as a function of time to rupture were plotted and compared against the criterion for allowable stress in ASME Section VIII, 0.67. It was shown that the 0.67-times-minimum-stress-to-rupture basis for S_t values in Subsection NH is quite conservative for the weldment data. Data also showed that the stress ratio was not affected either by welding processes including GTA, SMA and SA, or by the use of either standard or modified filler wire (DiStefano 1986). Note that the longest time of the creep rupture data was 10,000 h.

Swindeman (2009) revisited the creep rupture data of mod.9Cr-1Mo steel weldments and re-evaluated the adequacy of the mod.9Cr-1Mo steel weldment strength reduction factors (WSRFs) in ASME Subsection NH. An updated database was assembeld including the initial data used for developing the WSRFs in NH supplemented with new data that became available in recent years. More long-term creep rupture data are available with the longest time ≥ 60,000 h. Two major issues emerged from this review: (1) the WSRF values for mod.9Cr-1Mo steel weldments are lower than the values specified in NH; (2) the database is inadequate for the determination of WSRFs due to lack of long-term data above 540°C. It was recommended that further testing of mod.9Cr-1Mo steel weldments for long-term and low-stress conditions are needed.

DiStefano (1986) reported fatigue data of mod.9Cr-1Mo steel weldments under fully reversed, strain-control conditions. Fatigue tests were carried out at two strain ranges of 0.45 and 1.0% and temperatures between 25 and 593°C. The weldment was tempered at 760°C for 4.5 h before machining specimens. The specimens were fabricated with the major axis transverse to the weldment so that the gauge section was either all base metal, all as-deposited weld metal, or a combination of base, HAZ, and weld metal. The fatigue life was found the highest for the base metal and the lowest for the all-weld-metal for all test conditions. The ratio of base metal life to weld metal life was about 2. Specimens containing the HAZ and fusion line has fatigue lives be-

tween the above two types of specimens. All specimens showed cyclic softening with the base metal being softened more than the weld metal. Creep-fatigue data on mod.9Cr-1Mo steel weld metal or weldments are extremely limited.

Blass et al. (1991) provided additional fatigue data of G91 weldments for confirmation of the fatigue life reduction factors for G91 weldments. Twenty tubular specimens were made with longitudinal and circumferential welds. They were tested under axial or torsional strain control at total strain ranges of 0.4 to 1.5% at 538°C in air. In axial tests specimens with circumferential welds have shorter fatigue lives than those with longitudinal welds, and specimens with longitudinal welds had nearly the same fatigue lives as those without welds. In tortional tests, specimens with circumferential welds again showed the shortest fatigue life, but specimens with longitudinal welds also showed shorter fatigue lives than those without welds.

Bicego et al. (1998) reported fatigue data on cross weld specimens of P91, P92 and E911 steels. All three 9Cr steel variants showed a similar life reduction at 600°C with a factor of about 2 compared to the base metal. Takahashi and Tabuchi (2008) reported creep-fatigue data on G91 weldments at temperatures of 550-650°C at strain ranges of 0.35-1%. A tension hold time was applied with a period of 10 minutes to 10 hours. Round bar specimens of 8 mm diameter were made from the weld joint in a way that the boundary of weld metal and the HAZ is at the center of the specimen gauge. It was found that the life reduction due to the hold time is more pronounced at lower strain ranges and higher temperature. All creep-fatigue tested specimens failed in fine-grained HAZ.

A study on creep-fatigue of E911 weldments at 600°C (Mohrmann et al. 1998) showed that the fatigue life of the weldment was reduced by a factor of 2 compared with the base metal under continuous cycling. The application of the hold time further reduced the fatigue life. Recent work on creep and high temperature fatigue crack growth on welded P91 and P22 components in the European Commission funded project HIDA suggested that the creep-fatigue damage in P91 welded components could be even more severe than P22 because of Type IV cracking. Fatigue and creep-fatigue data of mod.9Cr-1Mo weldments are summarized in Table 6.5.

Table 6.5. Fatigue and creep-fatigue data for mod.9Cr-1Mo weldments.

Specimen Type	T (°C)	Strain ranges (%)	Type of tests	Hold time (min)	References
Base metal, weld metal, base-HAZ-weld	25, 593	0.45, 1	CC	-	DiStefano (1986)
Longitudinal and circumferential weld	538	0.4-1	CC-axial/tortional strain control	-	Blass (1991)
Cross weld	600	-	CC	-	Bicego et al. (1998)
Weld-HAZ-base	550, 600, 650	0.35, 0.5, 1	CC, TH	10 min–10 h	Takahashi and Tabuchi (2008)

Type IV cracking occurs in the fine grain or intercritical HAZ adjacent to the base metal in low-Cr and high-Cr ferritic steels. It is a life-limiting failure and has become a major mainte-

nance issue for power plant using Fe-Cr ferritic steels. Preliminary research indicated that Type IV cracking could be more problematic under creep-fatigue loading.

Type IV cracking in the HAZ is often observed in Grade 91 weldments, leading to premature failure of the welded components. Type IV cracking is a common phenomenon in many ferritic steels with high creep strength. The benefit achieved in the base metal can be severely reduced by Type IV failure. It has been reported that the creep rupture life of weldments of high-strength ferritic steels can be reduced as much as a factor of five (Ellis and Viswanathan 1998, Tabuchi et al. 2001, Albert et al. 2002). The loss of creep rupture strength in the weldment is more significant at higher temperature, lower stresses and longer service life (Natesan et al. 2008). Extrapolation of data obtained outside the Type IV regime to these test conditions can be dangerously misleading. As the cracking behavior depends on a number of factors including chemical composition, heat treatment, stress state, etc., there is no satisfactory method that allows for the estimation of Type IV cracking-limited creep rupture life. Despite that Type IV cracking is regarded as a life-limiting factor in the use of mod.9Cr-1Mo steel in power plants, no consideration of Type IV cracking has been made in ASME Subsection NH.

The creep-fatigue interaction effect is related to the creep strength of a material. Failure in the Type IV position has been observed under both creep and creep-fatigue loading. Recent work by Tabuchi et al. (2000) has shown that $M_{23}C_6$ precipitates and Lave phases form faster in the fine grain region of the HAZ in 9Cr martensitic-ferritic steels, which makes the Type IV position in these steels vulnerable.

6.2 Assessment of Creep-Fatigue Prediction Models

A number of life prediction models have been developed to compute the creep-fatigue life of structural components. Most of these models are empirical or phenomenological, and they are not derived directly from analysis of mechanisms underlying the damage processes. A number of materials parameters must be determined from best fit of experimental fatigue, creep, and creep-fatigue data. These models include:

- Linear damage rule
- Frequency separation equation
- Strain-range partitioning equation
- Damage rate equations
- Continuum damage mechanics models

Several mechanistic models have been developed based on the physical mechanisms of creep-fatigue damage. The damage mechanisms for high temperature fatigue in materials of interest fall under two basic categories, (1) mechanisms in which the environment plays a dominant role in crack initiation (e.g., oxide cracking in ferritic steels) and (2) mechanisms in which the damage is volumetric and environment plays a subordinate role (e.g., cavitation in austenitic stainless steels). Mechanistic models based on analysis of mechanisms for each type of damage provide valuable insight into the damage processes that are essential for extrapolating high temperature fatigue lives beyond their range of database, particularly in the time domain.

However, these models are not readily amenable to be used as design analysis tools. A number of empirical and mechanistic models are described in the following sections.

6.2.1 Linear Damage Rule

The Linear Damage Rule (Taira 1962, Spera 1969) is truly a predictive method in the sense that use of this rule requires no hold-time fatigue data. The database necessary for computation of life consists of monotonic stress-rupture lives and continuous-cycling fatigue lives. The number of cycles to failure, N_f, for a hold-time fatigue cycle is given by

$$\frac{N_f}{N_{fo}} + N_f \int_o^{t_h} \frac{dt}{t_R(\sigma)} = 1 \tag{6.1}$$

where, N_{fo} = cycles to failure in the absence of hold time and $t_R(s)$ = time to rupture at a stress s during hold time t_h.

Although the relevance of tensile creep rupture to the damage during compressive creep is questionable, following the procedure in the ASME Code Section III, Subsection NH, both compressive hold and tensile hold are assumed to be damaging. Equation (1) is called the Linear Time-Fraction Damage Rule because the creep damage is based on the time to creep rupture. An alternative to Eq. (6.1) is the Linear Strain-Fraction Damage Rule, which is given by

$$\frac{N_f}{N_{fo}} + N_f \int_0^{\Delta\varepsilon_c} \frac{d\varepsilon}{\varepsilon_f(\sigma)} = 1 \tag{6.2}$$

where, $\varepsilon_f(\sigma)$ = creep ductility at stress σ during hold, $d\varepsilon$ = increment of creep strain during hold, $\Delta\varepsilon_c$ is creep strain accumulated during each hold cycle.

Both the time-fraction and strain-fraction Linear Damage Rules consider either directly or indirectly the adverse effects of loss of ductility at low stress (or strain rates) during hold, but cannot distinguish between different wave shapes, such as, tensile, compressive, or symmetrical hold.

6.2.2 Frequency Separation Approach

This method, originally proposed by Coffin as the Frequency Modified Life Equation (Coffin 1976), was designed to take into account the effect of frequency on fatigue life:

$$N_f = \left(\frac{C_2}{\Delta\varepsilon_{in}} \right)^{1/\beta} \nu^{1-k} \tag{6.3}$$

where, ν is frequency of loading, $\Delta\varepsilon_{in}$ is cyclic inelastic strain range, C_2, β, k are material parameters (in a given environment).

It was originally proposed that all frequency effects would disappear (i.e., k = 1) if tests were conducted in vacuum; in this case, all data when plotted in terms of $\Delta\varepsilon_{in}$ versus N_f would collapse onto a single line independent of frequency, temperature, wave shape, etc. With further testing, it became evident that for certain materials (such as austenitic stainless steel), wave shape effects are important even in high vacuum (Coffin 1976). In order to incorporate wave shape effects, Eq. (6.3) was modified to the Frequency Separation Equation (Coffin 1976)

$$N_f = \left(\frac{C_2}{\Delta\varepsilon_{in}}\right)^{1/\beta} \nu^{1-k} \left(\frac{\nu_c}{\nu_t}\right)^c \tag{6.4}$$

where, ν_t is tension-going frequency, ν_c is compression-going frequency, and ν is $\dfrac{1}{1/\nu_t + 1/\nu_c}$ = frequency of cycling, and c is material parameter.

Notice that Eq. (6.4) reduces to Eq. (6.3) for symmetrical cycling. Equation (6.4) predicts that there is no saturation effect on life if, for example, tensile hold time per cycle is increased (or frequency decreased) indefinitely. Another characteristics of Eq. (6.4) is that although it distinguishes between cycles with tensile imbalance (e.g., tensile hold or slow-fast) and compressive imbalance (e.g., compressive hold or fast-slow), it averages out the details of the loading waveform. For example, Eq. (6.4) treats all tensile hold cycles of a given duration to be equally damaging, irrespective of where in the tension-going half of the cycle the hold time is imposed. Tests conducted at Argonne National Laboratory (ANL) and Oak Ridge National Laboratory (ORNL) have shown that this is not the case for either Type 304 stainless steel (Majumdar 1980) or 2.25Cr-1Mo steel (Brinkman et al. 1980).

6.2.3 Strain-Range Partitioning Approach

Strain Range Partitioning (SRP) Equations were proposed by Manson et al. (1971) to take into account the effects of wave shapes on creep-fatigue lives. The total inelastic strain range, $\Delta\varepsilon_{in}$, in the cycle is divided into four components:

$\Delta\varepsilon_{cp}$ = inelastic strain range where tensile creep is followed by compressive plasticity,
$\Delta\varepsilon_{pc}$ = inelastic strain range where tensile plasticity is followed by compressive creep,
$\Delta\varepsilon_{cc}$ = inelastic strain range where tensile creep is followed by compressive creep, and
$\Delta\varepsilon_{pp}$ = inelastic strain range where tensile plasticity is followed by compressive plasticity.

In any cycle, a maximum of three of the above four components may be present such that

$$\Delta\varepsilon_{in} = \Delta\varepsilon_{pp} + \Delta\varepsilon_{cc} + \Delta\varepsilon_{cp} \text{ (or } \Delta\varepsilon_{pc}) \tag{6.5}$$

Note that in Eq. (6.5), plastic strain and creep strain are not precisely defined. These concepts are tied to the classical treatment of the constitutive equation where the total inelastic strain is arbitrarily divided into plastic (short-term rate-independent) and creep (long-term rate-dependent) components. At elevated temperature, in contrast to room temperature, a given inelastic strain range due to "creep" (or slow strain rate) is found to be much more damaging than an identical

inelastic strain range due to "plasticity" (or fast strain rate). But how "creepy" or "plastic" inelastic strain range is for a given material depends not only on the strain rate but also on the temperature and environment. Instead of treating the damage due to inelastic strain range in a given environment as a function of the temperature-strain rate (or time) continuum, the SRP method effectively divides the temperature-strain rate (or time) continuum into two extreme limits, namely, "plastic" $\left(\dot{\varepsilon}=\infty\right)$ and "creep" $(\dot{\varepsilon}=0)$. As a result, the strain rate by itself does not enter into the SRP method. For a given inelastic strain range, each wave shape (i.e., cp, pc, pp, or cc) is assumed to result in a characteristic and basic damage in the material represented by the cycles N_{cp}, N_{pc}, N_{pp}, or N_{cc}, each of which may be (but is not necessarily) represented by a power function. Originally, the partitioned cycles N_{cp}, N_{pc}, N_{pp}, and N_{cc} were considered to be unique functions of the respective partitioned inelastic strain ranges $\Delta\varepsilon_{cp}$, $\Delta\varepsilon_{pc}$, $\Delta\varepsilon_{pp}$, and $\Delta\varepsilon_{cc}$ but independent of $\Delta\varepsilon_{in}$. The predicted number of cycles to failure was then given by the linear damage equation (Manson et al. 1971), i.e.,

$$\frac{1}{N_f}=\frac{1}{N_{pp}}+\frac{1}{N_{cc}}+\frac{1}{N_{cp}}\left(or\ \frac{1}{N_{pc}}\right). \tag{6.6}$$

It was subsequently proposed that the partitioned cycles are unique functions of the total inelastic strain range in a cycle, and that the number of cycles to failure is given by the interaction damage equation (Manson 1973)

$$\frac{1}{N_f}=\frac{F_{pp}}{N_{pp}}+\frac{F_{cc}}{N_{cc}}+\frac{F_{cp}}{N_{cp}}\left(or\ \frac{F_{pc}}{N_{pc}}\right) \tag{6.7}$$

where,

$$F_{pp}=\frac{\Delta\varepsilon_{pp}}{\Delta\varepsilon_{in}},\ F_{cc}=\frac{\Delta\varepsilon_{cc}}{\Delta\varepsilon_{in}},\ F_{cp}=\frac{\Delta\varepsilon_{cp}}{\Delta\varepsilon_{in}},\ F_{pc}=\frac{\Delta\varepsilon_{pc}}{\Delta\varepsilon_{in}}$$

Although the SRP method implicitly assumes that the various partitioned life equations, as functions of the inelastic strain range, are unique so that they must be the same whether derived from cyclic creep or cyclic relaxation tests, it has been observed both for Type 304 stainless steel (Diercks 1975) and 2.25Cr-1Mo steel (Brinkman et al. 1980) that the N_{cp} (or N_{cc}) values obtained from cyclic creep tests are almost always larger than those from cyclic relaxation tests. The primary reason for this observation is the fact that the creep strain rates in a cyclic creep test are relatively larger and therefore less damaging than in a cyclic relaxation test. A more quantitative demonstration of this fact can be given by using the damage-rate equation, which will be discussed in the next section. This deficiency in the SRP equation can be alleviated for hold-time fatigue tests by invoking the ductility-normalized SRP Equation (Halford et al. 1977), according to

$$N_{cp} = \varepsilon_f \alpha (\Delta\varepsilon_{in})^{\beta} \tag{6.8}$$

where, ε_f is creep ductility of a specimen in a monotonic creep-rupture test that lasts as long as the hold-time fatigue test.

Although this approach accounts for the deleterious effects of long hold-time fatigue cycles where the same wave shape persists all through life, it grossly underestimates the life under other loading conditions, such as loading of a specimen which undergoes a few large strain-fatigue cycles but which otherwise spends most of its life at a low stress. In other words, the ductility-normalized SRP equation considers the deleterious effect of a long hold time purely as an aging phenomenon and not as a combined stress-time or strain-rate effect. Although very long-term aging data are not available, aging of Type 304 stainless steel for 1000-5000 h at 538-650˚C (1000-1200˚F) improves rather than degrades both creep ductility at a given rupture time and creep-fatigue life at a given tensile hold time relative to those of unaged specimens (Majumdar et al. 1981). The deleterious effect of long hold times cannot, therefore, be explained solely as an aging phenomenon but must be due to a combined effect of stress and time (or strain rate).

Finally, the assumption of four basic independent damage mechanisms in all materials is not borne out by observation of the fractured surfaces of failed specimens. For example, Type 304 stainless steel sustains damage in the form of either a transgranularly growing crack or grain-boundary wedge cracks or cavities. No other type of damage has so far been uncovered. In fact, one cannot distinguish among pc-, pp- and cc-type loadings of Type 304 stainless steel by a visual observation of the fractured surfaces because they all exhibit similar striations.

6.2.4 Damage Rate Equations

The Damage Rate Equation was originally motivated by the observation (Diercks 1975) made while analyzing creep-fatigue data for Type 304 stainless steel by the SRP method, that the N_{cp} cycles obtained from cyclic creep tests were consistently larger than those from cyclic relaxation tests. The test results suggested that the faster strain rates in a cyclic creep test were less damaging than the relatively slower strain rates in a cyclic relaxation test. In order to take the effect of strain rate into account, Majumdar and Maiya (1976) proposed a single Damage Rate Equation,

$$\frac{1}{a}\frac{da}{dt} = \begin{Bmatrix} T \\ C \end{Bmatrix} |\varepsilon_p|^m |\dot{\varepsilon}_p|^k \tag{6.9}$$

where, a is current crack length, $\varepsilon_p, \dot{\varepsilon}_p$ = current total inelastic strain as measured from last reversal and strain rate, respectively, and *T, C, m, k* are material parameters.

It was proposed that the material parameters depended on whether the crack growth was transgranular or intergranular, such that their values changed as step functions when the strain rate crossed a characteristic value at a given temperature demarking transgranular from intergranular crack growth. It was assumed that cracks of initial length a_o exist in the specimen and

that the "failure" of the specimen occurs when the final crack size reaches a_f. For example, for symmetrical continuous cycling at zero mean stress and at a given strain rate, Eq. (6.9) may be integrated to give

$$N_f = \frac{m+1}{2A}\left(\Delta\varepsilon_{in}\right)^{-(m+1)}\dot{\varepsilon}_p^{\,1-k} \tag{6.10}$$

where

$$A = \frac{T+C}{2} / \ln\frac{a_f}{a_o} \tag{6.11}$$

$\Delta\varepsilon_{in}$ = total inelastic strain range, and $\dot{\varepsilon}_p$ = plastic strain rate of cycling.

Equation (6.10) is reduced to Coffin's Frequency Modified Life Equation (6.3), if the strain rate is replaced by the appropriate frequency. Equation (6.9) is also useful in showing why the linear damage rule [Eq. (6.6)] of SRP is not appropriate, and it directly suggests the validity of the interaction damage rule [Eq. (6.7)]. To show this, consider the cyclic creep (cp) loading case and assume the creep rate during hold (at constant stress σ) to be a constant given by

$$\dot{\varepsilon}_c = P\sigma^p \tag{6.12}$$

So that the creep strain, $\Delta\varepsilon_{cp}$, accumulated during the hold time t_h is $\Delta\varepsilon_{cp} = \dot{\varepsilon}_c t_h$; and assuming the stress σ to be related to the total inelastic strain range by

$$\sigma = Q\left(\Delta\varepsilon_{in}\right)^q. \tag{6.13}$$

Integrating Eq. (9) for this case, the number of cycles to failure is given by

$$\frac{1}{N_f} = \frac{2A}{m+1}\left(\Delta\varepsilon_{in}\right)^{m+1}\left(\dot{\varepsilon}_p\right)^{k-1} + \frac{\Delta\varepsilon_{cp}}{\Delta\varepsilon_{in}}\left[C_T\left(PQ\right)^{k_c-1}\Delta\varepsilon_{in}^{m+1+pq(k_c-1)}\right] \tag{6.14}$$

where, $C_T = T/\ln(a_f/a_O)$ and $\dot{\varepsilon}_p$ is the average plastic strain rate during cycling. Note that if the first term on the right-hand side of Eq. (6.14) is identified as $1/N_{pp}$ and the second term by $1/N_{cp}$, then in contradiction to the assumption in the linear damage rule [Eq. (6.6)], N_{cp} does not work out to be a unique function of $\Delta\varepsilon_{cp}$ because it also depends on $\Delta\varepsilon_{in}$. On the other hand, Eq. (6.14) naturally suggests the interaction damage rule [Eq. (6.7)], if one recognizes that usually $F_{pp} \approx 1$ and identifies N_{cp} by the relationship

$$\frac{1}{N_{cp}} = C_T (PQ)^{k_c - 1} \Delta\varepsilon_{in}^{m+1+pq(k_c-1)}, \tag{6.15}$$

which is uniquely determined by $\Delta\varepsilon_{in}$. Note that Eq. (6.15) turns out to be a power law because power laws are assumed in Eq. (6.12) and Eq. (6.13). If these latter two equations are replaced by any other functional form, the functional dependence of N_{cp} on $\Delta\varepsilon_{in}$ will be different from that given in Eq. (6.15) and may not be a power function. In any case, from the viewpoint of the Damage Rate Equation, the interactive damage rule [Eq. (6.7)] is appropriate for the cyclic creep loading. On the other hand, if one considers cyclic-relaxation loading (e.g., cp loading) and assumes that stress relaxation is governed by the power law Eq. (6.12) and $\Delta\varepsilon_{cp} = \Delta\sigma_{RELAX} / E$, then integration of the Damage Rate Equation gives

$$\frac{1}{N_f} = \frac{2A}{m+1}(\Delta\varepsilon_{in})^{m+1}\varepsilon_p^{\,k=1} + \frac{\Delta\varepsilon_{cp}}{\Delta\varepsilon_{in}}\left[\frac{C_T P^{k_c-1}}{E(1-p+pk_c)\Delta\varepsilon_{cp}}\Delta\varepsilon_{in}^{m+1+q(1-p+pk_c)}\left\{1-\left[1-\frac{E\Delta\varepsilon_{cp}}{Q\Delta\varepsilon_{in}^{q}}\right]^{1-p-pk_c}\right\}\right] \tag{6.16}$$

As in the cyclic creep case, if the interaction damage rule is to work, then N_{cp} should be defined by the following:

$$\frac{1}{N_{cp}} = \frac{C_T P^{k_c-1}}{E(1-p+pk_c)\Delta\varepsilon_{cp}}\Delta\varepsilon_{in}^{m+1+q(1-p+pk_c)}Q^{1-p+pk_c}\left\{1-\left[1-\frac{E\Delta\varepsilon_{cp}}{Q\Delta\varepsilon_{in}^{q}}\right]^{1-p-pk_c}\right\} \tag{6.17}$$

This shows that contrary to the assumption made in the SRP method, N_{cp} is not a unique function of $\Delta\varepsilon_{in}$ but also depends on $\Delta\varepsilon_{cp}$. Equation (6.17) gives a smaller numerical value for N_{cp} than Eq. (6.15) (for a given $\Delta\varepsilon_{in}$), which is in agreement with the experimental observation of Diercks (1975). The Damage Rate Equation, therefore, predicts that N_{cp} curves derived from cyclic relaxation tests should not be a unique function of $\Delta\varepsilon_{in}$ but should also depend on $\Delta\varepsilon_{cp}$ or, alternatively, on the duration of hold time. Experimental evidence for this prediction exists and will be discussed in a later chapter. Note that the key to the success of the SRP method in the cyclic creep case, but not in the cyclic relaxation case, is the fact that the plastic strain rate during hold is relatively constant in the former case but not in the latter.

Although both the Frequency Modified Life Equation and the interaction damage rule for the SRP method can be derived from Eq. (6.9), it has one important drawback, i.e., it cannot account for the relatively minor damage caused by a symmetrical-hold test in Type 304 stainless steel. Examination of fracture surfaces of test specimens of Type 304 stainless steel shows two main types of damage. Specimens that are tested under compressive-hold or symmetrical-loading cycles (e.g., symmetrical continuous or symmetrical hold-time tests) fail by the transgranular propagation of a crack. On the other hand, specimens that are tested under a tensile hold cycle show evidence of cavitation. It is concluded that grain-boundary cavities cannot grow

and may shrink under compression. All the evidence seems to indicate that, in general, a two-parameter rather than a one-parameter description of damage is necessary. Majumdar and Maiya (1979) generalized the Damage Rate Equation by introducing an independent cavity-growth equation in addition to the crack-growth Eq. (6.9)

$$\frac{1}{c}\frac{dc}{dt} = \begin{Bmatrix} G \\ -G \end{Bmatrix} \geq \left|\varepsilon_p\right|^m \left|\dot{\varepsilon}_p\right|^{k_C} \tag{6.18}$$

where $\pm G$ implies growth or shrinkage of cavities depending on whether the stress is tensile or compressive. It was proposed that the cracks would propagate transgranularly or intergranularly depending upon the extent of cavity growth in the grain-boundary region. Cavity growth does not occur if the strain rate is higher than a characteristic value, which is a function of the temperature and the metallurgical condition of the material. The parameters T, C, m, k, and k_c are treated as constants that are dependent only on the environment and test temperature and independent of whether the crack growth is transgranular or intergranular. It is assumed that a crack of initial length a_o and cavities of initial size c_o are nucleated early in life and grow according to Eqs. (6.9) and (6.18). "Failure" of the specimen is defined by the interaction equation

$$\frac{\ln a/a_o}{\ln a_f/a_o} + \frac{\ln c/c_o}{\ln c_f/c_o} = 1 \tag{6.19}$$

where, a_f is the final crack length at "failure" of a specimen that contains no cavity, e.g., a specimen under symmetrical continuous cycling, and c_f is the final cavity size in a specimen that is free of cracks and fails by cavity coalescence, e.g., in monotonic creep rupture. Equation (6.19) implies that the cavity size and spacing, while not affecting the crack growth rate directly, limit the final crack size at which the crack growth rate effectively becomes infinite or unstable. Negative cavity damage is ruled out, so that if c is computed to be less than c_o, the cavities are assumed to be annealed out. The Damage Rate Equations were used successfully to correlate creep-fatigue data in a number of materials under various loading wave-shapes (Majumdar and Maiya 1976, 1978). Although the cavity-growth equation was retained for materials like austenitic stainless steels, it was dropped for materials such as, 2.25Cr-1Mo steel, which show little or no evidence of cavitation when tested in air.

One basic assumption so far has been that the crack cavity growth rates are independent of each other. Testing of Type 304 stainless steel under various sequences of loading waveform (e.g., tensile hold cycles followed by compressive hold cycles) has provided evidence of an increase in crack growth rate due to the presence of grain-boundary cavities (Majumdar and Maiya 1980). To account for this observation, Eq. (6.9) has been replaced by the interactive Damage Rate Equation

$$\frac{1}{a}\frac{da}{dt} = \begin{Bmatrix} T \\ C \end{Bmatrix} \left(1 + \alpha \ln c/c_o\right) \left|\varepsilon_p\right|^m \left|\dot{\varepsilon}_p\right|^k \tag{6.20}$$

where α is a material parameter. The cavity-growth Eq. (6.18) is retained. "Failure" is assumed to occur when the crack length reaches a value of a_f or cavity size reaches a value of c_f, whichever occurs earlier. In other words, failure is assumed to be caused either by the growth of a crack or by the coalescence of cavities. In general, for repetitive cycling, the number of cycles to failure by crack propagation is given by

$$N_f = \left[-1 + \left\{ 1 + \frac{2D_C}{D_T} \right\}^{1/2} \right] / D_C \tag{6.21}$$

where

$$D_C = \int_{cycle} \left\{ \begin{matrix} A_g \\ -A_g \end{matrix} \right\} \left| \varepsilon_p \right|^m \left| \dot{\varepsilon}_p \right|^{k_c} dt \tag{6.22}$$

$$D_T = \int_{cycle} \left\{ \begin{matrix} C_T \\ C_C \end{matrix} \right\} \left| \varepsilon_p \right|^m \left| \dot{\varepsilon}_p \right|^{k} dt \tag{6.23}$$

In Eqs. (6.22) and (6.23), A_g or C_T is used in the presence of tensile stress and $-A_g$ or C_C is used in the presence of compressive stress;

$$A_g = \alpha G,$$

$$C_T = T / \ln\left(\frac{a_f}{a_o} \right), \tag{6.24}$$

$$C_C = C / \ln\left(\frac{a_f}{a_o} \right).$$

If the material does not cavitate, then the number of cycles to failure is obtained by taking the limit of Eq. (6.21) as $D_C \rightarrow 0$, which gives

$$N_f = 1 / D_T. \tag{6.25}$$

If, on the other hand, the material fails by cavity coalescence, the number of cycles to failure is given by

$$N_f = 1 / D_C^{'} \tag{6.26}$$

where

$$D_C^{'} = \int_{cycle} \begin{Bmatrix} C_g \\ -C_g \end{Bmatrix} \left|\varepsilon_p\right|^m \left|\dot{\varepsilon}_p\right|^{k_c} \, dt \tag{6.27}$$

$$C_g = G / \ln\left(\frac{c_f}{c_o}\right). \tag{6.28}$$

For hold-time cycles with inelastic strain range $\Delta\varepsilon_{in}$, hold time t_T at the peak tensile limit, hold time t_C at the peak compressive limit, and average plastic strain rate $\hat{\dot{\varepsilon}}_p$ during the ramp, the following equations may be written if the incremental plastic strain during hold is considered negligible in comparison with the plastic strain range during the ramp:

$$D_C = A_g \left(\Delta\varepsilon_{in}\right)^m \left[\int_o^{t_T} \left|\dot{\varepsilon}_p(t)\right|^{k_c} dt - \int_o^{t_C} \left|\dot{\varepsilon}_p(t)\right|^{k_c} dt\right] \tag{6.29}$$

where $\dot{\varepsilon}_p(t)$ represents the plastic strain rate during hold. Note that a negative value of D_C is not allowed, so that whenever D_C is computed to be negative, it must be set equal to zero; and

$$D_T = \frac{C_T + C_C}{m+1} \left(\Delta\varepsilon_{in}\right)^{m+1} \hat{\dot{\varepsilon}}_p^{k-1} + C_T \left(\Delta\varepsilon_{in}\right)^m \int_o^{t_T} \left|\dot{\varepsilon}_p(t)\right|^k dt \; + C_C \left(\Delta\varepsilon_{in}\right)^m \int_o^{t_C} \left|\dot{\varepsilon}_p(t)\right|^k dt \tag{6.30}$$

Therefore, the material properties that are needed for computing cycles to failure due to crack growth by Eq. (6.21) are A_g, m, k_c, C_T, C_C, and k. If the material fails by cavity coalescence, the number of cycles to failure is given by Eq. 6.26, where

$$D_C^{'} = C_g \left(\Delta\varepsilon_{in}\right)^m \int_o^{t_T} \left|\dot{\varepsilon}_p(t)\right|^{k_c} dt - \int_o^{t_C} \left|\dot{\varepsilon}_p(t)\right|^{k_c} dt, \tag{6.31}$$

In which case the material properties needed are C_g, m, and k_c.

For the case of slow-fast loading (slow tensile, fast compressive) with an average tensile plastic strain rate $\dot{\varepsilon}_s$ that is sufficiently slow at a given temperature so that cavity nucleation and growth are possible, and average compressive plastic strain rate $\dot{\varepsilon}_f$,

$$D_C = \frac{A_g}{m+1} \left(\Delta\varepsilon_{in}\right)^{m+1} \left[\dot{\varepsilon}_s^{k_C - 1} - \dot{\varepsilon}_f^{k_C - 1}\right] \tag{6.32}$$

$$D_T = \frac{1}{m+1} \left(\Delta\varepsilon_{in}\right)^{m+1} \left[C_T \dot{\varepsilon}_s^{k-1} + C_C \dot{\varepsilon}_f^{k-1}\right] \tag{6.33}$$

The cycles to failure by crack growth is given by Eq. (6.21). If the "slow" tensile strain rate is too fast for cavity nucleation and growth, the number of cycles to failure is given by Eq. (6.25). If the failure is caused by coalescence of cavities, then the number of cycles to failure is given by Eq. (6.26), where

$$D_C^{'} = \frac{C_g}{m+1}\left(\Delta\varepsilon_{in}\right)^{m+1}\left[\dot{\varepsilon}_s^{k_C-1} - \dot{\varepsilon}_f^{k_C-1}\right] \tag{6.34}$$

For the case of fast-slow loading (fast tensile, slow compressive) with average tensile plastic strain rate $\dot{\varepsilon}_f$ and average compressive plastic strain rate $\dot{\varepsilon}_s$, $D_C = 0$ (because D_C is computed to be negative, which is not allowed,

$$D_T = \frac{1}{m+1}\left(\Delta\varepsilon_{in}\right)^{m+1}\left[C_T\dot{\varepsilon}_s^{k-1} + C_C\dot{\varepsilon}_x^{k-1}\right] \tag{6.35}$$

and the number of cycles to failure is given by Eq. 6.25.

When Eq. (6.18) is used for the computation of cavity growth during monotonic creep, the time to creep rupture (t_R) caused by the growth and coalescence of creep cavities is given by the implicit equation

$$1 = C_g^{'}\int_o^{t_R}\varepsilon_p^m(t)\dot{\varepsilon}_p^{k_c}(t)dt \tag{6.36}$$

where

$$C_g^{'} = \frac{G}{\ln\left(c_f / c_o\right)}; \tag{6.37}$$

the definition of $C_g^{'}$ in Eq. (6.37) may be different from that in Eq. (6.28), because the spacing of cavities under monotonic and cyclic loading conditions is not, in general, the same.

With the plastic strain rate in Eq. (6.36) approximated by the steady-state creep rate $\dot{\varepsilon}_m$ and the current plastic strain ε_p by $\dot{\varepsilon}_m t$, the time to rupture can be shown to be

$$t_R = \left[\frac{m+1}{C_g^{'}}\right]^{1/(m+1)}\dot{\varepsilon}_m^{-\frac{k_c+m}{1+m}} \tag{6.38}$$

It is important to realize the assumptions and limitations of the Damage Rate Equations. First, the nucleation times for a crack and cavities are assumed to be negligible. At low strain

ranges, the predicted lives will tend to be conservative because the time for nucleating a crack (i.e., reaching a length of 1-10 μm) may be substantial, particularly for polished specimens. Further, the Damage Rate Equation assumes that a certain number of cavities are nucleated under tensile stress early in life and grow, but it ignores the fact that under tensile stress, cavities are nucleated continuously so that their number and spacing change with time. Also, the effects of the crack on the growth of cavities near its tip are ignored in the analysis.

6.2.5 Continuum Damage Mechanics Models

In a continuum mechanics theory (Lemaitre 1979, JianPing et al. 2003), σ is the nominal stress and D is damage, which is initially zero (no cracks) and unity when rupture occurs. D is an internal variable of irreversible processes, which takes into account the weakening of the material due to cracks, voids, etc. The effective stress $\sigma/(1-D)$ generally accounts for this weakening effect. The incremental damage equation is added to the set of customary constitutive equations of the material. For fatigue and creep processes, it is customary to introduce D_f and D_c as fatigue and creep damage functions and write the following incremental equations:

$$dD_f = f_f(\Delta\sigma, D_f, D_c)dN \tag{6.39a}$$

and

$$dD_c = f_c(\sigma, D_f, D_c)dt \tag{6.39b}$$

where $\Delta\sigma$ is range of effective stress, N is cycles and t is time. If it is assumed that D_f and D_c can be added linearly,

$$D = D_f + D_c \tag{6.40}$$

and

$$dD = f_f(\Delta\sigma, D)dN + f_c(\sigma, D)dt \tag{6.41}$$

Lemaitre Equations

The following functions f_f and f_c based on thermodynamic principles have been proposed by Lemaitre (1979)

$$dD_f = \frac{R_v}{\Omega(\gamma+1)} \frac{\Delta\varepsilon_p{}^{\gamma+1}}{(1-D)^{\alpha_1}} dN \tag{6.42a}$$

and

$$dD_c = \frac{R_v}{(1-D)^{\alpha_2}} \left(\frac{\sigma}{\lambda}\right)^r dt \tag{6.42b}$$

where α_1, γ, and Ω are temperature-dependent fatigue constants, α_2, λ, and r are temperature-dependent creep constants, $\Delta\varepsilon_p$ is plastic strain range, σ is von Mises effective stress, R_v is a triaxial coefficient given by the following

$$R_\nu = \frac{2}{3}(1+\nu) + 3(1-2\nu)\left(\frac{\sigma_H}{\sigma}\right)^2 \tag{6.43}$$

σ_H is hydrostatic stress, ν is Poisson's ratio. Using Eqs. 6.40-6.42.

$$dD = \frac{R_\nu}{\Omega(\gamma+1)} \frac{\Delta\varepsilon_p{}^{\gamma+1}}{(1-D)^{\alpha_1}} dN + \frac{R_\nu}{(1-D)^{\alpha_2}} \left(\frac{\sigma}{\lambda}\right)^r dt \tag{6.44}$$

ONERA Equations

A differential form of continuum damage equation has also been proposed by ONERA (Cailletaud and Chaboche 1982). The critical variables in this method are the stress for creep damage and maximum and mean stress for fatigue damage. However, as in the previous case, the fatigue and creep damages are added linearly to give a single damage measure *D*.

$$dD = \left(\frac{|\sigma|}{A}\right)^r (1-D)^k dt + \left(\frac{\sigma_{t,max} - \bar{\sigma}}{M(\bar{\sigma})(1-D)}\right)^\beta \left[1-(1-D)^{\beta+1}\right]^\alpha dN \tag{6.45}$$

where

$$1-\alpha = a\left\langle \frac{\sigma_{t,max} - \sigma_l(\bar{\sigma})}{\sigma_u - \sigma_{t,max}} \right\rangle; \quad \langle H \rangle = Max(0, H) \text{ and}$$

$$M(\bar{\sigma}) = M_o(1+b\bar{\sigma}); \quad \sigma_l(\bar{\sigma}) = \bar{\sigma} + \bar{\sigma}_{lo}(1+b\bar{\sigma})$$

D is damage, σ is stress, $\bar{\sigma}$ is mean stress, $\sigma_{t,max}$ is maximum stress. The model parameters are β, σ_u, σ_l, *M, a, k, r* and *A*. Equation (6.45) is integrated between $D = 0$ and $D = 1$ to give the cycles to failure for any type of loading. The model predicts non-linear creep-fatigue damage accumulation.

6.2.6 Oxide Cracking Model

Challenger et al. (1980) have proposed an oxide-cracking model for high temperature fatigue of isothermally annealed 2.25Cr-1Mo steel tested in air. As a first approximation, they consider a crack in the oxide to be equivalent to a crack in the metal. Briefly, their thesis is that when a new oxide forms, it has no strain in it regardless of the state of strain in the metal. Thus, if the oxide is formed during a peak-strain compressive hold period, cycling to peak tensile strain will put a tensile strain in the oxide equal to the total strain range for the cycle. Likewise, oxide formed during a peak tensile strain hold will be subjected to a maximum compressive strain equal to the total strain range. This argument explains the fact that compressive hold periods are

typically more damaging than tensile holds in this alloy, and, also seeks to explain the circumferential cracking observed in the oxide layer in compressive hold tests.

Based on estimated oxide growth rates and on the observed fact that the strain required to crack an oxide depends upon oxide thickness, the strain (ε_f^0) necessary to crack an oxide is estimated as

$$\varepsilon_f{}^o = \left(\frac{3.52x10^{-11}}{6.16x10^{-3}\sqrt{t}\, exp(-14759 / RT)} \right)^{1/2} \tag{6.46}$$

where, t is elapsed time (h), T is temperature (K), and R is universal gas constant, 1.986 cal/K-mole.

The actual strain to which the oxide is subjected ε_t^0, is given as the difference between the tensile strain amplitude and the strain at which the oxide is formed, so that, for example, $\varepsilon_t^0 \approx \Delta\varepsilon_t$ for a peak- compressive-strain hold and $\varepsilon_t^0 \approx 0$ for a peak-tensile-strain hold. For a hold at both tensile and compressive peak strains, or for other loops where significant amounts of oxide are formed at more than one location on the hysteresis loop, the authors propose the relation (6.47)

$$e_t{}^o = \Delta e_t \left(1 - \frac{t_T}{t_p} \right) \tag{6.47}$$

where, t_T = time spent in tension (strain half of the cycle), t_p = total cycle time. Equations (6.46) and (6.47) can be used to estimate the time (and thus cycles) until crack initiation. The method does not directly address crack propagation.

Majumdar (1981) combined Challenger et al.'s oxidation model with the Damage Rate Equation for crack growth and was able to predict fatigue failure lives of isothermally annealed 2.25Cr-1Mo steel tested at high temperature in air environment under a variety of loading types.

6.2.7 Cavitation Damage Model

In materials such as austenitic stainless steels, when a specimen is subjected to unsymmetrical cycling with a tensile bias, e.g., cycles with slow tensile strain rate followed by fast compressive strain rate or cycles that include a tensile hold time under constant stress (cyclic creep) or under constant strain (cyclic relaxation), the fracture surface is generally intergranular and leads to a much larger reduction of life as compared to symmetrical or compressive-hold cycling. When viewed under scanning electron microscopes, the fracture surface shows rounded cavities (r-type cavity) on grain boundaries that are normal to tensile stress. The fracture surface also shows wedge cracking (w-type cavity) near grain boundary triple-point junctions, which may be caused by coalescence of cavities near the grain boundary triple points (Min and Raj

1978). Typically, for relatively short hold time tests at large strain amplitudes, wedge cracks tend to predominate, while for long hold time tests at low strain amplitudes, r-type cavities tend to be dominant. The distribution of cavities is generally inhomogeneous. Some grain boundaries are highly resistant to cavitation while others are prone to cavitation (Don and Majumdar 1986). For grain boundaries that cavitate, the number and spacing of cavities depend on the strain rate and time in addition to metallurgical factors such as, alloy grain size and size and spacing of grain boundary precipitates.

The basic equation for the growth of a spherical cavity was derived originally by Hull and Rimmer (1959), who made the following assumptions:

(1) Cavities are distributed regularly on the grain boundary
(2) Rapid surface diffusion maintains spherical cavity shape
(3) The grains are rigid
(4) Grain boundary diffusion is much faster than matrix diffusion
(5) Grain boundary is a perfect source of vacancies (equilibrium between vacancy concentration and normal stress)
(6) Normal stress at the cavity surface is in equilibrium with surface tension forces
(7) Normal stress on the grain boundary is the same as the macroscopic applied stress
(8) There is no external constraint preventing the grain boundaries from moving apart.

Based on the above assumptions, the rate of change of cavity volume, v can be approximately expressed as follows:

$$\frac{dv}{dt} = 8\pi \frac{D_g \delta \Omega}{kT} \frac{(\sigma - 2\gamma / a)}{(4\ln(c/a) - (1 - a^2/c^2)(3 - a^2/c^2)} \tag{6.48}$$

where t is time, D_g is grain boundary self-diffusion coefficient, δ is the grain boundary thickness, Ω is the atomic volume, γ is surface tension, σ is the applied uniaxial stress, $2c$ is the cavity spacing, a is the cavity radius, kT is the energy measure of temperature. Unfortunately, measured cavity growth rates are many orders of magnitude smaller than that predicted by Eq. (6.48). Also, Eq. (6.48) predicts an inverse linear relationship between time to fracture and stress, whereas tests show that for polycrystalline materials, the following Monkman-Grant relationship is maintained approximately:

$$\dot{\varepsilon}_S t_f = \text{constant} \tag{6.49}$$

where $\dot{\varepsilon}_s$ is the steady state creep rate and t_f is the time to fracture. The discrepancy was addressed by Dyson (1976), who questioned the reasonableness of the assumption that normal stress on the grain boundary is the same as the macroscopic stress (assumption 7). He reported that since the cavitated grain boundaries are often relatively isolated, the rate at which the grain

boundary thickness d increases must be compatible with the rate at which creep deformation of the surrounding grains can accommodate such opening. The cavitated boundaries then shed load to the surrounding grains until the grain boundary thickness rate $\dot{\delta}$ is compatible with the deformation rate of the surrounding matrix. The relative importance of the two mechanisms, dislocation creep and grain boundary diffusion, on the volume growth rate of the cavity is dependent on the value of the parameter *a/L*, where *L* is a characteristic length defined by

$$L = \left(\frac{D_g \delta \Omega \sigma_e}{kT\dot{\varepsilon}_S} \right) \tag{6.50}$$

where, σ_e is the von Mises effective stress. For typical values of polycrystalline materials at half the absolute melting point and applied stress equal to G/1000, where *G* is the shear modulus, *L* ≈2-6 mm for f.c.c materials and ≈0.25-0.35 mm for b.c.c materials. The value of *L* increases by a factor of 20 when the stress is reduced by a factor of 10. When *a/L* <<1, grain boundary diffusion predominates over matrix creep and the cavity volume growth rate is reduced to Eq. (6.48). Otherwise, the constraint effect of the surrounding grains reduces the cavity volume growth rate greatly from that predicted by Eq. (6.48). This is often called the creep-constrained cavity growth rate. Rice (1981) has derived the following equation for creep-constrained cavity growth rate

$$\dot{a} = \frac{D_g}{a^2 h} \frac{\sigma_\infty}{\left[4\left(L^3/\alpha c^2 d\right) + \ln(1/f) - (3-f)(1-f)/2\right]} \tag{6.51}$$

where *h* and α are constants, *d* is the grain boundary facet length, and $f=a^2/c^2$.

Nielsen and Tvergaard (1998) combined a continuum damage mechanics of fatigue crack with diffusional cavity growth to account for creep-fatigue interaction. The analysis continues the traditional approach of separating inelastic strain into rate-independent plastic strain and rate-dependent creep strain. Their analysis does not include creep-constrained cavity growth, continuous cavity nucleation and grain boundary sliding. However, their analysis gives some insight into the mechanisms of creep-fatigue interaction under slow cycling.

6.2.8 Crack Initiation and Propagation Model

Environmental effects have complicated the understanding of creep-fatigue damage mechanisms in G91. Classical creep-damage such as cavitation and intergranular cracking were not observed in creep-fatigue tests in air. Recent study by Fournier et al. (2009) suggested that the fatigue life reduction in G91 under creep-fatigue loading is primarily associated with damage initiated by surface oxidation. Two types of oxide damage behavior were observed, as shown in Fig. 6.6. Type 1 damage is due to crack initiation caused by usual fatigue intrusion/extrusion process. Type 2 damage is caused by coalescence of multiple cracks, and cracks were initiated by brittle fracture of the oxide layer. The Type 2 damage is more damaging in that it is related to cracking of surface oxide layer when the viscoplastic strain per cycle is sufficiently high. A life

prediction model was proposed based on these damage mechanisms. The creep-fatigue life is composed of two parts, initiation life and propagation life, i.e.

$$N_f = N_i + N_p \tag{6.52}$$

For Type 1 damage, the initiation life is calculated by:

$$N_i = \frac{\alpha}{d\Delta\varepsilon_{vp}^2} \tag{6.53}$$

For Type 2 damage, crack initiation is assumed to occur at the first cycle because of brittle failure of the oxide layer. For both types of damage, the crack propagation life is modeled by:

$$\begin{aligned} N_p &= \int_{a_0}^{a_c} \frac{da}{da/dN} \\ \frac{da}{dN} &= \frac{\pi^2 \Delta\varepsilon_{vp} \Delta\sigma^2}{8\times\left(2\overline{T}\right)^2} \times a\left(1+\frac{\pi^2}{8}\left(\frac{\Delta\sigma}{2\overline{T}}\right)^2\right) \end{aligned} \tag{6.54}$$

where α is the temperature dependent constant, d is the grain size, $\Delta\varepsilon_{vp}$ is the viscoplastic strain range applied per cycle, $\overline{T}$ is the residual tensile strength after fatigue loading. The model was used to predict the creep-fatigue life for G91. All predictions fall intro the band of $N_{exp}/2$ and $2N_{exp}$, which indicates good agreement between experiments and predictions for creep-fatigue data.

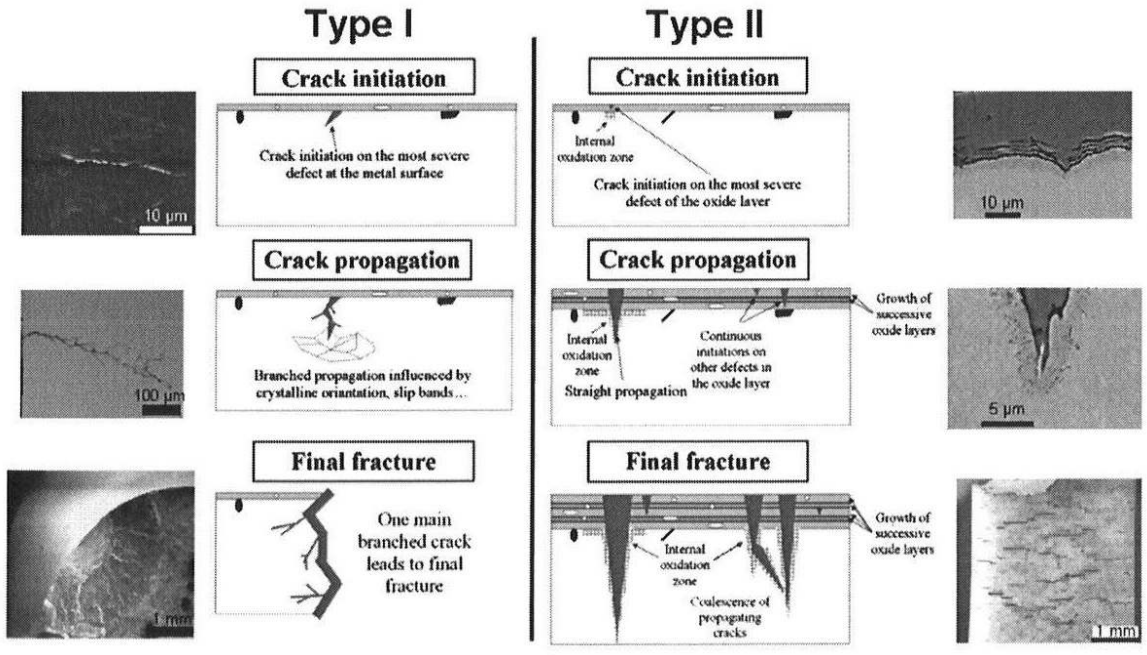

Figure 6.6. Schematics of two types of damage observed in 9-12% ferritic-martensitic steels (Fournier at al 2009).

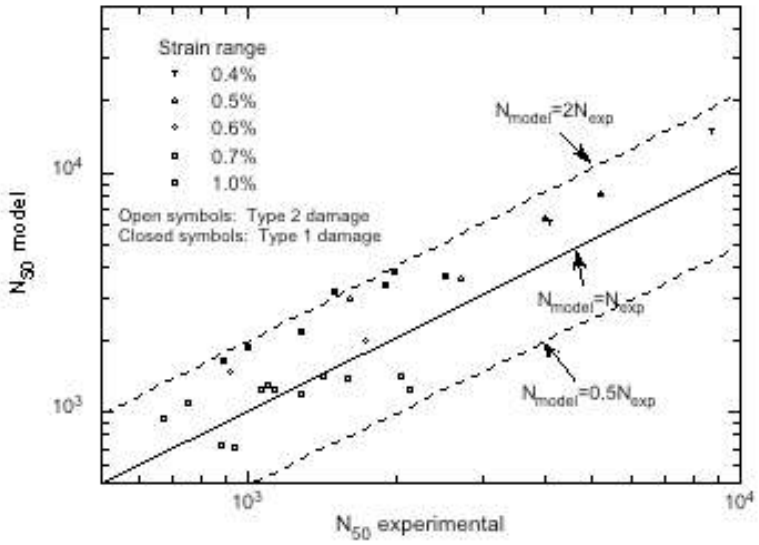

Figure 6.7. Comparison of predicted creep-fatigue life with experimental data (Fournier et al. 2009).

6.2.9 Coupled Deformation Damage Model

Attempts have been made to model cyclic softening effects in 9-12%Cr martensitic steels based on microstructural changes observed during fatigue cycling. Sauzay at al (2005) proposed a micromechanical model where cyclic softening is attributed to decrease of a back stress. The back stress was calculated using a Hall-Petch law for symmetric tile low-angle boundaries and the Taylor homogeneization model, and the cyclic evolution of the macroscopic stress was determined by viscoplastic strain variation and number of cycles.

A coupled deformation damage model was developed to describe cyclic softening and creep-fatigue behavior in ferritic-martensitic steels (Aktaa and Schmitt 2006, Aktaa et al. 2009, Aktaa and Petersen 2009). The inelastic strain rate modified (ISRM) damage model is coupled with a modified viscoplastic deformation model. Both models were developed within the framework of continuum mechanics using the phenomenological concept of state variables to describe complex irreversible processes like plastic deformation and damage. In the deformation model, viscoplasticity is described without separating time-dependent creep and time-independent plasticity. The total strain rate is divided into three components, i.e. elastic, inelastic and thermal:

$$
\begin{aligned}
\dot{\varepsilon} &= \dot{\varepsilon}^{el} + \dot{\varepsilon}^{in} + \dot{\varepsilon}^{th} \\
\varepsilon^{th} &= \alpha\left(T - T_0\right) \\
\varepsilon^{el} &= \frac{\sigma}{E} \\
\dot{\varepsilon}^{in} &= \left\langle \frac{|\Sigma| - k}{\mathrm{Z}} \right\rangle^{n} \operatorname{sgn}(\Sigma) \\
\Sigma &= \frac{\sigma}{\psi} - \Omega
\end{aligned}
\qquad (6.55)
$$

In the simplified ISRM damage model, the change of internal state variable, D for damage is described by:

$$\dot{D} = \left\langle \frac{\sigma}{A} \right\rangle^{r} \left| \dot{\varepsilon}^{in} \right| (1-D)^{-K} \tag{6.56}$$

The coupling of deformation and damage was achieved by replacing the stress in the deformation model by the so-called effective stress, defined as:

$$\tilde{\sigma} = \frac{\sigma}{1-D} \tag{6.57}$$

This gives that:

$$\varepsilon^{el} = \frac{\sigma}{E(1-D)} \quad \dot{\varepsilon}^{in} = \left\langle \frac{|\Sigma| - k}{Z} \right\rangle^{n} \operatorname{sgn}(\Sigma) \text{ with } \Sigma = \frac{\sigma}{\psi(1-D)} - \Omega \tag{6.58}$$

where α is the thermal expansion coefficient, T is the temperature, σ is the stress, E is the Young's modulus, Ω and ψ are internal state variables describing kinematic hardening and isotropic softening, respectively. K, k, A, Z, and r are material and temperature-dependent parameters.

The coupled deformation damage model has been applied to ferritic-martensitic steels, F82H and EUROFER 97 to describe their cyclic softening. As shown in an example in Fig. 6.8, the cyclic softening in F82H is well described by the model. Good agreement between experiment and modeling was also achieved in the calculation of fatigue life for EUROFER 97, as shown in Fig. 6.9.

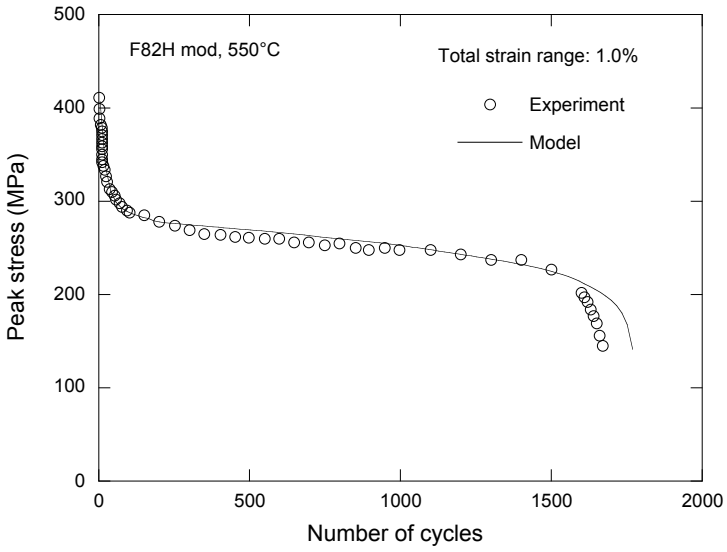

Figure 6.8. Comparison between experiment and modeling of cyclic stress response as a function of number of cycles (Aktaa and Schmitt 2006).

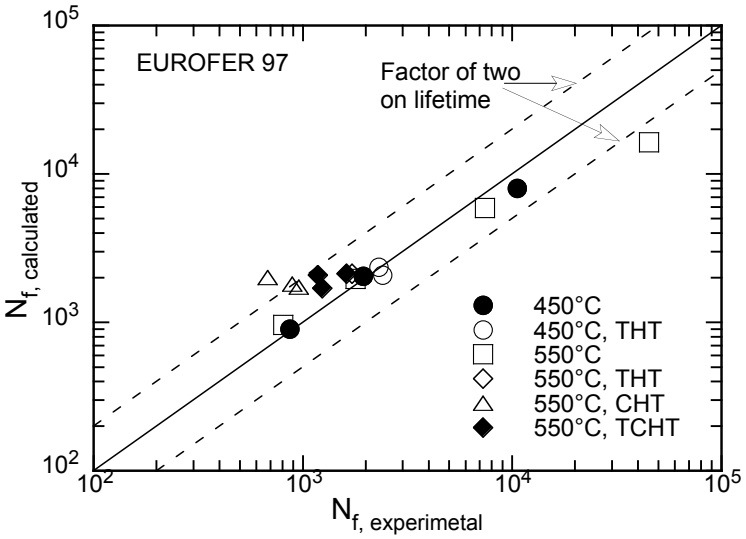

Figure 6.9. Comparison between experiment and modeling of number of cycles to failure for fatigue tests without hold time, with hold time in tension (THT), hold time in compression (CHT) and hold time in both tension and compression (TCHT) (Aktaa and Schmitt 2006).).

A significant literature exists for creep-fatigue life prediction methods. Most life-predictive methods useful for design application are empirical or semi-empirical in nature. Comparison of the various life-prediction methodology has shown that while each method can correlate any given set of data reasonably well, their predictions vary significantly when extrapolated to long term or low strain regimes where experimental data are non-existent but which are relevant to design loading conditions (Majumdar et al. 1981, Cailletaud et al. 1984). Although the mechanistic models are not amenable to design life prediction, they should provide important guidelines as to how the existing database could be extrapolated to design loading conditions.

With the recent push towards extending the design life of non-replaceable components of nuclear reactors to 60 years, it is critical that the models used to calculate design lives are accurate and reliable. This is more so for the creep-fatigue life, because the current life prediction methods are based empirically on laboratory test data that are necessarily short-term (typically a few thousand hours) in duration relative to the design life. Thus, design life prediction requires significant extrapolation beyond the database from which the empirical constants of the predictive methods are derived. The reliability of the life-prediction methods would be greatly enhanced if they were based on an understanding of the mechanisms underlying the damage processes. There have been many attempts since the 1960s that aimed towards such a goal.

6.3 ASME Creep-Fatigue Design Rules

Fatigue is one of the most frequent failures in pressure vessels and piping components. Section III recognizes fatigue as a possible failure mode and provides specific rules for its prevention. Subsection NB covers fatigue design for low temperature applications. For high temperature applications, creep must be considered in conjunction with fatigue, and Subsection NH Appendix T provides non-mandatory procedure.

Appendix T of Subsection NH – Rules for Strain, Deformation, and Fatigue Limits at Elevated Temperatures, provides allowable design fatigue strain ranges for NH materials. The fatigue design curves in Subsection NH are based on strain ranges, rather than stress amplitudes,

as in Subsection NB. The fatigue design allowable in Section NH is presented as total strain range vs. number of cycles. The fatigue data were developed from small, smooth, polished specimens tested under strain-controlled conditions in air. The design fatigue curves were determined from completely reversed loading conditions at strain rates greater than, or equal to, 1e-3/sec for 304 and 316SS, and 4e-3/s for 2.25Cr-1Mo and G91. As is in Subsection NB, the design curve was obtained from the mean failure curve by applying a factor of two on total strain range, or a factor of 20 on fatigue life, whichever results in a lower value. The design factor is often referred to as 2/20. The factor of 2/20 is intended to account for size effects, environment, surface finish and scatter of data. The factor of 20 consisted of the product of a factor of 2.0 to account for scatter in the data (e.g., minimum vs mean), a size effect factor of 2.5, and a factor of 4.0 to account for surface finish, and the fact that the test environment in the lab is typically better than in real applications (Rao 2002). The design fatigue strain ranges are given as a function of the number of allowable cycles in the range of $10–1\times10^6$ (1×10^8 for G91) over a range of temperatures. The maximum temperature allowed for 304 SS is 705°C, 316SS 705°C, 2.25Cr-1Mo 595°C, and 540°C for G91.

Subsection NH adopted the bilinear creep-fatigue damage rule for creep-fatigue design analysis, which was mainly based on the research on type 304 and 316 SS. In the Subsection NH creep-fatigue design procedure, the maximum equivalent strain range is calculated for each cycle type. Once the strain range is calculated, the fatigue damage ratio is computed by dividing the number of cycles for each cycle type by the allowable number of cycles for that cycle type from the ε-N curve, and summing over all cycles:

$$D_f = \sum_{i=1}^{n} \left(\frac{n}{N} \right)_i \tag{6.59}$$

The creep damage ratio, or time-fraction, is calculated by dividing the actual time for each cycle type by the allowable time for that cycle type determined from a stress-rupture curve such as for the maximum temperature in that cycle, and summing over all cycles:

$$D_c = \sum_{i=1}^{n} \left(\frac{\Delta t}{T_d} \right)_i \tag{6.60}$$

The fatigue- and creep-damage terms are evaluated in an uncoupled manner. The total creep-fatigue damage, D is determined by the linear damage rule:

$$D_f + D_c \le D \tag{6.61}$$

The resulted creep-fatigue interaction diagrams are given for the NH materials in Fig. T-1420-2 in Appendix T, shown here in Fig. 6.10.

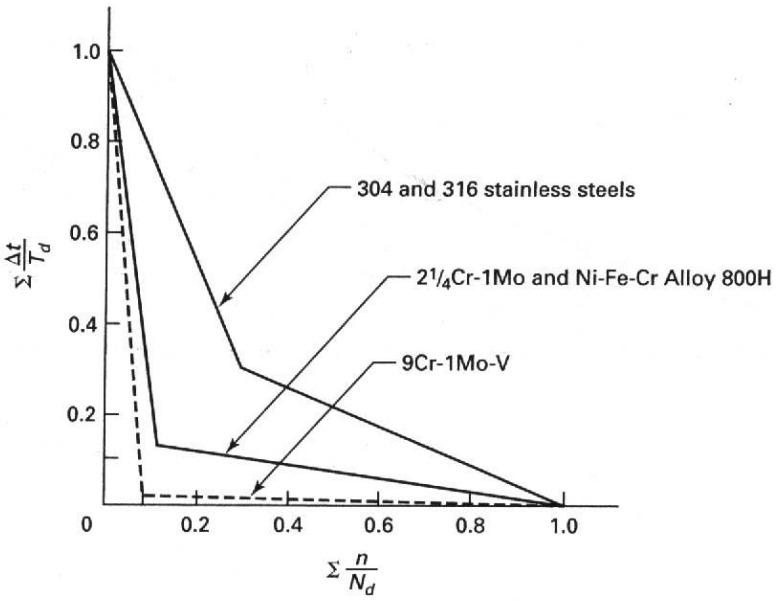

Figure 6.10. Creep-Fatigue Damage Envelope in NH.

The NH creep-fatigue interaction curves are established empirically through data correlation. Such an engineering approach often proves to be effective when it is supported by a robust database that is representative of the operating conditions and when it does not involve significant data extrapolation. A multi-pronged approach is employed in NH in order to ascertain that the design cyclic life determined from the creep-fatigue criterion is adequately conservative. It involves the following elements.

The continuous cycling fatigue design curves that are required to determine the denominator of the cyclic damage are obtained by the 2/20 factor. The stress rupture curves needed for determining the rupture time in the denominator of the time-fraction are constructed as expected minimum (or statistical lower bound) curves. These would cover various uncertainties and account for data scatter.

Creep-fatigue data from uniaxial tests with smooth specimens were used to develop the creep-fatigue rules. Adjustments based on multi-axial plasticity and Poisson ratio effects and a local geometric concentration factor are used in NH for structural applications that involve three-dimensional stress and strain states and geometrical discontinuities when simplified methods based on elastic analysis are used in design. When inelastic analysis is used in design calculations, the three-dimensional stresses are combined into an equivalent stress measure using the Huddleston failure criterion. The material constant in the Huddleston failure criterion is obtained by correlating the multi-axial (axial, torsion, internal pressure) creep rupture data with the uniaxial test results for each material.

Further, a safety factor (1/K'), ranging from 1.1 to 1.5, is applied to the equivalent stress obtained from either elastic or inelastic design analysis approach. The adjusted equivalent stresses (with safety factor) are used to determine the rupture times from the expected minimum stress-rupture curves in the time-fraction calculations. This is a source of significant conservatism since the rupture time has a strong dependence on the stress level.

There are other elements of the creep-fatigue procedure in NH that do not necessarily lead to accurate description of the individual phenomenon, e.g., the use of isochronous stress-strain curves to estimate stress relaxation or the use of monotonic stress-strain curves to estimate stresses from strains in materials that exhibit either cyclic hardening or softening behavior. However, what is essential is that the rules in NH, when used as an integral design procedure, delivers conservative designs. One way to ascertain such needed confidence is to qualify the NH rules by using creep-fatigue data from a variety of test conditions and geometries, including key feature tests.

Weldments

Welds and their base metals have different responses under static and cyclic loading. Creep and fatigue strength reduction factors of weldments were introduced in Subsection NH to ensure adequate life in welded components at elevated temperatures. The creep rupture strength of the weldment is often inferior to the base metal. Creep strength reduction factors of weldments were determined by comparison of the average creep-rupture curves of weldements with the minimum base metal curves. The weldment stress rupture factors were provided in the tabulated format as a function of temperature and temperature for a given base and filler metal in Subsection NH. The creep-rupture portion of the creep-fatigue design rule for weldments is adjusted by a weld strength reduction factor, R.

Weldment fatigue strength reduction factors were also introduced to account for the reduction in fatigue life of welds. A weldment often consists of regions with different microstructure and mechanical properties. The variations in material strength can lead to non-uniform deformation and strain concentration in the softest region, so-called a "metallurgical notch." Early weldment failure can be expected because of the metallurgical notch. The factor of two on cycles was used to derive the weldment fatigue design curve.

6.4 Issues and Resolutions

A number of issues related to materials performance under creep-fatigue loading and creep-fatigue design methodology have been identified. Required actions to resolve the issues are outlined below:

***Issue**: Creep-fatigue life predictive models and design rules for the 60-year design life*

To develop the 60-year creep-fatigue design rule, a large database is needed on each NH material with effects of various factors including strain range, strain rate or frequency, waveform, hold time, temperature, environment, and metallurgical conditions. As discussed in previous sections, there exists an extensive database of creep-fatigue for austenitic stainless steels, and to a less extent for annealed 2.25Cr-1Mo steel, and to an even lesser extent for mod.9Cr-1Mo steel. These data were generated largely during the LMFBR program campaign supported by the USDOE in 1970s-80s. Many of these data were used to develop the high temperature design rules in Subsection NH. Some of these data are available in Nuclear Systems Materials Handbook. These data are of great value in developing mechanistic predictive models and establishing appropriate design rule for the design life of 60 years. However, these data are

archived in report format, and some of raw data that are of particular interest for new analysis can only be found on papers recorded by chart recorders. In addition, a significant number of new data have been made available in recent years. An expanded database including data from previous reactor campaign and recently generated data will provide a valuable resource for analysis, evaluation and development of new predictive models and improved design rules, particularly for the concern of the 60-year design life. A common database is also important in that predictive capabilities of various models can be compared in an objective manner when a same set of data is evaluated and analyzed.

Resolution:

An updated database of creep-fatigue properties for each NH material needs to be established to include the data generated from previous DOE programs and reported in recent literature. The quality of the data will be assessed in terms of material composition, product form, thermo-mechanical treatment, specimen type and location, testing techniques, testing conditions, environment control, and availability of raw data. This database will be used to evaluate the ability of creep-fatigue predictive models and develop appropriate design rule for a 60-year design life. Confirmatory creep-fatigue tests will be performed to validate the models.

***Issue**: Extrapolation of laboratory short-term hold time data to long-term hold time behavior under actual reactor conditions*

The repeated startup- and shutdown-operations during reactor service lead to creep-fatigue type loading with long hold time periods. Such long hold time experiments cannot be easily implemented in laboratory due to the complexity and expense of creep-fatigue testing. It is inevitable that laboratory short-term hold time data have to be extrapolated to realistic reactor conditions. Time is nevertheless a key parameter with regard to microstructural evolution and resulting mechanical response. A complete understanding of the creep-fatigue damage mechanisms is of critical importance in the development of reliable life prediction models and extrapolation procedure.

As discussed in previous sections, most of the available creep-fatigue data have been generated with relatively short hold times. With long hold time, a saturation effect of the hold time on life has not been well characterized. The trends showed by experimental data may not clearly demonstrate the expected differences under reactor operating conditions. For instance, a large number of air data for annealed 2.25Cr-1Mo steel showed more deleterious effects of compressive holds on the fatigue life with no clear indication of creep cavitation damage, whereas in sodium environment, intergranular cracking is evident under creep-fatigue loading. There is a possibility that true creep-fatigue damage could occur even in air tests with sufficiently long tensile hold times.

Resolution

Creep-fatigue tests with sufficiently long hold times should be conducted to determine the saturation limit of the hold time. Both non-interrupted and interrupted tests are recommend-

ed. Interrupted tests are particularly useful for analyzing the stress relaxation behavior and its correlation with microstructure evolution and damage development.

The reliability of data extrapolation to the regimes not covered by testing data relies on a solid understanding of basic mechanisms involved in high-temperature material responses. Ashby-type deformation and fracture mechanism maps have been successfully applied to creep damage (Li and Zinkle 2004, 2007). Fatigue mechanism maps have also been developed to characterize various processes in fatigue damage (Pederson 1990). These maps provide useful guidance in identifying deformation and failure mechanisms, defining operating conditions and developing new alloys. The danger of extrapolating data across boundaries between different mechanisms is also demonstrated (Li and Zinkle 2005, 2007). We propose to extend the mechanism map concept to creep-fatigue damage of nuclear reactor materials, and construct the maps using mechanism-based constitutive equations. A mechanistic approach to the prediction of creep-fatigue lifetime and failure mode will be established for robust data extrapolation.

Considering the cost and limitation of performing long-term tests, accelerated testing techniques should be developed to accurately assess material behavior in relatively short time periods and in simulated reactor operating conditions.

Issue: *Applicability of linear damage rule to creep-fatigue with significant environmental effects*

The linear damage rule currently adopted by the ASME NH was developed primarily for austenitic stainless steels that exhibit true creep-fatigue damage with intergranular cracking under tensile-hold conditions at elevated temperatures. The applicability of the linear damage rule is questionable in predicting or extrapolating data for the material that shows strong environments effects. For instance, in annealed 2.25Cr-1Mo steel, compressive holds are more damaging than tensile holds at elevated temperatures in air, and no clear indication of cavitation and intergranular cracking has been observed. Though the ASME design rule provides provision that compressive and tensile holds are treated as equally damaging, it inevitably creates overconservatism in the design. Furthermore, the linear damage rules say nothing about the environmental effect, whereas an oxidation-fatigue interaction is attributed to the creep-fatigue life reduction rather than the classical creep-fatigue damage with creep cavitation. This is particularly true for the vastly available short-term creep-fatigue data obtained in air tests. Although it is desirable to use a universal damage model to all materials, it may be necessary to develop material-specific creep-fatigue design rule that takes into account the characteristic damage mechanisms in each class of materials in a given environment.

Resolution*:*

A proper database for ferritic steels that can be applied to validate the creep-fatigue linear damage rule should be established. Creep-fatigue data that involve significant environmental effect should be treated with a creep-fatigue-oxidation model that incorporates the environment-assisted and/or -enhanced creep-fatigue interaction. The new methodology should take into account of various metallurgical factors and waveform effects.

Issue: *Reliable creep-fatigue design rule for G91*

To address the long-standing issue of creep-fatigue design rule for G91, it is essential to develop a better understanding of creep-fatigue interaction mechanisms in G91. Though creep-fatigue data of G91 have been generated to the extent that a linear-damage-based creep-fatigue design rule has been established, additional testing, analysis and modeling are clearly needed to answer a number of questions.

One of the key issues with G91 is the environmental effect. There is indication that true creep-fatigue damage occurs at temperatures of 600°C and above or at lower temperatures with sufficiently long hold times in protective environments. Environmental effects, when appear to be significant on specimens, make the transferability of lab data to components questionable. For the analysis of true creep-fatigue damage in G91, proper experimental data are needed to eliminate/minimize the environmental effects. When the environmental effects have to be treated, strain rate dependence and oxidation-fatigue interaction must be accounted for in predictive models and design rules.

Cyclic softening and accompanied microstructural changes have significant implications for elevated temperature design for G91. A number of studies have shown that microstructural evolution is accelerated under cyclic loading with hold times relative to isothermal annealing and pure creep loading. The resultant changes in strengthening mechanism not only affect creep-fatigue properties but also change other properties such as tensile and creep strength, and strain rate sensitivity and stress relaxation behavior. Current linear damage rule in creep-fatigue design use creep rupture data in combination with pure fatigue data to predict creep-fatigue failure. Either pure creep or fatigue may not truly represent the accelerated microstructural changes and loss of strengthening mechanisms under creep-fatigue loading. The current understanding of these effects is inadequate to allow confident use of the high temperature design rules of this class of alloys. Improved creep-fatigue design rule for G91 is needed to take into account of cyclic strain softening.

Recognizing multiple factors playing roles in creep-fatigue interaction in G91, it is important to understand the sensitivity of each factor, and identify the relative importance of these factors. A systematic study is recommended to understand creep-fatigue failure in G91 and to establish a reliable creep-fatigue damage model.

Resolution*:*

- Creep-fatigue tests at selected test temperatures and hold times should be performed to obtain stress relaxation data to validate/improve the current creep-fatigue diagram.
- Low-strain range, long-term tensile hold time tests at 550°C in air are needed to determine if inergranular caviation occurs during a sufficiently long hold time.
- Additional creep-fatigue data in protective environments are needed to confirm cavitation-based intergranular failure and to provide proper data for modeling using the NH linear damage rule.
- Interrupted creep-fatigue experiments are necessary to characterize cyclic softening and stress relaxation behavior and the accompanied microstructural changes. Mechanistic models that incorporate cyclic softening effects in creep-fatigue are needed.

- Cyclically softened materials should be compared with thermally aged material, and produce cyclically softened microstructure by thermal aging for further mechanical property testing. Tensile and creep tests of cyclically softened G91 are necessary to understand the effect of cyclic softening on creep and load carrying capability and for the design against accidental events.

***Issue**: Data need on creep-fatigue of weldments*

Life prediction of welded components subject to creep-fatigue loading is a critical design issue. The database of creep-fatigue in weldments is much smaller than that for the base metal. The creep-fatigue procedure in NH was established based on creep-fatigue data for base metal. It does not have a separate creep-fatigue procedure for welds. The adequacy of the NH creep-fatigue design procedure for weldments needs to be verified by sufficient weldment creep-fatigue data. Type IV cracking in ferritic steels has not been addressed in the current creep-fatigue design rules.

Resolution:

- Creep-fatigue tests of 316SS weldments with long hold times at 550°C are needed.
- Perform creep-fatigue tests on mod.9Cr-1Mo steel weldments made by various welding processes. Tests should include several different test temperatures and hold times with the focus on low-strain-range, long-hold-time tests at 550°C. Attention should be paid on Type IV cracking.
- Perform creep-fatigue tests of 2.25Cr-1Mo steel weldments at 550°C with focus on Type IV cracking.
- Type IV cracking occurs due to non-uniform microstructure between the weld and the base metal. Phase transformation and microstructural evolution under dynamic welding conditions and post-weld heat treatment and their association with mechanical response under creep, fatigue and creep-fatigue loading should be characterized theoretically and experimentally. The microstructure including grain, subgrain and precipitate structure from in the heat affect zone should be characterized with a range of welding parameters and alloy compositions. Microstructure in the different regions of the HAZ should be simulated by heat treatment and specimens are tested to obtain mechanical property information. "Microstructure Atlas" of mod.9Cr-1Mo weldments should be established with correlation between microstructure and tensile, toughness, creep and fatigue strength.

***Issue**: Improved creep-fatigue design rules for weldments*

The ASME NH creep-fatigue design rules were developed based on the properties of base metals. There are no specific design rules for weldments.

Resolution:

A database of creep-fatigue for weldments should be assembled to determine the adequacy of the current weldment creep-fatigue design rules and to develop improved creep-fatigue rules for weldments.

7. FATIGUE AND CREEP CRACK GROWTH

7.1 Fatigue Crack Growth

Cyclic deformation in the plastic regime can either result in hardening or softening of metals but, in either case, they tend towards a steady state condition, typically reached in about 10% of fatigue life, sometimes called a saturation regime which tends to last until the end of cyclic life. However, there are some metal alloys that do not exhibit hardening or softening, rather they develop the saturation regime behavior from the beginning. Figure 7.1 from Saxena (1998) shows a schematic representation of the stress-strain behavior in an element of the material ahead of a growing crack tip under small scale yielding conditions. Region 1 undergoes elastic deformation, while Region 2 is the beginning of the monotonic plastic zone in which yielding occurs during the first cycle. Region 3 is located at the boundary of the monotonic and cyclic plastic zones; in this zone, yielding takes place during each loading and unloading cycle and deformation occurs in accordance with the cyclic stress-strain curve. Finally, in Region 4, the amount of cyclic plasticity increases as the distance to the crack tip decreases. As with linear elastic fracture mechanics, the size of the plastic zone is related to the stress intensity (ΔK in this case) and the stress; but when the plastic zone is comparable to the size of the crack and the remaining ligament, small scale yielding is no longer relevant and the use of a cyclic stress intensity parameter, K, will not be useful to correlate with fatigue crack growth (FCG) behavior. Thus, in this case, the load-displacement behavior shows a substantial amount of hysteresis and this requires the use of nonlinear fracture mechanics.

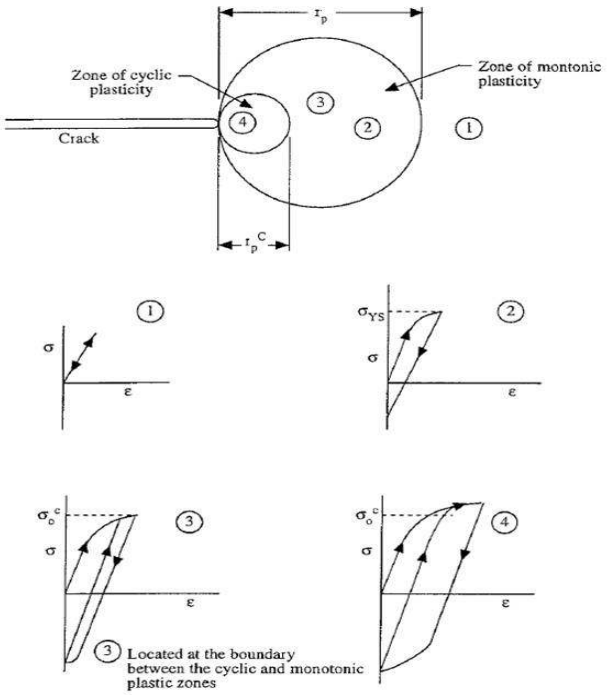

Figure 7.1. Stress-strain behavior of an element of material approaching the crack tip Saxena (1998).

In terms of damage ahead of the crack tip, fatigue damage take place on crystallographic slip planes at low applied stress. In this case, crack initiation and growth takes place along the slip planes and has a zig-zag appearance; however, as strain range is increased and deformation overcomes the crystallographic slip planes and becomes more homogeneous, with the result that the crack growth appears smoother. These two descriptions of crack growth are defined as Stage I and Stage II, respectively. Moreover, it is the strain range experienced by the material near the crack tip that provides the driving force for FCG, with the strain range in that region being both a function of distance from the crack tip and the ΔK. Another significant aspect incorporated in the mechanism of crack growth is the phenomenon of crack closure; this is a condition during which the crack surfaces remain closed at the crack tip during part of the fatigue cycle and mitigates the effect of the measured ΔK on crack growth. There are various models for predicting crack closure effects and one in particular, the Budiansky and Hutchinson Model, is described in detail by Saxena (1998). These conditions lead to use of an effective ΔK, ΔKeff as a correlating parameter for FCG and there a number of models for application of that parameter. Also, the J-integral has been applied to FCG correlation in the presence of large plastic deformation. Figure 7.2 schematically depicts the small vs large crack growth behavior at low load ratios (where load ratio, R, is the ratio of minimum to maximum loads, and R<0.5); Stage III shown in this diagram represents a region in which the crack growth increases dramatically and becomes unstable leading to failure.

Of course, the above description of FCG mechanisms is extremely brief and the reader is referred many references incorporated in the book by Saxena (1998). The developments of models and the experimental data accumulated over many decades has lead to a number of ASTM Standard Test Methods for determining FCG rates, such as E-647, Standard Test Method for Measurement of Fatigue Crack Growth Rates (ASTM 2008).

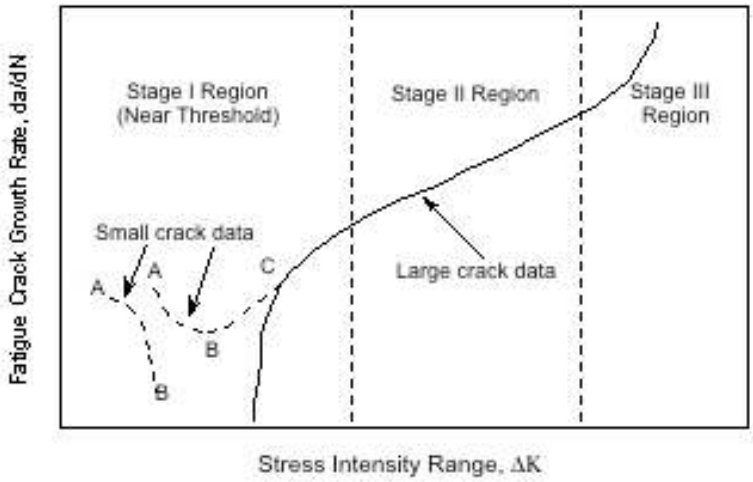

Figure 7.2. Schematic of a large and small fatigue crack propagation behavior illustrating the small crack effects Saxena (1998).

7.2 Creep and Creep-Fatigue Crack Growth

Although FCG can take place at lower temperatures where creep deformation is not an active participant in behavior, higher temperature exposure in the creep regime can lead to the phenomenon known as creep crack growth (CCG). Creep deformation occurs at elevated tem-

peratures as a function of time at sustained stress. Creep deformation and creep rupture are discussed in chapter 5 of this report. Of course, the presence of a crack is necessary to move into the regime where CCG may occur. Linear-elastic and elastic-plastic fracture mechanics concepts are not applicable to the case of crack growth in the presence of significant creep strains, and a concept of time-dependent fracture mechanics is needed for prediction of crack growth under creep conditions. Adding cyclic fatigue loading in the presence of CCG further complicates the situation requiring consideration of creep-fatigue crack growth (CFCG).

This report provides a very brief summary of the CCG and CFCG concepts based on a few key references and the book by Saxena (1998). Both CCG and CFCG are time-dependent extensions of macroscopic cracks at temperatures that exceed about 30% of the melting temperature of the metallic component in absolute temperature scale. A macroscopic crack is one that is larger than the relevant microstructural length for crack growth, e.g., grain size. Current nuclear standards employed to correlate creep and CFCG data for structural flaw evaluations are based on engineering parameters such as stress intensity factor (KI), stress intensity factor range (ΔKI), C^* -integral, and C_t parameter.

As discussed in 7.1.1 for FCG, a time-dependent fracture mechanics concept had to be developed for application to creep and CFCG. Analogous to the J integral for time-independent fracture, the C^* integral (Landes and Begley, 1976) was an early development as a characterizing parameter for CCG. HRR-type crack-tip stress and deformation rate fields, with C^* as the amplitude of the singularities, were established for steady-state creep using the elastic-viscous analogy. Since C^* is defined under steady-state creep conditions, it depends only on load and the geometry of the crack and of the structure and is independent of time. A number of developments in this field include:

- Riedel and Rice (1980) and Ohji et al. (1979) on crack-tip stesses and deformation rates.
- Bassani and McClintock (1981) introduced a crack-tip parameter, $C(t)$, to characterize the HRR-type crack-tip fields.
- Riedel and co-workers (1981-1987) developed crack-tip characterizing parameters for other material models and loading conditions.
- Saxena (1986) introduced a parameter called C_t that can be determined directly from the load-line displacement measurements to correlate with creep and CFCG data in both transient and steady-state regimes.
- Hui and Riedel (1981) established crack-tip fields for a steadily growing crack.
- Webster and Ainsworth (1994) developed use of the reference stress concept as a simplified method to calculate C^*. Their work resulted in development of the British R5 procedures for high-temperature defect assessment.

During a constant load creep crack growth test, the value of C* increases with crack length as shown in Figure 7.3 for a CCG test of 304 stainless steel at 594°C and, according to Saxena (1998), demonstrated the validity of C* for correlating CCG rates. Two specimen types are depicted in that figure, the CT (compact tension) specimen and the CCT (center-crack tension) specimen. Thus, C* seems to work relatively well for steady-state conditions, but stress and temperature gradients, etc., so there is a need for what Saxena describes as small-scale creep and transition creep conditions, and which led Saxena (1986) to development of the C_t parameter

Since the creep zone in the crack-tip region is much more compliant than the surrounding elastic material, the problem of small-scale secondary creep can be conceptualized as a stationary crack in an elastic material, but with a longer effective crack length than the physical crack length. This

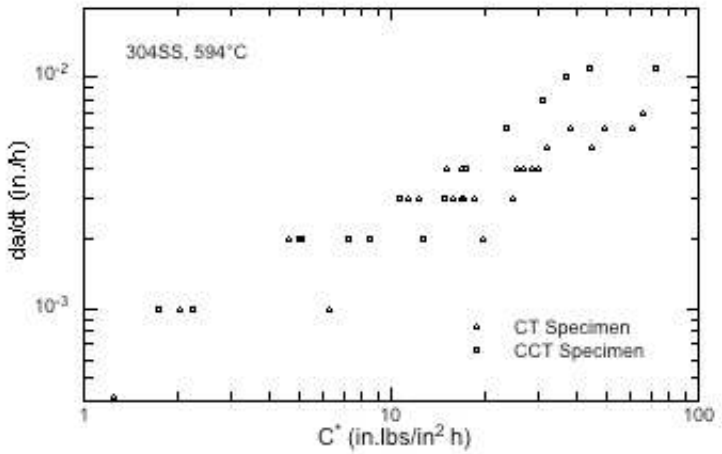

Figure 7.3. Creep crack growth rate as a function of the C*-integral for 304 stainless steel (Saxena 1998).

is the same effective crack length concept employed in LEFM to address the problem of small-scale yielding in elastic-plastic fracture. It was found that applications of the C(t) integral to characterize CCG rates were not very successful. The C_t parameter of Saxena was developed to provide a parameter to characterize CCG rates under a wide range of conditions from small-scale to extensive steady state creep. Saxena (1986, 1998) presented a detailed discussion on mathematical mechanics development of C_t.

Bassani et al. (1989) carried out experimental verification of the use of C_t as a correlation parameter for CCG data. The CCG data were obtained from CT specimens, tested at 538ºC (1000ºF) and 593ºC (1100ºF), for a Cr-Mo (1Cr-1Mo-0.25V) steam turbine rotor steel. Bassani et al. (1989) correlated the measured creep crack growth rates, da/ dt, with the parameters K_{eff}, C^* and C_t. The values of the C_t parameter were determined based on the interpolation formula. The results are shown in Fig. 7.4. In the legends of these figures, SG-CT denotes 1T CT specimens with side grooves and CT denotes 0.25TCT specimens without side-grooves. The K_{eff} parameter is the plastically corrected stress intensity factor. Figure 7.4 shows that the data correlations with K_{eff} and C^* are not good for these tests, but that the data tend to collapse onto a single trend when correlated with C_t. By analyzing the ratio of C^* to C_t, Bassani et al. (1989) concluded that the creep crack growth rate data shown in Fig. 7.4 were under transient conditions and under steady state conditions. Thus, the results support the use of C_t as a correlation parameter for the creep crack growth rate from small-scale secondary creep, through the transition, to extensive secondary creep conditions.

The above discussions and references were directed at the phenomena of crack growth occurring only by cyclic fatigue or only by creep deformation. The phenomenon of crack growth by the combined effects of creep and fatigue lies in the realm of CFCG. Crack growth under CFCG conditions involves the interactions of elastic, cyclic, and creep deformations at the crack tip which leads to complex transient crack-tip fields. Extrapolation of test results from experiments to long term operating conditions in component applications represents a significant

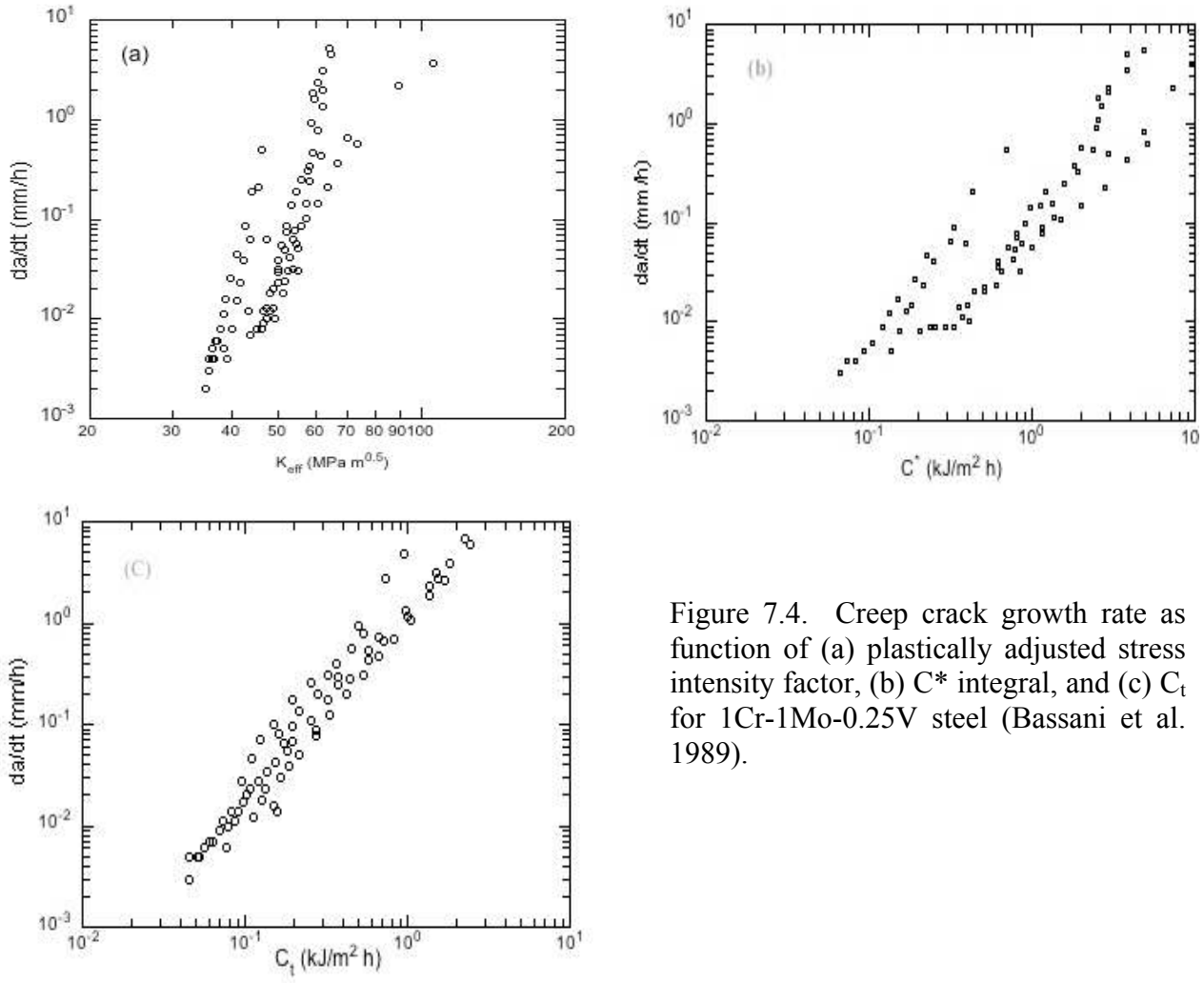

Figure 7.4. Creep crack growth rate as function of (a) plastically adjusted stress intensity factor, (b) C* integral, and (c) C_t for 1Cr-1Mo-0.25V steel (Bassani et al. 1989).

challenge. Part of the challenge is due to the fact that the crack-tip stress fields under creep-fatigue conditions are complex, making analytical results difficult to develop even for laboratory experiments. However, as is often done in such a case, the use of simplifying assumptions allows one to establish a basis for ultimate development of more complex descriptions of the behavior as done by Riedel (1983, 1986).

Riedel and others have developed cyclic crack growth rate formulations based on detailed crack-tip stress and deformation fields and on two different cyclic crack growth mechanisms of alternating slip and cavitation damage. While the crack-tip fields are obtained under different limiting and simplifying assumptions and the cyclic crack growth mechanisms considered do not necessarily encompass all possible mechanisms (e.g., the effect of crack closure has not been incorporated), those detailed analytical results provided by Riedel (1986) have led to the identification of the ranges in which different loading parameters and crack growth mechanisms dominate. The appropriate creep-fatigue loading parameters for different loading frequencies are summarized in Table 7.1.

Table 7.1. Creep-fatigue crack growth loading parameters (Riedel 1986).

Loading frequency range	Appropriate loading parameter (s)	Remarks
$f > 1/t_1$ [(1)]	ΔJ	Rapid strain-reversed cycling. When instantaneous plasticity is confined to a small plastic zone, ΔJ is proportional to $(\Delta K_I)^2$, and ΔK_I becomes the appropriate loading parameter.
$f << 1/t_1$	C*	Slow, continuous cycling
$f \sim 1/t_1$	ΔK_I, $\Delta J_{pl,}$ and C*	Transition range between slow and fast cyclic loading

[(1)] t_1 is transition time from small-scale to extensive secondary creep.

The loading frequency dependences of the cyclic crack growth rates as predicted by various crack growth mechanisms are compared in Fig. 7.5 (Riedel, 1986). The mechanism that gives the highest cyclic crack growth rate at a given loading frequency is expected to dominate among competing mechanisms. At a high loading frequency or a short hold time, cyclic crack growth by alternating slip is the dominant mechanism, whereas cyclic crack growth by the mechanism of cavity growth and coalescence with the macro-crack dominates in the slow-cycling, or long-hold-time, range. Note that cyclic plasticity effects due to repeated loading and unloading are not included in the above concepts.

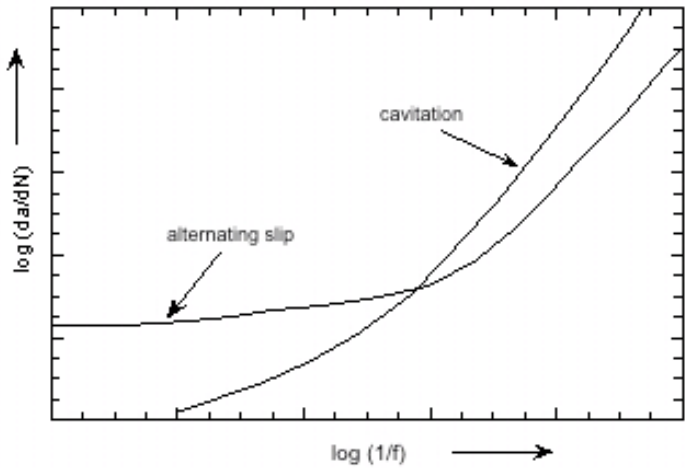

Figure 7.5. Cyclic crack growth rate vs inverse loading frequency for various mechanisms (Reidel, 1986). Schematic for n=6 and χ =5.

Regarding CFCG correlations, Saxena (1998) points out that a simple partitioning of cycle-dependent and time-dependent contributions to total crack growth represents an initial attempt at correlating CFCG data with a mathematical description. However, he points out that experimental results clearly show that crack growth rate for loading cycles with a 100 s hold time was less than that with 0 hold time and that those data clearly challenge the simple partitioning approach. Fig. 7.6 shows this effect for 1Cr-1Mo-0.25V steel. Saxena (1998) goes on to discuss an approach assuming that the cyclic- and time-dependent mechanisms are competing and the crack growth rate is determined by whichever of the two is greater.

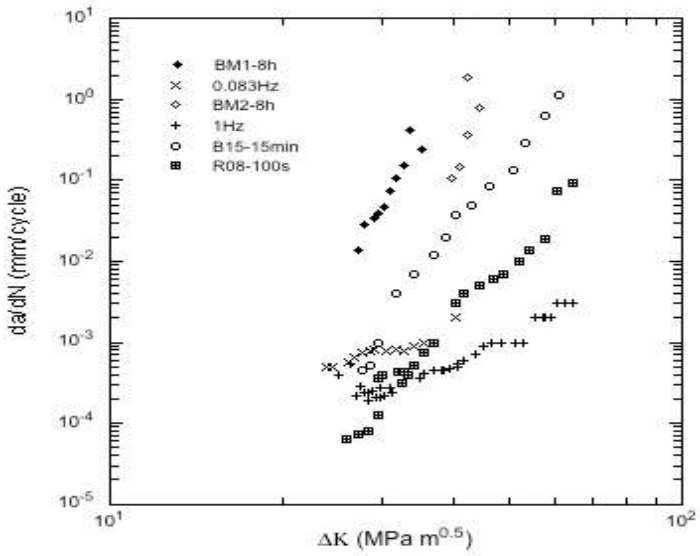

Figure 7.6. Cyclic crack growth rate, da/dn, as a function of K for 1Cr-1Mo-0.25V steel at 538°C for loading waveforms with varying hold times from 0 to 8 hours. The 0 hold time tests were at loading frequencies of 1Hz and 0.083Hz. The loading/unloading times for the 0.083Hz match the loading/unloading times for the hold time tests (Adefris et al. 1996).

Demonstrating a different correlating parameter, other CFCG data for a 1¼ Cr-½Mo steel at 538ºC (1000ºF) were developed by Yoon et al. (1993). The tests were conducted using trapezoidal waveforms with different hold times. However, load-line displacement measurements were only made for tests with tensile hold times of 98 and 600 s due to test equipment limitations. The load-line displacements from these two tests were used to determine $(C_t)_{avg.}$ The results are plotted in Fig. 7.7 against the averaged crack growth rate. Liaw and Saxena (1986) had also developed creep crack growth data for the same 1¼ Cr-½Mo steel and at the same test temperature. The values of the C_t parameter determined from load-line displacement measurements and the corresponding crack growth rates are also included in Fig. 7.7 for comparison. The creep and creep-fatigue crack growth data follow a single trend line. This observation has important implication if it is shown that it is a general result for different materials and creep-fatigue loading conditions. The single trend line implies that the crack growth behaviors during the tensile hold portion of a creep-fatigue test and during a creep crack growth test are identical and that the crack growth rates can be correlated with the C_t parameter, or its average, under different conditions (Saxena, 1998).

7.3 International Codes CFCG prediction

The creep-fatigue crack growth models employed in international codes are briefly outlined in this section and are not presented in detail but are referenced for the interested reader. They have been developed principally for stainless steels and Cr-Mo steels. Most of the models do not include consideration of the more complex types of creep-fatigue interactions.

French A16

French A16 is referred to the procedures in Appendix A16 of the French RCC-MR Code. RCC-MR is a high-temperature design code that provides design rules for fast breeder reactors, including high temperature components. A16 contains a creep-fatigue crack growth procedure for defect assessment of components operating in the creep regime, Drubay et al. (2003).

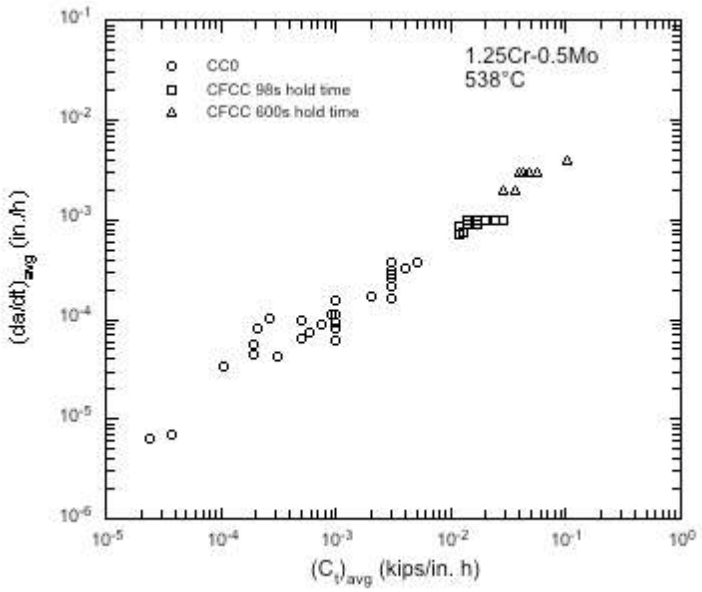

Figure 7.7. (da/dt)*avg* vs $(C_t)_{avg}$ data for 1¼Cr-½Mo steel from CFCG tests. (*Ct*)*avg* is from load-line displacement measurements. d*a*/d*t* vs *t C* data from CCG tests are superposed in the figure for comparison (Yoon et al. 1993).

British R5

R5 is a guideline for assessing the high-temperature response of structural components under creep and creep-fatigue loading conditions. It was originally developed to support the British CO_2-cooled AGR fleet. R5 contains a creep-fatigue crack growth procedure for defect assessment in high temperatures. The amount of crack growth within a creep-fatigue cycle is determined similar to that in the French A16 procedure. The fatigue contribution to the crack growth within a cycle is also determined in a similar manner as the A16 procedure. The effects of *R* -ratio and crack closure are also included in the effective stress intensity factor range. However, for crack growth during the tensile hold period, allowance is made for extensive secondary creep conditions and the elastic transient effect under small-scale secondary creep. R5 does not tabulate material-specific correlation parameters for creep and fatigue crack growth. However, potential data sources are provided, and test procedures to determine these correlation parameters are recommended. It is stated in R5 that the creep and creep-fatigue crack growth procedures have been qualified for stainless steels and Cr-Mo steels.

Japanese JNC method

The Japan Nuclear Cycle Development Institute (JNC) has also developed creep-fatigue crack growth procedure in support of the structural integrity assessment of fast breeder reactor components. The JNC creep-fatigue crack growth model is essentially the same as the French A16 procedure, where extensive secondary creep conditions are assumed for creep crack growth Wakai et al. (2002, 2003). The creep-fatigue crack growth models in A16, R5, and JNC are almost identical, except that R5 includes the elastic transient effect through an approximate creep crack growth correlation for $C(t)$. However, the major differences in these procedures lie in the simplified methods employed to conservatively estimate ΔK_{eff} and C^* for different complex primary and secondary loading conditions using the reference stress approach.

7.4 Creep Crack Growth Mechanisms

Cavity nucleation, growth, and coalescence, and their subsequent linkage with a macroscopic crack, are generally regarded as the mechanisms responsible for intergranular crack growth under creep conditions. Cavities can be nucleated at grain junctions or at grain boundary inclusion interfaces. Following the work of Chuang et al. (1979), the mechanisms that govern the diffusive cavity growth process and the behaviors of the grains and the grain boundaries are briefly described herein in order to provide a background on the underlying mechanisms of creep crack growth.

At elevated temperatures there are a number of processes by which the changes in shape of a cavity on a grain boundary can occur. They include (i) self-diffusion along the cavity surface, (ii) bulk diffusion through the grains, and (iii) evaporation and condensation. Chuang et al. (1979) considered a model of a free surface with doubly periodic curvatures and compared the characteristic relaxation times of atom flux by surface diffusion and by bulk diffusion. For some common metals in the temperature range of 0.5 to 0.8 T_m, where T_m is the melting temperature, they found that surface diffusion is the dominant diffusive mechanism governing cavity growth. Similarly, they found that the contribution to mass transport by surface diffusion dominates over that by evaporation-condensation. Thus, for this temperature range, surface diffusion can be considered as the controlling mechanism that determines the cavity shape. Those atoms that diffuse along the cavity surface toward the cavity tip (or equivalently, the vacancies diffuse away from the cavity tip) can be removed by either through the cavity tip and into the adjacent grain boundaries or through the adjacent grains. Chuang et al. (1979) examined the characteristic relaxation times for grain boundary diffusion and lattice diffusion and found that grain boundary diffusion is the dominant mechanism for the removal of atoms from the cavity tip in the same temperature range of 0.5 to 0.8 T_m. A schematic showing the atom flow along the cavity surface and into the grain boundary is given in Fig. 7.8.

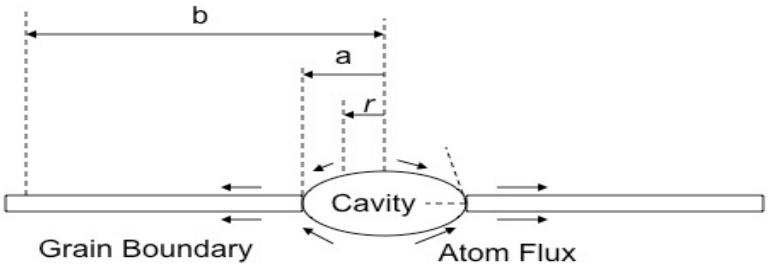

Figure 7.8. Grain boundary cavity, showing atom flow from cavity surface toward its tip, and into the grain boundary (Chuang et al. 1979).

As the atoms diffuse into the grain boundary, the neighboring grains can accommodate the influx of atoms in a number of ways. When the grain boundary diffusion is fast, the atoms spread uniformly along the grain boundary and the neighboring grains act as though they are rigidly translated relative to each other to accommodate the additional atoms in the grain boundary. On the other hand, if the grain boundary diffusion is slow, the neighboring grains would need to deform either elastically or by creep deformation near the cavity tip in order to accommodate the local effective thickening of the grain boundary due to the atom influx from the cavity tip. Extensions of this basic model have been published since Chuang et al. (1979), and have focused on micromechanical descriptions of the cavity growth process, effects of constraint, etc.

7.5 Assessment of Database

7.5.1 Low Chromium Steels

The creep crack growth data for three low chromium steels, 2¼Cr–1Mo, 1¼Cr–½Mo, and ½Cr– ½Mo–½V, and their weldments were assembled by Saxena et al. in an EPRI report (1988). The collected data were reanalyzed using the C_t parameter so that the creep crack growth behaviors of these steels can be compared on a consistent basis. The creep crack growth data were generated from base metals, base metals that had been exposed to service, heat-affected zones in ex-service weldments, simulated heat-affected zones, and fusion lines. The prior austenite grain size of these materials ranges from 20 to 190 μm. The tensile and secondary creep deformation behaviors of the materials were determined in order to provide needed material parameters to evaluate C_t . The temperature range of the creep crack growth tests was 538–550ºC.

Figs. 7.9 to 7.11 show the creep crack growth rate correlations with C_t for base-metal, weld-metal, heat-affected zone, and fusion-line data collected for the study (Saxena, 1988). The upper bound correlations corresponding to a two-sigma shift from the mean are shown in Table 7.2. The data and correlation shown in Fig. 7.9 might, at first glance, imply that the three low chromium steels, with or without service exposure, have the same creep crack growth behavior since the data all fall within the same scatter band of the power-law correlation. However, the magnitude of C_t (as well as C^*) depends on creep deformation. The pre-service and post-service creep behaviors of these steels are different. Therefore different C_t values will result even if the temperature and loading conditions are the same. The correlation would then predict different creep crack growth rates.

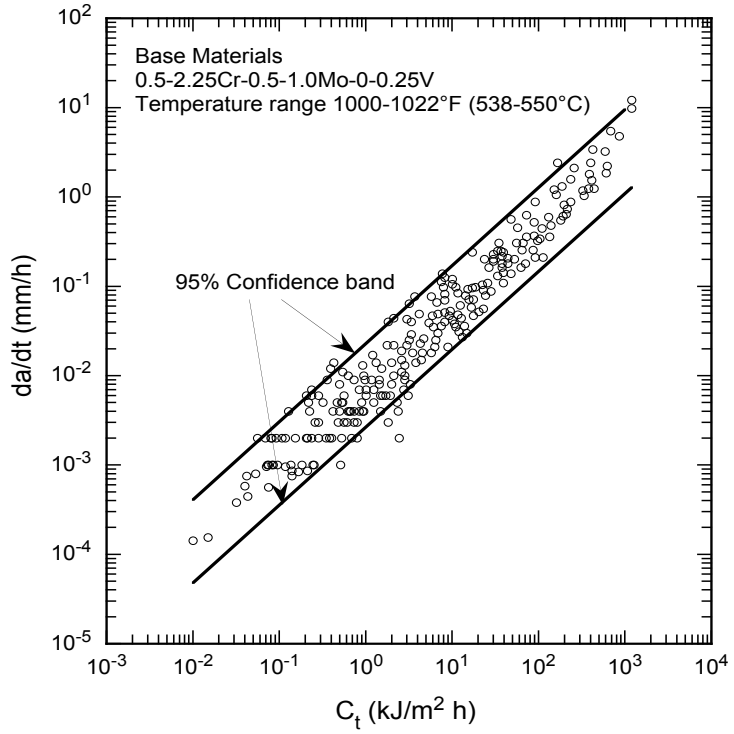

Figure 7.9. Low chromium steels. CCG rate vs C_t for base metals, exposed and unexposed to service. CCG test temperature range is 538–550ºC (Saxena et al. 1988).

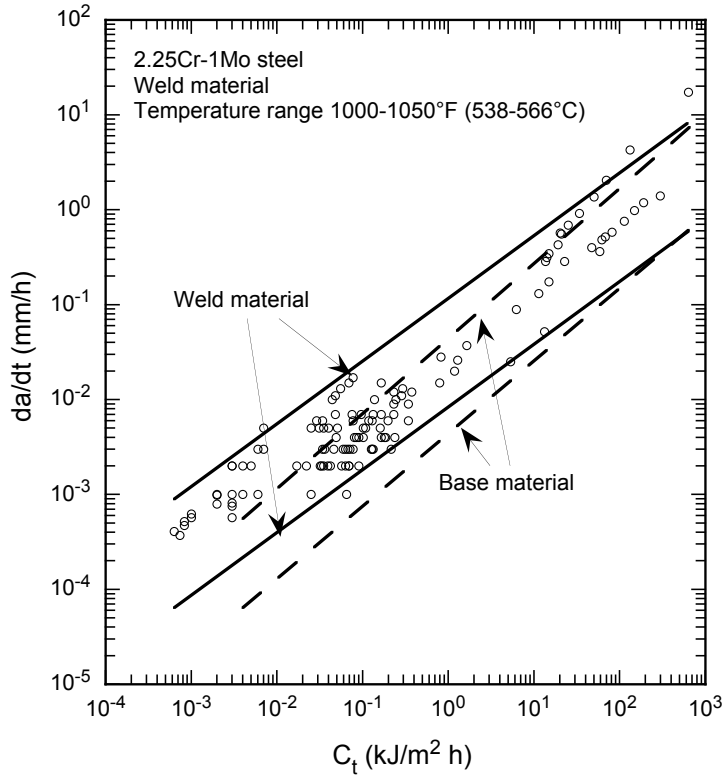

Figure 7.10. 2¼Cr-1Mo weldment CCG rate vs C_t for base metals, exposed and unexposed to service. CCG test temperature range is 538–550ºC. The scatter band from the base metals is superposed on the plot (Saxena et al. 1988).

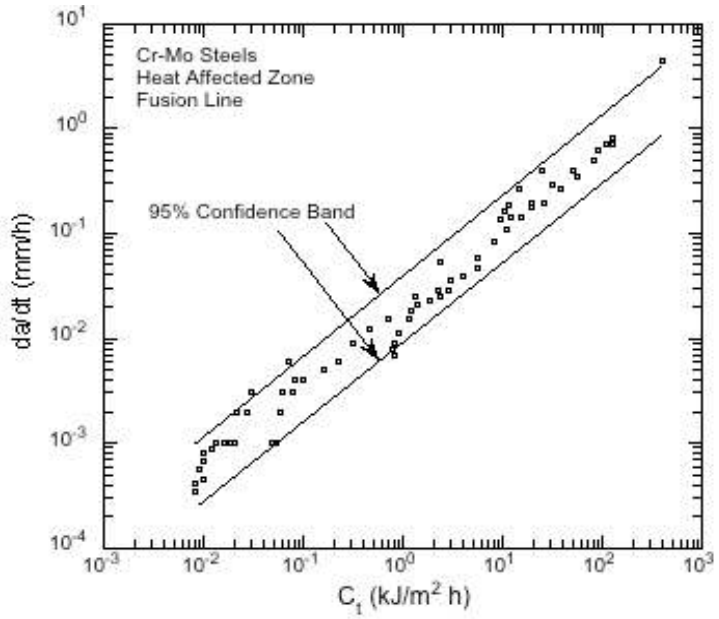

Figure 7.11. Cr-Mo steels heat-affected-zone and fusion-line CCG rates vs C_t (Saxena et al. 1988).

From Table 7.2, it is seen that for a given value of C_t , the creep crack growth rate is the highest for the 2¼Cr-1Mo weld metal, followed by the heat-affected-zone and fusion-line materials, and the lowest from all the base metals considered. Since C_t depends on the creep deformation parameters, information on the creep parameters is required to rank the creep crack growth rates among the materials listed in Table 7.2 for given temperature and loading conditions.

Table 7.2. Crack growth rate correlations for various materials

Material	SI units[(a)]	US customary units[(b)]
All base metals	$da/dt = 0.0373(C_t)^{0.805}$	$da/dt = 0.094(C_t)^{0.805}$
2¼Cr-1Mo weld metal	$da/dt = 0.102(C_t)^{0.674}$	$da/dt = 0.131(C_t)^{0.674}$
2¼Cr-1Mo and 1¼Cr-½Mo heat-affected zone and fusion line	$da/dt = 0.0692(C_t)^{0.792}$	$da/dt = 0.0163(C_t)^{0.792}$

(a) da/dt in units of mm/h, C_t in units of kJ/m^2-h
(b) da/dt in units of in/h, C_t in units of in-kips/in^2-h

The data and correlation shown in Fig. 7.9 might, at first glance, imply that the three low chromium steels, with or without service exposure, have the same creep crack growth behavior since the data all fall within the same scatter band of the power-law correlation. However, the magnitude of C_t (as well as C*) depends on creep deformation. The pre-service and post-service creep behaviors of these steels are different. Therefore different C_t values will result even if the temperature and loading conditions are the same. The correlation would then predict different creep crack growth rates. From Table 7.2, it is seen that for a given value of C_t , the creep crack growth rate is the highest for the 2¼Cr-1Mo weld metal, followed by the heat-affected-zone and fusion-line materials, and the lowest from all the base metals considered. Since C_t depends on the creep deformation parameters, information on the creep parameters is required to rank the creep crack growth rates among the materials listed in Table 7.2 for given temperature and loading conditions.

7.5.2 Modified 9Cr-1Mo Steel

The ASME Boiler and Pressure Vessel Code specifies that Modified 9Cr-1Mo is to be used in the normalized (in the temperature range of 1038–1149ºC) and tempered (at a minimum temperature of 732ºC) condition. It has a lower thermal expansion coefficient and higher thermal conductivity than austenitic stainless steels, resulting in more resistance to thermal fatigue.

Ancelet and Chapuliot (212) reported the results of creep crack growth tests of Modified 9Cr-1Mo performed at 550ºC. There were five tests, with each test carried out using side-grooved 1T CT specimens. The creep crack growth rates are correlated with C^* that was calculated using the formula from ASTM E 1457, 1998 Edition. The creep crack growth rate data are shown in Fig. 7.12; the data points corresponding to small-scale secondary creep and the transition to extensive secondary creep have been removed from the figure.

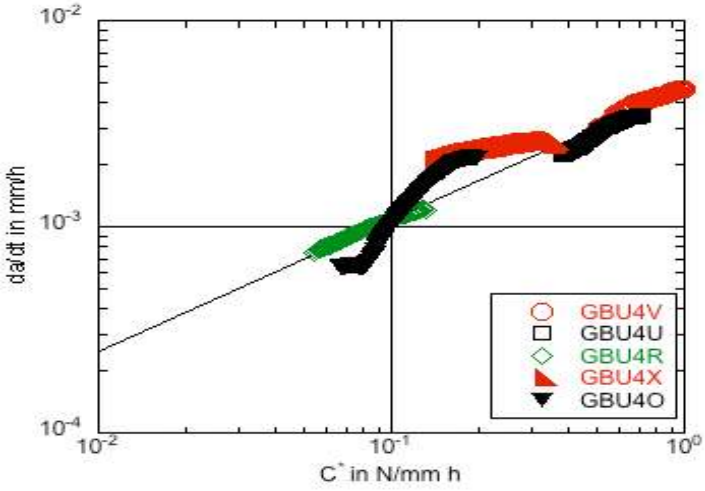

Figure 7.12. Modified 9Cr-1Mo CCG data at 550°C. Transient data have been removed from the plot (Ancelet and Chapuliot 2008).

The best-fit creep crack growth rate correlation shown in Fig. 7.12 has the form

$$da/dt = 0.0048(C^*)^{0.642}\text{, at } 550°C \qquad (7.1)$$

where d*a*/d*t* is in the units of mm/h, and *C** is in the units of N/(mm□h), and the correlation is valid in the range 0.04N/(mm•h)<*C** <1N/(mm•h).

Reytier (2004) also presented the results of fatigue crack growth tests on Modified 9Cr-1Mo in an accompanying test program. The fatigue crack growth tests were conducted per ASTM E647, 1999 Edition on 1T CT specimens at 550ºC. The cycling frequency is 0.1 Hz and the *R*-ratio is 0.1. The cyclic crack growth rate data vs the stress intensity factor range are shown in Fig. 7.13. Reytier (2004) reported a best fit of the FCG data in the Stage II Paris regime as

$$da/dt = 7.1\times10^{-7}(\Delta K_I)^{1.85}\text{, at } 550°C \qquad (7.2)$$

where da/dN is in the units of mm/cycle, and ΔK_I is in the units of MPa√m, and the correlation is valid in the range 14< ΔK_I <34 MPa√ m.

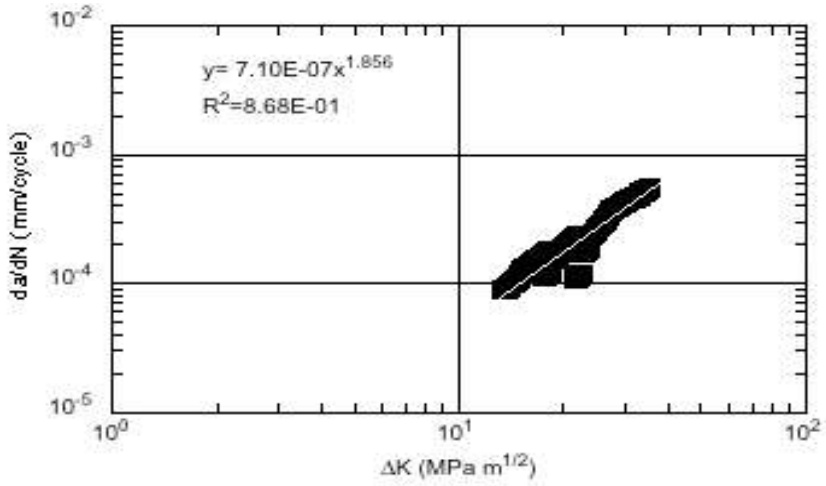

Figure 7.13. Modified 9Cr-1Mo FCG data in the Stage II Paris regime, 550ºC (Reytier 2004).

Wasmer et al. (2003) had presented the results of creep crack growth tests at 625°C using side-grooved 1T CT specimens machined from the pipe product form of Modified 9Cr-1Mo. The creep crack growth test procedure of ASTM E 1457, 2000 Edition was followed. They have also performed creep-fatigue crack growth tests at low frequencies equal to or less than 0.01 Hz. The crack growth rate data are shown in Fig. 7.14. The values of C^* were computed from load-line displacement rate due to creep using ASTM E 1457, 2000 Edition. The best-fit correlation is given as

$$da/dt = 1.44(C^*)^{0.60}, \text{ at } 625°C \tag{7.3}$$

where da/dt is in the units of mm/h, and C^* is in the units of MPa/h. Wasmer et al. (2003) reported that the fracture surfaces for both types of tests were mainly intergranular.

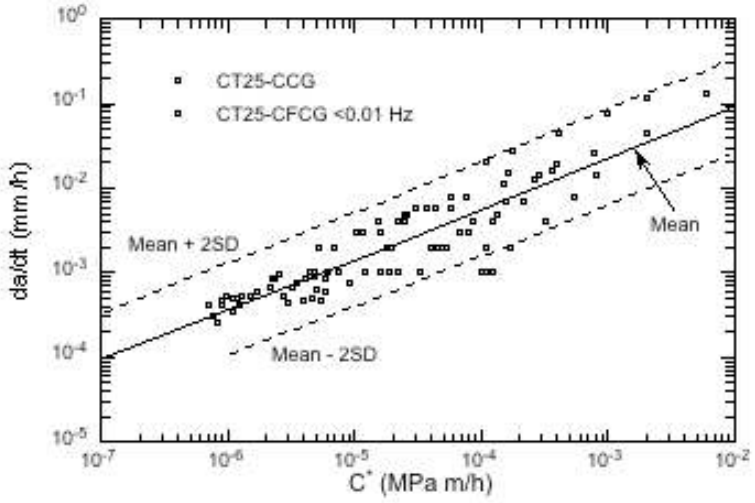

Figure 7.14. Modified 9Cr-1Mo CCG and CFCG rates at 625°C from CT specimens (Wasmer et al. 2003).

Shibli et al. (1998) had reported the creep crack growth and fatigue crack growth test results for Modified 9Cr 1Mo from the European Union HIDA Program at temperatures in the range of 538 to 593ºC. They did not show the plots of the crack growth data but had reported the best fit correlations:

$$da/dt = 3.03\times10^{-3}(C^*)^{0.0626}, \text{ 538 to 593°C for base metal} \tag{7.4}$$

$$da/dN = 6.499\times10^{-8}(\Delta K_I)^{2.458}, \text{ 538 to 593°C for base metal} \tag{7.5}$$

where the creep crack growth rate, da/dt, is in the units of mm/h, C^* is in the units of J/m^2h , the cyclic crack growth rate, da/dN, is in the units of mm/cycle, and ΔK_I is in the units of $MPa\sqrt{m}$.

7.5.3 Modified 9Cr-1Mo Welds

Modified 9Cr-1Mo welds are prone to the so-called Type IV cracking which is initiated within the fine-grained transformation band along the outer margins of the heat-affected zone. Shibli and Mat Hamata (2001) presented an overview of the crack growth test results from Modified 9Cr-1Mo weld metal and heat-affected zone from two European round-robin test programs. The test temperature for the SOTA program was 600ºC. CT specimens were machined from the

welds, with the crack tip placed either in the weld metal, the coarse-grain region of the heat-affected zone, or the fine grain region (Type IV) of the heat-affected zone. Figures 7.15 and 7.16 show the creep crack growth data for weld metal and heat-affected zone, respectively. The CCG rate data scatter band for Modified 9Cr-1Mo base metal is superposed on these two plots to show the expected increase in the data scatter from testing weld metal and heat-affected zone. Four different test facilities were involved in obtaining the data in each of these two figures. Dogan and Petrovski (2001) have given the best-fit curves for these same data sets as

$$da/dt = 0.186\times10^{-3}\times(C^*)^{0.9036}, \text{ at } 600°C \text{ for weld metal} \quad (7.6)$$

$$da/dt = 0.333\times10^{-3}\times(C^*)^{0.7467}, \text{ at } 600°C \text{ for heat-affected zone} \quad (7.7)$$

where da/dt is in the units of mm/h and C^* in the units of N/m/h , for both equations.

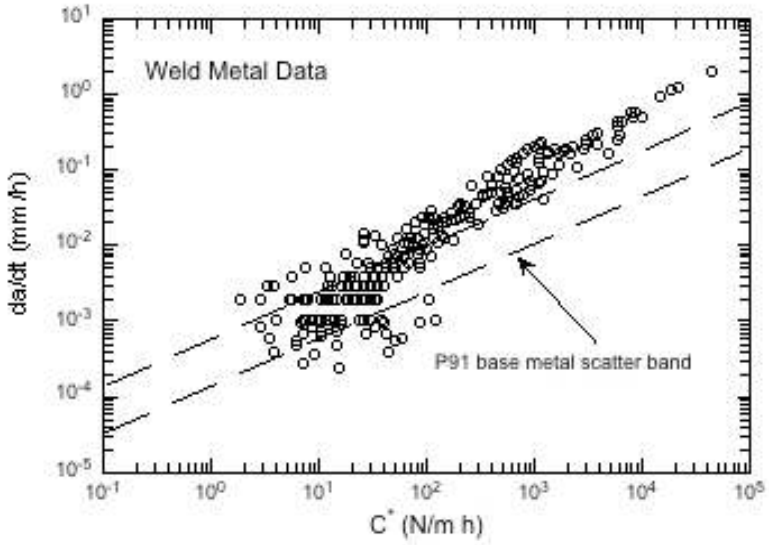

Figure 7.15. Modified 9Cr-1Mo weld metal crack growth data at 600ºC. The base metal crack growth rate scatter band is superposed on the plot. Test data from the SOTA Program (Shibli and Mat Hamata 2001).

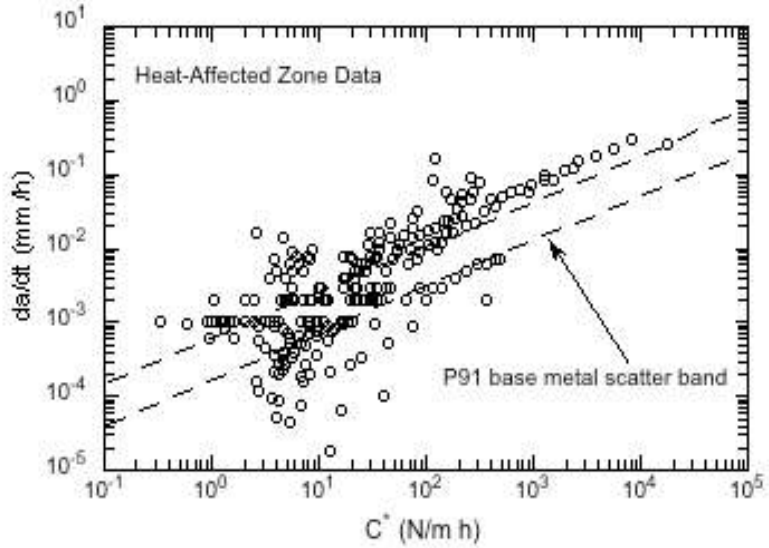

Figure 7.16. Modified 9Cr-1Mo heat-affected-zone crack growth data at 600ºC. The base metal crack growth rate scatter band is superposed on the plot. Test data from the SOTA Program (Shibli and Mat Hamata 2001).

Crack growth test results from the HIDA program under creep and creep-fatigue loads were also summarized by Shibli and Mat Hamata (2001). The test temperature was 625ºC. Test specimens were made from the Modified 9Cr-1Mo base metal and heat-affected zone. For heat-affected zone specimens, the initial notch was placed at the center of the heat-affected zone. Most of the test specimens were 1TCT specimens. There were two 2T CTs and one single-edge-notch tension (SENT) specimen. The frequencies of the cyclic loads were 0.01 and 0.001 Hz. Fig. 8.17 shows the crack growth rate vs C^* for both base metal and heat-affected zone specimens. Separate regression lines were provided for the data from base metal and heat-affected zone. However, the equations for the best fits were not provided. The crack growth rates for the heat-affected zone are higher than those in the base metal, as expected.

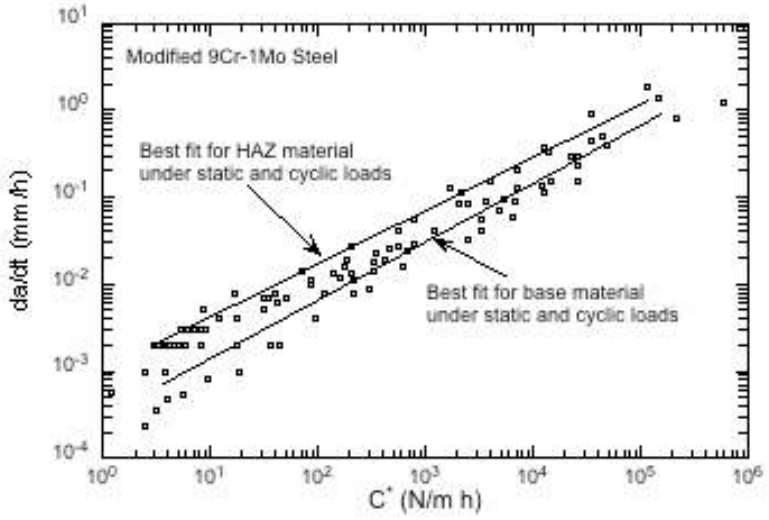

Figure 7.17. Modified 9Cr-1Mo base metal and heat-affected zone CCG and CFCG data at 625ºC. Test data from the HIDA Program (Shibli and Mat Hamata 2001).

7.5.4 Austenitic Stainless Steels

The materials tested in the HIDA Program included 316 and 316L (N) stainless steels. The 316L (N) stainless has similar chemical composition as 316 stainless except that the carbon content is lowered and nitrogen is added to compensate for the loss of strength from the lower carbon content. The creep crack growth data are summarized by Shibli et al. (1998). Fig. 7.18 shows the CCG rate vs C^* plot of the data obtained from tests at temperatures below 600°C. Tests were performed using CT specimens. It can be seen in Fig. 7.18 that the CCG rates for 316L (N) stainless steel were lower than those for 316 stainless steel at the same temperature (550°C). A similar plot for the data obtained from tests at 600, 625 and 700,°C is shown in Fig. 7.19. The specimens used in this set of tests include CT, single-edge-notch-tension (SENT), single-edge-notch bend (SENB), and center-cracked panel (CCP) specimens. The data from tests at 700°C were from 316L (N) stainless steel. The best-fit corrections are

$$da/dt = 9.721\times10^{-5}\times(C^*)^{0.734}\ ,\ T< 600°C \tag{7.8}$$

$$da/dt = 9.285\times10^{-5}\times(C^*)^{0.739}\ ,\ T> 600°C \tag{7.9}$$

where da/dt is in the units of mm/h and C^* is in the units of $J/m^2/h$.

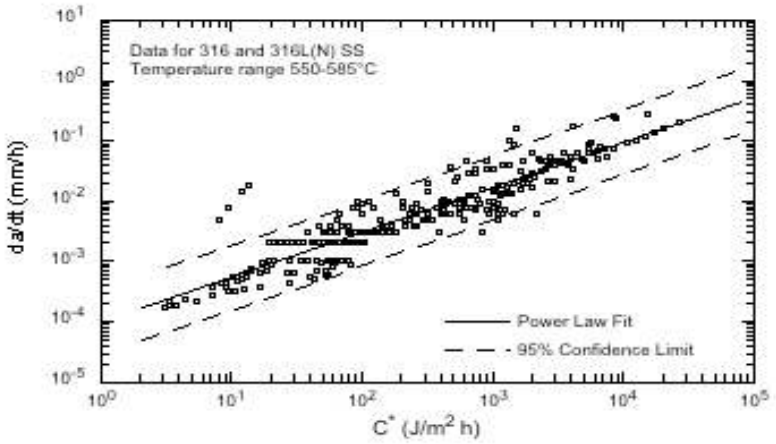

Figure 7.18. 316 and 316L (N) stainless steel CCG data at temperature below 600°C (Shibli et al. 1998).

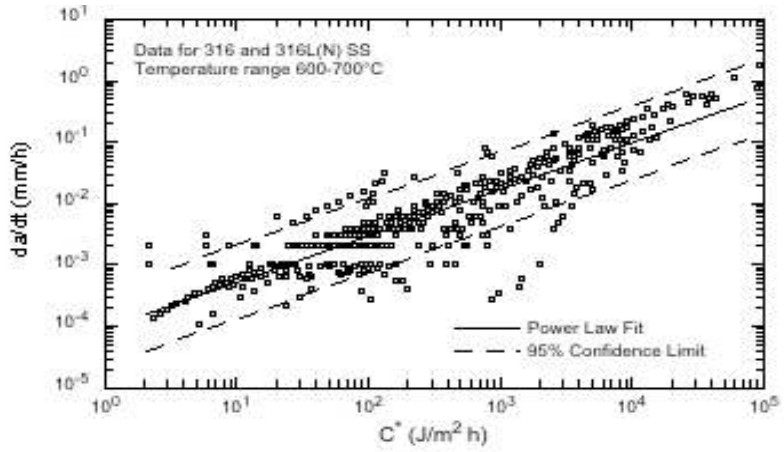

Figure 7.19. 316 and 316L (N) stainless steels CCG data at 600, 625, and 700°C (Shibli et al. 1998).

Tabuchi et al. (1990) conducted CCG tests on 316 stainless steel at 550, 650, 750 and 800°C, using CT specimens. A plot of da/dt vs *C** is shown in Fig. 7.20. The fracture surfaces of the broken specimens were examined, and Tabuchi et al. grouped them into wedge-type cracking, transgranular fracture, and cavity formation. As can been seen from the legend of Fig. 7.20, the fracture mode changed as the load was decreased at 650 and 750°C.

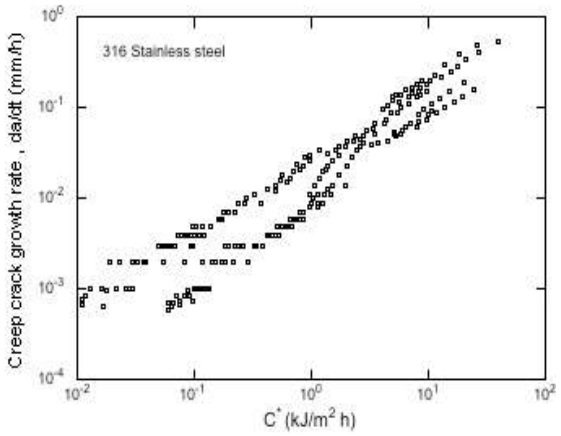

Temperature (°C)	Applied stress (MPa)	Fracture mode
550	489, 409, 363	W
650	322, 296	W
	262, 245	T
750	174, 148	T
	123, 95	C
800	114, 78	C

Figure 7.20. 316 stainless steel (Tabuchi et al. 1990). Fracture mode of the test: W=wedge cracking, T=transgranular fracture, and C=cavity formation

7.6 Issues and Resolutions

In the R5, RCC-MR, API 579/ASME FFS and Japanese guidelines, creep-fatigue interaction for the crack growth behavior is not directly accounted for. However, such interaction might be important during the heat-up and cool-down operations of the LMR. Thus, there are uncertainties in the applicability of the current fit-for-service analysis procedures for LMR applications. Critical assessment of these procedures and their potential improvements are required. While creep fatigue crack growth is the most severe mode of high-temperature crack growth, creep crack growth received the most attention in the literature reviewed. The following identifies key development needs.

The results from time-dependent fracture mechanics developments still represent the state of the art. Most of the subsequent work in the 1990s and 2000s had concentrated mostly on developing CCG correlations and formulating flaw assessment procedures using C^*. All the design codes and assessment guidelines reviewed are based heavily on the use of the C^* parameter and the secondary creep material model. Exceptions are the works of Saxena and co-workers on the C_t parameter. The adequacy of these approaches needs to be critically examined.

Transferability from laboratory results to structural components is an issue. The ASTM standard E1457 provides test methods to determine steady-state creep crack growth rate and the C^* parameter, which is the relevant crack-tip characterizing parameter under extensive secondary creep conditions. There are conditions specified in the standard on the range of validity of the data that can be used to determine these two quantities. When applying a correlation between steady-state creep crack growth rate and C^* established per E1457 to structural applications, a set of criteria must be provided in design codes and assessment guidelines that are analogous to the stringent validity requirements of E1457. Similar criteria for other relevant crack-tip characterizing parameters are also necessary for their use in crack growth calculations, including the effects of crack tip constraint and the underlying crack growth mechanisms.

The C^* approach assumes that steady-state secondary creep persists for all times. It is important to provide criteria for the onset of accelerated, tertiary creep crack growth in design codes and assessment guideline, analogous to the use of onset of third stage creep as one of the criteria in setting the time-dependent stress limit in the ASME B&PVC, Sect. III, Subsection NH.

Overall, there is more empiricism in the creep-fatigue crack growth approach to crack growth calculations than the creep crack growth approach. Advances in the understanding and quantification of the interaction between FCG and CCG and the development of a practical methodology to perform crack growth calculations would be most helpful. The European Commission SOTA and HIDA programs have generated a reasonable-sized crack growth database for Modified 9Cr-1Mo and its associated weldment. There was a good coverage of the test temperatures; however, data from lower temperatures than those used in the SOTA and HIDA programs would be more prototypical. Access to the raw data in terms of load-line displacement and potential drop records would be required in order to evaluate other, potentially more relevant crack-tip characterizing parameters. Otherwise, new data would have to be generated. The thickness of the welds used in these two test programs was not known, nor the post-weld heat treatment given to those welds. It is important to generate crack growth data from the type of welds anticipated

for the LMR components and the type of welding process and post-weld treatment that would have to be used in the field due to manufacturing related constraints.

A significant data gap for all candidate materials is the lack of crack growth data from a liquid sodium environment and key feature tests. Performance of FCG experiments in liquid sodium is not simple, but certainly not as complex as performing CCG and CFCG experiments in that medium. But, such experiments with significant hold times in the sodium environment are critically important since no data exist for the candidate materials.

8. FRACTURE TOUGHNESS

8.1 Scientific Understanding

Ritchie, Knott and Rice (1973) proposed a micromechanical model for brittle fracture in ferritic steels that was based on the observation that cleavage microcracks emanate from brittle particles that fracture under the high process zone stress fields near a blunting crack. According to this model, brittle fracture occurs when the elevated normal stress ($\sigma_n = M\sigma_y$) in front of a notch or crack tip exceeds a critical local fracture stress for transgranular cleavage (σ^*_c) over a critical microstructural volume of material ($V^{*)}$, where σ_y is the yield stress and M is a constraint factor varying between ≈2 and 4 depending on the notch geometry and the strain hardening rate. Such a model is manifested primarily through determination of the fracture toughness for a given material. Fracture toughness as an engineering parameter, however, is a development from the 1960s, with determinations of material toughness being made primarily with impact testing of bend specimens, such as with the Charpy V-notch impact test. Section III of the ASME Code contains requirements for toughness of materials based on the application, with Class 1 components being portions of the primary pressure boundary (RPV, primary piping, etc.), Class 2, Class 3, etc. Requirements for material toughness in Section III are defined in terms of Charpy impact toughness, except that the drop-weight nil-ductility transition temperature is also required for Class 1 components. Both 9Cr-1MoV (grade 91) and 2.25Cr-1Mo (grade 22) are approved in Section III, including in Subsection NH for high temperature applications. However, 2.25Cr-1Mo-0.25V steel is not approved in Section III, although it is approved for Section VIII applications.

Although radiation effects is not a major focus of this report, it is important to recognize that all body-centered cubic alloys undergo a transition from low temperature brittle cleavage behavior to high temperature ductile behavior and such behavior may be significantly changed by neutron irradiation. It is also instructive to realize that, in addition to the obvious effect of the amount of exposure, the irradiation temperature is a major factor. When subjected to neutron radiation, depending on the specific material's radiation sensitivity, radiation-induced hardening (i.e., increases in σ_y) is invariably accompanied by an upward shift in the transition temperature as shown in Fig 8.1 for the reduced activation FM steel Eurofer 97 irradiated to 2.3dpa and 8dpa at ≈300^{o}C (Rensman, 2005). Irradiation to 8dpa induces an upwards shift of the DBTT of ≈150^{o}C and also results in a substantial decrease of the ductile toughness regime (usually designated upper-shelf energy).

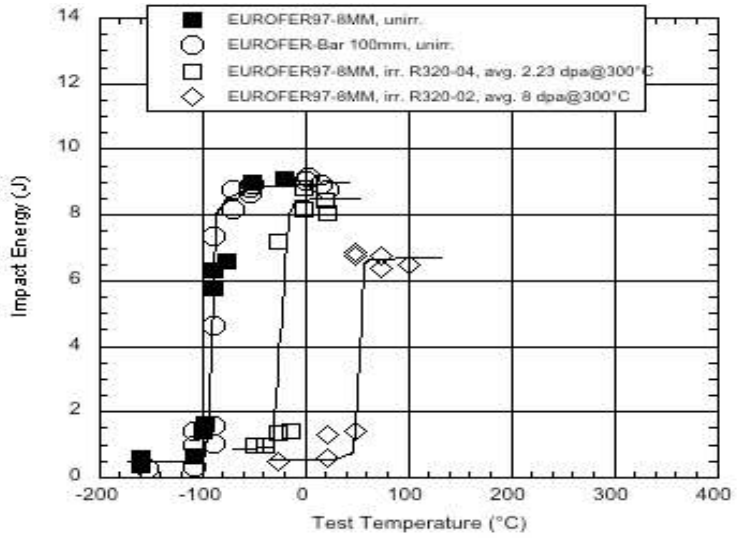

Figure 8.1. DBTT shifts in Eurofer 97 for miniaturized CVN specimens, irradiated to 2.3 and to 8dpa at 300°C (Rensman, 2005).

An extensive body of literature dealing with radiation–induced shifts in DBTT for the 9-12%Cr FM steels was compiled by Klueh and Harries (2001), and has been expanded during the past several years with results from irradiation experiments in the EU, Japan and in the US by Rensman (2005, 2002), Shiba (1996), Schneider (2003), and Jitsukawa (2002). Additionally, significant data on F-M steels are also available in Klueh and Nelson (2007) and for 9Cr-1MoV in DiStefano, et al. (1986). More recently Yamamoto et al. (2006) compiled an extensive data-base on the hardening-induced embrittlement of the FM steels. The shifts in Charpy transition temperature ΔT_c, were analyzed as a function of T_i and dpa for the F82H, 9Cr-1Mo and 9Cr-W alloy classes and fitted to a simple square root dependence of dose , $\Delta T_c = k_c\sqrt{dpa}$. The dose dependence of transition temperature shifts for F82H and for the 9Cr-1Mo FM steels are shown in Figs. 8.2 (a) and (b), respectively. The values of the slope k_c are higher for F82H in each temperature range and there is a positive slope for F82H even for the irradiation temperatures above the hardening regime, (450-592°C).

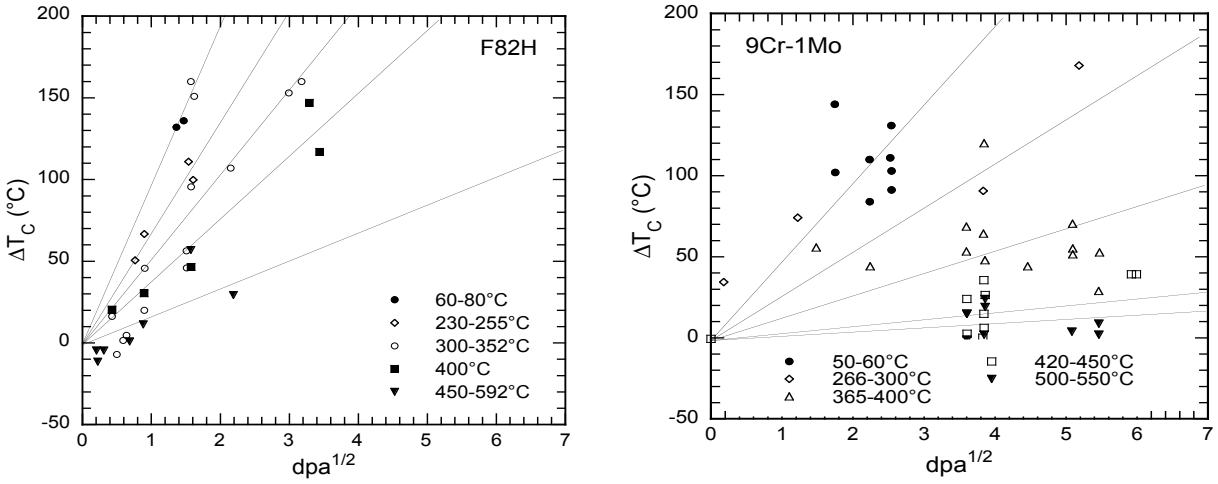

Figure 8.2. (left) Temperature shifts for F82H fitted to √dpa dependence for a range of T_i, and (right) Temperature shifts for 9Cr-1Mo fitted to a √dpa dependence (Yamamoto et al. 2006).

Combining the √dpa dependence of hardening with temperature shift data for these 3 groups of alloys, the radiation hardening/Charpy shift coefficients, $C_c = \Delta T_c/\Delta\sigma_y$,were determined to be 0.18, 0.30 and 0.38 C/MPa for 9Cr-1Mo, 9Cr-W and F82H alloys respectively. These different values of C_c reflect underlying differences in radiation hardening behavior arising from compositional and microstructural differences between the alloy groups. An important conclusion from this work is that the Charpy shift coefficient for F82H ($C_c \approx 0.38\ ^oC/MPa$) is lower than the coefficient measured for the shift in the fracture toughness reference temperature T_o, ($C_k \approx 0.58^oC/MPa$). This indicates that the sub-sized Charpy test provides a non-conservative estimate of the hardening-induced embrittlement and reinforces the need for fracture toughness data on these materials as discussed below. Thermal aging at high temperatures may also affect the toughness of the material in a negative manner and the effects of irradiation and thermal aging on ferritic steels are discussed in Natesan et al. (2008).

Miniaturized Charpy specimens (MCVN) are often used for such irradiation experiments due to the relatively small size of irradiation capsules and because of significant gamma heating. However, the DBTT is not an intrinsic property of the material and the values obtained vary widely depending on a number of variables such as specimen size, notch geometry and loading rate. Although the results provide important information regarding the effects of irradiation on toughness of a material, the actual values of the transition temperature or of the absorbed energy at a given temperature are of only qualitative use in predicting the behavior of a structural component under a given set of operating conditions. Whereas toughness tests with notched impact specimens provide a qualitative measure of toughness, fatigue-precracked specimens provide quantitative measures for use in predicting critical crack sizes and allowable stresses in the presence of defects of known sizes. The most common parameter of fracture mechanics is the plane-strain fracture toughness, defined as "the crack extension resistance under conditions of crack-tip plane strain." The plane strain fracture toughness is considered a material property and is designated K_{Ic}, the critical value of the mode I (opening mode) stress-intensity factor determined in accordance with ASTM Test Method E399 (2002). LEFM is valid only for the case of a very small, contained plastic zone (surrounded by a large elastic region) ahead of the crack tip. The basic principle is that unstable fracture will occur when the applied stress intensity factor exceeds the plane-strain fracture toughness, i.e., $K_I > K_{Ic}$. For materials of even moderately high toughness, e.g., low alloy Mn-Mo-Ni steels used for light-water reactor pressure vessels, very large specimens may be needed to determine a valid K_{Ic} because K_{Ic} increases with increasing temperature.

When large deformations occur, the precepts of LEFM are violated and nonlinear fracture mechanics methods must be utilized to evaluate structural integrity. Because fracture stress increases with decreasing flaw size, fracture toughness specimens of practical size for routine use often experience yielding before fracture. Methods are needed to characterize the material fracture resistance with a small specimen for application to a large structure: thus, the question of scaling from a specimen with a large plastic zone to a structure with a small plastic zone is required. The most widely used EPFM criterion is the J-integral, first introduced by Rice (1968) and first incorporated in a consensus-testing standard in 1981, i.e., ASTM E813 (1981). It is a line integral that describes the stress-strain field at the tip of a crack by assuming a path of integration far from the crack tip but lying completely inside the body. It provides a means of analyzing the far-field region to infer the behavior of the near-field region which may experience substantial plastic deformation. Since its initial development, the J integral has been developed

into a relatively mature and accepted fracture criterion, as evidenced by the development of various test standards to measure the resistance of a material to onset of ductile crack extension, J_{Ic}, the description of a J-resistance (J-R) curve, and the value of J at the onset of cleavage fracture, J_c. Figure 8.3 from ASTM E1820 (2005) shows a typical load vs load-line displacement trace from a single specimen unloading compliance test, the J vs crack extension plot (resulting from analysis of the load-displacement trace) used to determine the J-R curve, the J_{Ic}, and a dimensionless parameter that describes the material resistance to stable crack growth, the tearing modulus (a dimensionless parameter based on the J-R curve slope dJ/da). As with LEFM conditions, the EPFM parameters of ductile fracture toughness resistance are also dependent on specimen size.

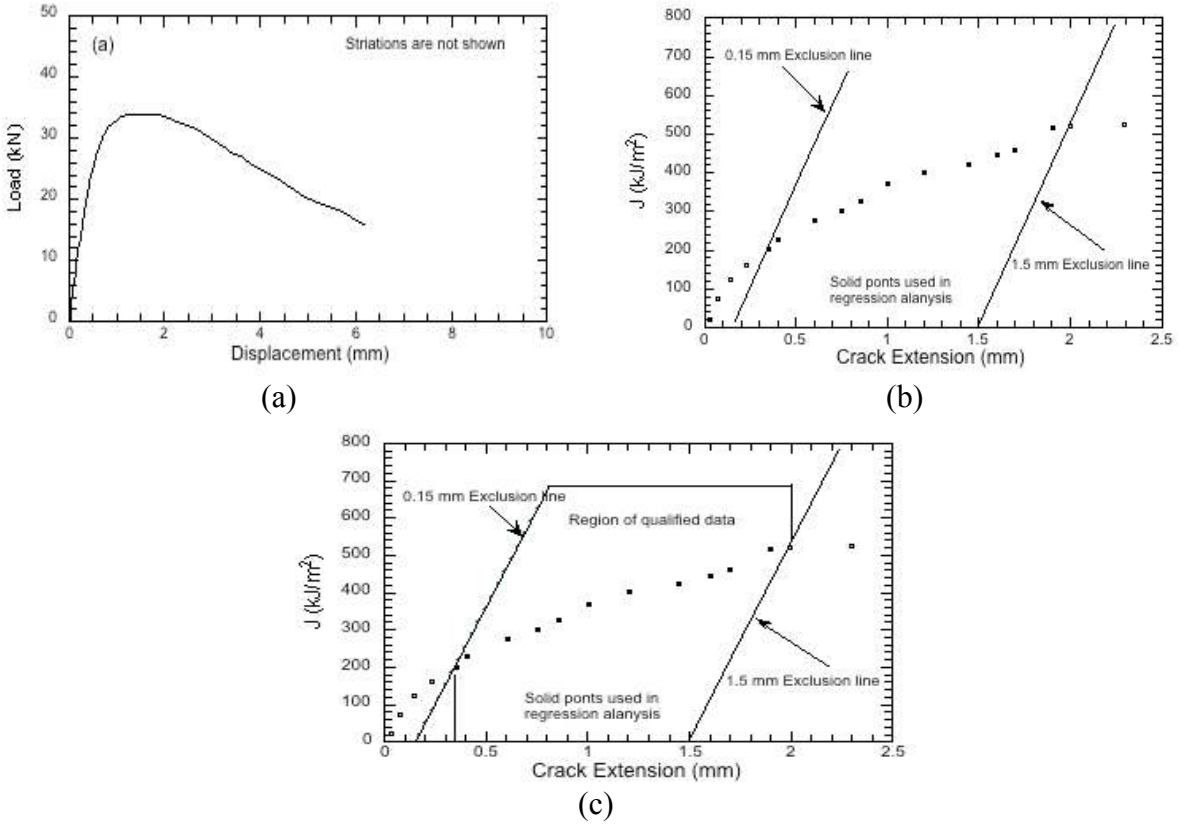

Figure 8.3. Schematic diagrams showing (a) a typical load vs load-line displacement trace from a single specimen unloading compliance test, (b) the J vs crack extension plot (resulting from analysis of the load-displacement trace) used to determine the J-R curve, J_{Ic}, and the tearing modulus (based on the J-R curve slope dJ/da), and (c) the region of qualified data for the analysis (ASTM, 2005).

If the specimen experiences brittle cleavage fracture prior to the full development of a resistance curve, the J-integral value at the onset of fracture, J_c, is used to calculate an equivalent stress intensity factor, K_{Jc}. It is this parameter that is used to determine the parameter T_o, the temperature at which the mean fracture toughness (K_{Jc}) of a minimum specified number of 1T specimens (25 mm thick) is 100 MPa$\sqrt{m}$. This parameter provides a measure of the fracture toughness transition temperature using the Master Curve (MC) concept developed by Wallin (1984); this concept has been further developed as a consensus test standard in ASTM E 1921

(2005). The procedure in E 1921 allows the determination of T_o with a relatively small number of relatively small specimens, as shown in Figure 9.4 (McCabe et al. 2000). For specimens of other than 1T size, the MC procedure incorporates a weakest link concept of fracture that allows for normalization of results to 1T size, with T_0 determined by fitting of a curve of a fixed universal (assumed) shape.

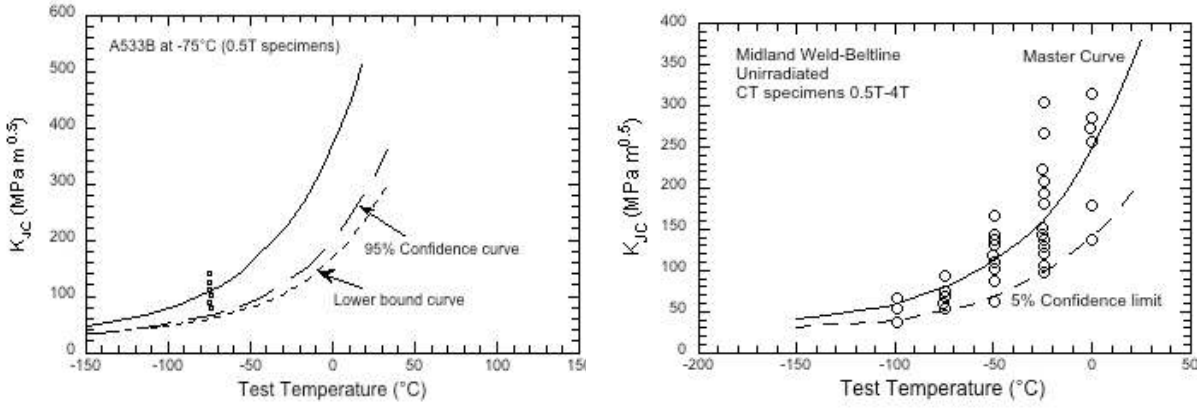

(a) (b)

Figure 8.4. The test procedure in E-1921 allows the determination of T_o with a relatively small number of relatively small specimens. The results from (a) six small (0.5T) specimens tested at one temperature provide an excellent characterization of the results from (b) a large number of specimens up to 4T size (McCabe et al. 2000).

8.2 Assessment of Database

Odette et al. developed a fracture toughness database for F82H, an 8Cr2WV steel, and demonstrated that the MC concept is applicable for this steel (Odette et al. 2004). Figure 8.5 shows the fracture toughness vs test temperature data for the IEA heat of F82H after making adjustments to account for constraint loss effects and statistical stressed volume effects inherent in the wide range of specimen geometries used to compile the data base. The F82H database is reasonably represented by a master curve with a $T_o = -91^oC$.

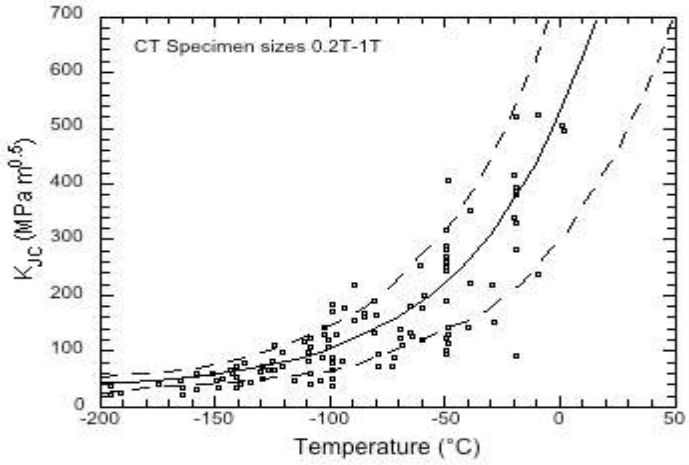

Figure 8.5. Fracture toughness data for uniradiated F82H versus temperature after correcting for various specimen size effects (Odette et al. 2004).

James and Carlson (1985) performed both fracture toughness and fatigue crack growth experiments with grade 91 steel. The fracture toughness experiments were performed at 24°C and were conducted using both the multiple specimen technique and the unloading compliance technique to allow for comparisons of techniques. They determined a J_{Ic} value of 85.5 kJ/m^2 using ASTM E813-1981 and a value of 79.7 kJ/m^2 using a different fitting method; the average tearing modulus was 84. Figure 8.6 shows a compilation of all the data obtained at 24°C, showing the higher J-integral values determined with the unloading compliance method, which resulted in higher tearing modulus values than with the multiple specimen method.

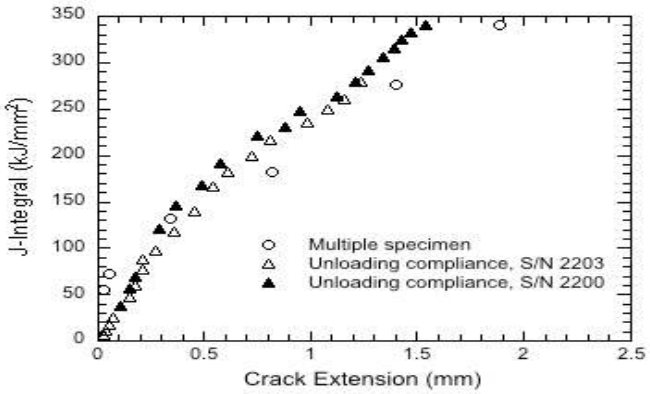

Figure 8.6. Superposition of the four unloading compliance J-R curves and the multiple specimen J-R curve (James and Carlson, 1985).

Yoon and Yoon (2006) tested a 16-mm thick plate of normalized and tempered grade 91 steel using precracked Charpy (PCVN) and 0.5PCVN specimens. Comparisons were made with results from similar tests of A508 grade 3 steel. The Grade 91 steel gave a 41J temperature of -56°C with Charpy impact tests, a result similar to that of the A508 steel. J-R test results at room temperature and at 288°C are shown in Figs. 8.7 (a) and (b), respectively. As shown, the J-R curve for the grade 91 is lower than that of the A508 at room temperature, but they are essentially the same at 288°C. The authors reported no J_{Ic} values, but the curves shown in Fig. 8.7 appear to show much higher values than reported by James and Carlson (1985). Fig. 8.8 shows K_{Jc} data from Yoon and Yoon with T_0 values of -68 and -72°C for the PCVN and half-size PCVN specimens, respectively.

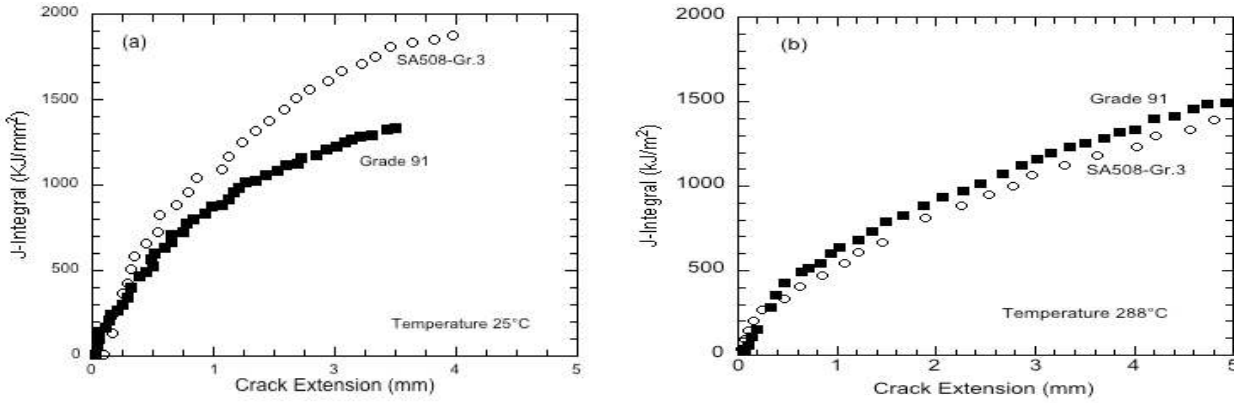

Figure 8.7. Comparison of the J-R curves between Grade 91 and SA508-Gr.3 at (a) RT and (b) 288°C (Yoon and Yoon, 2006).

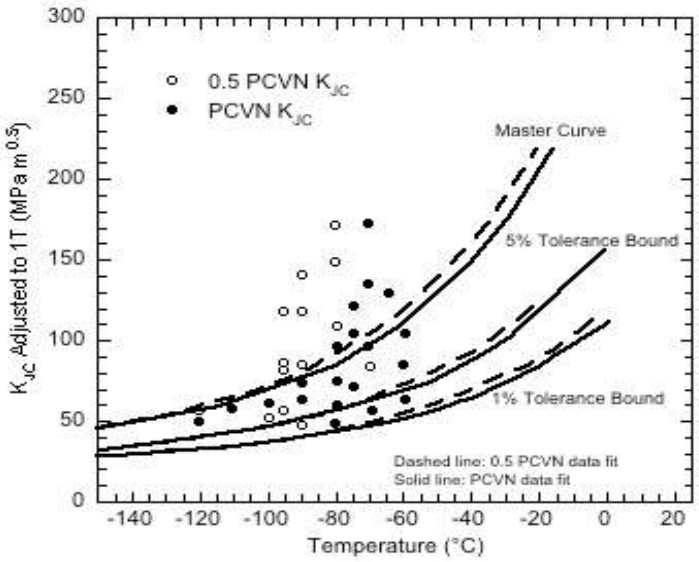

Figure 8.8. Master curve for Grade 91 obtained using the PCVN and 0.5PCVN specimens (Yoon and Yoon, 2006).

Sasikala and Ray (2008) tested a 12-mm thick normalized and tempered grade 91 steel plate, using 0.4T compact specimens. Tests were conducted at 27, 380, and 530°C. At 27°C, they determined a conservative value for J_{Ic} of 290 kJ/m^2, and J_{Ic} values of 460 and ≈700 kJ/m^2 at 380 and 530°C, respectively. Interestingly, they reported the specimen tested at 380°C exhibited a substantial crack pop-in of about 0.2 mm. These J_{Ic} values are similar to those inferred from the data shown in Fig. 8.7 by Yoon and Yoon (2006).

In another experimental study, Sathyanarayanan et al. (2008) performed impact tests of PCVN specimens of grade 91 steel with enhanced phosphorus content to determine a dynamic T_0, T_0^{dy}, They determined a T_0^{dy} of 14°C, compared to a value of -52°C for a heat of plain 9Cr-1Mo steel. They attributed the high T_0^{dy} value of the phosphorus-enhanced grade 91 to segregation of P along the grain boundaries, observations which were supported by scanning electron fractography.

Zhu et al. (1991) also used instrumented impact tests of PCVN specimens to determine J_{Id} and K_{Id} values at 20, 200, and 650°C. Various methods for calculating JId were used, including the stretch zone width method (SZW) of Kobayashi (1984). From the SZW method, JId values of 102, 82, and 54 kJ/m2 were calculated at 20, 200, and 650°C, respectively. These values were calculated based on the assumption that crack initiation begins at a load which is the average of yield and maximum loads.

Figure 8.9 (Klueh and Harries 2001) shows fracture toughness J_{Ic} and tearing modulus (T) data for grade 91 steel in the unirradiated condition and in three irradiated conditions. The unirradiated data are indicated by the open symbols. Values of J_{Ic} average about 70 kJ/m^2 for tests from room temperature to 400°C. At the highest temperatures, the J_{Ic} values decreased about 50% relative to the unirradiated values, while the tearing modulus decreased by more than a factor of two. The J_{Ic} values do not appear to decrease with increasing dose, although the amount of data is small with which to make a definitive judgment. It is clear from the data dis-

cussed in the review of Klueh and Harries (2001) that the effects of irradiation on the ductile fracture toughness of F-M steels is quite varied and deserves considerable attention.

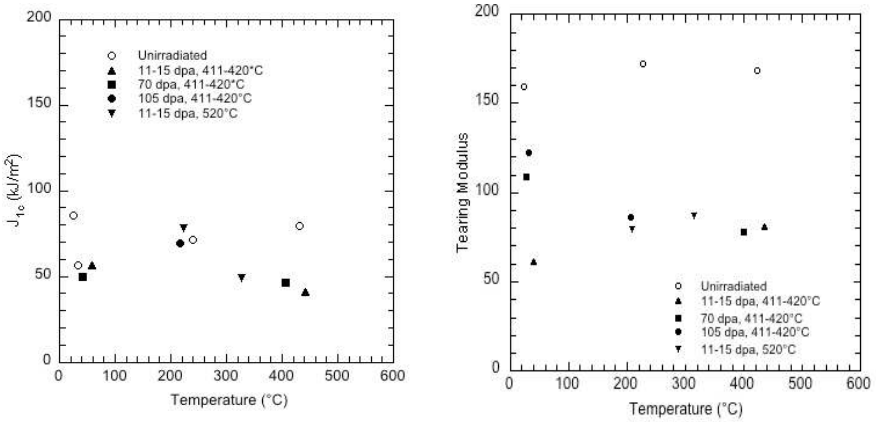

Figure 8.9. The (left) fracture toughness and (right) tearing modulus of modified 9Cr-1Mo steel irradiated in FFTF to doses as high as 105 dpa, and tested at temperatures from room to about 425°C.

Nanstad et al. (2007) tested a 9Cr-1Mo-V steel in the annealed condition with various types and sizes of specimens to evaluate the potential loss of constraint that results in a T_0 bias often observed with PCVN specimens of LWR RPV steels (Nanstad et al. 2007). Figure 8.10 shows data from testing of compact specimens from 0.2 to 1T size compared with data from 0.2T bend and PCVN specimens. As shown, the Master Curve fit to all the data gives a T_0 value of -25.4°C; T_0 values of -30 and -25°C were determined with the 1TC(T) and PCVN specimens, respectively. Thus, the results for the annealed grade 91 steel exhibit a T_0 42°C higher than that for the normalized and tempered material tested by Yoon and Yoon (2006).

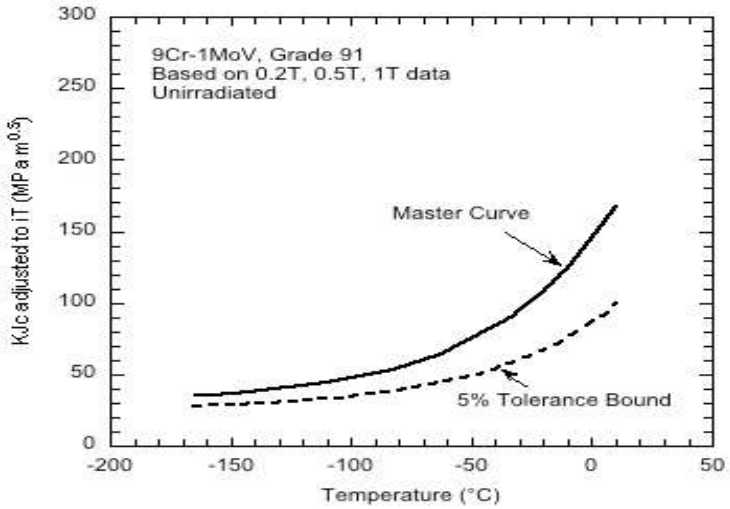

Figure 8.10. Fracture toughness, K_{Jc}, values adjusted to 1T size for 9Cr-1MoV steel in annealed condition. The overall T_0 value is -25.4°C with all specimen types giving the same T_0 within 2°C (Nanstad et al. 2007).

8.3 ASME Code

Steels with lower chromium than the 9Cr steels discussed above also present an option for application in structural components. Standard 2.25Cr-1Mo (grade 22) is approved for high temperature application in subsection NH of the ASME Code. There is considerable experience with this steel in the petrochemical and power-generation industries. Grade 22 steel is a relatively low strength material, but there are other similar low Cr steels available with higher strength,

although they are not included in Subsection NH. An advanced 2.25C-1.6WVNb steel (Grade 23), however, is approved in Section VIII of the Code. Grade 23 has elevated-temperature strength approaching that of some of the high-chromium steels. Grade 24 (2.25Cr-1MoVTi) is stronger than the Grade 22, but not as strong as Grade 23. There are also steels with a base composition of 3Cr-3W-0.25V-0.1C (3Cr3WV) that have elevated-temperature strength with a bainitic microstructure and a high number density of fine, needle-like MX precipitates in the matrix. A version with 0.07 wt% Ta further improves strength and toughness. The strength properties of these steels exceed those of Grades 23 and 24.

For 2.25Cr-1Mo steel, an example of J-R fracture toughness at 250°C is shown in Fig. 8.11 (Bryan, et. al., 1987). The material was specially heat treated, but did have yield strength typical of grade 22. The fracture toughness tests were performed with 1T compact specimens (25-mm thick) and the specimens were tested with 10% side-grooves on each side.

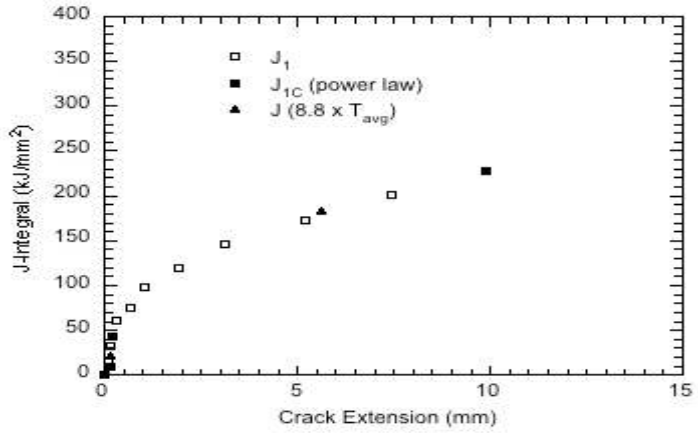

Figure 8.11. J-integral vs crack extension results at 250°C for specially heat treated 2.25Cr-1Mo (yield strength of 270 MPa at room temperature).

Figure 8.12 shows the effect of test temperature on the same material from 100 to 250°C (Bryan et al. 1987). As shown in the figure, the higher temperatures result in substantially lower J-R curves. For the tests shown at 100, 175, and 250°C (average of four tests at each temperature), the J_{Ic} values were 80, 50, and 35 kJ/m^2, respectively. Similarly, the tearing modulus values were 95, 75, and 51, respectively. Thus, the increasing temperature caused significant decreases in both the ductile fracture toughness initiation, J_{Ic} and the tearing resistance as indicated by the tearing modulus.

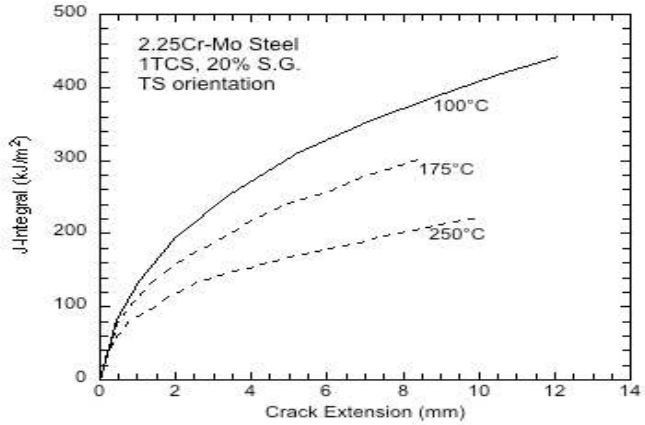

Figure 8.12. J-integral vs crack extension results at 100, 175, and 250°C for specially heat treated 2.25Cr-1Mo (yield strength of 270 MPa at room temperature). The results demonstrate a significant loss of tearing resistance with increasing temperature.

There are no data at elevated temperatures for some of the advanced Cr-Mo steels, e.g., NF616, 3Cr3WV, etc., although there is fracture toughness testing currently underway in the AFCI Structural Materials Program.

8.4 Issues and Resolutions

It is not clear which components and materials may require fracture toughness data in LMR application. For pressurized components, transition range fracture toughness data are needed for heat-up and cool-down transients. At operating temperatures, however, ductile fracture toughness, J_{Ic} and tearing modulus, are needed. It is clear that there are insufficient fracture toughness data for all potential Cr-Mo steels in the elevated temperature regime in which the LMR would operate. Development of such data at temperatures to 500-600°C in the unirradiated condition and in an air environment would not represent a major effort for even a few different materials. However, obtaining such data for the materials as-irradiated and in a liquid sodium environment would represent a major effort in terms of both funding and time. In addition to the need for data on base metal, welds and heat-affected-zones are at least as important. Moreover, research to develop a more complete understanding of the mechanisms, thermal, irradiation, and chemical based, would help provide additional bases for material selection and for long term predictability.

9. ASME CODE ACTIVITY ON NEGLIGIBLE CREEP

9.1 Categories of Negligible Creep Criteria

Jetter et al. (2009) have recently conducted a study on the impact of material and design criteria on the assessment of negligible creep. They have investigated three categories of negligible creep criteria. The first criterion is based on the limits of applicability of a particular section of the ASME Section III code. This corresponds to the temperature transition, 370ºC for ferritics and 427ºC for austenitics, from Subsection NB to Subsection NH.

The second criterion is based on allowable stress crossover. For primary stress limits, NH has criteria, which are based on both time independent properties, i.e. yield and tensile strength, and time dependent, creep properties. Although there are complications arising from the way in which calculated stresses are categorized for comparison with the tabulated allowable values, basically the transition is the temperature for a given design life where the allowable stress transitions from being governed by time independent to time dependent properties. This is a primary membrane stress-based criterion that is appropriate for wall-thickness sizing consideration.

The third criterion concerns with a more complex issue of creep effects on cyclic life. Cyclic life is governed by localized stresses. At gross and local structural discontinuities and accounting for general and local thermal stresses, the localized stress field can, and usually will, be significantly greater than the primary membrane stress. Because the stress is higher, for a given service life the onset of creep effects in these localized areas will occur at a lower temperature than is the case for primary stress fields. Currently in NH there are two considerations for the

assessment of negligible creep from the cyclic life perspective, creep-fatigue damage and strain limits or ratcheting.

In NH, creep-fatigue life is evaluated with a linear damage fraction summation given by:

$$\sum_j \left(\frac{n}{N_d} \right)_j + \sum_k \left(\frac{\Delta t}{T_d} \right)_k \le D \tag{9.1}$$

where n and N_d are the number of cycles of type j and the allowable number of cycles of the same cycle type, respectively; and Δt and T_d are the actual time at stress level k and the allowable time at that stress level, respectively. D is the allowable combined damage fraction. The time fraction in the above equation was used to assess negligible creep by estimating the maximum effective stress under cyclic loading and then calculating the creep damage due to that stress, conservatively assuming that the peak stress did not relax, e.g. creep is negligible. This leads to the first of two expressions for assessing negligible creep in NH:

$$\sum_i \frac{t_i}{t_{id}} \le 0.1 \tag{9.2}$$

where t_i is the duration of time that the metal is at temperature T_i and t_{id} is the allowable time at T_i as determined from the tabulated minimum stress-to-rupture values based on a stress given by $1.5S_y$ and S_y is the tabulated yield strength at T_i. In the above definition, the 1.5 factor times S_y is based on two considerations. First, there is a factor of 1.25 to account for the use of average properties to determine stress/strain history for Appendix T evaluations (NH-3214.2) and to be consistent with the definition of the isochronous stress-strain curves when using the results of elastic analysis. Next there is a factor of 1.2 to account for cyclic strain hardening. Note that this last factor, 1.2, may not be appropriate for cyclically strain softening materials.

Unlike the austenitic stainless steels, Mod. 9Cr-1Mo cyclically strain softens. Thus the use of a stress of $1.5S_y$ in entering the minimum stress-to-rupture curves would lead to an unrealistically low value of t_{id}, and at times, would render the breakdown of the entire procedure as instantaneous creep rupture would be predicted. Jetter et al. (2009) has generated the negligible creep curves for Mod. 9Cr-1Mo based only on Eq. (9.2) but for $s = 1,$ and 1.25, where $s \times S_y$ is the stress that enters the minimum stress-to-rupture curves. The plot is shown in Fig. 9.1. These curves have been constructed based on extrapolating the creep rupture data to 60 years.

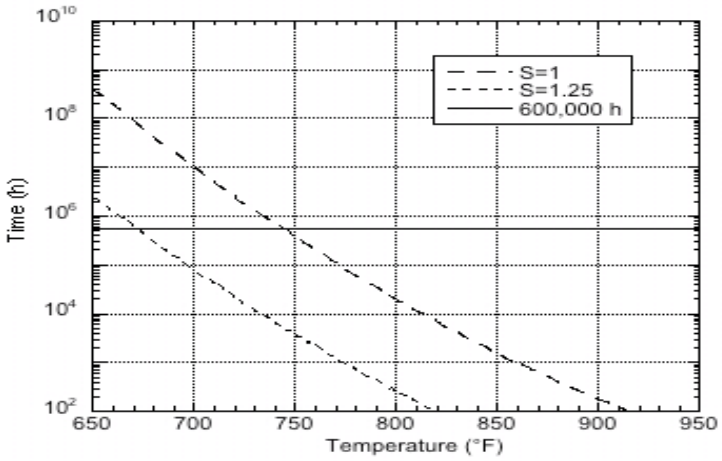

Figure 9.1. Negligible creep curves for Mod. 9Cr-1Mo based only on the time-fraction criterion (Jetter et al. 2009).

On the basis that Mod. 9Cr-1Mo cyclically strain softens, use of the $s=1$ curve is considered appropriate. Note that this conceptually corresponds to a 20% reduction in stress due to cyclic strain softening from an average stress given by $1.25S_y$.

The second expression in NH is conceptually based on satisfying the strain limits using simplified inelastic analysis (T-1330). The T-1330 rules are based on an elastic core stress which has a maximum value given by the average yield strength, $1.25S_y$. The creep strain at this stress is limited to 1%. For creep to be considered negligible, the creep strain is then limited to 0.2%, approximately the same as the inelastic strain at yield. This leads to the second expression for assessing negligible creep in NH:

$$\sum_i \varepsilon_i \le 0.2\% \tag{9.3}$$

where ε_i is the creep strain that would be accumulated at a stress level of $1.25S_y$ applied for the time duration that the metal is at T_i. Although NH does not provide explicit guidance for determination of creep strain, the strain due to creep may be determined from the isochronous stress-strain curves by entering them at a stress of $1.25S_y$ for the applicable time duration and then subtracting out the elastic plus plastic strain form the hot tensile curve at the same stress.

9.2 Issues and Resolutions

9.2.1 Time-Fraction Criterion

Cyclic stress-strain curves in the temperature range where negligible creep occurs provide important information on the selection of the stress value in the construction of the negligible creep curves. The time-fraction calculation depends on creep rupture data. Thus the construction of negligible creep curves for a component life of 60 years would engender the same issues as identified in Section 5 on the extrapolation of creep rupture data to 60 years.

9.2.2 Strain Criterion

The purpose of the third negligible creep criterion discussed in the previous sections is to render the effect of creep on the fatigue performance to be insignificant. This means that the fatigue rules in Subsection NB can be used with confidence to design components for cyclic service when the temperatures are below the negligible creep curve. In the creep-fatigue procedure of Subsection NH, the strain range, ε_t, that is employed to enter the fatigue curve is given in Paragraph T-1432 of Subsection NH as

$$\varepsilon_t = K_v \Delta\varepsilon_{\text{mod}} + K\Delta\varepsilon_c \tag{9.4}$$

where K_v is the multiaxial plasticity and Poisson ratio adjustment factor, $\Delta\varepsilon_{\text{mod}}$ is the modified maximum equivalent strain range, K is the local geometric concentration factor, and $\Delta\varepsilon_c$ is the creep strain increment. Thus the strain range is influenced by creep, as indicated by the term $K\Delta\varepsilon_c$. Currently, there is no restriction on the magnitude of this creep contribution in the negligible creep criterion of Subsection NH. Addition of such a requirement is necessary in order remove this potential non-conservatism in the negligible creep criterion of Subsection NH. This issue is being considered by a task force on negligible creep criteria sponsored by the Subgroup on Elevated Temperature Design, which is under the Boiler and Pressure Vessel Committee on Construction of Nuclear Facility Components of the ASME Broad on Nuclear Codes and Standards.

10. ASME CODE ACTIVITY ON CREEP-FATIGUE EVALUATION

A three-year collaboration between DOE and ASME was established in 2006 that addressed topics in support of an industrial stakeholder's application for licensing of a Generation IV nuclear reactor. Tasks 3 and 5, which had been concluded, focused on the creep-fatigue procedure, within the time-fraction framework of Subsection NH. The overlaps of these two tasks were intended to bring different international perspective on Subsection NH. Natesan et al. (2008) had summarized the objectives of these two task efforts:

Task 3:

- Compare the Subsection NH and RCC-MR creep-fatigue procedures for Mod. 9Cr-1Mo steel.
- Explore the extent to which data for Mod. 9Cr-1Mo presently available in Subsection NH and RCC-MR are thought to be validated.
- Recommend improvements to existing Subsection NH creep-fatigue procedure for Mod. 9Cr-1Mo steel.
- Define a test program to validate the improved creep-fatigue procedure for Mod. 9Cr-1Mo steel.

Task 5:

- Collect creep, creep-fatigue and fatigue (when available) data for Mod. 9Cr-1Mo in air, vacuum, and sodium environment.

- Evaluate creep-fatigue procedures from Subsection NH, RCC-MR, and the Japanese high temperature design code.

A new Task 10 was initiated in 2008 as a follow-on task to continue the development of creep-fatigue code rules. The objects of Task 10 were:

- Review creep-fatigue methodologies, including damage-based, strain-based, and methods not involving separate accounting of creep and fatigue damage in various design codes.
- Assess procedures and relevant literature.
- Assess the potential of deploying these methods in Subsection NH either to remove excessive conservatism or to resolve NH issues identified by the U.S. Nuclear Regulatory Commission.
- Provide rationale and propose implementation strategies for these methods, where applicable.
- Propose methods to address the effects of aging, surface conditions, and geometric discontinuity.
- Recommend requisite requirements for codification, including data generation, data extrapolation strategies, and feature testing to validate methods.

The creep-fatigue methodologies examined in Task 10 include:

- Modified ductility exhaustion method from Takahashi (2008)
- Modified strain range separation method from Hoffelner (2009)
- Omega-based creep-fatigue method from Prager (2009)
- Hybrid method of time-fraction and ductility exhaustion from the High Pressure Institute of Japan (2005)
- Simplified model test approach from Jetter (2009)

Majumdar et al. (2009) have briefly summarized the technical background of each of these methods. These five creep-fatigue methodologies have been applied to Mod. 9Cr-1Mo by Asayama (2008) with respect to the task objectives listed above. This task is at the stage of completion.

11. RECOMMENDED RESEARCH AND DEVELOPMENT

We have performed an in-depth assessment of the technical issues involved with the current materials such as Type 304 and 316 austenitic stainless steels and ferritic steels such as 2.25Cr-1Mo and 9Cr-1Mo. In Table 11.1, we have listed the technical issues, approach for the resolution of those issues, and the priority among the issues for conducting needed research for resolution.

Table 11.1. A listing of technical issues, resolution approach, and priority for resolution

Technical Issue	Resolution Approach	Priority
Creep-fatigue predictive mod-	• Develop an updated creep-fatigue database	High

els and design rules for the 60-year reactor lifetime	for each NH material to include the data generated from previous DOE programs and available in recent literature. The quality of the data will be assessed in terms of material composition, product form, thermo-mechanical treatment, specimen type and location, testing techniques, testing conditions, environment control, and availability of raw data. • Develop creep-fatigue predictive models and design rules for the 60-year design life using the updated database. • Perform confirmatory tests to validate models	High High
Extrapolation of laboratory short-term hold time data to long-term hold time behavior under actual reactor conditions	• Perform (interrupted) creep-fatigue tests with sufficiently long hold times to determine the saturation limit of the hold time and to analyze the stress relaxation behavior and its correlation with microstructure and damage development. • Construct creep-fatigue mechanism maps for NH materials using mechanism-based constitutive equations. • Develop a mechanistic approach to the prediction of creep-fatigue lifetime and failure mode for reliable data extrapolation.	High High High
	• Develop accelerated testing techniques to accurately assess creep-fatigue behavior in relatively short time periods and in simulated reactor operating conditions.	Medium
Applicability of linear damage rule to creep-fatigue with significant environmental effects	• Establish a proper database for ferritic steels that can be applied to validate the creep-fatigue linear damage rule. • Creep-fatigue data that involve significant environmental effect should be treated with a creep-fatigue-oxidation model that incorporates the environment-assisted and/or – enhanced creep-fatigue interaction.	Medium Medium
Reliable creep-fatigue design rule for G91	• Perform creep-fatigue tests at selected test temperatures and hold times to obtain stress relaxation data to validate/improve the current creep-fatigue diagram	High
	• Perform low-strain range, long-term tensile hold time tests at 550°C in air to determine if intergranular cavitation occurs during a sufficiently long hold time	Medium

	• Perform creep-fatigue tests in protective environments to provide proper data for creep-fatigue linear damage rule modeling	High
	• Perform interrupted creep-fatigue experiments to characterize cyclic softening and stress relaxation behavior and accompanied microstructural changes. • Develop mechanistic predictive models of creep-fatigue interaction that incorporate cyclic softening effects.	Medium High
	• Compare cyclically softened materials with thermally aged material, and produce cyclically softened microstructure by thermal aging for mechanical property testing. • Perform tensile and creep tests of specimens with cyclically softened microstructure to understand the effect of cyclic softening on creep and load carrying capability for the design against accidental events.	High High
Data needs on creep-fatigue of weldments	• Perform creep-fatigue tests of 316 SS weldments at 550°C with long hold times	Medium
	• Perform creep-fatigue tests on mod.9Cr-1Mo steel weldments with various welding parameters. Tests should include different test temperatures and hold times. Attention should be paid on Type IV cracking. • Establish "Microstructure Atlas" of mod.9Cr-1Mo weldments with correlation between microstructure and mechanical properties to understand Type IV cracking	High Medium
	• Perform creep-fatigue tests of 2.25Cr-1Mo steel weldments at 550°C with focus on Type IV cracking.	Low
Develop improved creep-fatigue design rules of weldments	• Establish a database of creep-fatigue for weldments • Develop improved creep-fatigue rules of weldments	Medium Medium
Thermal aging effects on design allowables for the 60-year design life	• Perform thermodynamic and kinetic modeling of microstructural evolution during thermal aging with experimental validation to develop a better understanding of the thermal aging effects for reliable data extrapolation to the 60-year design life. Areas include precipita-	High

	tion and coarsening kinetics and synergistic effects of thermal aging and mechanical loading. • Develop mechanistic models to correlate microstructural changes with associated mechanical properties during long-term thermal aging. Perform confirmatory tests of aged and cyclic-softened materials to validated the models	High
	• Collect long-term thermally-aged, long-term creep-tested specimens for detailed microstructural characterization to construct "Microstructure Atlas" of long-term aged materials and correlation between microstructure and mechanical properties • Develop strength reduction factors for times to 600,000 h	Medium Medium
	• Develop accelerated testing techniques to accurately assess material behavior in relatively short time periods and in simulated reactor operating conditions. These techniques need to be based on improved understanding of thermal aging effects and mechanistic models	High
Incorporation of thermal aging effects in creep-fatigue design rules	• Establish a creep-fatigue database of thermally-aged materials • Perform additional testing to better understand the thermal aging effects on creep-fatigue damage, particularly for cyclic softened materials such as ferritic steels. • Develop an improved creep-fatigue design methodology incorporating the material's softening behavior. • Perform confirmatory tests to validate the improved design rules.	High High Medium Medium
Long-term thermal aging effects on weldments	• Characterize microstructure of thermally aged or creep-tested mod.9Cr-1Mo steel weldments. • Material currently in service should also be characterized if possible for comparison with laboratory data.	High Medium
	• Perform thermodynamic and kinetic modeling of microstructural evolution under dynamic welding processes with experimental validation. • Perform tensile, toughness, creep on speci-	High Medium

	mens with simulated microstructure • Mapping of microstructure in the HAZ and their associated tensile properties to provide valuable information in understanding weldment cracking under mechanical and thermal loading.	High
	• Establish a creep-fatigue database of thermally-aged weldments • Perform additional creep-fatigue tests on weldments to fill data gaps • Incorporate aging effects in creep-fatigue design rules for weldments.	Medium Medium Medium
Development of improved unified viscoplastic constitutive equations	• Develop improved evolution equations for back stresses and drag stress to more accurately model uniaxial and multiaxial ratcheting, cyclic hardening/softening, and thermal aging behaviors of 316 stainless steel and Mod. 9Cr-1Mo. Initial modeling efforts will be based on existing literature data. • Develop recommendations for further testing and application.	High Medium
	• Develop mechanistically motivated unified viscoplastic constitutive equations by establishing linkage between deformation mechanisms and state variables of constitutive models. Initial modeling efforts will be based on existing literature data. • Develop recommendations for further testing and application.	Medium Medum
Development of Mechanisms-based finite element methodologies for predicting creep rupture for materials with 60-year design life	• Develop micromechanical finite element methods to incorporate effects of grain boundary (GB) cavities, GB diffusion, grain deformation by creep, and GB sliding. • Develop a mechanisms-based methodology for constructing creep fracture maps by using results from micromechanical finite element analyses and existing creep rupture data. • Develop recommendations for further testing and application.	High High Medium
Assessment of the limitations of the *C** parameter in characterizing creep fracture and development of improved creep crack growth procedures in design codes and assess-	• Perform critical evaluation of C* parameter relative to C_t parameter and other available parameters, with recommendations for further R&D emphasis and application.	Medium

ment guidelines.		
Transferability of creep crack growth from laboratory results to structural components.	• Establish a set of criteria for application of creep crack growth to structural components that are analogous to the stringent validity requirements of E1457. • It is important to provide criteria for the onset of accelerated, tertiary creep crack growth in design codes and assessment guidelines, analogous to the use of onset of third stage creep as one of the criteria in setting the time-dependent stress limit in the ASME B&PVC, Sect. III, Subsection NH.	Medium Medium
Empiricism in the creep-fatigue crack growth approach to crack growth calculations.	• Perform experiments and modeling studies necessary to advance understanding and quantification of the interaction between FCG and CCG and the development of a practical methodology to perform crack growth calculations. • Plan and coordinate experimental research activities with those for creep-fatigue.	Medium Medium
Crack growth database for G91 and its associated weldments.	• Perform experiments to obtain data from lower temperatures than those used in the SOTA and HIDA programs. • Plan and coordinate experimental research activities with those for creep-fatigue. • Obtain access to the SOTA and HIDA raw data in terms of load-line displacement and potential drop records in order to evaluate other, potentially more relevant crack-tip characterizing parameters. Otherwise, new data would have to be generated. • It is important to generate crack growth data from the type of welds anticipated for the LMR components and the type of welding process and post-weld treatment that would have to be used in the field due to manufacturing related constraints. • Perform scoping experiments to obtain creep and creep-fatigue crack growth data in sodium to assess if there is any deleterious environment effect that would accelerate the crack growth rate	High Medium High Medium Medium
Fracture toughness data for ferritic steels; G22, G91.	• Develop transition range fracture toughness data for materials to be used for pressurized components subjected to heat-up and cool-down transients.	Medium

	• For all ferritic steels, develop ductile fracture toughness, J_{Ic}, and tearing modulus data at operating temperatures in an air environment.	Medium

12. SUMMARY

The AFCI program has selected a sodium-cooled reactor concept for actinide burning, commercial demonstration and superior safety and reliability of next-generation advanced reactors. Advanced materials are one of the key elements in advancing sodium reactor technology. Several conceptual designs have been proposed, and all these reference design concepts favor austenitic stainless steels and ferritic/martensitic steels for the structural applications. Advanced materials are a critical element in the development of sodium reactor technologies. Enhanced materials performance not only improves safety margins and provides design flexibility, but also is essential for the economics of future advanced sodium reactors.

Qualification and licensing of advanced materials are prominent needs for developing and implementing advanced sodium reactor technologies. However, the development of sufficient database and qualification of these materials for application in LMRs require considerable amount of time and resources. In the meantime, the currently available materials will be used in the early development of fast reactors. So far only five materials are qualified for use in elevated-temperature nuclear structural components, including Type 304 SS, Type 316 SS, 2.25Cr-1Mo steels, mod.9Cr-1Mo steel, and Alloy 800H. Though there is extensive database and industrial experience with Type 304 and Type 316 austenitic stainless steels and 2.25Cr-1Mo and mod.9Cr-1Mo ferritic steels, there are still several technical issues that need resolution in a timely manner.

The present report addresses several key technical issues for the currently available materials for structural applications in LMRs. The 60-year design life for the LMR presents a significant challenge to the development of database, extrapolation/prediction of long-term performance, and high temperature structural design methodology. The current Subsection NH is applicable to the design life only up to 34 years. No experimental data contain test durations of 525,000 hours, and it is impractical to conduct such long-term tests in any types of testing. So far the longest creep tests for Grade 91 and Grade 92 steels have run up to 100,000 hours. It has been noted that there is a large drop in creep rupture strength in long-term tests for these high-Cr creep-resistant steels, which may result in overestimation of the long-term creep strength and allowable stress. The report addresses in detail the need for a mechanistic understanding of the structural materials, from the standpoint of the effects of thermal aging, creep deformation, creep fracture, fatigue and creep-fatigue, creep-fatigue predictive models, fatigue and creep crack growth, and fracture toughness. Based on an in-depth assessment of the available data and mechanistic understanding, key technical issues are identified and discussed for each of the property areas. Furthermore, we have proposed viable approaches to resolve the issues and prioritized our recommendations.

13. REFERENCES

Adefris, N.B., A. Saxena, and D.L. McDowell, 1996, Fatigue and Fracture of Engineering Materials and Structures 19, No. 4, 401-411.

Aktaa, J. and C. Petersen, 2009, Eng. Fract. Mech. 76, 1474.

Aktaa, J. and R. Schmitt, 2006, Fus. Eng. Des. 81, 2221.

Aktaa, J., M. Weick and C. Petersen, 2009, J. Nucl. Mater. 386-388, 911.

Albert, K., M. Matsui, T. Watanabe, H. Hongo, K. Kubo, and M. Tabuchi, 2002, ISIJ Int. 42 1497.

American Society for Metals, 1985, Metals Park, OH, 149-177.

Ancelet, O. and S. Chapuliot, 2008, Proceedings of the Eighth International Conference on Creep and Fatigue at Elevated Temperatures, American Society of Mechanical Engineers, New York, NY, CREEP2007-26192.

ANL-ABR-1, 2006, "Advanced Burner Test Reactor Preconceptual Design Report," Argonne National Laboratory report ANL-AFCI-173.

Asayama, T., 2008, Task 10: Update and Improve Subsection NH – Alternative Simplified Creep-Fatigue Design Methods, DOE/ASME Gen IV Materials Project administered by ASME ST LLC.

Ashby, M.F., C. Gandhi, and D. M. R. Taplins, 1979, Acta Metallurgica, Vol. 27, pp. 699-729.

ASTM, 1981, Standard Test Method for J_{IC}, a Measure of Fracture Toughness, E813-81, *Annual Book of ASTM Standards,* Vol. 03.01, American Society for Testing and Materials.

ASTM, 2002, Standard Test Method for Plane-Strain Fracture Toughness of Metallic Materials, E399, *Annual Book of ASTM Standards*, Vol. 03.01, ASTM International.

ASTM, 2005, Standard Test Method for Determination of Reference Temperature, T_o, for Ferritic Steels in the Transition Range, E1921-02, *Annual Book of ASTM Standards*, Vol.03.01, ASTM International.

ASTM, 2005, Standard Test Method for Measurement of Fracture Toughness, E1820, *Annual Book of ASTM Standards*, Vol. 03.01, ASTM International.

ASTM, 2008, Standard Test Method for Measurement of Fatigue Crack Growth Rates, E647, *Annual Book of ASTM Standards*, Vol. 03.01, ASTM International.

Bassani, J.L. and F.A. McClintock, 1981, International Journal of Solids and Structures **17**, 479-492.

Bassani, J.L., D.E. Hawk, and A. Saxena, 1989, Nonlinear Fracture Mechanics: Volume I-Time-Dependent Fracture, ASTM STP 995, eds. A. Saxena et al., American Society for Testing and Materials, Philadelphia, PA, 7-26.

Berling, J.T. and J.B. Conway, 1969, 1st International Conference on Pressure Vessel Technology, Delft, p. 1233.

Berling, J.T. and T. Slot, 1969, in Fatigue at High Temperature, ASTM STP 459, American Society for Testing and Materials, p.3.

Bhanu, K., M. Valsan, S.L. Mannan, 1990, Mater. Sci. Eng., A 130, 67.

Bicego V, Bontempi P, Mariani R, Taylor N, 1998, in 'Materials for advanced power engineering 1998', Proceedings of the 6th Liege Conference, Volume 5, Part 1.

Blass, J.J., R.L. Battiste and D.G. O'Connor, 1991, "Reduction Factors for Creep Strength and Fatigue Life of Modified 9Cr-1Mo Steel Weldments," CONF-910602-16.

Booker, M.K. and S. Majumdar, 1982, A review of time-dependent fatigue behavior and life prediction for 2.25Cr-1Mo steel, CONF-820121-2.

Brinkman, C. R., 1980, "Creep-fatigue effects in structural materials used in advanced nuclear power generating systems." CONF-800741-1.

Brinkman, C. R., 1985, "Influence of Tempering Temperature on the Continuous-Cycle Fatigue Behavior of Modified 9Cr-1Mo Steel," pp. 5-12-13 in Mechanical Properties Design Data Program Anneal Progress Report for Period Ending January 31, 1985, ORNL/LMR/IMM-85/3.

Brinkman, C. R., J. P. Strizak, and M. K. Booker, 1980, "The Influence of Environment, Metallurgical Variables, and Prolonged Test Times on the Fatigue and Creep-Fatigue Behavior of Annealed 2-1/4Cr-1Mo Steel," Oak Ridge National Laboratory Report ORNL-5625.

Brinkman, C. R., M.K. Booker, J.P. Strizak, and T. Weerasooriya, 1978, "Fatigue behavior of 2.25Cr-1Mo steel in support of steam generator development," CONF 781177-1, ORNL report.

Brinkman, C.R, J.P. Strizak, and J.F. King, 1970, "Elevetated-temperature fatigue characteristics of transition joint weld metal and composite material in support of LMFBR Steam Generator Development," CONF-770524-3.

Brinkman, C.R., 2001, "Elevated Temperature Mechanical Properties of an Advanced Type 316 Stainless Steel," Journal of Pressure Vessel Technology, Vol. 123, No. 1, pp. 75-80.

Brinkman, C.R., D.J. Alexander, and P.J. Maziasz, 1990, "Modified 9Cr-1Mo Steel for Advanced Steam Generator Applications," presented at the Joint ASME/IEEE Power Generation Conference, Boston, MA, October 21-25.

Brinkman, C.R., G.E. Korth and J.M. Beeston, 1973, "Comparison of the strain-controlled low cycle fatigue behavior of stainless type 304/308 weld and base material," Proc. Inter. Conf. Creep & Fatigue in Elevated Temperature Applications, Inst. Mech. Eng., London.

Brinkman, C. R., G. E. Korth and R . P. Hobbins, 1972, Nucl. Tech. 16, 299.

Brinkman, C. R., J. P. Strizak, M. K. Booker and C. E. Jaske, 1976, J. Nucl. Mater. 62, 181.

Bryan, R. H., et al, 1987, "Pressurized-Thermal Shock Test of 6-in.-Thick Pressure Vessels. PTSE-2: Investigation of Low Tearing Resistance and Warm Prestressing," Oak Ridge National Laboratory, NUREG/CR-4888 (ORNL-6377).

Burke, J. and V. Weiss, 1983, in Fatigue Environment and Temperature Effects, New York, Plenum, p. 241.

Burlet, H., and G. Cailletaud, 1986, "Numerical Techniques for Cyclic Plasticity at Variable Temperature," Engineering Computation, Vol. 3, pp. 143-153.

Cabrillat, M. T., M Mottot. C Escaravage. L Allais. B Riou, 2006, Creep fatigue Behavior and damage assessment for Mod 9 Cr-1 Mo steel–PVP2006-ICPVT11-93238–Proceedings of PVP200- ICPVT11-2006 ASME Pressure Vessels and Piping Division Conference.

Cailletaud G. and J. L. Chaboche, 1982, Proc. ASME-PVP Conference, Orlando, Florida, June 27-July 2, ASME paper No. 82-PVP-79.

Cailletaud, G., Kaczmarek, H., and Policella, H. (1984). Mech. Mat., 3:333–347.

CEA-DMN/SRMA/LC2/NT/2004-2613/A –Durée de vie en fatigue des aciers 9Cr-1Mo. Interaction fatigue-fluage -.Avancement des Etudes au 01/01/2004.

CEA-N.T. SRMA 92-1984 November 1992 F.A. 5513-4830 rev. 0 –Fatigue Relaxation A 550°C d'un acier 9Cr1Mo Nb V (9Cr 1Mo modifié).

Chaboche, J.L, 1989, International Journal of Plasticity, Vol. 5, pp. 247-302.

Chaboche, J.L, and D. Nouailhas, 1989, Journal of Engineering Materials and Technology, Vol. 111, pp. 424-430.

Chaboche, J.L., K. Dang Van, and G. Cordier, 1979, SMiRT 5 Transactions, Vol. L, Berlin.

Challenger, K. D., A. K. Miller, and C. R. Brinkman, 1980, Progress Report to the U.S. Department of Energy, SU-DMS-80-R-2.

Challenger, K.D., A. K. Miller and C.R. Brinkman, 1981, Trans. ASME, J. Eng. Mater. Tech. 103.

Chaswal, V., G. Sasikala, S.K. Ray, S.L. Mannan, B. Raj, 2005, Mater. Sci. Eng. A395, 251.

Chuang, T.-J., K.I. Kagawa, J.R. Rice and L.B. Sills, 1979, Acta Metallurgica, 27, 265-284.

Coffin, L.F., 1976, Symp. On Creep-Fatigue Interaction, ASME MPC-3, R. M. Curran, Ed., American Society of Mechanical Engineers, New York, pp. 349-363.

Coffin, L.F., Jr, 1977, in Time-dependent Fatigue of Structural Alloys, Oak Ridge National Laboratory, ORNL-5073.

Corum, J.M., 1990, J. Pres. Ves. Tech. 112, 333.

Cumino, G., S. Di Cuonzo, A. Di Gianfransesco, and O. Tassa, 2002, Lat. Am. Appl. Res. 32.

Dawson, R. A. T., W. J. Elder, G. T. Hill and A. T. Price, 1967, International Conference on Thermal and High Strain Fatigue, London, England, Pergamon Press, p. 40.

Diercks, D. R., 1975, Advances in Design for Elevated Temperature Environment, American Society of mechanical Engineers, New York, pp. 29-38.

Distefano, J. R. and V. K. Sikka, 1986, Summary of Modified 9Cr-1Mo Steel Development Program 1975-1985, ORNL-6303.

DiStefano, J.R., V. K. Sikka, et al., 1986, Summary of Modified 9Cr-1Mo Steel Development Program: 1975-1985, ORNL-6303.

Dogan, B. and B. Petrovski, 2001, International Journal of Pressure Vessels and Piping 78, 795-805.

Don, J. and S. Majumdar, 1986, "Creep Cavitation and Grain Boundary Structure in Type 304 Stainless Steel," Acta Metall. Vol. 34, No. 5, pp. 961-967.

Drubay, B. et al., 2003, International Journal of Pressure Vessels and Piping 80, 499-526.

Dyson, B. F., 1976, Metal Science, Vol.10, pp. 349-353.

Ehlers, R. and H. Riedel, 1981, Advances in Fracture Mechanics, Proceedings of ICF5, Vol.2, eds. D. Francois et al., Pergamon Press, New York, NY, 691-698.

Ellis, F. V. and R. Viswanathan, 1998, Proc. Int. Conf. on Integrity of high-temperature welds, Inst. Mech. Eng, p. 125.

Ermi, A. M. and J. Moteff, 1982, Met. Trans. 13A, 1577.

Fields, R. J., T. Weerasooriya, and M. F. Ashby, 1980, Metallurgical Transaction A, Vol. 11A, pp. 333-347.

Fournier, B. M. Sauzay, C. Caes, M. Mottot, M. Noblecout, and A. Pineau, 2006, Mater. Sci. Eng. A 437, 197.

Fournier, B., M. Sauzay, C. Caes, M. Noblecout, V. Rabeau, A. Bougault, and A. Pineau, J Nuclear Materials, 386-388 (2009) 418.

Furuya, K., N. Nagata and R. Watanabe, 1980, J. Nucl. Mater. 89, 372.

Gieseke, B. G., C.R. Brinkman and P.J. Maziasz, 1993, Microstructures and Mechanical Properties of Aging Material, The Minerals. Metals & Materials Society.

Goyal, S., R. Sandhya, M. Valsan, K. B. S. Rao, 2009, Inter. J. Fatigue 31, 447.

Halford, G. R., J. F. Saltsman, and M. H. Hirschberg, 1977, Proc. Conf. on Environmental Degradation of Engineering Materials, V.P.I. & State University, Blacksburg, VA, pp. 599-612.

Hassan, T., and S. Kyriakides, 1994, International Journal of Plasticity, Vol. 10, No. 2, pp. 149-184.

Hecht, R. L. and J. R. Weertman, 1998, Metall. Mater. Trans A 29A, 2137.

High Pressure Institute of Japan, 2005, Report: HPIS C107 TR 2005.

Hoffelner, W., 2009, in PVP 2009 Conference Proceedings, paper PVP2009-77705, ASME, New York, NY.

Horak, J. A., V. K. Sikka, and D. T. Raske, 1985, International Conference on Nuclear Plant Aging, Availability Factor and Reliability Analysis, San Diego, CA.

Horak, J. A. and V. K. Sikka and D. T. Raske, 1983, "Review of mechanical properties and microstructures of Type 304 and 316 stainless steel after long-term aging," CONF-8310710-6.

Hui, C. Y. and H. Riedel, 1981, International Journal of Fracture **17**, No. 4, 409-425.

Hull, D. and D. E. Rimmer, 1959, Phil. Mag., Vol. 4, pp. 673-687.

Husslage, W. and B. R. Drenth, 1980, in Proc. Second Intl. Conf. on Liquid Metal Technology in Energy Production, CONF-800401, p. 22-48.

Ishiguro, T., Y. Murakami, K. Ohnishi, and J. Watanabe, 1982, "A 2 1/4Cr-1Mo Pressure Vessel Steel with Improved Creep Rupture Strength," ASTM STP 755, pp. 129-147.

James, L.A. and K. W. Carlson, 1985, J. Pressure Vessel Technology, 107.

Jaske, C. E., B. N. Leis, and C. E. Pugh, 1975, Oak Ridge National Laboratory, CONF-751106-61975.

Jetter, R. I., 1998, in PVP-Vol 5. Fatigue, Fracture, and High Temperature Design Methods in Pressure Vessel and Piping, Book No. H01146, ASME, New York, NY.

Jetter, R. I., T. -L. Sham, and R. W. Swindeman, 2009, in proceedings of PVP 2009, PVP2009-77953, American Society of Mechanical Engineering, New York.

JianPing, J., M. Guang, S. Yi, and X. SongBo, 2003, Intl. J. Pressure Vessels and Piping, Vol. 80, pp. 389-396.

Jitsukawa, S., M. Tamura, B. van der Schaff, R. L. Klueh, A. Alamo, C. Petersen, M. Schirra, P. Spaetig, G. R. Odette, A. A. Tavassoli, K. Shiba, and A. Kimura, 2002, J. Nucl. Mater., 307-311, Part 1, p179.

JNC, 2003, TN9450 2003-004, Material test data of 2.25Cr-1Mo Steel and Mod.9Cr-1Mo Steel.

Jones, W. B., 1981, in Ferritic Steels for High-Temperature Applications, Proc. ASM Inter. Conf. Production, Fabrication, Properties and Application of Ferritic Steels for High-Temperature Applications, p. 221.

Kannan, R., R. Sandhya, V. Ganesan, M. Valsan, and K. Bhanu Sankara Rao, 2009, J. Nucl. Mater. 384, 286.

Kawashima, F., A. Ishikawa, and Y. Asada, 1999, Nuclear Engineering and Design, Vol. 193, 327–336.

Kim, J. T., B. H. Kim, B. O. Kong, and D. J. Kim, 2006, PVP2006-ICPVT-11-93218, Proceedings of PVP2006-ICPVT-11, 2006 ASME Pressure Vessels and Piping Division Conference, July 23-27, 2006, Vancouver, BC, Canada.

Kim, S. and J. R. Weertman, 1988, Metall Trans. A 19A, 999.

Klueh, R. L. and D. R. Harries, 2001, Monograph 3, published by ASTM.

Klueh, R. L., 1977, CONF-771010-5.

Klueh, R. L., 1981, J. Nucl. Mater. 96, 187.

Klueh, R. L., 1983, "Tensile behavior of three commercial ferritic steels after low-temperature irradiation," CONF-830659-2.

Klueh, R. L. and A. T. Nelson, 2007, Proc.1st Symp. on Nuclear Fuels and Structural Materials for Next Generation Nuclear Reactors, *J.Nucl.Mats*. 371, Issues 1-3, pp 1-384.

Klueh, R. L. and D. R. Harries, 2001, in High-Chromium Ferritic and Martensitic Steels for Nuclear Applications, ASTM West Conshohocken, PA.

Kobayashi, T., 1984, Engineering Fracture Mechanics, 19, 49.

Kohno, M. and M. Katsumata, 1992, J. Iron & Steel Inst. Japan, 78, 1593.

Korth, G. E. and M. D. Harper, 1976, Properties of Reactor Structural Alloys after Neutron or Particle Irradiation, ASTM STP-570, p. 172.

Krempl, E., 1999, in Creep and Damage in Materials and Structures, Eds. H. Altenbach and J.J. Skrzypek, Springer-Verlag, New York, pp. 285-348.

Kschinka, B. A. and J. F. Stubbins, 1989, Mater. Sci. Eng. A110, 89.

Kushima, H., T. Watanabe, M. Murata, K. Kamihira, H. Tanaka, and K. Kimura, 2005, European Creep Collaborative Committee (ECCC) Creep Conference; 20050912-14, London.

Landes, J. D. and J. A. Begley, 1976, in Mechanics of Crack Growth, ASTM STP 590, American Society for Testing and Materials, Philadelphia, PA, pp. 128-148.

Lemaitre, J. and J. -L. Chaboche, 1994, Mechanics of Solid Materials, Cambridge University Press.

Lemaitre, J., 1979, Trans. ASME J. Eng. Mater. Technol, Vol. 101, pp. 284-292.

Li, M. and S. J. Zinkle, 2004, J. ASTM Int. 1, 502.

Li, M. and S. J. Zinkle, 2005, J. ASTM International, 2.

Li, M., and S. J. Zinkle, 2007, Journal of Nuclear Materials, Vol. 361, Issues 2-3, 15, pp. 192-205.

Liaw, P. K. and A. Saxena, 1986, Final Report CS-4688, Electric Power Research Institute.

Maiya P. S. and S. Majumdar, 1977, Met. Trans. 8A, 1651.

Majumdar, S. and P. S. Maiya, 1976, Symp. On Creep-Fatigue Interaction, ASME MPC-3, R. M. Curran, Ed., American Society of Mechanical Engineers, New York, pp. 323-335.

Majumdar, S. and P. S. Maiya, 1979, Can. Metall. Q, Vol. 18, pp. 57-64.

Majumdar, S. and P. S. Maiya, 1980, J. Eng. Mater. Technol., Vol. 102, pp.159-167.

Majumdar, S. and P.S. Maiya, 1978, Inelastic Behavior of Pressure Vessel and Piping Components, PVP-PB-028, American Society of Mechanical Engineers, New York, pp. 43-54.

Majumdar, S., 1980, Mech. Prop. Design Data Program Semiannual Report for Period Ending July 31, 1980, ORNL/MSP/1.3-80/2, pp. 2-46, 2-47, 2-48.

Majumdar, S., 1981, Argonne National Laboratory, unpublished information.

Majumdar, S., Meimei Li, K. Natesan, T. -L. Sham, and R. K. Nanstad, 2009, ANL-AFCI-263, Argonne National Laboratory.

Majumdar, S., P. S. Maiya, and M. K. Booker, 1981, Argonne National Laboratory, unpublished information.

Manson, S. S., 1973, in Fatigue at Elevated Temperatures, eds. A. E. Carden, A. J. McEvily, and C. H. Wells, ASTM STP 520, American Society for Testing Materials, Philadelphia, PA, 744-782.

Manson, S. S., G. R. Halford, and M. H. Hirschberg, 1971, Proc. 1st Symp. on Design for Elevated Temperature Environment, San Francisco, May 10-12, pp. 12-24.

Marshall, M. 1984, Austenitic Stainless Steels–Microstructure and Mechanical Properties, Elsevier Applied Science Publishers, London and New York.

Matsuoka, S., S. Kim, and J. R. Weertman, 1984, pp. 507-16 in Proc. Topical Conference on Ferritic Alloy for Use in Nuclear Energy Technologies, Snowbird, Utah, June 19-23, 1983, The Metallurgical Society of the American Institute of Mining, Metallurgical, and Petroleum Engineers, New York.

McCabe, D. E., R. K. Nanstad, and M. A. Sokolov, 2000, in Effects of Radiation on Materials: 19th International Symposium, ASTM STP 1366, pp. 306-319.

Min, B. K. and R. Raj, 1978, Fatigue Mechanisms, J. T. Fong, Ed., ASTM STP 675, pp. 569-591.

Mohrmann, R., T. Hollstein, R. Westerheide, 1998, in Materials for Advanced Power Engineering, Proceedings of the 6th Liege Conference, Volume 5, Part 1.

Moosbrugger, J.C., 1992, Journal of Engineering Materials and Technology, Vol. 114, pp. 354-361.

Nanstad, R. K., D. E. McCabe, M. A. Sokolov, and J. G. Merkle, 2007, Paper PVP2007-26651, Proceedings of PVP 2007, ASME Pressure Vessel and Piping Division Conference.

Natesan, K., M. Li, O. Chopra, S. Majumdar, 2009, J. Nucl. Mater. 392, 243.

Natesan, K., M. Li, S. Majumdar, R. K. Nanstad, and T. –L. Sham, 2008, Argonne National Laboratory report, ANL-AFCI-244.

Nielsen, H. S. and V. Tvergaard, 1998, Int. J. of Damage Mechanics, Vol. 7, pp. 3-23.

Odette, G. R., T. Yamamoto, H. Kishimoto, M. A. Sokolov, P. Spatig, W. J. Yang, J. W. Rensman, and G. E. Lucas, 2004, J. Nucl. Mater., 329-333, 1243-1247.

Ogata, T. and M. Yaguchi, 2005, ECCC Creep Conference.

Ohashi, Y., M. Kawai, and T. Momose, 1986, J. Engrg. Mat. and Tech., 108, 68-74.

Ohji, K. and S. Kubo, 1988, in High Temperature Fracture and Fatigue, Current Japanese Materials Research, Vol. 3, Elsevier Applied Science, Tokyo, pp. 91-113.

Ohji, K., K. Ogura and S. Kubo, 1979, Japan Society of Mechanical Engineering, No.790-13, 18-20

Ohno, N., 1982, Journal of Applied Mechanics, Vol. 49, pp. 721-727.

Ohno, N., and J. -D. Wang, 1993, International Journal of Plasticity, Vol. 9, pp. 375-390.

Ohno, N., and M. Abdel-Karim, 2000, Journal of Engineering Materials and Technology, Vol. 122, pp. 35-41.

Ohno, N., M. Abdel-Karim, M. Kobayashi, and T. Igari, 1998, International Journal of Plasticity, Vol. 14, pp. 355-372.

ORNL/9CR/90-2, 1990, JAPC-USDOE Joint Study on Structural Design Methods and Data for Modified 9 Cr-1 Mo Steel–Annual Report for the period April1, 1989-March 31, 1990.

ORNL/9CR/91-1, 1991, JAPC-USDOE Joint Study on Structural Design Methods and Data forModified 9 Cr-1 Mo Steel–Annual Report for the period April 1, 1990–March 31, 1991

ORNL/9CR/92-2, 1992, JAPC-USDOE Joint Study on Structural Design Methods and Data forModified 9 Cr-1 Mo Steel–Annual Report for the period April 1, 1991–March 31, 1992.

Paul, V. T., S. Saroja, and M. Vijayalakshmi, 2008, J. Nucl. Mater. 378, 273.

Pedersen, O. B., 1990, Acta. Metall. Mater. 38, 1221.

Prager, M., 1998, Fitness-for-Service Evaluations in Petroleum and Fossil Power Plants, PVP-Vol. 380, ASME, pp. 291-299.

Prager, M., 2009, STP-PT-027, ASME ST LLC, New York, NY.

Pugh, C. E., K. Liu, J. M. Corum, and W. L. Greenstreet, 1972, ORNL/TM/3602, Oak Ridge National Laboratory.

Rao, K. B. S., M. Valsan, V. S. Srinivasan, S. L. Mannan, 1996, Proc. Tech. Committee Meeting, Manchester, UK, 11-13.

Rao, K. R., 2002, Companion Guide to the ASME B&PV Code.

Raske, D. T., 1977, CONF-770524-1.

RCC-MR, Design and Construction Rules for Mechanical Components of Fast Breeder Reactor Nuclear Island, French Design Code for Fast Reactors issued by AFCEN.

Rensman, J. W, 2005, NRG Iradiation Testing; Report on 300C and 6-C irradiated RAFM steels, NRG Petten (20023/05.68497.P).

Rensman, J. W, J. van Hoepen, B. M. Bakker, R. den Boef, P van den Broek, and E. D. L. van Essen, 2002, J. Nucl. Mater., 307-311, Part 1, 1113.

Reytier, M., 2004, Power Plant: Operation Maintenance and Materials Issues **3**, No. 2.

Rice, J. R. 1968, Journal of Applied Mechanics, 35, 379-386.

Rice, J. R., 1981, Acta Metall., Vol. 29, pp. 675-681.

Rie, K.T., R. M. Schmidt, B. Ilschner, and S. W. Nam, 1988, in Low Cycle Fatigue, ASTM STP 942, ASTM, Philadelphia, p. 313.

Riedel, H. and J. R. Rice, 1980, Fracture Mechanics: Twelfth Conference, ASTM STP 700, American Society for Testing and Materials, Philadelphia, PA, 112-130.

Riedel, H. and V. Detampel, 1987, International Journal of Fracture, 33, 239-262.

Riedel, H. and W. Wagner, 1981, Advances in Fracture Mechanics, Proceedings of ICF5, eds. D. Francois et al., Vol. 2, Pergamon Press, New York, NY, 683-688.

Riedel, H. and W. Wagner, 1985, Advances in Fracture Research '84 – Proceedings of ICF6, Vol. 3, eds. S. R. Valluri et al., Pergamon Press, Oxford, UK, 2199-2206.

Riedel, H., 1981, Journal of the Mechanics and Physics of Solid 29, 35-49.

Riedel, H., 1985, Flow and Fracture at Elevated Temperature, ed. R. Raj, American Society for Metals, Metals Park, OH, 1985, 149-177.

Riedel, H., 1986, Fracture at High Temperatures, Springer-Verlag, New York, NY.

Riedel, H., Elastic-Plastic Fracture: Second Symposium, Volume I – Inelastic Crack Analysis, ASTM STP 803, eds., C. F. Shih and J. P. Gudas, American Society for Testing and Materials, Philadelphia, PA, 1983, I-505-I-520.

Riou, B. 2007, Doc. 12-9045964-001.

Ritchie, R. O., F. Knott, and J. R. Rice, 1973, J. Mech. Phys. Solids, 21, p 395.

Rive, D., C. Escaravage, and B. Riou, 1991, SMiRT 11 Transactions, Vol L, pp. 139-144.

Ruggles, M. B. and T. Ogata, 1994, ORNL/M-3198.

Sanchez-Hanton, J. J. and R. C. Thomson, 2007, Mater. Sci. Eng. A 460-461, 261.

Sasikala, G. and S. K. Ray, 2008, Matls Sci and Eng. A 479, 105-111.

Sathyanarayanan, S., A. Moitra, K. G. Samuel, G. Sasikala, S. K. Ray, and V. Singh, 2008, Matls. Sci. and Eng., A, 488, 519-528.

Sauzay, M., B. Fournier, M. Mottot, A. Pineau, and I. Monnet, 2008, Mater. Sci. Eng., A 483-484, 410.

Sauzay, M., H. Brillet, I. Monnet, M. Mottot, F. Barcelo, B. Fournier and A. Pineau, 2005, Mater. Sci. Eng. A 400–401, pp. 241–244.

Saxena, A., 1986, Fracture Mechanics: Seventeenth Volume, ASTM STP 905, eds. J.H. Underwood et al., American Society for Testing and Materials, Philadelphia, PA, 185-201.

Saxena, A., 1998, Nonlinear Fracture Mechanics for Engineers, CRC Press LLC.

Saxena, A., J. Han and K. Banerji, 1988, Topical Report EPRI CS-5585, Electric Power Research Institute.

Schmitt, R. and W. Scheibe, 1983, "Effects of hold-time and irradiation on the low-cycle fatigue behavior of 1.4948 (AISI 304) and 1.4919 (AISI 316)," SMiRT7, L10-5.

Schneider, H-C, B.Dafferner, and J.Aktaa, 2003, J.Nucl.Mater. 321, p135.

Shankar, V. and M. Valsan, 2006, Mater. Sci. Eng. A437, 413.

Shiba, K., M Suzuki, and A. Hishinuma, 1996, J Nucl.Mater. 233-237, p 30.

Shibli, I. A. and N. Mat Hamata, 2001, International Journal of Pressure Vessels and Piping 78, 785-793.

Shibli, I. A., B. Al-Abed, and K. Nikbin, 1998, Materials at High Temperatures, 15, No. 3/4, 143-149.

Sikka, V. K. 1982, ORNL/TM-8371, Oak Ridge National Laboratory, Oak Ridge, TN.

Sklenicka, V., K. Kucharova, M. Svoboda, L. Kloc, J. Bursk, and A. Kroupa, 2003, Mater. Charact. 51, 35.

Smith, D. L., G. J. Zeman, K. Natesan, and T. F. Kassner, 1976, Proc. Intl. Conf. Liquid Metal Technology in Energy Production, CONF- 760503-Pl, 359.

Sonoya, K., I. Nonaka and M. Kitagawa, 1991, ISIJ International 31, 1424.

Spera, D. A., 1969, "Calculation of Thermal Fatigue Life Based on Accumulated Creep Damage," NASA Technical Note, NASA-TN-D-5489.

Srinivasan, V. S., A. Nagesha, and M. Valsan, 2005, Trans. Indian Ins. Met. 58. Nos 2-3. pp. 261-267.

Srinivasan, V. S., A. Nagesha. M. Valsan. K. Bhanu Sankara Rao. S.L. Mannan, and Baldev Raj, 2005, Trans. Indian Ins. Met. Vol 58. Nos 2-3. pp. 261-267.

Swindeman, R. W. 1985, Proceedings of ASTM Symposium on Low Cycle Fatigue - Directions for the Future, Sponsored by ASTM Committee E-9 on Fatigue, Sept. 30-Oct. 4 , 1985, Bolton Landing, N.Y. , American Society for Testing and Materials, Philadelphia.

Swindeman, R. W., 1988, in Low Cycle Fatigue, ASTM STP 942, H.D. Solomon et al. Eds., American Society for Testing and Materials, Philadelphia, pp. 107-122.

Swindeman, R. W., 2008, Draft Task 6 Report, ASME ST LLC.

Swindeman, R. W., 2009, ASME/DOE Gen-IV Materials Project, Task 6, Part II and Part III.

Swindeman, R. W., P. J. Maziasz, and C. R. Brinkman, 2000, Proc. 2000 Intern Joint Power Generation Conference, July 23-26, p. 399.

Swindeman, R. W., P. J. Maziasz, and I. G. Wright, 2001, presented at the EPRI Conference on 9Cr Materials Fabrication and Joining Technologies, July 10-11, Myrtle Beach, South Carolina, USA.

Tabuchi, M., K. Yagi, and T. Ohba, 1990, ISIJ International 30, No. 10, 847-853.

Tabuchi, M., T. Watanabe, K. Kubo, M. Matsui, J. Kinugawa, and F. Abe, 2001, Int. J. Press. Ves. Pip. 78, 779.

Tabuchi, M., Takashi Watanabe, Kiyoshi Kubo, Masakazu Matsui, Junichi Kinugawa and Fujio Abe, 2000, in the Proceedings of the 2nd International HIDA Conference on 'Advances in Defect Assessment in High Temperature Plant', 4-6 Oct. 2000, held at MPA, Stuttgart, Germany.

Taira, S., 1962, Creep in Structures, N.J. Hoff, Ed., Springer-Verlag, Berlin, pp. 96-119.

Takahashi, Y. and M. Tabuchi, 2008, in Advances in Materials Technology for Fossil Power Plants Proceedings from the 5th International Conference, p. 762.

Takahashi, Y., 2008, International Journal of Pressure Vessels and Piping, Vol. 85, pp. 406-422.

Wakai, T., C. Poussard, and B. Drubay, 2002, Nuclear Engineering and Design 212, 125- 132.

Wakai, T., C. Poussard, and B. Drubay, 2003, Nuclear Engineering and Design 224, 245-252.

Wallin, K., 1984, *Engineering Fracture Mechanics*, 19(6), 1085-1093.

Warening, J. 1981, Fatigue Engg. Mater. Struct. 4, 131.

Wasmer, K., K. M. Nikbin, and G. A. Webster, 2003, International Journal of Pressure Vessels and Piping, 80, 489-498.

Webster, G. A. and R. A. Ainsworth, 1994, High Temperature Component Life Assessment, Chapman and Hall, London.

Wood, D. S., J. Wynn, A. B. Baldwin and P. O'Riordan, 1980, Fatigue Engg. Mater. Struct. 3, 89.

Yaguchi, M., and Y. Takahashi, 1999, JSME International Journal, Series A, Vol. 42, No. 1, pp 1-10.

Yaguchi, M. and Y. Takahashi, 2000, International Journal of Plasticity, Vol. 16, pp. 241–262.

Yaguchi, M. and Y. Takahashi, 2005a, International Journal of Plasticity, Vol. 21, pp. 43–65.

Yaguchi, M. and Y. Takahashi, 2005b, International Journal of Plasticity, Vol. 21, pp. 835–860.

Yamaguchi, K., M. Hayakawa, K. Kobayashi, Strength, 2006, Fracture and Complexity, vol. 4, p. 55.

Yamamoto, T., G. R. Odette, H. Kishimoto, J. W. Rensman, and P Miao, 2006, J. Nucl. Mater. 356, 27-49.

Yong, J. O., S. W. Nam, and J. H. Hong, 2000, Metall. Mater. Trans. A 31A, 1761.

Yoon, J. H. and E. P. Yoon, 2006, Metals and Materials Int., 12 (6), 477-482.

Yoon, K. B., A. Saxena, and P. K. Liaw, 1993, International Journal of Fracture, 59, 95-114.

Yukawa, S. 1993, Welding Research Council Bulletin 378, Welding Research Council, New York, NY..

Zhu, L. H., Q. Z. Zhao, H. C. Gu, and Y. S. Lu, 1991, Eng. Frac. Mech., 64, 327-336.

Nuclear Engineering Division
Argonne National Laboratory
9700 South Cass Avenue, Bldg. 212
Argonne, IL 60439-4838

www.anl.gov

Argonne National Laboratory is a U.S. Department of Energy laboratory managed by UChicago Argonne, LLC